UNIVERSITE MONTPELLIER II
SCIENCES ET TECHNIQUES DU LANGUEDOC

THESE de DOCTORAT

pour l'obtention du titre de

DOCTEUR DE L'UNIVERSITE MONTPELLIER II

Discipline :	Mathématiques et modélisation
Ecole doctorale :	I2S (Information, Structures, Systèmes)
Laboratoire d'accueil :	CERFACS
Directeur de thèse:	Franck Nicoud

présentée et soutenue publiquement

par

M. **Camilo F. SILVA**

le 9 Novembre 2010

NUMERICAL STUDY OF COMBUSTION NOISE IN GAS TURBINES

---

composition du JURY

W. Schröder	Professor RWTH Aachen University	Rapporteur
W. Polifke	Professor TU München	Rapporteur
T. Schuller	Professor Ecole Centrale Paris	Examinateur
A. Morgans	Professor Imperial College	Examinateur
S. Moreau	Professor Université de Sherbrooke	Examinateur
B. Mohammadi	Professor Université de Montpellier II	Examinateur
F. Nicoud	Professor Université de Montpellier II	Directeur de Thèse

Résumé

La recherche en bruit de combustion est de nos jours majoritairement consacrée au développement d'outils de calcul du bruit rayonné par les flammes. Les méthodes actuelles de CFD telles que la LES ou la DNS sont capables de fournir le champ acoustique rayonné par des sources de bruit, mais elles sont cependant limitées, en raison de leur fort coût de calcul, à des domaines de faible taille. Pour surmonter cette limitation, des méthodes hybrides ont été proposées dans le passé. Dans cette approche, les sources de bruit sont découplées du son rayonné et calculées par les méthodes DNS et LES. L'analogie acoustique permet alors de calculer le son rayonné par des codes acoustiques, moins coûteux en temps de calcul.

L'objet de cette étude est de développer un outil numérique sur la base de l'analogie acoustique de Phillips pour de faibles nombres de Mach. Il permet de prendre en compte l'impact des conditions limites sur le champ acoustique résultant. La LES et le code de calcul acoustique développé ont été utilisés pour évaluer le bruit produit par une flamme turbulente confinée. Les deux techniques donnent des résultats en accord tant que les bonnes quantités sont comparées: il a été observé que le signal de pression obtenu directement à partir de la LES contient une quantité non négligeable de fluctuations hydrodynamiques, lesquelles doivent être négligées si on cherche à comparer seulement les champs acoustiques issus des deux codes.

L'hypothèse d'un nombre de Mach faible est totalement réaliste si l'on considère l'écoulement présent dans une chambre de combustion. Elle conduit à des simplifications significatives lorsque les analogies acoustiques sont considérées. Cependant, cette hypothèse ne peut pas être utilisée pour l'écoulement en amont (entrée d'air, compresseur) ou en aval (turbine, tuyère) des chambres de combustion aéronautiques. Un outil numérique a été développé pour pallier à ce problème. Il est basé sur les équations d'Euler Quasi-1D, qui prennent en compte des écoulements convectifs, non isentropiques et non isenthalpiques. Cet outil permet d'estimer les conditions limites acoustiques qui doivent être imposées sur les entrées/sorties d'une chambre de combustion pour prendre en compte la présence d'un écoulement de nombre de Mach non négligeable, alors que les calculs acoustiques sont eux effectués sous cette hypothèse fortement restrictive.

Mots clés : *LES, bruit de combustion, analogies acoustiques*

Abstract

Today, much of the current effort in combustion noise is the development of efficient numerical tools to calculate the noise radiated by flames. Although unsteady CFD methods such as LES or DNS can directly provide the acoustic field radiated by noise sources, this evaluation is limited to small domains due to high computational costs. Hybrid methods have been developed to overcome this limitation. In these schemes, the noise sources are decoupled from the radiated sound. The sources are still calculated by DNS or LES solvers whereas the radiated sound is evaluated by acoustic tools using an acoustic analogy.

In the present study, a numerical tool based on the Phillips' analogy for low Mach numbers flows has been developed. This tool accounts for the role of the boundary conditions in the resulting acoustic field. Both LES and the acoustic solver developed here are used to assess the noise produced by a turbulent swirled-stabilized flame generated in a staged combustor. Good agreements are obtained between both techniques as long as the good quantities are compared: the pressure signal obtained directly from LES contains a non negligible amount of hydrodynamic fluctuations that must be removed when a suitable comparison is sought with the acoustic solver.

The low Mach number assumption is completely realistic when considering the flow within a combustion chamber; it also conducts to considerable simplifications when leading with acoustic analogies. However, it cannot be used for the upstream (air-intake, compressors) and downstream (turbines, nozzle) of an aeronautical combustion chamber. A numerical tool is developed based on the quasi-1D Linearized Euler Equations in order to account for convective, non-isentropic and non-isenthalpic flows. By means of this tool, it is possible to estimate the acoustic boundary conditions that should be imposed at the inlet/outlet of a given combustion chamber when performing low-Mach number acoustic computations.

keywords: *LES, combustion noise, acoustic analogies*

Contents

List of Figures

List of Tables

1

General Introduction

Contents

Seeing a powerful jet aircraft take off and land, listening to its strong fierce roars when it is passing by, still inspire awe in many of us. Captured by the magic of flight we usually forget all the possible annoyances that aviation can produce. For instance, this amazing roar can quickly become a painful nuisance as there is one departure every 30 seconds in some of the biggest airports around the world [46]. In our skies, up to 25 millions flights take place each year and according to ICAO air-traffic forecasts, this number will double by the year 2025 [35]. In terms of ease of mobility this is good news for humanity, however, some problems can be magnified: consumption of non-renewable energy sources; air pollution; and no less important, noise. In the last few decades, engineers and scientists have been working together on these three subjects. Their understanding, prediction and mitigation is crucial.

Noise beyond 75 dB has been proved to be very harmful [58] (see Table 1.1) and particularly annoying for frequencies between 3000Hz-6000 Hz [104] [1]. According to the International Program on Chemical Safety (WHO 1994), an adverse effect of noise is defined as a change in the morphology and physiology of an organism that results in: noise-induced hearing impairment; interference with speech communication; disturbance of rest and sleep; psychophysiological, mental-health and performance effects; effects on residential behavior and annoyance; as well

Noise Produced (dB)	Exposed population highly annoyed (%)
45	1
50	5
55	10
60	17
65	26
70	37
75	49

Table 1.1: EU recommended relationships between annoyance and aircraft noise

as interference with intended activities [104]. But humans are not the only ones that suffer from noise pollution; significant structural damage can occur to aircrafts when vibrations are generated at specific frequencies.

But what is aircraft noise? Aircraft noise is the superposition of propagating pressure fluctuations that are generated by different mechanisms belonging to the aircraft. These pressure fluctuations propagate to both inwards into the cabine, affecting the passengers, and outwards to the environment, annoying the inhabitants of nearby regions. Within an aircraft, several sources of noise can be identified as shown in Fig. (1.1)

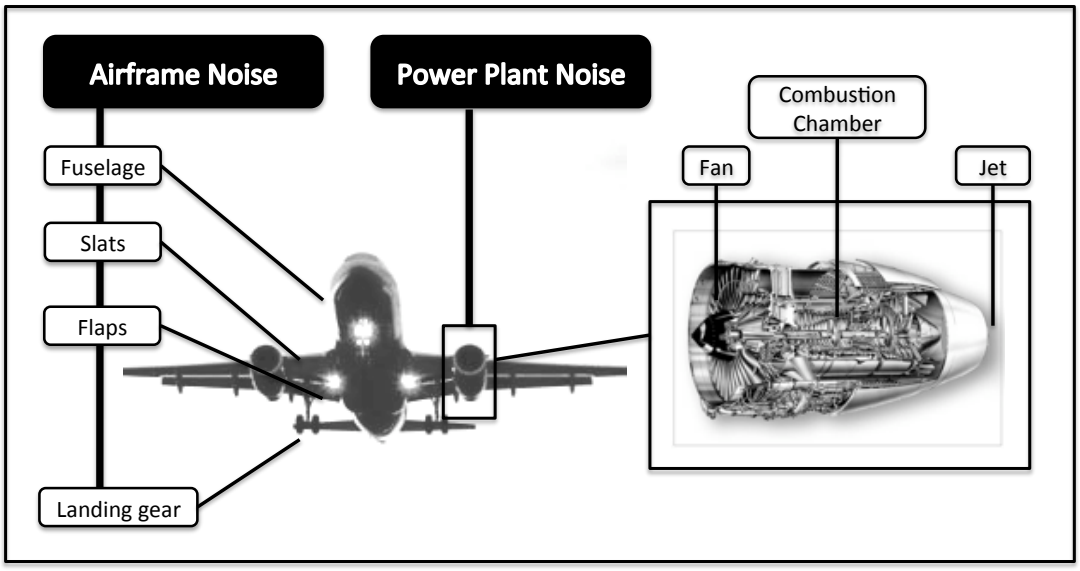

Figure 1.1: Main sources of aircraft noise

[1]Our hearing systems are not equally sensitive to all sound frequencies (ISO 1987a). Thus, not all frequencies are perceived as being equally loud at the same sound pressure level, and when calculating overall environmental noise ratings it is necessary to consider sounds at some frequencies as more important than those at other frequencies.

One can identify from Fig. (1.1) the airframe noise and power-plant noise. The scale of turbulence induced by the airframe varies considerably and a multifrequency noise signal is then produced. During the final landing approach, airframe noise rises significatively. The deployment of high-lift devices (slats and flaps) and the landing gear not only create drag but also considerable levels of noise. Of these two sources, the landing gear produces the most intense noise, giving a spectrum-level increase of 5-10 dB and changing the directivity of the overall source to near-spherical [94]. Aircraft propulsion systems, however, are without a doubt the major sources of aircraft noise. Propulsion systems come in many forms: the jet, the turbofan, piston and turbine driven propellers, the helicopter rotor and the developing 'open rotor' or advanced, high-cruise-speed propeller. The level of noise produced by any of these engines is related to the maximum thrust level and the thermodynamical cycle performed. As a consequence, take-off is one of the noisiest phases of flight (75 dB-85 dB at about 3 miles) [58] since at this stage, the highest levels of power are reached.

Three main sources of noise can be identified in a turbofan aeronautical engine: the fan-stator interaction; the core noise; and the exhaust jet flow. Vortex shedding is created when the incoming stream of air flows through the fan. These wakes slap against the stators like waves on a beach generating in turn important acoustic waves. The design of blades (profile, thickness, number) for both fan and stator, the angular velocity of the fan and the absorption treatment for tones in the inlet nacelle/bypass air ducts are the main mechanisms to control fan noise. Core noise is the noise produced inside the combustion chamber and is related to the interactions that can arise between the flame and the surroundings. No significant progress has been done to control core noise so far as it is little understood. Absorbing materials to damp acoustic waves is out of the question in this extremely hot region; any fundamental advancement would consist in controlling combustion dynamics. Finally, it remains the so-called jet noise. The pure jet engines and the low-bypass-ratio engines have extremely high exhaust velocities, which in turn cause the highest levels of noise when compared to fan and core noise. Strong turbulence is created when a high velocity stream of hot gases is discharged into the atmosphere. The shear layer generated accounts for strong fluctuations of the largest turbulent eddies which in turn generate big amplitude and low frequency pressure waves. Levels of jet noise have been decreased mainly by velocity reduction of the jet flow that mixes with the ambient air. The design of high by-pass ratio engines has been conclusive on this matter since reductions up to 10 dB have been reached [58]. As a conclusion, it can be stated that due to the different improvements in the science of noise reduction, relevant to jet and fan noise, the relative importance of combustion noise tends to increase. Those seeking advancement in the field of noise reduction are now looking towards combustion.

1.1 Noise in a combustion chamber

Acoustics in a combustion chamber (CC) is generated by different physical mechanisms which, coupled or not, occur either inside, outside or at the boundaries of the combustor:

- **Inside:** A combustion chamber is the part of an engine in which fuel is burnt. In aeronautical engines, this chemical reaction should generate considerable levels of thermal power $\int \dot{Q} dv$ and for that reason flames must be turbulent and generally stabilized by a swirled flow [74]. Noise is linked to fluctuations of thermodynamical quantities (density ρ, pressure p, temperature T, entropy s, ...) that are somehow generated by the unsteady velocity field and the turbulent flame.

- **Outside:** Clearly, acoustic pressure waves exist as well both upstream (compressor stages and diffusor) and downstream (turbines and nozzle). These pressure oscillations might travel either with or against the mean flow reaching the combustion chamber. Subsequently, they interact with the turbulent flow/flame and the surroundings (walls, multiperforated plates, injectors, etc).

- **At the combustion chamber boundaries:** Acoustic waves can be produced when either vortical or entropy waves reach zones of non-homogeneous mean flow [12, 55]. It usually happens at the 'HPD' (high pressure distributor) just after the combustion chamber.

It is naive to believe that all these phenomena always happen independently of each other. In some cases, they are totally coupled and their study becomes clearly extremelly difficult. Classically, one can identify three different interactions that in the worst cases, when acoustic energy is not efficiently dissipated, lead to instabilities:

- **flame/entropy/acoustics** In this case hot spots (entropy) are produced by the unsteady flame. These hot spots travel downstream at the flow velocity until reaching the HPD where acoustic waves are generated [12, 55]. These acoustic waves will travel upstream attaining the reactive region. They will modify, as a consequence, the flame dynamics and therefore the fluctuating entropy. When acoustic and entropy waves are coupled, a combustion instability called 'rumble' might appear. This instability is characterized by its low frequencies (50-150 Hz) and can take place during the startup phase of aeronautical engines [23].

- **turbulence/acoustics/boundaries** Everywhere where turbulence is enhanced, acoustic waves are generated. Acoustic waves can propagate until they are reflected on any boundary and travel-back reaching the vortical zone. Turbulence, i.e. hydrodynamic perturbations, will be in turn modified by this acoustic field and the close loop may restart. If the hydrodynamic preferential frequency coincides with a multiple of the acoustic resonant frequency of the specific configuration, significant unstable interactions may occur.[81]. A 'hydrodynamic instability' would be said to have appeared.

- **flame/acoustics/boundaries** A volumetric expansion due to the unsteady heat release is created. Acoustic waves are therefore generated and propagate until they attain reflecting boundaries where they will be sent back. These waves propagate back, reaching the flame and consequently influencing it by modifying the unsteadiness of the heat release.

When an unstable coupling of this nature takes place, one will talk about 'thermoacoustics instabilities' [78, 22]. This is a broad field of study within the combustion community [48]. Efforts have been done over several decades to understand the influence of acoustics on flame dynamics [78, 18, 19, 73, 87, 49, 86, 88, 63]

Understanding combustion noise in real engines means understanding all these coupled phenomena. However, the most clear starting point to study combustion noise is to 'un-couple' all these mechanisms, focusing on one at a time. As a consequence, it is assumed that the sources of noise (flame, turbulence, etc) are independent of the acoustic field generated. In other words, that no instabilities occur. Still, the following noise generation phenomena remain and must be considered:

- **flame/entropy/acoustics → 'indirect combustion noise'**. The sources of noise are the entropy waves when crossing non-homogeneous regions (zones with mean flow gradients).
- **Turbulence/acoustics → 'aerodynamic noise'**. The unsteady turbulent field is the source of noise. The influence of walls as scattering/reflecting mechanism (ex: wing airfoils, cavities) are also usually considered into the physical formulations.
- **flame/acoustics → 'direct combustion noise'**. The unsteady heat release acts as a distribution of acoustic monopoles which generate pressure fluctuations.

1.2 Scope of the present work

Combustion noise has been widely studied in open flames. These predictions are based on what is known as hybrid methods. In these approaches the sources of noise are computed separately from the radiated acoustic field. Unsteady CFD methods as LES or DNS are used to compute the sources of noise whereas wave equations coming from acoustic analogies are employed to compute the sound radiation produced by these sources. LES or DNS are rarely used to estimate acoustic fluctuations directly, since these fluctuations are much smaller in comparison to first order fluctuations, as velocity or temperature perturbations. The first objective of this thesis regards this concern. It is seen how much the computation resolution of LES influence the quality of the estimations of noise. A second objective is linked to the hybrid approach for the estimation of combustion noise. No significative studies within the combustion community have been performed to evaluate whether or not hybrid approaches are appropriate to compute noise of confined flames. Confinement of flames leads to possible complexities: one of them is that pressure fluctuations produced by the flame might contain an important contribution of hydrodynamics since in confined flames turbulence might be significative everywhere. Another significant concern is the evaluation of acoustic-flow interactions. When sound propagates through a quiescent homogeneous field, as in the far field for an open flame, no acoustic-flow interactions exist. In confined domains, on the contrary, this interaction might

be crucial everywhere and therefore acoustic phenomena as scattering or refraction might be of considerable importance. Other issue to take into account in noise produced by confined flames is the influence of acoustic boundary conditions since acoustic waves reflected by the system boundaries contribute to the overall noise inside the domain. During this thesis, an acoustic solver has been developed that resolves a simplified version of the Phillips' equation. The purpose of this acoustic tool is to understand the problematic described above and to state the possible advantages and constraints that a hybrid approach might present when estimating noise from confined flames. Also, procedures and numerical tools for post-processing LES data are developed.

An important issue of low Mach number acoustic codes, as the Helmholtz solvers or the acoustic solver developed during this thesis, is the implementation of reliable acoustic boundary conditions at inlets/outlets. These boundary conditions are expressed usually in terms of the acoustic impedance that in turn depends on the mean flow through the boundaries. The acoustic impedance is hardly obtained either experimentally or numerically. In order to obtain values of the acoustic impedance at the inlet/outlet of the combustion chamber from numerical CFD simulations it would be necessary to model the entire engine. An alternative then relies on what is known as quasi-1D Linearized Euler solvers. These numerical tools resolve the linearized Euler Equations LEE for systems in which changes in the mean flow, due to changes in the section area, are accounted for (see Fig. 1.2). In despite of this, the majority of the existing linearized Euler solvers consider isentropic and isenthalpic flows. In other words, neither changes in entropy nor in the total pressure are allowed. During this thesis, the development of a quasi-1D Euler solver was performed in which changes in entropy and total enthalpy through the domain are considered. As a consequence, a first approximation of the acoustic impedances at the inlet/outlet of an aeronautical combustion chamber can be obtained including the effect that compression/expansion stages might have on the acoustics of the system.

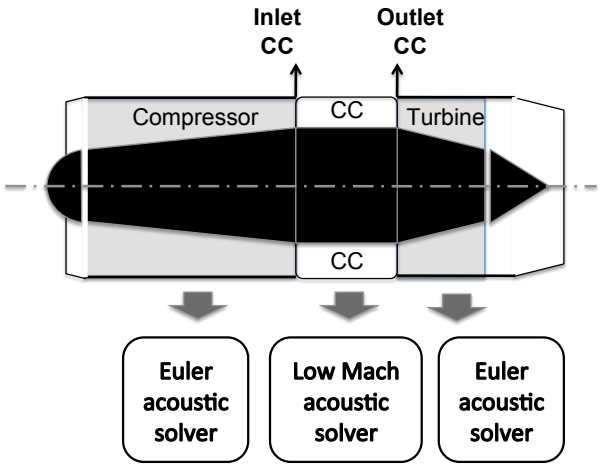

Figure 1.2: Acoustic solvers: The Euler acoustic solver is used beforehand to provide proper boundary conditions to the low Mach number acoustic solver.

1.3 Organization of the manuscript

This manuscript is organized as follows: first, the two considered approaches for the evaluation of combustion noise (the direct and hybrid approaches) are described in the second chapter. The governing equations of turbulent reactive flows are exposed as well as the governing equations for Large Eddy Simulation. Subsequently, both Lighthill and Phillips' analogies are derived from the governing equations and some overview about the analytical solution of the Lightill's analogy is provided. The third chapter is focused on the numerical solution of a simplified Phillips' equation. The acoustic code developed during this thesis (AVSP-f) is explained in order to focus on the discretization of the wave equation and the mathematical procedures involved in the solution of the underlying linear system. The forth chapter presents the test cases set up for the validation of the acoustic code including the noise produced by monopole sources and by a two dimensional laminar premixed flame. In the fifth chapter the computation of the noise generated by a three dimensional turbulent premixed combustor is exposed. Both direct and hybrid approaches are used for the estimation of combustion noise. The sixth chapter consists in a review of the different analytical approaches proposed in the past in order to evaluate impedances of isentropic and isenthalpic quasi-1D ducts [55]. These analytical methods are then compared to the solutions of the quasi-1D LEE system solved thanks to a numerical tool developed (SNozzle) during this work. Finally in the last chapter, the acoustic modes of a real gas turbine combustor are computed by a Helmholtz solver in which the impedance evaluated numerically by SNozzle is imposed as an acoustic boundary condition. The effect of this boundary condition on the acoustic modes evaluated is discussed.

2

Computation of noise generated by combustion

Contents

2.1 Introduction

Studies on combustion noise carried out by Bragg in 1963, recognized that a flame behaves as a monopole radiator [9], due to the isotropic volumetric expansions induced by the dilatation of gases once combustion occurs. Further on, the same year, Smith & Khilam stated that a turbulent flame could be seen as acoustically equivalent to a set of monopole sources, each of them radiating at different strengths, frequencies and phases [95]. Thomas & Williams in 1966 [100] did perhaps the first significative experimental study concerning direct combustion noise.

In their experiment they fill soap bubbles with a reactive mixture and recorded the farfield pressure generated by the burning of each isolated bubble. The noise (far-field pressure signal p') was then expressed in terms of the volume acceleration over the reactive region induced by the non-steady combustion. This expression yields

$$p'(\boldsymbol{r},t) = \frac{\rho_\infty}{4\pi r}\frac{d^2\Delta V}{dt^2} \tag{2.1}$$

where ρ_∞ is the far field air density at the measurement location $\boldsymbol{r}$ and r designates the distance between the compact flame and the observation point. Two years later, Price [76] and Hurle [34] proposed a relation that accounts for the rate of consumption of reactants as responsible for this density dilatation

$$p'(\boldsymbol{r},t) = \frac{\rho_\infty}{4\pi r}\left(\frac{\rho_u}{\rho_b - 1}\right)\left[\frac{dQ}{dt}\right]_{t-\tau} \tag{2.2}$$

In this expression ρ_u/ρ_b designates the volumetric expansion ratio of burnt to unburnt gases, Q the total volumetric rate of consumption of reactants and τ is the time required for acoustic propagation from the combustion region to the measurement point r. Anyway, the first to generalize these studies starting from the Navier-Stokes equations and deriving an analytical expression was Strahle [98]. Following the procedure developed by Lighthill [50, 51], Strahle proposed a rearrengement of the Navier-Stokes equations in which the acoustic field is separated from the generators of combustion noise [99]. In order to obtain a compact formulation, he considers that the acoustic wave length λ is large compared to any flame length scale L ($\lambda \gg L$). This expression, which is valid for low Mach numbers, is recognized as the main result in combustion noise theory [13]

$$p'(\boldsymbol{r},t) = \frac{\gamma - 1}{4\pi r c_1^2}\int_{V_c}\frac{\partial\dot{\omega}_T}{\partial t}\left(\boldsymbol{r}_0, t - \frac{|\boldsymbol{r}-\boldsymbol{r}_0|}{\bar{c}}\right)dV(\boldsymbol{r}_0) \tag{2.3}$$

Here γ is the specific heat ratio, c_1 is the sound speed in the burnt gases and $\dot{\omega}_T$ the volumetric heat release rate in the combustion zone. Equation (2.3) proves the relation (2.2) obtained on a more intuitive basis. The reactive source $\partial\dot{\omega}_T/\partial t$ is an efficient acoustic radiator, a monopole, that has been proved to be much more important when compared to the classical aerodynamic source from Lighithill analogy, the double divergence of the Reynolds tensor, which is in fact a quadrupolar term [32]. A dimensional analysis performed on the sound power produced by these sources in combustion systems shows that the acoustic power from the combustion process is of the order of $1/M^4$ larger than the acoustic power generated by turbulence [102, 38]. Hence, for low Mach-number flows, the quadrupole source term can be neglected. Note that to decrease pressure losses induced by high speed flows, most combustion systems indeed operate at low Mach numbers [105].

There are two main concerns when formulating acoustic analogies[1]:

1. The precision of the acoustic analogy chosen. It depends on the capacity of the propagation operator to take into account the interactions between the acoustic field and the flow itself and, in particular, the effects of convection and refraction of waves.
2. The inclusion of radiating surfaces into the mathematical formulation either as additional sources or merged in the acoustic operator.

In combustion noise formulations derived from Lighthill's analogy, one considers an observer in a uniform medium at rest receiving acoustic radiation from a distribution of sources of sound. It is inherently assumed that the source lies in a limited region which is surrounded by a uniform fluid to which the acoustic wave equation applies. These analogies actually do include scattering mechanisms, but the drawback is that they are implicitly present into the sources formulation [4]. It leads to several constraints since a completely decoupling of sources from the radiated sound is not reached. As a consequence, density fluctuations ρ' cannot be neglected when evaluating this sources, and, if doing so, little errors will be added in the computation of sources. This little errors will be magnified when solving the acoustic analogy and consequently considerable miss-predictions of noise would be obtained. The first significant step to include flow-acoustic interactions in the wave operator is due to Phillips [66] (1961). In this expression mean flow-acoustic interactions are taken into account into the acoustic operator. Some years later Chiu & Summerfield [14] (1974) and Kotake [39] (1975) extended Phillips formulation to reactive flows. The resulting formulation raised several advantages as for example to account for scattering of acoustic waves when changes in the mean sound velocity are present, which is naturally the case for reactive flows. Unfortunately, as shown by Lilley, all the acoustic-flow interactions are not included on the left-hand side of this equation, and flow effects on acoustics are still contained in the linear compressible part of the aerodynamic source term. Lilley [52, 53] proposed an equation in which sound propagation effects are separated from sound generation as explained by Goldstein [31]. The wave operator of Lilley's equation is the correct wave operator containing all mean flow-acoustic interactions. An extension of this equation to reactive flows is proposed by Bailly [4]. Another method to account for all acoustic-flow interactions is to force the Linearized Euler Equations LEE by appropriate source terms [6, 24, 25]. One of the first applications of this numerical strategy was carried out by Béchara [7] for predicting subsonic jet noise. The LEE do not only describe acoustic perturbations: instability waves of the Kelvin-Helmholtz type are also solutions. On the other hand, Bui [10] proposed to use the acoustic perturbation equations (APE) system combined with specific source terms in order to investigate combustion noise. The homogeneous APE system is used to describe wave propagation in the presence of a mean flow without exciting vortical or entropy waves [26]. It should be noted that all refraction effects are not included in the homogenous system [1].

[1]The term 'analogy' refers to the idea of representing a complex fluid mechanism of any aero/thermo-acoustic process by an acoustically equivalent source term and an acoustic operator

The extensions to reactive flows of Lighthill's, Phillip's and Lilley's analogies in addition to LEE and APE formulations have been proved successful for the study of noise generated by open flames [40, 99, 16, 10, 36]. Studying noise radiated by such flames is important in order to characterize the position, directivity and strength of each of the sources present [95]. Anyway, in order to go further in the study of combustion noise the inclusion of reflecting surfaces is mandatory. This is an issue where aeroacoustics is a head on top of combustion acoustics. In aeroacoustics theory, Curle extended Lighthill's analogy in order to account for turbulence-body interactions and introduced a corresponding additional source mechanism that involves the reaction force exerted by the body on the surrounding field, equivalent to an acoustic dipole [20, 85]. This acoustic analogy has been deeply studied in cavity noise. When these bodies are moving at not negligible velocities Curle's analogy must be re-formulated. This was done by Ffowcs-Williams and D. L. Hawkings at the end of the sixties [106]. Ffowcs-Wiliams and Hawkings theory has been broadly implemented in the study of noise radiation by wing airfoils [60, 15] and aerodynamic rotors [27].

2.2 Direct Computation of noise through Large Eddy Simulation

2.2.1 Governing equations of turbulent reacting flows

In terms of the material derivative $\left(\frac{D}{Dt} = \frac{\partial}{\partial t} + u_j \frac{\partial}{\partial x_j}\right)$ the Navier-Stokes equations for mass and momentum read

$$\frac{D\rho}{Dt} = -\rho \frac{\partial u_j}{\partial x_j} \tag{2.4}$$

$$\rho \frac{Du_i}{Dt} = -\frac{\partial p}{\partial x_i} + \frac{\partial \tau_{ij}}{\partial x_j} + \rho f_i \tag{2.5}$$

where ρ, u, p, τ_{ij} and f_i stand for the density, the velocity, the pressure, the viscous tensor and the volume force respectively. The subindices $i = 1$ to 3 and $j = 1$ to 3 denote the component of the specific vector/tensor. The equation that characterizes reacting flows is the one denoting the balance of species k.

$$\rho \frac{DY_k}{Dt} = \dot{\omega}_k - \frac{\partial}{\partial x_i}\left(\rho V_{k,i} Y_k\right) = \dot{\omega}_k - \frac{\partial J_k}{\partial x_i} \tag{2.6}$$

where Y_k is the mass fraction of species k, $\dot{\omega}_k$ is the reaction rate of the species k, $V_{k,i}$ is the diffusion velocity of species k in the direction i and J_k is the diffusion flux of species k. The energy equation can be defined in multiple forms [74]. The equation for the total energy $e_t = e + u_i^2/2$ is

$$\rho \frac{De_t}{Dt} = -\frac{\partial q_i}{\partial x_i} - \frac{\partial}{\partial x_i}\left(pu_j\right) + \frac{\partial}{\partial x_j}\left(\tau_{ij}u_j\right) + \dot{\mathcal{Q}} + \rho f_i u_i \tag{2.7}$$

Here q_i represents the energy flux and and $\dot{\mathcal{Q}}$ is the heat source term. $\dot{\mathcal{Q}}$ can be, for instance, the energy released by an electrical spark, a laser or a radiative flux. It should not be confused with the heat released by combustion. The balance equation of enthalpy is the one used to account for the energy balance in the present study:

$$\rho \frac{Dh}{Dt} = \frac{Dp}{Dt} - \frac{\partial q_i}{\partial x_i} + \tau_{ij}\frac{\partial u_i}{\partial x_j} + \dot{\mathcal{Q}} + \rho f_i u_i \tag{2.8}$$

This equation is derived by combining the balance equation for the internal energy e with the definition of enthalpy $dh = de + d(p/\rho)$. The term $\tau_{ij}\frac{\partial u_i}{\partial x_j}$ is known as the dissipation function and represents the work done by the viscous stresses due to the deformation of a fluid particle.

2.2.2 Large Eddy Simulation

The dynamics of reactive flows is exactly described by the Eqs. (2.4)-(2.8). Nevertheless, no analytical solution exists for such a non-linear and coupled differential system of equations. There is only one way to follow so that Navier-Stokes equations become solvable: discretize them. The numerical schemes used for such discretizations must be of high order so that numerical stability and precision is assured, and the grid must be extremely refined so that 'physical' solutions are obtained: reactive flows contain fluid structures that range from the smallest scales of turbulence (the kolmogorov scale $\eta \sim Re^{-3/4}$ m) or the flame thickness ($\sim 10^{-4}$ m) to the scales that can be of the size of the entire physical domain as the acoustic waves length (~ 1 m). It is then understandable that with today computer's performance it is impossible to resolve such equations for systems size that exceed some centimeters. A system as big as a combustion chamber is therefore unresolvable. Fortunately, an approach solution has been proposed [79] in which only the bigger scales of turbulence are explicitly computed and the smallest are modeled. This technique is known as the Large Eddy Simulation LES. In order to solve only the large structures of turbulence, Navier Stokes equations must be filtered:

$$\bar{f}(\boldsymbol{x}) = \int f(\boldsymbol{x}')L(\boldsymbol{x}-\boldsymbol{x}')d\boldsymbol{x}' \tag{2.9}$$

where L stands for the LES filter. The Favre filter is the one usually applied and is defined as [2] $\widetilde{f} = \overline{\rho f}/\bar{\rho}$. The filtered quantity ($\bar{f}$ or $\widetilde{f}$) is explicitly resolved in the numerical simulation whereas $f' = f - \bar{f}$ corresponds to the unresolved part.

[2] The meaning of the symbols $\bar{()}$ and $\widetilde{()}$ given in this section stands only for this section.

From this definition it is possible to write the system of equations that govern LES for non-reacting flows. It yields [74]

Mass

$$\frac{\partial \bar{\rho}}{\partial t} + \frac{\partial}{\partial x_j}\left(\bar{\rho}\widetilde{u}_j\right) = 0 \tag{2.10}$$

Momentum

$$\frac{\partial \bar{\rho}\widetilde{u}_i}{\partial t} + \frac{\partial}{\partial x_j}\left(\bar{\rho}\widetilde{u}_i\widetilde{u}_j\right) + \frac{\partial \bar{p}}{\partial x_i} = \frac{\partial}{\partial x_j}\left[\bar{\tau}_{ij} - \bar{\rho}\left(\widetilde{u_i u_j} - \widetilde{u}_i\widetilde{u}_j\right)\right] \tag{2.11}$$

Chemical species

$$\frac{\partial \bar{\rho}\widetilde{Y}_k}{\partial t} + \frac{\partial}{\partial x_j}\left(\bar{\rho}\widetilde{u}_j\widetilde{Y}_k\right) = \frac{\partial}{\partial x_j}\left[\overline{V_{k,j}Y_k} - \bar{\rho}\left(\widetilde{u_j Y_k} - \widetilde{u}_j\widetilde{Y}_k\right)\right] + \bar{\omega}_k \tag{2.12}$$

Enthalpy

$$\begin{aligned}\frac{\partial \bar{\rho}\widetilde{h}_s}{\partial t}\frac{\partial}{\partial x_j}\left(\bar{\rho}\widetilde{u}_j\widetilde{h}_s\right) = \overline{\frac{Dp}{Dt}} + \frac{\partial}{\partial x_j}\left[\overline{\lambda\frac{\partial T}{\partial x_j}} - \bar{\rho}\left(\widetilde{u_j h_s} - \widetilde{u}_j\widetilde{h}_s\right)\right] + \overline{\tau_{ij}\frac{\partial u_j}{\partial x_i}} \\ - \frac{\partial}{\partial x_j}\left(\overline{\rho\sum_{k=1}^{N} V_{k,j}Y_k h_{s,k}}\right) + \bar{\omega}_T\end{aligned} \tag{2.13}$$

where h_s stands for the sensible enthalpy of the mixture. The quantities $(\widetilde{u_i u_j} - \widetilde{u}_i\widetilde{u}_j)$, $(\widetilde{u_j Y_k} - \widetilde{u}_j\widetilde{Y}_k)$, $(\widetilde{u_j h_s} - \widetilde{u}_j\widetilde{h}_s)$, $\overline{V_{k,i}Y_k}$ and $(\bar{\omega}_k)$ are known as the unresolved Reynolds stresses, unresolved species flux, unresolved enthalpy flux, filtered laminar diffusion fluxes and filtered chemical reaction rate respectively. These terms, which need to be modeled, are the quantities that account for the influence of the small structures on the entire physical system. LES system of equations for reactive flows may vary somehow with respect to Eq. (2.10) - Eq. (2.13) due to the combustion model applied. As an example in the Thickened Flame combustion model TF [11, 17, 74], viscous terms (as for instance the filtered diffusive species flux $\bar{J}_{j,k}$ and the filtered heat flux $\bar{q}_i$) and notably the filtered chemical reaction rate $\bar{\omega}_k$ are weighted by several factors in order to account for the 'new' thickness of the flame.

Large Eddy Simulation has become an important tool for the simulation and post-processing analysis of turbulent flows. It offers the best promise in the foreseeable future for the estimation of noise from flows at Reynolds Numbers of interest in both open and closed systems. In aeroacoustics, LES plays an important role in the study of aerodynamical generated noise of numerous practical cases that range from air jets, high-lift devices or landing gears in an aircraft to the rear-view mirror of a car or the blades of a wind turbine [65, 8]. In reactive flows, LES has been successfully applied to partially premixed and non-premixed open flames [70, 36] as

well as in more complex cases such as gas turbine combustors [21, 82, 90]

Direct computations of noise resolve the flow field together with the sound radiation. A compressible LES code is therefore required in addition to high-resolution numerical schemes in order to minimize both dispersion and dissipation. Moreover, the computational domain must be large enough to include the sources of noise as well as part of the acoustic near field [54]. Very expensive computational costs can arise since hydrodynamic and acoustic scales differ by a large amount in typical applications where the Mach number is moderate. This is even more true when dealing with thermoacoustics since the transport equation of each species (Eq. 2.12) must be considered in order to solve the problem of compressible multicomponent reactive flows. Hybrid methods for noise computation has been developed in order to overcome these constraints.

2.3 Hybrid computation of noise: Acoustic Analogies

In hybrid approaches, the computation of sound is made in two different steps. The sources of noise are modeled first, which requires a proper estimation of the flow and the flame dynamic properties. These sources are assumed independent of any acoustic quantity. The far field acoustic radiation is then predicted from the different noise sources. Acoustic propagation is calculated based on equations relevant to acoustic phenomena. The derivation of a wave equation governing sound propagation in an arbitrary mean flow (and therefore accounting for mean flow-acoustic interactions) remains a difficult and controversial task in aeroacoustics [4]. Since the sources of noise and the acoustic radiation are computed separately, the computational effort is less critical than in direct sound computations. The sources of noise can be computed by numerical codes with lower-resolution schemes provided that numerical dissipation is carefully controlled [103] and that the acoustic source formulations fulfill true radiation characteristics (dipole, quadrupole, etc). Regarding thermoacoustics, and more specifically combustion noise, it has been established that turbulent flames behave like low frequency monopoles [9]. After the different sources have been computed, the sound radiation, due to these sources, is evaluated by solving the wave operator coming from an acoustic analogy equation [28, 36, 97]. Notably, Strahle's formulation of Lighthill's analogy [50, 98] and the extension of the Phillips' analogy [39] which takes into account the conservation equation of multicomponent reacting flows. Alternative methods include the Linearized Euler equations or its APE formulation [10, 5].

2.3.1 An energy expression useful for acoustics

The combustion process, and therefore the heat released by combustion $\dot{\omega}_T$ is contained into enthalpy h. This thermodynamical variable can be expressed as the sum of both sensible enthalpy of the mixture h_s and the enthalpy of formation of the mixture Δh_f^0.

$$h = h_s + \Delta h_f^0 \tag{2.14}$$

Both h_s and Δh_f^0 can be expressed as the sum of the contributions of each species k. Hence:

$$h = \sum_k h_{s,k} Y_k + \sum_k \Delta h_{f,k}^0 Y_k \tag{2.15}$$

Introducing now the specific heat of species k at constant pressure $c_{p,k}$, the material derivative of sensible enthalpy h_s can be obtained by

$$\frac{Dh_s}{Dt} = \frac{D}{Dt}\sum_k h_{s,k} Y_k = \frac{D}{Dt}\sum_k c_{p,k} T Y_k \tag{2.16}$$

$$= \sum_k c_{p,k} T \frac{DY_k}{Dt} + \sum_k c_{p,k} Y_k \frac{DT}{Dt} \tag{2.17}$$

$$= \sum_k h_{s,k} \frac{DY_k}{Dt} + c_p \frac{DT}{Dt} \tag{2.18}$$

And as a consequence

$$\frac{Dh}{Dt} = \sum_k h_{s,k} \frac{DY_k}{Dt} + c_p \frac{DT}{Dt} + \sum_k \Delta h_{f,k}^0 \frac{DY_k}{Dt} \tag{2.19}$$

Expression (2.19) can be re-stated considering changes in pressure , density and mass fraction rather than changes in temperature. Considering the ideal gas equation,

$$P = r\rho T = \left(R \sum_k \frac{Y_k}{W_k} \right) \rho T \tag{2.20}$$

where W_k is the molecular weight of species k and $R = 8.314\ J\ mol^{-1}K^{-1}$, the differential of temperature yields

$$dT = \left.\frac{\partial T}{\partial p}\right|_{\rho,Y_k} dp + \left.\frac{\partial T}{\partial \rho}\right|_{p,Y_k} d\rho + \sum_k \left.\frac{\partial T}{\partial Y_k}\right|_{\rho,p,Y_{l\neq k}} dY_k \tag{2.21}$$

$$dT = \frac{1}{\rho r} dp - \frac{T}{\rho} d\rho - T \sum_k \frac{W}{W_k} dY_k \tag{2.22}$$

The term $T\sum_k \frac{W}{W_k} dY_k$ can be expressed as $Td(\ln r)$. Replacing Eq. (2.22) into Eq. (2.19) leads to

$$\rho\frac{Dh}{Dt} = \rho c_p\left[\frac{1}{\rho r}\frac{Dp}{Dt} - \frac{T}{\rho}\frac{D\rho}{Dt} - T\frac{D}{Dt}(\ln r)\right] + \rho\sum_k\left(h_{s,k} + \Delta h^0_{f,k}\right)\frac{DY_k}{Dt} \tag{2.23}$$

The last term of Eq. (2.23) can be developed so that heat release due to combustion $\dot{\omega}_T$ comes up. This term is defined as $\dot{\omega}_T = -\sum_k(h_{s,k} + \Delta h^0_{f,k})\dot{\omega}_k$ [74]. Using the balance of species (Eq. 2.6) results in

$$\sum_k\left(h_{s,k} + \Delta h^0_{f,k}\right)\left(\dot{\omega}_k - \frac{\partial J_k}{\partial x_i}\right) = \sum_k h_{s,k}\dot{\omega}_k + \sum_k \Delta h^0_{f,k}\dot{\omega}_k - \sum_k h_{s,k}\frac{\partial J_k}{\partial x_i} - \sum_k \Delta h^0_{f,k}\frac{\partial J_k}{\partial x_i} \tag{2.24}$$

$$= -\dot{\omega}_T - \sum_k h_k\frac{\partial J_k}{\partial x_i} \tag{2.25}$$

Equation (2.8) is combined with Eqs. (2.23),(2.25) so that

$$\begin{aligned}&\frac{c_p}{r}\frac{Dp}{Dt} - c_pT\frac{D\rho}{Dt} - \rho c_pT\frac{D}{Dt}(\ln r) - \dot{\omega}_T - \sum_k h_k\frac{\partial J_k}{\partial x_i}\\ =&\frac{Dp}{Dt} - \frac{\partial q_i}{\partial x_i} + \tau_{ij}\frac{\partial u_i}{\partial x_j} + \dot{\mathcal{Q}} + \rho f_i u_i\end{aligned} \tag{2.26}$$

Dividing everywhere by (c_pT) and neglecting volume forces ($f_i = 0$) yields

$$\begin{aligned}&\frac{Dp}{Dt}\left(\frac{1}{rT} - \frac{1}{c_pT}\right) - \frac{D\rho}{Dt} - \rho\frac{D}{Dt}(\ln r)\\ &+\frac{1}{c_pT}\left[-\dot{\omega}_T - \sum_k h_k\frac{\partial J_k}{\partial x_i} + \frac{\partial q_i}{\partial x_i} - \tau_{ij}\frac{\partial u_i}{\partial x_j} - \dot{\mathcal{Q}}\right] = 0\end{aligned} \tag{2.27}$$

A similar derivation for the material derivative of the density ρ can be found in [4]. The resulting expression is really useful to study acoustics, as both $\frac{D\rho}{Dt}$ and $\frac{1}{c^2}\frac{Dp}{Dt}$ appear explicitly. Reorganizing Eq. 2.27 and knowing that $c_p = r\gamma/(\gamma-1)$

$$\boxed{\frac{D\rho}{Dt} = \frac{1}{c^2}\frac{Dp}{Dt} + \frac{(\gamma-1)}{c^2}\left[-\dot{\omega}_T - \sum_k h_k\frac{\partial J_k}{\partial x_i} + \frac{\partial q_i}{\partial x_i} - \tau_{ij}\frac{\partial u_i}{\partial x_j} - \dot{\mathcal{Q}}\right] - \rho\frac{D}{Dt}(\ln r)} \tag{2.28}$$

where the velocity of sound $c = \sqrt{\gamma rT}$ has been introduced.

2.3.2 The Lighthill's Analogy

When considering frozen vortical structures or a frozen flame, clearly all the forces implied in each of these physical mechanisms are totally balanced and no sound is produced. But once unsteadiness occurs, these forces are not balanced anymore. In the case of turbulence, for example, the reciprocal motion of the surrounding gas tries to compensate for this 'unexpected' dynamics. Nevertheless, this reciprocal motion fails in completely absorbing the vortical energy and therefore local compressions and dilatations due to compressibility are transmitted to the adjacent particles: sound has been generated. Into the source region (vortex/flame dynamics) the flow can be consider incompressible, forasmuch as the compressible part of the pressure fluctuation p'_a is much smaller than the pressure fluctuations generated by both unsteady vorticity p'_h (if sound is generated by turbulence) or unsteady temperature p'_f (if sound is generated by combustion). In this region, pressure fluctuations can be then computed by solving a poisson equation $\nabla^2 = \psi$ where ψ is a function of the implied sources. In the far-field, on the contrary, the fluctuations due to acoustics p'_a are much more important than the significatively much smaller p'_h,p'_f. In the case of turbulence, for instance, it is known that hydrodynamic pressure fluctuations are negligible in the far field since they typically decay at least as the inverse third power of the distance to the sources [80]. Pressure fluctuations p'_a may be assessed then by solving an acoustic wave equation.

Lighthill's analogy is considered as the starting points of aeroacoustics as a research field. The Navier-Stokes equations are rearranged so that the resulting formulation has the 'shape' of a inhomogeneous wave equation: in the left hand side (LHS) the acoustic operator and at the right hand side (RHS) the sources responsible for noise generation. Neglecting volume forces, the mass and momentum equations (Eqs. 2.4 and 2.5) can be expressed in their conservative forms:

$$\frac{\partial \rho}{\partial t} + \frac{\partial \rho u_j}{\partial x_j} = 0 \tag{2.29}$$

$$\frac{\partial \rho u_i}{\partial t} + \frac{\partial \rho u_i u_j}{\partial x_j} = -\frac{\partial p}{\partial x_i} + \frac{\partial \tau_{ij}}{\partial x_j} \tag{2.30}$$

Applying the time derivative $\frac{\partial}{\partial t}$ to Eq. (2.29), the spatial derivative $\frac{\partial}{\partial x_i}$ to Eq. (2.30) and substracting them results in

$$\frac{\partial^2 \rho}{\partial t^2} - \frac{\partial^2 p}{\partial x_i^2} = \frac{\partial^2}{\partial x_i \partial x_j}\left(\rho u_i u_j - \tau_{ij}\right) \tag{2.31}$$

In order to construct the D'Alembertian operator, the term $\frac{1}{c_\infty^2}\frac{\partial^2 p}{\partial t^2}$ is added to both RHS and LHS of Eq. (2.31). c_∞ represents the sound velocity in the quiescent propagation media (far field). It

yields

$$\frac{1}{c_\infty^2}\frac{\partial^2 p}{\partial t^2} - \frac{\partial^2 p}{\partial x_i^2} = \frac{\partial^2}{\partial x_i \partial x_j}\left(\rho u_i u_j - \tau_{ij}\right) - \frac{\partial^2 \rho}{\partial t^2} + \frac{1}{c_\infty^2}\frac{\partial^2 p}{\partial t^2} \tag{2.32}$$

A density-pressure relation for the region far from noise sources (subindex ∞) is now added to the RHS of Eq. (2.32). This term ($\frac{1}{c_\infty^2}\frac{\partial^2 p_\infty}{\partial t^2} - \frac{\partial^2 \rho_\infty}{\partial t^2}$) is in fact zero since at infinity the flow is considered at rest and isentropic. Eq. (2.32) becomes

$$\frac{1}{c_\infty^2}\frac{\partial^2 p}{\partial t^2} - \frac{\partial^2 p}{\partial x_i^2} = \frac{\partial^2}{\partial x_i \partial x_j}\left(\rho u_i u_j - \tau_{ij}\right) - \frac{\partial^2}{\partial t^2}\left[(\rho - \rho_\infty) - \frac{1}{c_\infty^2}(p - p_\infty)\right] \tag{2.33}$$

The last term of Eq. (2.33), discussed by Morfey [61] in 1973, is known as the excess of density $\rho_e = (\rho - \rho_\infty) - \frac{1}{c_\infty^2}(p - p_\infty)$ and can be seen as an estimator of the deviation from the adiabatic relation $d\rho = dp/c_\infty^2$. Eventually, the Lightill analogy reads

$$\boxed{\frac{1}{c_\infty^2}\frac{\partial^2 p}{\partial t^2} - \frac{\partial^2 p}{\partial x_i^2} = \frac{\partial^2}{\partial x_i \partial x_j}\left(\rho u_i u_j - \tau_{ij}\right) - \frac{\partial^2 \rho_e}{\partial t^2}} \tag{2.34}$$

For an isentropic flow the excess of density ρ_e is clearly zero. In such a case, the responsible for noise generation is the unsteady turbulence, $\frac{\partial^2}{\partial x_i \partial x_j}\left(\rho u_i u_j - \tau_{ij}\right)$, a term which is known as the aerodynamic source of noise. Moreover, at high Reynolds number the contribution of the viscous tensor τ_{ij} is negligible in comparison to the Reynolds tensor $\rho u_i u_j$. Reactive flows are, on the contrary, of course non-isentropic. It will be seen in the following that in such flows the term ρ_e is the responsible for most of the noise production. The purpose now is to express the material derivative of the excess of density $\frac{D\rho_e}{Dt}$ as function of the material derivative of density $\frac{D\rho}{Dt}$.

$$\frac{D\rho_e}{Dt} = \frac{\partial \rho_e}{\partial t} + u_j \frac{\partial \rho_e}{\partial x_j} = \frac{\partial \rho_e}{\partial t} + \frac{\partial}{\partial x_j}(\rho_e u_j) - \rho_e \frac{\partial u_j}{\partial x_j} \tag{2.35}$$

$$= \frac{\partial \rho_e}{\partial t} + \frac{\partial}{\partial x_j}(\rho_e u_j) + \frac{\rho_e}{\rho}\frac{D\rho}{Dt} \tag{2.36}$$

Replacing by the definition of ρ_e

$$\frac{D}{Dt}\left[(\rho-\rho_\infty)-\frac{1}{c_\infty^2}(p-p_\infty)\right]=\frac{\partial\rho_e}{\partial t}+\frac{\partial}{\partial x_j}(\rho_e u_j)+\left[(\rho-\rho_\infty)-\frac{1}{c_\infty^2}(p-p_\infty)\right]\frac{1}{\rho}\frac{D\rho}{Dt} \tag{2.37}$$

$$\frac{D\rho}{Dt}-\frac{1}{c_\infty^2}\frac{Dp}{Dt}=\frac{\partial\rho_e}{\partial t}+\frac{\partial}{\partial x_j}(\rho_e u_j)+\frac{D\rho}{Dt}-\frac{\rho_\infty}{\rho}\frac{D\rho}{Dt}-\frac{1}{c_\infty^2\rho}(p-p_\infty)\frac{D\rho}{Dt} \tag{2.38}$$

and resolving for $\frac{\partial\rho_e}{\partial t}$

$$\frac{\partial\rho_e}{\partial t}=\frac{\rho_\infty}{\rho}\frac{D\rho}{Dt}+\frac{1}{c_\infty^2\rho}(p-p_\infty)\frac{D\rho}{Dt}-\frac{1}{c_\infty^2}\frac{Dp}{Dt}-\frac{\partial}{\partial x_j}(\rho_e u_j) \tag{2.39}$$

The energy equation in terms of the material derivative of the density $\frac{D\rho}{Dt}$ was obtained in section 2.3.1. Equation (2.28) is thus introduced leading to

$$\begin{aligned}\frac{\partial\rho_e}{\partial t}=&\frac{\rho_\infty}{\rho}\frac{(\gamma-1)}{c^2}\left(-\dot{\omega}_T-\sum_k h_k\frac{\partial J_k}{\partial x_i}+\frac{\partial q_i}{\partial x_i}-\tau_{ij}\frac{\partial u_i}{\partial x_j}-\dot{\mathcal{Q}}\right)-\rho_\infty\frac{D}{Dt}(\ln r)\\&+\frac{1}{c_\infty^2\rho}(p-p_\infty)\frac{D\rho}{Dt}-\frac{1}{c_\infty^2}\left(1-\frac{\rho_\infty c_\infty^2}{\rho c^2}\right)\frac{Dp}{Dt}-\frac{\partial}{\partial x_j}(\rho_e u_j)\end{aligned} \tag{2.40}$$

The complete equation is then obtained in the frame of Lighthill's analogy. This exact reformulation of the Navier-Stokes equations reads

$$\boxed{\begin{aligned}\frac{1}{c_\infty^2}\frac{\partial^2 p}{\partial t^2}-\frac{\partial^2 p}{\partial x_i^2}=&\frac{\partial^2}{\partial x_i\partial x_j}\left(\rho u_i u_j-\tau_{ij}\right)\\&+\frac{\partial}{\partial t}\left[\frac{\rho_\infty}{\rho}\frac{(\gamma-1)}{c^2}\left(\dot{\omega}_T+\sum_k h_k\frac{\partial J_k}{\partial x_i}-\frac{\partial q_i}{\partial x_i}+\tau_{ij}\frac{\partial u_i}{\partial x_j}+\dot{\mathcal{Q}}\right)+\rho_\infty\frac{D}{Dt}(\ln r)\right]\\&+\frac{1}{c_\infty^2}\frac{\partial}{\partial t}\left[\left(1-\frac{\rho_\infty c_\infty^2}{\rho c^2}\right)\frac{Dp}{Dt}-\frac{p-p_\infty}{\rho}\frac{D\rho}{Dt}\right]\\&+\frac{\partial^2}{\partial x_j\partial t}(\rho_e u_j)\end{aligned}} \tag{2.41}$$

As it can be observed, the sources contributing to noise in reacting flows are multiple. It is observed that the heat release $\dot{\omega}_T$, the diffusion flux of species J_k as well as the non-isomolar combustion due to changes in r generate noise. The heat flux q_i, the dissipation function $\tau_{ij}\frac{\partial u_i}{\partial x_j}$ and the energy sources applied to the system $\dot{\mathcal{Q}}$ are also responsible for noise generation. The terms present on the third line of Eq. (2.41) are related to the inhomogeneities of the flow respect

to the propagation media. Finally, the last term of Eq. (2.41) stands for the noise produced by the acceleration of density inhomogeneities and should be related to the indirect combustion noise.

Lighthill's analogy is a suitable formulation when sources are compact and the radiation of sound takes place in a quiescent field. Extensions of Lighthill's analogy in order to account for turbulence-body interactions has been derived by Curle [20] and Ffowcs-Williams and Hawkings [106]. As stated in the introductory part of this section, the acoustic operator of Lighthill's analogy does not account for acoustic-flow interactions. All these possible interactions are implicitly included in the source terms and therefore density fluctuations on the sources cannot be neglected. However, in order to compute this compressible sources it would be necessary to resolve the pressure field in which these sources are embedded or, in other words, to solve the problem itself. Some simplifications then must be considered.

Simplifying Lighthill's Analogy

Equation (2.41) is an exact derivation of the Navier-Stokes equation and therefore until now no assumptions or simplifications have been done. Nevertheless, this equation in this way does not present a significant utility. Assumptions must be considered so that Lighthill's equation become tractable and therefore solvable. The idea is then only to consider the predominant mechanisms generators of noise. In doing so, diffusive fluxes of species J_k and the dissipation function $\tau \frac{\partial u_i}{\partial x_j}$ are first neglected. $\dot{\mathcal{Q}}$ vanishes if no external energy sources are applied to the system and $\frac{\partial q_i}{\partial x_i}$ is zero if heat fluxes are considered small. Moreover, at high Reynolds number the viscous tensor τ_{ij} is negligible if compared to the Reynolds stresses $\rho u_i u_j$ and the propagation media is considered homogenous ($p, \rho, c \rightarrow p_\infty, \rho_\infty, c_\infty$) so that all the third line disappears. Further on, combustion can be considered isomolar if air is used as oxidizer so that $\frac{D}{Dt}(\ln r)$ vanishes and for low Mach numbers $\mathcal{M}$ the acceleration of density inhomogeneities $\frac{\partial^2}{\partial x_j \partial t}(\rho_e u_j)$ can be neglected . The simplified Lighthill Equation then reads

$$\frac{1}{c_\infty^2}\frac{\partial^2 p}{\partial t^2} - \frac{\partial^2 p}{\partial x_i^2} = \frac{\partial^2}{\partial x_i \partial x_j}\left(\rho_\infty u_i u_j\right) + \frac{(\gamma - 1)}{c_\infty^2}\frac{\partial \dot{\omega}_T}{\partial t} \tag{2.42}$$

Hassan demonstrates in his work [32] that noise produced by combustion is much more important than the one generated by turbulence. Note that the combustion source of noise is a monopole ($\frac{\partial}{\partial t}$) whereas the aerodynamic source of noise is a quadrupole ($\frac{\partial^2}{\partial x_i^2}$). A quadrupolar source of noise is known to be a bad radiator of sound if compared to a monopolar source and therefore the aerodynamic source can be neglected. Finally, heat release $\dot{\omega}_T$ and pressure p are decomposed by its mean and fluctuating parts ($p = \bar{p} + p'$, $\dot{\omega}_T = \bar{\dot{\omega}}_T + \dot{\omega}'_T$). Combustion noise in a quiescent media is given then by

$$\boxed{\frac{1}{c_\infty^2}\frac{\partial^2 p'}{\partial t^2} - \frac{\partial^2 p'}{\partial x_i^2} = \frac{(\gamma-1)}{c_\infty^2}\frac{\partial \dot{\omega}'_T}{\partial t}} \tag{2.43}$$

where $\frac{\partial \bar{p}}{\partial x_i} \approx 0$ due to the $\mathcal{M} = 0$ assumption. It is useful also to solve this wave equation in the frequency domain. Considering harmonic perturbations of pressure p' and the heat release $\dot{\omega}'_T$:

$$p'(\boldsymbol{x}, t) = \Re(\hat{p}(\boldsymbol{x})e^{-i\omega t}) \tag{2.44}$$

$$\dot{\omega}'_T(\boldsymbol{x}, t) = \Re(\hat{\dot{\omega}}_T(\boldsymbol{x})e^{-i\omega t}) \tag{2.45}$$

where $\omega = 2\pi f$ and f is the oscillation frequency in Hertz. Equation (2.43) then becomes

$$\boxed{\frac{\partial^2 \hat{p}}{\partial x_i^2} + \frac{\omega^2}{c_\infty^2}\hat{p} = -i\omega\frac{(\gamma-1)}{c_\infty^2}\hat{\dot{\omega}}_T} \tag{2.46}$$

Equation (2.46) is commonly known as the Helmholtz equation. Expressions (2.43) and (2.46) can be easily solved by means of the Green's functions as shown in section 2.3.4.

2.3.3 The Phillips' Analogy

Lighthill's theory considers the radiation of sound throughout a uniform media caused by stationary or moving sources. In spite of the fact that directivity is accounted for in Lighthill's formulation, this directivity is only caused by the convective pattern of sources (if any) which is not completely true. In real flows the propagation media is non-homogeneous at least in the vicinity of the sources region (within about a wavelength or so) and most of the directivity encountered in an acoustic field is originated by the acoustic-mean flow interactions that takes place in this non-homogeneous near field [31].

Phillips' rearrangement of the Navier-Stokes equations is considered as the first significative work that takes into account some of all possible acoustic-flow interactions. In this moving-media wave equation, acoustic-mean flow interactions are accounted for in the respective acoustic operator. Combining first and second law of thermodynamics results in

$$\frac{1}{c_p}\frac{Ds}{Dt} = \frac{1}{\gamma p}\frac{Dp}{Dt} - \frac{1}{\rho}\frac{D\rho}{Dt} \tag{2.47}$$

A new variable is introduced by Phillips [66] and is defined as $\pi = \frac{1}{\gamma}\ln(p/p_\infty)$. It can be

straightforward included in Eq. (2.47)

$$\frac{1}{c_p}\frac{Ds}{Dt} = \frac{D\pi}{Dt} - \frac{1}{\rho}\frac{D\rho}{Dt} \tag{2.48}$$

and by using the continuity equation

$$\frac{1}{c_p}\frac{Ds}{Dt} = \frac{D\pi}{Dt} + \frac{\partial u_j}{\partial x_j} \tag{2.49}$$

The variable π can also be introduced in the momentum equation. It yields

$$\frac{Du_i}{Dt} + \frac{1}{\rho}\frac{\partial p}{\partial x_i} - \frac{1}{\rho}\frac{\partial \tau_{ij}}{\partial x_j} = 0 \quad \rightarrow \quad \frac{Du_i}{Dt} + c^2\frac{\partial \pi}{\partial x_i} - \frac{1}{\rho}\frac{\partial \tau_{ij}}{\partial x_j} = 0 \tag{2.50}$$

The material derivative $\frac{D}{Dt}$ is now applied to the Eq. (2.49) and the spatial derivative $\frac{\partial}{\partial x_i}$ to the momentum equation.

$$\frac{D}{Dt}\left(\frac{1}{c_p}\frac{Ds}{Dt}\right) - \frac{D}{Dt}\left(\frac{D\pi}{Dt}\right) - \frac{D}{Dt}\left(\frac{\partial u_j}{\partial x_j}\right) = 0 \tag{2.51}$$

$$\frac{\partial}{\partial x_i}\frac{Du_i}{Dt} + \frac{\partial}{\partial x_i}\left(c^2\frac{\partial \pi}{\partial x_i}\right) - \frac{\partial}{\partial x_i}\left(\frac{1}{\rho}\frac{\partial \tau_{ij}}{\partial x_j}\right) = 0 \tag{2.52}$$

The operation $\frac{D}{Dt}\left(\frac{\partial}{\partial x_j}\right)$ is not commutative. As a consequence

$$\frac{D}{Dt}\frac{\partial}{\partial x_i} = \frac{\partial^2}{\partial t \partial x_i} + u_j\frac{\partial^2}{\partial x_i \partial x_j} \tag{2.53}$$

$$\frac{\partial}{\partial x_i}\frac{D}{Dt} = \frac{\partial^2}{\partial x_i \partial t} + \frac{\partial}{\partial x_i}\left(u_j\frac{\partial}{\partial x_j}\right) = \frac{\partial^2}{\partial x_i \partial t} + \frac{\partial u_j}{\partial x_i}\frac{\partial}{\partial x_j} + u_j\frac{\partial^2}{\partial x_i \partial x_j} \tag{2.54}$$

$$\frac{\partial}{\partial x_i}\frac{D}{Dt} = \frac{D}{Dt}\frac{\partial}{\partial x_i} + \frac{\partial u_j}{\partial x_i}\frac{\partial}{\partial x_j} \tag{2.55}$$

Replacing the subindex j to i in Eq. (2.49) and accounting for the previous relation, Eq. (2.51) becomes

$$\frac{D}{Dt}\left(\frac{1}{c_p}\frac{Ds}{Dt}\right) - \frac{D^2\pi}{Dt^2} - \frac{\partial}{\partial x_i}\frac{Du_j}{Dt} + \frac{\partial u_j}{\partial x_i}\frac{\partial u_i}{\partial x_j} = 0 \tag{2.56}$$

Finally, Eqs. (2.52) and (2.56) are sum leading to the final expression for the Phillip's analogy.

$$\frac{D^2\pi}{Dt^2} - \frac{\partial}{\partial x_i}\left(c^2\frac{\partial \pi}{\partial x_i}\right) = \frac{\partial u_j}{\partial x_i}\frac{\partial u_i}{\partial x_j} - \frac{\partial}{\partial x_i}\left(\frac{1}{\rho}\frac{\partial \tau_{ij}}{\partial x_j}\right) + \frac{D}{Dt}\left(\frac{1}{c_p}\frac{Ds}{Dt}\right) \tag{2.57}$$

In order to have an explicit expression for Phillip's analogy with all the possible sources in a reacting flow, the energy equation Eq. (2.28) is combined with Eq. (2.47) leading to

$$\frac{1}{c_p}\frac{Ds}{Dt} = \frac{(\gamma-1)}{\rho c^2}\left[\dot{\omega}_T + \sum_k h_k \frac{\partial J_k}{\partial x_i} - \frac{\partial q_i}{\partial x_i} + \tau_{ij} : \frac{\partial u_i}{\partial x_j} + \dot{\mathcal{Q}}\right] + \frac{D}{Dt}(\ln r) \tag{2.58}$$

The Phillip's equation for reacting flows reads

$$\begin{aligned}\frac{D^2\pi}{Dt^2} - \frac{\partial}{\partial x_i}\left(c^2\frac{\partial \pi}{\partial x_i}\right) &= \frac{\partial u_j}{\partial x_i}\frac{\partial u_i}{\partial x_j} - \frac{\partial}{\partial x_i}\left(\frac{1}{\rho}\frac{\partial \tau_{ij}}{\partial x_j}\right) \\ &+ \frac{D}{Dt}\left[\frac{(\gamma-1)}{\rho c^2}\left(\dot{\omega}_T + \sum_k h_k \frac{\partial J_k}{\partial x_i} - \frac{\partial q_i}{\partial x_i} + \tau_{ij} : \frac{\partial u_i}{\partial x_j} + \dot{\mathcal{Q}}\right)\right] \\ &+ \frac{D^2}{Dt^2}(\ln r)\end{aligned} \tag{2.59}$$

Equation (2.59) was introduced by Chiu & Summerfield [14] and Kotake [39]. This expression accounts for some acoustic-flow interactions since gradients of the sound velocity c are included in the acoustic operator. It has several advantages compared to Lighthill's analogy since mean temperature and density of the propagation media are not assumed homogeneous in space, which is clearly the case for reacting flows. The term responsible for noise generation due to hydrodynamic fluctuations is now defined as $\frac{\partial u_j}{\partial x_i}\frac{\partial u_i}{\partial x_j}$. The density contribution in this term has been removed, contrary to its form in the Lighthill's analogy $\frac{\partial^2}{\partial x_i \partial x_j}(\rho u_i u_j)$. It is clear then that for Low Mach numbers there is not anymore ambiguity in this source definition since acoustic-flow interactions are not more included in this term [4]. Nevertheless, Lilley [52] demonstrated that when the Mach number is not negligible, acoustic-flow interactions are still contained in the compressible part of u_i. Another interesting remark done by Bailly [4] is that in this equation the source responsible for indirect noise (the acceleration of density inhomogeneities) does not longer appears. It is recommended thereby that if indirect noise is not negligible and not strong changes in the mean flow are present, Lighthill's analogy should be the formulation under consideration.

Simplifying Phillips' Analogy

Phillips' equation (Eq. 2.59), as Lighthill's formulation, is an exact rearrangement of the fluid dynamics equations. Similar assumptions as those made in section 2.3.2 are considered here. It is assumed then that the diffusion of species J_k, the dissipation function $\tau\frac{\partial u_i}{\partial x_j}$, external energy sources $\dot{\mathcal{Q}}$, heat fluxes $\frac{\partial q_i}{\partial x_i}$, the viscosity stresses τ_{ij}, changes in the molecular weight of the mixture $\frac{D}{Dt}(\ln r)$ and the Reynolds stress tensor $\rho u_i u_j$ are neglected in comparison to the monopolar source of noise $\frac{\partial \dot{\omega}_T}{\partial t}$. The simplified Phillips' equation then reads:

$$\frac{D^2\pi}{Dt^2} - \frac{\partial}{\partial x_i}\left(c^2\frac{\partial \pi}{\partial x_i}\right) = \frac{\partial}{\partial t}\left(\frac{\gamma-1}{\rho c^2}\dot{\omega}_T\right) \tag{2.60}$$

All quantities are decomposed by their mean and fluctuating parts. Small acoustic perturbations respect to the mean pressure are considered so that $\pi = p'/(\gamma\bar{p})$. Another assumption usually made is to consider the Mach number characterizing the flow $\bar{\mathcal{M}}$ as small. In doing so, the convective part of the material derivative vanishes and $\frac{D}{Dt} \approx \frac{\partial}{\partial t}$. This version of Phillips' equation would read

$$\frac{1}{\gamma\bar{p}}\frac{\partial^2 p'}{\partial t^2} - \frac{\partial}{\partial x_i}\left(\frac{c^2}{\gamma\bar{p}}\frac{\partial p'}{\partial x_i}\right) = \frac{\partial}{\partial t}\left(\frac{\gamma-1}{\rho c^2}\dot{\omega}_T\right) \tag{2.61}$$

It should be noted that no assumptions about uniformity of the propagation media until now has been done. Nevertheless this is necessary if solvable Phillips' equation is sought. It is then assumed that the fluctuations of speed of sound can be neglected. Note anyway that changes in the mean flow are still considered ($\frac{\partial \bar{c}}{\partial x_i} \neq 0$)

$$\boxed{\frac{\partial^2 p'}{\partial t^2} - \frac{\partial}{\partial x_i}\left(\bar{c}^2\frac{\partial p'}{\partial x_i}\right) = (\gamma-1)\frac{\partial \dot{\omega}'_T}{\partial t}} \tag{2.62}$$

Equation (2.62), as done for the Lighthill's case, can also be expressed in the frequency domain. Usually, a spectral evaluation of acoustics presents several advantages. In linear acoustics, for instance, it is possible to study the contribution of each frequency separately since they do not interact which each other. In doing so, acoustic boundary conditions can be well characterized by an acoustic property called impedance, which most of the time is a function of the frequency of oscillation. Dealing with boundary conditions is more challenging when considering the time domain formalism. Another advantage of a frequential definition is that in a spectral evaluation there is not necessity of any transient computation to reach a stationary state. Applying harmonic perturbations (Eqs. 2.44 and 2.45) on p' and $\dot{\omega}'_T$ results in a Helmholtz equation written as

$$\boxed{\frac{\partial}{\partial x_i}\left(\bar{c}^2\frac{\partial \hat{p}}{\partial x_i}\right)+\omega^2\hat{p}=-i\omega(\gamma-1)\hat{\omega}_T} \tag{2.63}$$

There is not known analytical Green's functions associated with this wave operator [4], and so no integral formulation giving the far field pressure. Most of the time this equation is solved numerically as in the present study.

2.3.4 Solving Lighthill's analogy analytically

In the Lighthill's Analogy the D'alembertian is the operator which describes the acoustic radiation due to all the different sources present (Eq. 2.41). This inhomogeneous wave equation can be expressed as

$$\frac{1}{c_\infty}\frac{\partial^2 p}{\partial t^2}-\frac{\partial^2 p}{\partial x_i^2}=q \tag{2.64}$$

where q is an arbitrary source and c_∞ is the propagation speed of the acoustic perturbations. Explicit integral solutions for this hyperbolic equation are available by means of the Green's theorem. The integral solutions obtained accounts for the effect of sources, boundary conditions and initial conditions in a relative simple formula. A Green function is written as $G(\boldsymbol{x},t|\boldsymbol{y},\tau)$ and should be red "as the measurement of G at the observation point $\boldsymbol{x}$ at time t due to a pulse δ produced at position $\boldsymbol{y}$ at time τ". Mathematicaly it yields

$$\frac{1}{c_\infty}\frac{\partial^2 G}{\partial t^2}-\frac{\partial^2 G}{\partial x_i^2}=\delta(\boldsymbol{x}-\boldsymbol{y})\delta(t-\tau) \tag{2.65}$$

The delta function $\delta(t)$ is not a common function with a pointwise meaning, but a generalized function formally defined by its filter property:

$$\int_{-\infty}^{\infty}F(x)\delta(x-x_0)dx=F(x_0) \tag{2.66}$$

for any well-behaving function $F(x)$. Moreover, Green functions have two important properties that must be taken into account for further developments. The first one is called 'causality' which states that at a time before the pulsation occurs ($t<\tau$), $G(\boldsymbol{x},t|\boldsymbol{y},\tau)$ is equal to zero as well as its temporal derivative. The second property is called 'reciprocity' and is defined as

$$G(\boldsymbol{x},t|\boldsymbol{y},\tau)=G(\boldsymbol{y},-\tau|\boldsymbol{x},-t) \tag{2.67}$$

Using now the reciprocity relation and interchanging the notation $\boldsymbol{x} \leftrightarrow \boldsymbol{y}$ and $\boldsymbol{t} \leftrightarrow \boldsymbol{\tau}$ it can be proved that the Green's function also satisfies the equation:

$$\frac{1}{c_\infty}\frac{\partial^2 G}{\partial \tau^2} - \frac{\partial^2 G}{\partial y_i^2} = \delta(\boldsymbol{x}-\boldsymbol{y})\delta(t-\tau) \tag{2.68}$$

A formal solution of the inhomogeneous wave equation

$$\frac{1}{c_\infty}\frac{\partial^2 p'}{\partial \tau^2} - \frac{\partial^2 p'}{\partial y_i^2} = q(\boldsymbol{y},\tau) \tag{2.69}$$

can be obtained by multiplying Eq. (2.68) by $p(\boldsymbol{y},\tau)$ and Eq. (2.69) to $G(\boldsymbol{x},t|\boldsymbol{y},\tau)$, substracting them and finally integrating τ between t_0 and t, and $\boldsymbol{y}$ over V. This leads to:

$$\int_{t_0}^{t}\int_V \left[\left(\frac{1}{c_\infty^2}\frac{\partial^2 G}{\partial \tau^2} - \frac{\partial^2 G}{\partial y_i^2} - \delta(t-\tau)\delta(\boldsymbol{x}-\boldsymbol{y})\right)p'(\boldsymbol{y},\tau) - \left(\frac{1}{c_\infty}\frac{\partial^2 p'}{\partial \tau^2} - \frac{\partial^2 p'}{\partial y_i^2} - q\right)G(\boldsymbol{x},t|\boldsymbol{y},\tau)\right]d\boldsymbol{y}d\tau = 0 \tag{2.70}$$

$$\int_{t_0}^{t}\int_V \left[p'\frac{1}{c_\infty^2}\frac{\partial^2 G}{\partial \tau^2} - p'\frac{\partial^2 G}{\partial y_i^2} - G\frac{1}{c_\infty^2}\frac{\partial^2 p'}{\partial \tau^2} + G\frac{\partial^2 p'}{\partial y_i^2} + qG\right]d\boldsymbol{y}d\tau - p'(\boldsymbol{x},t) = 0 \tag{2.71}$$

Reorganizing the terms

$$p'(\boldsymbol{x},t) = \int_{t_0}^{t}\int_V qG d\boldsymbol{y}d\tau - \int_{to}^{t}\int_V \left(p'\frac{\partial^2 G}{\partial y_i^2} - G\frac{\partial^2 p'}{\partial y_i^2} -\right)d\boldsymbol{y}d\tau + \frac{1}{c_\infty^2}\int_{t_0}^{t}\int_V \left(p'\frac{\partial^2 G}{\partial \tau^2} - G\frac{\partial^2 p'}{\partial \tau^2}\right)d\boldsymbol{y}d\tau \tag{2.72}$$

And finally integrating by parts results in

$$p'(\boldsymbol{x},t) = \int_{t_0}^{t}\int_V qG d\boldsymbol{y}d\tau - \int_{t_0}^{t}\int_S \left(p'\frac{\partial G}{\partial y_i} - G\frac{\partial p'}{\partial y_i}\right)n_i d\sigma d\tau - \frac{1}{c_\infty^2}\left[\int_V \left(p'\frac{\partial G}{\partial \tau} - G\frac{\partial p'}{\partial \tau}\right)d\boldsymbol{y}\right]_{t_0} \tag{2.73}$$

The first integral is the convolution of the source q with the pulse response G, the Green's function. The second integral represents the effect of differences between the actual physical boundary conditions on the surface S and the conditions applied to G. When G satisfies the same locally reacting linear boundary conditions as the actual field, this surface integral vanishes. In this case, the Green's function under consideration is called 'taylored'. On the other hand, this surface integral can also vanishes when no boundaries conditions are applied (free-

field). Finally, the last integral represents the contribution of the initial conditions at t_0 to the acoustic field and disappears if the causality condition is applied. Free-field noise computation can then be performed by the following expression

$$p'(\boldsymbol{x},t) = \int_{t_0}^{t}\int_{V} q(\boldsymbol{y},\tau)G(\boldsymbol{x},t|\boldsymbol{y},\tau)d\boldsymbol{y}d\tau \tag{2.74}$$

If noise is generated by the unsteady heat release rate induced by combustion and if the propagation of noise takes place in free-field, the simplified Lighthill's equation Eq. (2.43) applies

$$\frac{1}{c_\infty^2}\frac{\partial^2 p'}{\partial t^2} - \frac{\partial^2 p'}{\partial x_i^2} = \frac{(\gamma-1)}{c_\infty^2}\frac{\partial \dot{\omega}'_T}{\partial t} \tag{2.75}$$

The farfield pressure is then given by

$$p'(\boldsymbol{x},t) = \int_{t_0}^{t}\int_{V} G(\boldsymbol{x},t|\boldsymbol{y},\tau)\frac{(\gamma-1)}{c_\infty^2}\frac{\partial \dot{\omega}'_T}{\partial t}d\boldsymbol{y}d\tau \tag{2.76}$$

On the other hand, the 3D temporal Green's function is defined as

$$G(\boldsymbol{x},t|\boldsymbol{y},\tau) = -\frac{\delta(t-r/c_\infty)}{4\pi r} \tag{2.77}$$

where $r = |\boldsymbol{x}-\boldsymbol{y}|$. As a result, the farfield pressure radiated by a free turbulent flame can be obtained

$$p'(\boldsymbol{x},t) = \frac{(\gamma-1)}{4\pi r c_\infty^2}\frac{\partial}{\partial t}\int_{V} \dot{\omega}'_T\left(\boldsymbol{y}, t-\frac{r}{c_\infty}\right)d\boldsymbol{y} \tag{2.78}$$

Expression (2.78) can be found in the work of Strahle [98, 99] for instance. It can be noted from this expression that the farfield pressure radiated from a turbulent flame results from the contribution over the combustion region of elementary sources formed by the local time rates of change of the heat release rate. Each source produces an elementary contribution at the measurement location after a time delay corresponding to propagation between the source inside the combustion region and the point of observation in the farfield. Scaling rules can also be derived from Eq. (2.78) for the thermo-acoustic efficiency η_{ta}, defined as the ratio between the radiated acoustic power and the thermal power released in the flow (typically $\eta_{ta} \sim 10^{-6} - 10^{-5}$) for combustion noise in absence of instabilities.

Useful Green's functions

The 3D free-field Green's function expressed in the temporal domain has already been given in Eq. (2.77). This function has been widely used in combustion noise studies since it is associated with the radiation of sound from a monopolar 'spherical' source, which is the basis of combustion noise theory. In addition to this 3D Green's function, the 2D temporal Green's function can also be useful for the study of noise radiation in academic cases. It reads

$$G(\boldsymbol{x}, t|\boldsymbol{y}, \tau) = -\frac{c_\infty H\left[(t-\tau) - r/c_\infty\right]}{2\pi\sqrt{c_\infty^2(t-\tau)^2 - r^2}} \tag{2.79}$$

where H is the Heavyside function, $H(u) = 1$ if $u > 0$ and $H(u) = 0$ otherwise. Another useful approach in combustion noise is the study of noise radiation under spectral analysis. Green's functions G are therefore expressed in the frequency domain by applying a Fourier transform defined as follows

$$\widehat{G}(\boldsymbol{x}|\boldsymbol{y}, \omega) = \int_{-\infty}^{\infty} G(\boldsymbol{x}, t|\boldsymbol{y}, \tau) e^{-i\omega t} dt \tag{2.80}$$

By doing so, both 3D and 2D Green's functions in terms of frequency are obtained:

3D spectral Green's function

$$\widehat{G}(\boldsymbol{x}|\boldsymbol{y}, \omega) = \frac{e^{-ikr}}{4\pi r} \tag{2.81}$$

2D spectral Green's function

$$\widehat{G}(\boldsymbol{x}|\boldsymbol{y}, \omega) = \frac{\boldsymbol{i}}{4} H_0^{(2)}(kr) \tag{2.82}$$

where $H_0^{(2)}(kr)$ is the Hankel function of second kind and order 0 and $r = |\boldsymbol{x} - \boldsymbol{y}|$. These Green's functions satisfy the wave equation written in the frequency domain

$$\left(\frac{\partial^2}{\partial x_i^2} + \frac{\omega^2}{c_\infty^2}\right) \widehat{G}(\boldsymbol{x}|\boldsymbol{y}, \omega) = \delta(\boldsymbol{x} - \boldsymbol{y}) \tag{2.83}$$

3

Development of a numerical tool for combustion noise analysis, AVSP-f

Contents

It has been seen in section 2.3.4 that when considering the D'Alembert operator in the wave equation, it is possible to obtain an explicit solution by means of Green's functions. Notably, this is the case for the Lighthill's equation in both time and frequency domain (Eq. 2.43 and 2.46). On the contrary, Phillips analogy (Eq. 2.59) has no known analytical solutions since its wave operator is much more complex. Even if this equation is simplified to Eq. (2.62) of Eq. (2.63), the fact of having a wave operator that accounts for changes in the mean speed of sound prevents deriving an explicit solution of this wave equation.

3.1 Discretizing the Phillips' equation

When neglecting convection, the Phillips' wave operator reads

$$\frac{\partial}{\partial x_i}\left(\bar{c}^2\frac{\partial}{\partial x_i}\right) = \nabla\cdot\bar{c}^2\nabla \tag{3.1}$$

This operator may be discretized by different strategies, e. g.: finite differences, finite elements or finite volumes. The method chosen is the finite volume method. There is one main reason for doing so: three-dimensional and complex geometries are aimed. It means that it is indispensable to consider unstructured meshes, which are clearly much easier accounted in the finite volume discretization technique rather than finite differences. Also, the fact that finite volumes methods have been conceived under the conservative philosophy, conservation equations are satisfactorily fulfilled as long as the method is well applied in each of the control volumes. Furthermore, finite volumes methods are both less expensive and much easier to understand and to program than finite elements. Each step within the finite volume algorithm has a physical meaning which is clearly a great advantage. There is however one main drawback when using finite volumes: it is difficult to develop higher order schemes than those of second order when leading with three-dimensional geometries. The reason is that finite volumes have to be well optimized in each of their steps (numerical interpolation, differentiation and integration) which is clearly a not easy task.

Within the finite volume method several strategies arise. There are two common formulations: the cell-centered and cell-vertex method. In the first, the discrete values of the conserved variables are stored at the center of the control volume (the grid cell) and values at the nodes are obtained by averaging between the values of the neighboring cells. In the cell-vertex formulation the discrete conservative quantities are stored at vertices of the control volumes (or grid nodes) and values of mean fluxes are obtained by averaging all along the faces of the grid cell. The cell-vertex formulation is the one used in this study and has been inherited by the numerical scheme used in the AVBP solver [3].

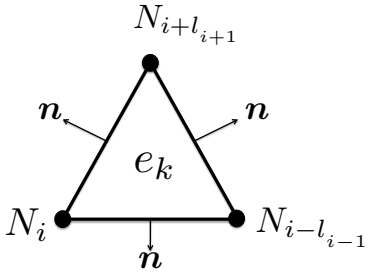

Figure 3.1: A triangular element

For simplicity let us consider a triangular cell although a similar analysis can be straightfor-

ward carried out for tetrahedra. The notation used here is shown in Fig. 3.1. The index e_k stands for a cell element k that is composed by three nodes $N_{i\pm \boldsymbol{l}}$. Each face of this triangle is characterized by its normal vector $\boldsymbol{n}$. The gradient operator for a quantity $\hat{p}$ corresponding to a cell element e_k is discretized following Green's theorem. It reads

$$\nabla \hat{p} \Big|_{e_k} = \frac{1}{V_{e_k}} \oint_{\partial e_k} \hat{p}_{e_k} \boldsymbol{n} dS \tag{3.2}$$

where $\hat{p}_{e_k}$ and V_{e_k} stands respectively for the pressure and the volume associated to the cell e_k. Let us remind that in the cell-vertex method all quantities are stored in the vertices of the cell. As a result, $\hat{p}_{e_k}$ must be expressed as an interpolation function g of the neighboring nodes N_o. Hence $\hat{p}_{e_k} = g(\hat{p}_o)$ where $\boldsymbol{o} = ..., i - l_{i-2}, i - l_{i-1}, i, i + l_{i+1}, i + l_{i+2}, ...$ is a vector that contains the neighbor nodes for a given node i and $\boldsymbol{l}$ is a vector that contains the distance between the node i and its neighbors [1]. Equation (3.2) is then expressed as:

$$\nabla \hat{p} \Big|_{e_k} = \frac{1}{V_{e_k}} \oint_{\partial e_k} g(\hat{p}_o) \boldsymbol{n} dS = \boldsymbol{h}_{e_k}(\hat{p}_o) \tag{3.3}$$

The triangular cell of Fig. 3.1 makes part of a whole set of triangular elements as shown in Fig. (3.2). Following Green's theorem, the divergence of $\bar{c}^2 \nabla \hat{p}$ for the node N_i is discretized as

$$\left(\nabla \cdot \bar{c}^2 \nabla \hat{p}\right) \Big|_{N_i} = \frac{1}{V_{N_i}} \oint_{\partial N_i} \bar{c}^2_{N_i} \nabla \hat{p} \Big|_{e_{k+\boldsymbol{\alpha}}} \cdot \boldsymbol{n} dS \tag{3.4}$$

$$\left(\nabla \cdot \bar{c}^2 \nabla \hat{p}\right) \Big|_{N_i} = \frac{1}{V_{N_i}} \oint_{\partial N_i} \bar{c}^2_{N_i} \boldsymbol{h}_{e_{k+\boldsymbol{\alpha}}}(\hat{p}_o) \cdot \boldsymbol{n} dS \tag{3.5}$$

where $\boldsymbol{\alpha}$ is a vector that contains the distance between the cell e_k and its the neighbors.

Note that a volume V_i is associated to the Node i and that this volume is enclosed by surfaces ∂V_{N_i} [2]. This volume V_i is shown in the shaded region of Fig. 3.2 and ∂N_i is represented by the thick black line enclosing it. Let us consider now what happens when this Node N_i is placed in a boundary of the computational domain. Such a case is represented by Fig. 3.3.

The analysis is similar to that of the Eq. (3.5). Nevertheless, the Volume of the node N_i has been truncated. The surface enclosing V_{N_i} is still represented by ∂V_{N_i} as before but in the present case ∂V_{N_i} is splitted in $S_{1,i}$ and $S_{2,i}$ being $S_{2,i}$ the surface corresponding to the node N_i adjacent to the computational boundary.

[1] Let us recall that for unstructured meshes a cell can be composed by nodes that are not numerate consecutivelly (e.g.: if a node $i = 5$ has adjacent nodes numbered 9 and 13, then l is 4 and 8 respectively)

[2] We talk about a 'volume' V_{N_i} being enclosed by 'surfaces' ∂V_{N_i}. Of course for the present two dimensional case the volume and the surface become a surface and an edge respectively.

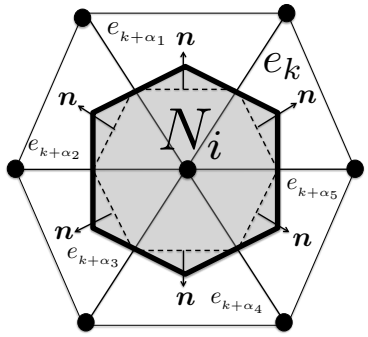

Figure 3.2: A set of six triangular cells embedded in a mesh grid

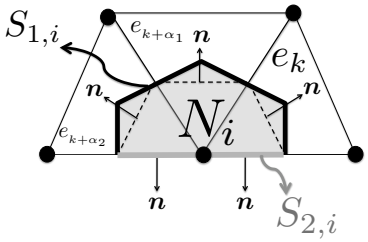

Figure 3.3: A set of three triangular cells boundarying the computational domain

$$\frac{1}{V_{N_i}} \oint_{\partial N_i} \bar{c}_{N_i}^2 \nabla \hat{p} \Big|_{e_{k+\alpha}} \cdot \boldsymbol{n} dS = \frac{1}{V_{N_i}} \left(\oint_{S_{1,i}} \bar{c}_{N_i}^2 \boldsymbol{h}_{e_{k+\alpha}}(\hat{p}_o) \cdot \boldsymbol{n} dS \right) + \frac{1}{V_{N_i}} \left(\oint_{S_{2,i}} \bar{c}_{N_i}^2 \boldsymbol{h}_{e_{k+\alpha}}(\hat{p}_o) \cdot \boldsymbol{n} dS \right) \quad (3.6)$$

The flux of the pressure gradient across the surface $S_{2,i}$ is associated to the boundary conditions imposed to the surface. This boundary condition can be expressed in terms of an acoustic impedance $\hat{Z}$ and pressure $\hat{p}$. Hence $(\nabla \hat{p} \cdot \boldsymbol{n}_{S2,i}) = f\left(\hat{Z}_{Ni}, \hat{p}_i\right)$. Expression (3.6) becomes

$$\frac{1}{V_{N_i}} \oint_{\partial N_i} \bar{c}_{N_i}^2 \nabla \hat{p} \Big|_{e_{k+\alpha}} \cdot \boldsymbol{n} dS = \frac{1}{V_{N_i}} \left(\oint_{S_{1,i}} \bar{c}_{N_i}^2 \boldsymbol{h}_{e_{k+\alpha}}(\hat{p}_o) \cdot \boldsymbol{n} dS \right) + \frac{1}{V_{N_i}} \left(\oint_{S_{2,i}} \bar{c}_{N_i}^2 f(\hat{Z}_{N_i}, \hat{p}_i) dS \right) \quad (3.7)$$

Finally, the Helmholtz equation Eq. (2.63) for the node N_i reads

$$\begin{aligned} \left[\nabla\left(\bar{c}^2\nabla\hat{p}\right)+\omega^2\hat{p}\right]_{N_i} &= -\boldsymbol{i}\omega(\gamma-1)\hat{\omega}_T\Big|_{N_i} \\ \frac{1}{V_{N_i}}\left(\oint_{S_{1,i}}\bar{c}^2_{N_i}\boldsymbol{h}_{e_{k+\alpha}}(\hat{p}_o)\cdot\boldsymbol{n}dS\right)+\frac{1}{V_{N_i}}\left(\oint_{S_{2,i}}\bar{c}^2_{N_i}f\left(Z_{N_i},\hat{p}_i\right)dS\right)+\omega\hat{p}_i &= -\boldsymbol{i}\omega(\gamma-1)\hat{\omega}_{T,i} \end{aligned} \tag{3.8}$$

Equation (3.8) must be solve for each node N_i of the computational domain. In matrix representation, this equation can be written as

$$\left[\boldsymbol{A_{i,j}}+\boldsymbol{B_{i,j}}\right]\hat{p}_o=\boldsymbol{C_j} \tag{3.9}$$

where

$$\boldsymbol{A_{i,j}}\hat{p}_o=\frac{1}{V_{N_i}}\left(\oint_{S_{1,i}}\bar{c}^2_{N_i}\boldsymbol{h}(\hat{p}_o)\cdot\boldsymbol{n}dS\right)+\omega^2\hat{p}_i \tag{3.10}$$

$$\boldsymbol{B_{i,j}}\hat{p}_o=\frac{1}{V_{N_i}}\left(\oint_{S_{2,i}}f(Z_{N_i},\hat{p}_i)dS\right) \tag{3.11}$$

The matrix $\boldsymbol{A_{i,j}}$ is a $n\times n$ sparse polydiagonal matrix where n stands for the total number of nodes in the computational grid. The number of diagonals depends on the degree of the interpolation used to relate the neighboring values of N_i to obtain the respective value at N_i. It should be clear then that $\boldsymbol{A}_{i,j}\neq 0$ when $\boldsymbol{A}_{i,j}=\boldsymbol{A}_{i,o}$, or in other words, $\boldsymbol{A}_{ij}$ is non-zero for the neighboring nodes implied into the respective interpolation procedure. As a result $\boldsymbol{A}_{i,j}=0$ if $j\neq\boldsymbol{o}$, i.e., $j>i+\boldsymbol{l}$, and if $j<i-\boldsymbol{l}$. As a consequence, $\boldsymbol{A}_{i,j}=0$ for elements far from the mean diagonal. This can be observed in Fig. 3.4a. Let us recall that $\boldsymbol{l}$ can contain high values for unstructured meshes.

Matrix $\boldsymbol{B_{i,j}}$ is a $n\times n$ sparse polydiagonal matrix and is associated to the boundary conditions. It is non-zero when both the node N_i lies on one of the boundary surfaces and $\hat{Z}_{Ni}\neq 0$. As a consequence, $\boldsymbol{B}$ does not play any role when Neumann boundary conditions are used: $\hat{Z}_{Ni}=0$ or $\hat{u}\propto\nabla\hat{p}=0$, i.e., when solid boundaries (walls) are considered. A typical distribution of the non-zero elements of matrix $\boldsymbol{B_{i,j}}$ is shown in Fig. (3.4b)

$$\boldsymbol{C_j}=-\boldsymbol{i}\omega(\gamma-1)\hat{\omega}_{T,i} \tag{3.12}$$

$\boldsymbol{C_{i,j}}$ is a vector of size n. It contains the sources of the acoustic problem, in our case the unsteady heat release rate ($\hat{\omega}_T$). The majority of its values are zero, except for those ones where the flame is present. The matrices $\boldsymbol{A_{i,j}}$, $\boldsymbol{B_{i,j}}$ and the vector $\boldsymbol{C_j}$ are shown in Fig. (3.4)

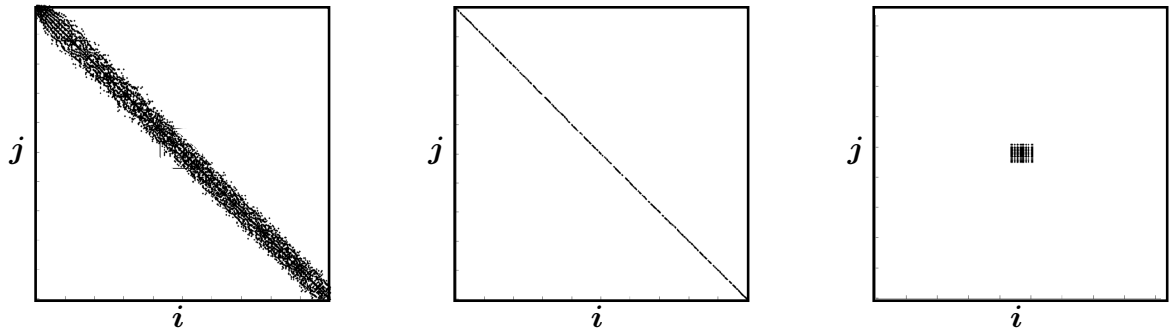

a) $\boldsymbol{A_{i,j}}$ b) $\boldsymbol{B_{i,j}}$ c) $\boldsymbol{C_j C_j^T}$

Figure 3.4: Typical Matrices for a non-structured 3D problem [93]. Non-zero entries are shown as dark points. Here $\boldsymbol{C^T}$ is the transpose of $\boldsymbol{C}$. The dyadic product $\boldsymbol{CC^T}$ is shown to display the non-zero elements of $\boldsymbol{C_j}$

3.2 Boundary Conditions in AVSP-f

There are three types of acoustic boundaries in the numerical tool AVSP-f. The first one is of the Dirichlet type. It means that at the boundary a zero pressure fluctuation $\hat{p}$ is imposed. This represents usually the boundary condition used at the outlet of the domain when this one is open to the atmosphere. In order to impose $\hat{p} = 0$, it is necessary to remove the concerned nodes from the matrix $\boldsymbol{A_{i,j}}$ so that the linear system to resolve is well-posed. Equation (3.9) becomes:

$$\left[\boldsymbol{A_{i,j}} + \boldsymbol{B_{i,j}}\right] \hat{p}_o = \boldsymbol{C_j} \quad \Rightarrow \quad \left(\boldsymbol{A_{i,j}} \Big|_{i,j \notin \partial S_D} \right) \hat{p}_o = \boldsymbol{C_j} \tag{3.13}$$

where S_D stands for the surfaces in which the homogeneous Dirichlet Boundary condition is applied. Another important boundary condition corresponds to totally reflecting boundaries, usually applied to walls and inlets. It is of the type of Neumann since what is imposed here is the gradient of $\hat{p}$. The linearized momentum equation for low Mach number flows in the frequency domain reads

$$i\omega \hat{\boldsymbol{u}} \cdot \boldsymbol{n} = \nabla \hat{p} \cdot \boldsymbol{n} \tag{3.14}$$

It is clear that no fluctuations of velocity are allowed normal to the surface ($\hat{u} \cdot \boldsymbol{n} = 0$) if the gradient of the fluctuating pressure normal to the boundary is zero ($\nabla \hat{p} \cdot \boldsymbol{n} = 0$). For this homogeneous Neumann boundary condition, the system to resolve is

$$\left[\boldsymbol{A_{i,j}} + \boldsymbol{B_{i,j}}\right] \hat{p}_o = \boldsymbol{C_j} \quad \Rightarrow \quad \boldsymbol{A_{i,j}} \hat{p}_o = \boldsymbol{C_j} \tag{3.15}$$

in which $\boldsymbol{B_{i,j}} = 0$. Finally, there is another boundary condition that imposes a relation between the acoustic velocity normal to the surface $\hat{\boldsymbol{u}} \cdot \boldsymbol{n}$ and the acoustic pressure $\hat{p}$. Injecting the definition of the acoustic impedance $\hat{Z} = \hat{p}/i\omega\hat{\boldsymbol{u}} \cdot \boldsymbol{n}$ into Eq. (3.14) leads to:

$$\hat{Z}\nabla\hat{p} \cdot \vec{n} - i\omega\hat{p} = 0 \tag{3.16}$$

This type of boundary condition is known as a 'Robin' boundary condition. Note that $\boldsymbol{B_{i,j}} \neq 0$ as soon as $\hat{Z} \neq 0$ and $\hat{Z} \neq \infty$ over some piece of the boundaries of the flow domain.

3.3 Solving the system $\mathcal{A}x = b$

From Eq. (3.9) it can be seen that the algebraic system to solve is of the form $\mathcal{A}x = b$. Several approaches can be used to solve linear systems; they are divided mainly in two groups: non-iterative methods or 'direct' methods and iterative methods. Within 'direct' methods, two approaches are most often used: the LU (or Gauss Elimination) and the QR decomposition. Both of them have the same philosophy: "divide and conquer". In mathematical terms it means

$$\mathcal{A} = LU \quad \text{or} \quad \mathcal{A} = QR \tag{3.17}$$

where $\mathcal{A}$ is a $n \times n$ matrix, L is a lower triangular $n \times n$ matrix, U is an upper triangular $n \times n$ matrix, Q is an orthonormal[3] $n \times n$ matrix and R is an upper triangular $n \times n$ matrix. When solving the linear system by the LU decomposition, three steps are followed

1. $\mathcal{A}x = b \rightarrow LUx = b$
2. solve $Lw = b$ for the unknown w
3. solve $Ux = w$ for the unknown x.

If a QR decomposition is preferred, three steps are also considered

1. $\mathcal{A}x = b \rightarrow QRx = b$
2. solve $Qw = b$ for the unknown w

[3] An orthornormal matrix is a matrix with n orthogonal columns in which the norm of each column is equal to one.

3. solve $Rx = w$ for the unknown x.

Both of these methods are suitable when dealing with small matrices (n<1000 say), but not for very big systems since the number of floating operations scales as n^3.

In order to reduce the dimension of the problem, the matrix $Q \in \mathbb{C}^{n\times n}$ is reduced to a rectangular matrix $\widehat{Q}_m \in \mathbb{C}^{n\times m}$ where $m < n$ and the symbol $\widehat{()}$ represents a rectangular matrix. This $\widehat{Q}_m$ matrix is then multiplied to the original matrix $\mathcal{A}$ resulting in a system $\mathcal{A}\widehat{Q}_m = \widehat{D}$. It yields

$$\mathcal{A}x = b \quad \rightarrow \quad \mathcal{A}x_j = b - r_m \quad \rightarrow \quad \mathcal{A}\left(x_0 + \widehat{Q}_m y\right) = b - r_m \quad \rightarrow \quad r_0 - \widehat{D}y = r_m \tag{3.18}$$

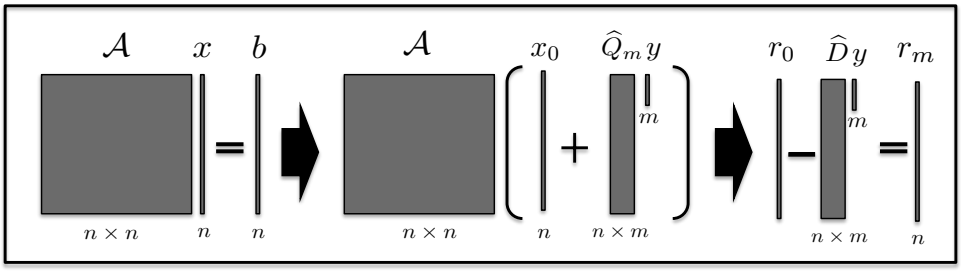

Figure 3.5: Reduction of the linear system

where x_0 is an initial estimation of x_m, x_m is the approximation of the solution x at the m iteration and $r_m = b - \mathcal{A}x_m$ is the corresponding residual of x_m. Figure 3.5 shows that the system to solve clearly reduces in size. To resolve the system $\mathcal{A}x = b$ for x has become an analog problem: resolve $r_0 - \widehat{D}y = r_m$ for y so that r_m is minimized. It should be clear then that if r_m goes to zero for a given vector y, then the corresponding $x_m = x_0 + \widehat{Q}_m y$ can be considered a good solution of the linear system $\mathcal{A}x = b$. It follows

$$\boxed{\text{Find } y \text{ such that} \quad \|r_0 - \widehat{D}y\|_2 = \|r_m\|_2 \quad \text{is minimized}} \tag{3.19}$$

where $\|\cdot\|_2$ is the norm in the Euclidean space. This problem (Eq. 3.19) is solved by the *least square* methodology [45] which will be explained in section 3.3.2. The subsequent step is to decompose the matrix remembering the philosophy 'divide and conquer'. The *LU* decomposition is not considered here since this method only accounts for square matrices. Another possibility would be the *QR* decomposition. Nevertheless, it has been demonstrated that the algorithm following this procedure is unstable [101]. The reliable technique to use is known as the *Hessenberg* decomposition. The matrix $\widehat{D}$ under this method becomes

$$\widehat{D} = \widehat{Q}_{m+1}\tilde{H}_m \tag{3.20}$$

where $\widehat{Q}_{m+1} \in \mathbb{C}^{n \times m+1}$ is an orthonormal matrix and $\tilde{H}_m \in \mathbb{C}^{m+1 \times m}$ is un upper-Hessenber matrix [4].

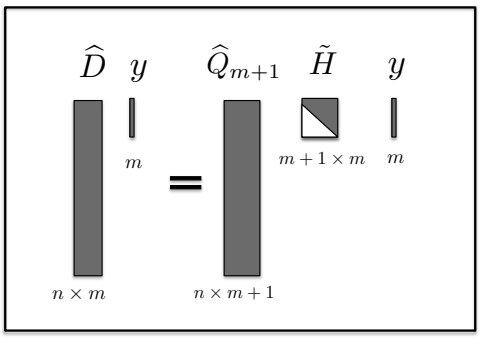

Figure 3.6: Hessenberg decomposition

The least square problem is now given by

$$\boxed{\text{Find } y \text{ such that} \quad \|r_0 - Q_{m+1}\tilde{H}_m y\|_2 = \|r_m\|_2 \quad \text{is the minimized}} \tag{3.21}$$

Let us introduce $r_0 = q_1\|r_0\|$ (see Eq. 3.43). The vector q_1 can be expressed as $Q_{m+1}e_1 = q_1$ where e_1 is the canonical unit vector $e_1 = (1, 0, 0, ...)$. Furthermore, the invariance of inner products means that the angles between vectors are preserved, and so are their lengths: $\|Qx\| = \|x\|$. The final expression results in

$$\|Q_{m+1}\left(\|r_0\|e_1 - \tilde{H}_m y\right)\|_2 = \|\left(\|r\|e_1 - \tilde{H}_m y\right)\|_2 \tag{3.22}$$

leading to

$$\boxed{\text{Find } y \text{ such that} \quad \|\left(\|r\|e_1 - \tilde{H}_m y\right)\|_2 = \|r_m\|_2 \quad \text{is minimized}} \tag{3.23}$$

Once y is found through the *least square* methodology, a solution for the $\mathcal{A}x_m \approx b$ problem can be found by solving $x_m = x_0 + \widehat{Q}_m y$. There are still two crucial issues to resolve:

1. How to construct such matrices $\widehat{Q}_m$ and $\tilde{H}_m$?.
2. What is the 'least square problem' about ?

These two issues will be addressed in sections (3.3.1) and (3.3.2) respectively.

[4] An upper- Hessenberg matrix H is a matrix with zeros below the first subdiagonal

3.3.1 On the Arnoldi algorithm

The most important idea to draw from concepts of inner products and orthogonality is this: inner products can be used to decompose arbitrary vectors into orthogonal components [101]. For example, suppose that $\{q_1, q_2, \cdots, q_n\}$ is an orthonormal set, and let a be an arbitrary vector. The quantity $q^* a$ is then a scalar[5]. Utilizing these scalars as coordinates in an expansion, a vector v is defined.

$$v = a - (q_1^* a)q_1 - (q_2^* a)q_2 - \cdots - (q_n^* a)q_n \tag{3.24}$$

It is clear that the vector v is orthogonal to $\{q_1, q_2, \cdots, q_n\}$. This can be verified by multiplying all terms by q_i^*

$$q_i^* v = q_i^* a - (q_1^* a)(q_i^* q_1) - (q_2^* a)(q_i^* q_2) - \cdots - (q_n^* a)(q_i^* q_n) = q_i^* a - (q_1^* a)(q_i^* q_i) = 0 \tag{3.25}$$

Equation 3.24 is the basis of orthogonal decomposition. Let us consider now a matrix $\mathcal{A}$ composed by n columns a_j.

$$\mathcal{A} = \left[\begin{array}{c|c|c|c|c} & & & & \\ a_1 & a_2 & a_3 & \cdots & a_n \\ & & & & \end{array}\right] \tag{3.26}$$

At the very beginning no q_j exists. It must be built iteratively as follows:

$$v_1 = a_1 \quad \rightarrow \quad q_1 = \frac{v_1}{\|v_1\|} \tag{3.27}$$

since q_1 must be also normalized. Subsequently, q_2 should be then

$$v_2 = a_2 - (q_1^* a_2)q_1 \quad \rightarrow \quad q_2 = \frac{v_2}{\|v_2\|} \tag{3.28}$$

And after n steps, the q_n vector is computed

[5]The symbol $()^*$ represents the complex conjugate of given a quantity

$$v_n = a_n - \sum_{j=1}^{n} (q_j^* a_n) q_j \quad \rightarrow \quad q_n = \frac{v_n}{\|v_n\|} \tag{3.29}$$

This procedure of obtention of q_n orthonormal matrices is known as the *Gram-Schmidt Orthogonalization*. This algorithm is useful to understand the basic procedure of orthogonalization. Moreover, in addition to the matrix Q, the upper triangular matrix R is obtained straightforward by doing

$$r_{ij} = q_i^* a_j \quad \text{for every} \quad i \neq j \quad \text{and} \quad r_{ii} = \|v_i\| \tag{3.30}$$

In practice, the Gram-Schmidt formula are not applied since it has been demonstrated that this algorithm turns out to be unstable. The *Modified Gram-Schmidt* algorithm computes the same result but with a more stable algorithm as follows.

$$v_j^{(1)} = a_j \tag{3.31}$$
$$v_j^{(2)} = v_j^{(1)} - q_1 q_1^* v_j^{(1)} \tag{3.32}$$
$$v_j^{(3)} = v_j^{(2)} - q_2 q_2^* v_j^{(2)} \tag{3.33}$$
$$\vdots \tag{3.34}$$
$$v_j^{(j)} = v_j^{(j-1)} - q_{j-1} q_{j-1}^* v_j^{(j-1)} \tag{3.35}$$

recalling that $\sum_{j=1}^{n} (q_j^* v) q_j = \sum_{j=1}^{n} (q_j q_j^*) v$. This algorithm should be red as:

$$\boxed{v_1^{(1)} \rightarrow v_2^{(1)}, v_2^{(2)} \rightarrow \cdots \rightarrow v_i^{(1)}, v_i^{(2)}, \cdots, v_i^{(i)} \rightarrow \cdots} \tag{3.36}$$

It has been explained how to perform a QR factorization with an efficient algorithm. However, as stated before, the QR factorization is not the best strategy to decompose a matrix such as $\widehat{D}$ (Eq. 3.18). A better method is to factorize by $\widehat{Q}_{m+1}$ and $\tilde{H}$. The procedure performed to this purpose is similar to the Modified Gram-Schmidt orthogonalization and is known as the *Arnoldi* Algorithm [2].

$$A\widehat{Q}_m = \widehat{Q}_{m+1}\tilde{H}_m \tag{3.37}$$

The 1st to mth column of this equation can be written as follows:

$$Aq_1 = h_{11}q_1 + h_{21}q_2 \tag{3.38}$$
$$Aq_2 = h_{12}q_1 + h_{22}q_2 + h_{32}q_3 \tag{3.39}$$
$$Aq_3 = h_{13}q_1 + h_{23}q_2 + h_{33}q_3 + h_{43}q_4 \tag{3.40}$$
$$\vdots \tag{3.41}$$
$$Aq_m = h_{1m}q_1 + \cdots + h_{mm}q_n + h_{m+1,m}q_{m+1} \tag{3.42}$$

And the vectors v_j are obtained as

$$q_1 = r_0/\|r_0\| \tag{3.43}$$
$$v_j^{(1)} = Aq_j \tag{3.44}$$
$$v_j^{(2)} = v_j^{(1)} - q_1 q_1^* v_j^{(1)} \tag{3.45}$$
$$v_j^{(3)} = v_j^{(2)} - q_2 q_2^* v_j^{(2)} \tag{3.46}$$
$$\vdots \tag{3.47}$$
$$v_j^{(j)} = v_j^{ji-1)} - q_{j-1} q_{j-1}^* v_j^{(j-1)} \tag{3.48}$$

Finally, all the elements q_j and h_{ij} are computed by

$$\text{for } j = 1 : m-1 \rightarrow \quad q_{j+1} = v_j/\|v_j\| \quad \text{and} \quad h_{ij} = q_i^* \mathcal{A} q_j \quad \text{for every} \quad i \neq j+1 \quad \text{and} \quad h_{j+1,j} = \|v_j\|$$

It should be evident from Eqs. (3.38) and (3.42) that the vectors $\{q_j\}$ form bases of the successive *Krylov subspaces* generated by $\mathcal{A}$ and r defined as follows:

$$\mathcal{K}_m = \langle r_0, \mathcal{A}r_0, ..., \mathcal{A}^{n-1}r_0 \rangle = \langle q_1, q_2, ..., q_m \rangle \subseteq \mathbb{C}^n \tag{3.49}$$

where $\langle \cdot \rangle$ means the span of. The Arnoldi process can be described as the systematic construction of orthonormal bases for successive Krylov subspaces knowing that the Krylov $n \times m$ matrix K_n is written as

$$K_n = \left[\begin{array}{c|c|c|c|c} & & & & \\ r_0 & Ar_0 & A^2r_0 & \cdots & A^{n-1}r_0 \\ & & & & \end{array} \right] \tag{3.50}$$

3.3.2 The least square problem

Let us consider an overdetermined problem of the form

$$\widehat{A}x = b \tag{3.51}$$

This problem has not exact solution. Nevertheless the residual $r = \widehat{A}x - b$ will be minimized if a vector x is found such that $r \perp range(\widehat{A})$. In mathematical terms, it can be expressed by the inner product

$$\widehat{A}^* r = 0 \quad \text{or} \quad \widehat{A}^*\widehat{A}x = \widehat{A}^* b \tag{3.52}$$

or if applying the QR factorization

$$(\widehat{Q}_m R)^* r = 0 \quad \text{or} \quad R^*\widehat{Q}_m^*\widehat{Q}Rx = R^*\widehat{Q}_m^* b \quad \text{and then} \quad \widehat{Q}_m Rx = \widehat{Q}_m\widehat{Q}_m^* b \tag{3.53}$$

and as a consequence

$$\widehat{A}x = \widehat{Q}_m\widehat{Q}_m^* b = Pb \tag{3.54}$$

where $P \in \mathbb{C}^{m\times m}$ is the orthogonal projector onto $range(\widehat{A})$. It is important to understand that we have transformed a problem with no solution $\widehat{A}x = b$ (Eq. 3.51) into a problem with an exact solution $\widehat{A}x = Pb$. This exact solution x for the problem $\widehat{A}x = Pb$ is also the vector that minimizes the residual for the first problem $r = \widehat{A}x - b$. In terms of the problem of our interest (Eq. 3.23), the expression giving the solution for y reads

$$y = R^{-1}\widehat{Q}_m^* \|b\| e_1 \tag{3.55}$$

where the Hessenberg Matrix has been factorized $\tilde{H}_m = \widehat{Q}_m R$.

3.4 GMRES

The Generalized Minimal RESidual (GMRES) method is a very well known algorithm for solving linear systems of considerable size. It was proposed by Saad and Schultz in 1986 [83] in order to solve large, sparse and non Hermitian linear systems. GMRES belongs to the class of Krylov based iterative methods and is composed by the procedures described in the previous sections. Fig. 3.7 shows a scheme in which the GMRES method is summarized.

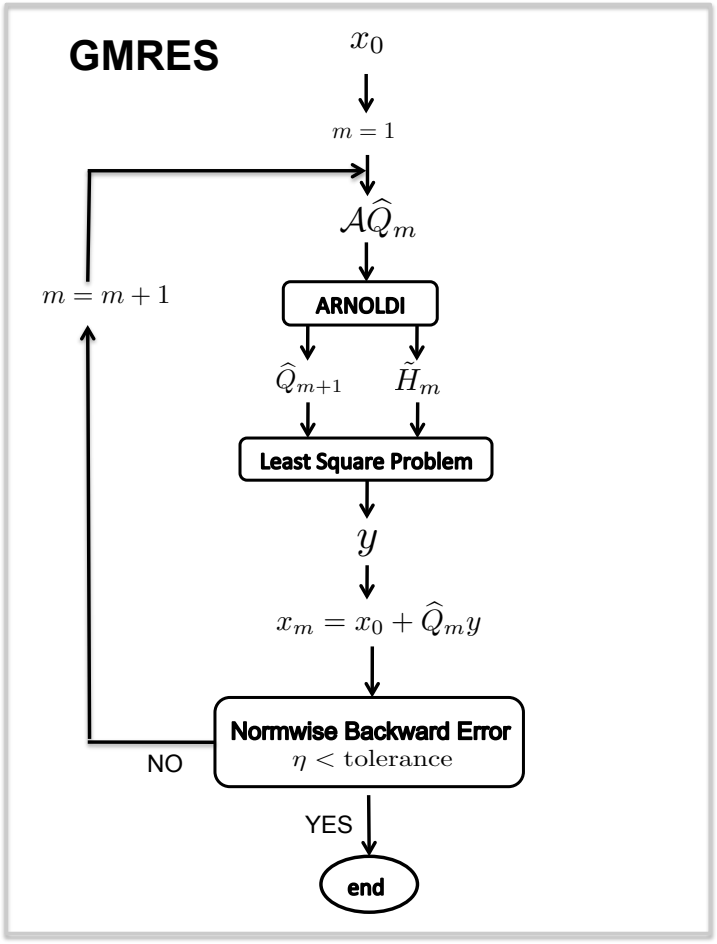

Figure 3.7: The GMRES Algorithm

GMRES has been chosen to solve the problem of Eq. (3.9) due to its portability, simplicity, flexibility and efficiency. It is important to emphasize that the fact that GMRES belongs to the class of Krylov based iterative methods allows to solve the linear system by using only Matrix-vector products instead of storing the full matrix $\mathcal{A}$.

Stopping criteria of GMRES

In order to analyze the convergence of GMRES, it is important to know which mathematical properties of $\mathcal{A}$ determine the size of $\|r\|$. There are two main observations. The first is that GMRES converges monotonically $\|r_{m+1}\| \leq \|r_m\|$. The reason is that $\|r_m\|$ is as small as possible for the subspace $\mathcal{K}_m$. By enlarging $\mathcal{K}_m$ to the space $\mathcal{K}_{m+1}$, it is only possible to decrease the residual norm, or at worst leave it unchanged. The second is that after at most n steps the process must converge, at least in the absence of round errors $\rightarrow \|r_n\| = 0$.

Many algorithms of numerical linear algebra satisfy a condition that is both stronger and simpler than stability. We say that an algorithm $\tilde{f}$ for a problem f is backward stable if $\tilde{f}(x) = f(\tilde{x})$ for some approximated solution $\tilde{x} = x_m$. Here $\tilde{x} = x + \delta x$ and $\tilde{f} = f + \delta f$ are a perturbed solution and a perturbed function respectively. The *normwise backward error* η is then defined as:

$$\eta = \frac{\|x_m - x\|}{\|x\|} = \frac{\|\mathcal{A}^{-1}(b - r_m) - \mathcal{A}^{-1}b\|}{\|\mathcal{A}^{-1}b\|} = \frac{\|r_m\|_2}{\|b\|_2} \tag{3.56}$$

The backward error measures the distance between the data of the initial problem and those of the perturbed problem. The best η one can require from an algorithm is a backward error of the order of the machine precision. In practice, the approximation of the solution is acceptable when its backward error is lower than the uncertainty on the data.

3.4.1 Preconditioning

The convergence of a matrix iteration depends on the properties of the matrix, i.e., the eigenvalues, the singular values, or sometimes other information. It is interesting to comprehend that in many cases, the problem of interest can be transformed so that the properties of the matrix are improved drastically. This process of 'preconditioning' is essential to most successful applications of iterative methods.

Suppose we wish to solve an $n \times n$ nonsingular system $\mathcal{A}x = b$. For any nonsingular $n \times n$ matrix M, the system $M\mathcal{A}x = Mb$ has the same solution. If we solve this system iteratively, the convergence will depend on the properties of $M\mathcal{A}$ instead of those of $\mathcal{A}$. If this *preconditioner* M is well chosen, the problem may be solved much more rapidly. The best choice ever for a preconditioner is the inverse of the system matrix $\mathcal{A}$, i.e., $M = \mathcal{A}^{-1}$. Of course it would be ridiculous to use $\mathcal{A}^{-1}$ as a preconditioner since this is already the solution of the problem. The idea is then to make M^{-1} as close as $\mathcal{A}$ as possible. In other words, to make the eigenvalues of $M^{-1}\mathcal{A}$ be close to 1 and $\|M^{-1}\mathcal{A} - I\|_2$ small where I is the identity matrix. In doing so, a quickly convergence of the solution is expected.

Two well known preconditioning methods are the *Diagonal scaling or Jacobi* ($M^{-1} = diag(\mathcal{A})$)

and the *Incomplete Cholesky or LU factorization*. These last are known as 'incomplete' since M^{-1} is allowed only to have nonzeros in the positions where $\mathcal{A}$ has non zeros. This is done in order to keep the sparsity of the original matrix A. A Complete Cholesky or LU factorization would destroy zeros leading to a dense M matrix. These preconditioner are appropiated for ill-conditioned problems of small size. But for big and ill-conditioned $\mathcal{A}$ matrices, these methods are not the best suited.

3.4.2 Dynamic preconditioning: the embedded GMRES

The right preconditioning of the $\mathcal{A}x = b$ problem reads

$$\mathcal{A}x = \mathcal{A}Mc = b \tag{3.57}$$

The traditional way to solve this system would be first to find a matrix M such that $\mathcal{A}M$ is well conditioned; second, to solve the system for the vector c; and finally to find x from $x = Mc$. In this procedure it is imperative to explicitly construct and store the matrix M. A better way to apply preconditioning would be to find a preconditioning matrix of size $n \times m$ by solving an second linear system. In other words, applying GMRES to find a good preconditioner. Recalling Eq. (3.18), we add the preconditioning matrix M into the computation

$$\mathcal{A}x = \mathcal{A}\left(x_0 + \widehat{Q}_m y\right) = b - r_m \quad \rightarrow \quad \mathcal{A}x = \mathcal{A}\left(x_0 + M\widehat{Q}_m c\right) = b - r_m \tag{3.58}$$

where $x = x_0 + M\widehat{Q}_m c$. The matrix $\widehat{Z}_m$, which is the proyection of M in the krylov space, is defined as $\widehat{Z}_m = M\widehat{Q}_m$. Eq. (3.58) becomes

$$\mathcal{A}\left(x_0 + \widehat{Z}_m c\right) = b - r_m \tag{3.59}$$

The preconditioning matrix M is let it to be $\mathcal{A}^{-1}$, so that $\mathcal{A}M^{-1} = I$. The vector z_m of the matrix $\widehat{Z}_m$ can now be found by solving the linear system

$$z_m = Mq_m \quad \rightarrow \quad \mathcal{A}z_m = q_m \tag{3.60}$$

which is clearly a problem of the type $\mathcal{A}x = b$. Once the vector z_m is found, the orthogonalization (finding q_m) is carried out applying the Arnoldi procedure to $\mathcal{A}\widehat{Z}_m$ instead of $\mathcal{A}\widehat{Q}_m$, resulting in a faster convergence. Figure 3.8 represents the procedure just described.

As it can be observed from Fig. 3.8 the system $\mathcal{A}x = b$ is solved by one GMRES algorithm embedded in another GMRES. As a consequence, the present strategy is called *the embedded*

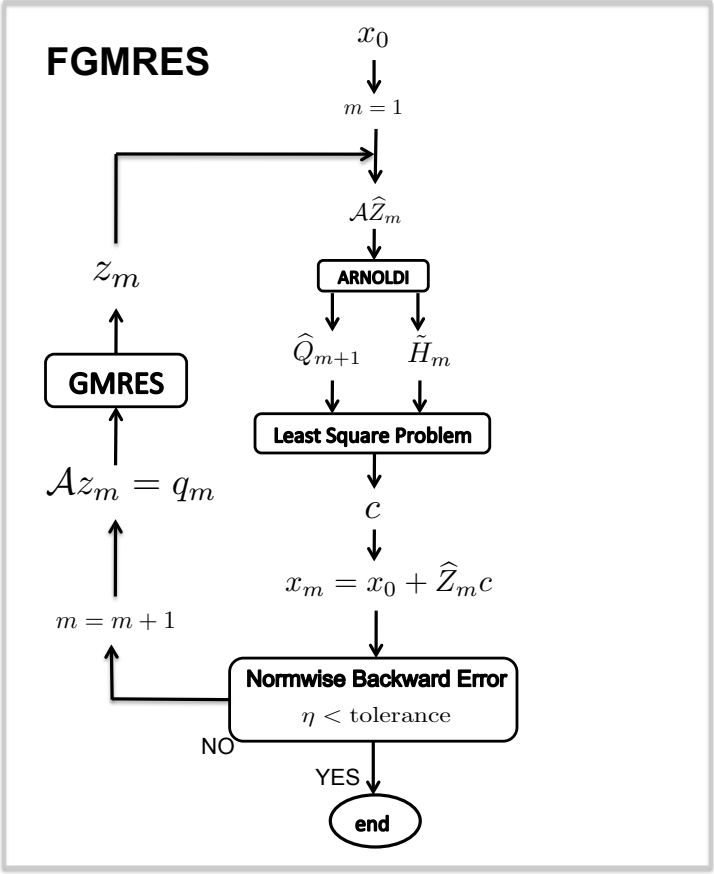

Figure 3.8: The embedded GMRES Algorithm

GMRES and is the one applied in the present study to solve the linear system

$$\underbrace{\left(\nabla \cdot \bar{c}^2 \nabla + I\omega^2\right)}_{\mathcal{A}} \underbrace{\hat{p}}_{x} = \underbrace{i\omega(\gamma - 1)\hat{\omega}_T}_{b} \tag{3.61}$$

which represents the propagation of noise due to a thermal source. Note that Eq. (3.61) must be solved once for each frequency ω. As a result, in order to build a proper spectrum of $\hat{p}$ (e.g.: 0-1000 Hz ; $\Delta f = 10Hz$) this system must be solved around hundred times.

AVSP-f uses a CERFACS implementation of the GMRES algorithm for both real and complex, single and double precision arithmetics suitable for serial, shared memory and distributed memory computers [29, 30].

4

Validation of the acoustic code AVSP-f

Contents

4.1 Fundamental validation cases

The sound radiation produced by arbitrary 2D monopoles embedded in a free and quiescent field is computed by the numerical tool AVSP-f. Non-reflecting boundary conditions are applied on the computational boundaries in order to mimic the free-field condition. Results obtained by AVSP-f are subsequently compared to those evaluated analytically.

The non-homogenous Helmholtz equation can be written as

$$\nabla^2 \hat{p}(\boldsymbol{x}, \omega) + k^2 \hat{p}(\boldsymbol{x}, \omega) = \frac{\hat{S}(\boldsymbol{y}, \omega)}{\bar{c}^2} \tag{4.1}$$

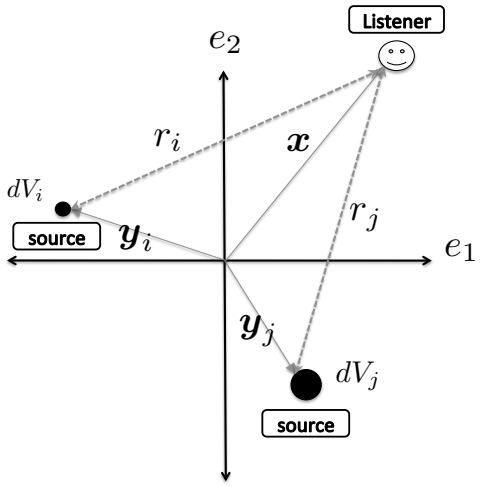

Figure 4.1: Monopoles placed at $\boldsymbol{y}$ and listener placed at $\boldsymbol{x}$

where $k = \omega/\bar{c}^2$ and $\hat{S}(\boldsymbol{y}, \omega)$ is a forcing source term. In this equation $\boldsymbol{y}$ represents the distance from the source to the reference point and $\boldsymbol{x}$ represents the distance from the observer to the reference point as illustrated in Fig. 4.1. The solution of this equation can be found by applying Eq. (2.74)

$$\hat{p}(\boldsymbol{x}, \omega) = \int\limits_{V_0(y)} \frac{\hat{S}(\boldsymbol{y}, \omega)}{\bar{c}^2} \hat{G}(\boldsymbol{x}|\boldsymbol{y}, \omega) \boldsymbol{d}y \tag{4.2}$$

The 2D spectral Green's function, given by Eq. (2.82), is inserted into Eq. (4.2) resulting in

$$\hat{p}(\boldsymbol{x}, \omega) = \frac{i}{4\bar{c}^2} \int\limits_{V_0(\boldsymbol{y})} \hat{S}(\boldsymbol{y}, \omega) H_0^2(kr) \boldsymbol{d}y \tag{4.3}$$

where $r = |\boldsymbol{x} - \boldsymbol{y}|$ and H_0^2 is the Hankel function of the second kind and order 0.

4.1.1 A Monopole in free space

One fundamental validation for an acoustic code is to test its ability to compute the radiation of sound due to a source. As a consequence, for the present case only one monopole is considered and no boundary conditions are taken into account. Moreover, as mentioned before, the mean field is considered homogeneous. These conditions are imposed so that a perfect isotropic radiation pattern is obtained. The source is pointwise and is defined as

$$\widehat{S}(\boldsymbol{y}, \omega) = \hat{S}_0 \delta(y - y_0) e^{-i\phi} \tag{4.4}$$

where $\hat{S}_0 = 1E10\, W/m^3 s$, $y_0 = [0.0, 0.0]\, m$, $\phi = 0\, rad$, and $\omega = 2\pi \cdot 5000\, rad/s$. The same case is computed with the numerical tool AVSP-f. The outputs of this code are the fields of both modulus $|\hat{p}|$and argument $arg(\hat{p})$ of the acoustic pressure. They are illustrated in Fig. 4.2. The reconstruction of the acoustic field in the time domain for $t_0 = 0$ is computed by $p' = |\hat{p}| \cos(arg(\hat{p}))$ and is shown in Fig. 4.3. Fig. 4.4 shows the isotropic pattern in the sound radiation produced by a monopolar source. It is also observed from this figure that a good agreement is reached between analytical an numerical results.

a) Modulus of Pressure $|\hat{p}|$ b) Argument of pressure $arg(\hat{p})$

Figure 4.2: Outputs of AVSP-f. Monopole case

Figure 4.3: Acoustic field produced by a monopole. $p' = |\hat{p}| \cos(arg(\hat{p}))$

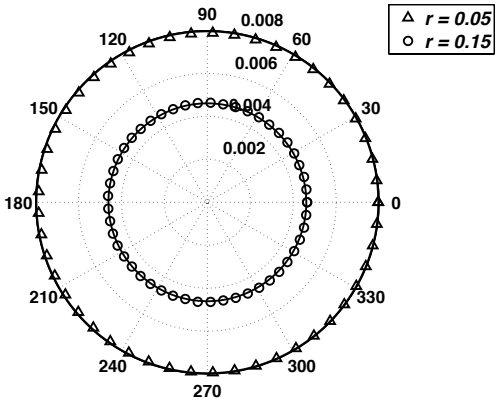

a) Directivity of a monopole
for two different radii.
[—— Analytics, (○△) AVSP-f]

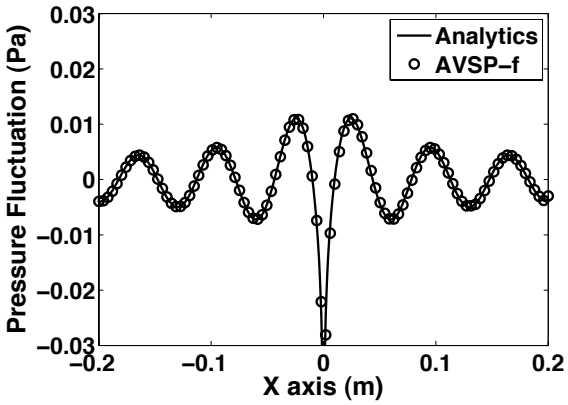

b) Pressure fluctuation
along the horizontal e_1 axis
[—— Analytics, (○) AVSP-f]

Figure 4.4: Analytical solution vs Numerical solution.

4.1.2 A Dipole in free space

Once pure radiation is tested in section (4.1.1), the influence on the acoustic field of another monopole is tested. If this monopole radiates sound out of phase with respect to the first monopole, a substraction of acoustics fluctuations will occur leading to a diminution of the acoustic amplitude in some regions. If this phase shift is equal to π a perfect cancelation should occur in the plane of antisymmetry between the two monopoles. Two monopoles with such a shift phase conform a dipole. The source is defined as

$$\hat{S}(\boldsymbol{y},\omega) = \hat{S}_0\delta(y-y_1)e^{-i\phi_1} + \hat{S}_0\delta(y-y_2)e^{-i\phi_2} \tag{4.5}$$

where $\phi_1 = \phi_2 + \pi$. From Eq. (4.3)

$$\hat{p}(\boldsymbol{x},\omega) = \frac{i}{4c_0^2}\int\limits_{V_0(\mathbf{y})} \left(\hat{S}_0\delta(y-y_1)e^{-i\phi_1} + \hat{S}_0\delta(y-y_2)e^{-i\phi_2}\right) H_0^2(kr)dV \tag{4.6}$$

Finally

$$\hat{p}(\boldsymbol{x},\omega) = \frac{i}{4c_0^2}\left(\hat{S}_0\delta(y-y_1)e^{-i\phi_1}\right) H_0^2(kr_1)dV_1 + \frac{i}{4c_0^2}\left(\hat{S}_0\delta(y-y_2)e^{-i\phi_2}\right) H_0^2(kr_2)dV_2 \tag{4.7}$$

where $\hat{S}_0 = 1E10\ W/m^3s$, $y_1 = [-0.02, 0.0]\ m$, $y_2 = [0.02, 0.0]\ m$, $\phi_1 = 0\ rad$, $\phi_1 = \pi\ rad$, and $\omega = 2\pi \cdot 5000\ rad/s$. Fig. (4.5) shows the solution given by the code AVSP-f. The reconstruction of the acoustic field at $t_0 = 0$ is evaluated by $p' = |\hat{p}| \cos(arg(\hat{p}))$. This acoustic field is shown in Fig. 4.6. It can be observed from Fig. 4.6 and Fig. 4.7 that AVSP-f succeeds in recovering the acoustic field produced by a dipole. The zone of silence is well seen in the line of antisymmetry between the two monopoles, i.e., the 90° and 270° directions.

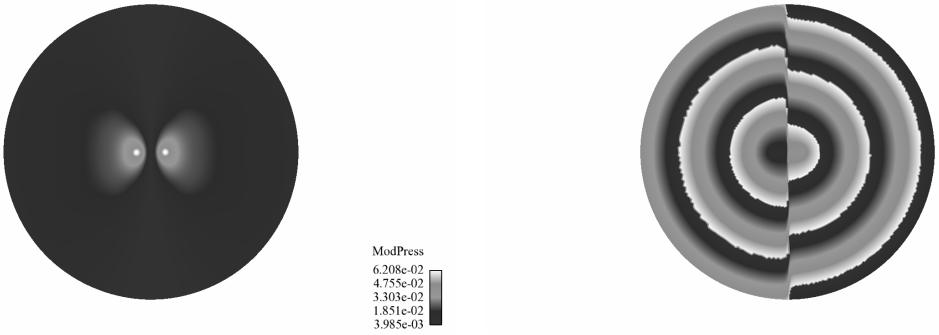

a) Modulus of Pressure $|\hat{p}|$ b) Argument of pressure $arg(\hat{p})$

Figure 4.5: Outputs of AVSP-f. Dipole case

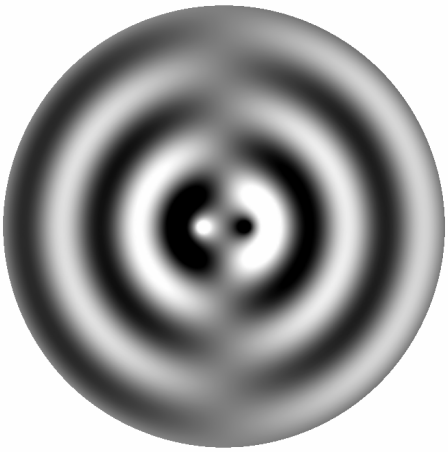

Figure 4.6: Acoustic field produced by a dipole. $p' = |\hat{p}| \cos(arg(\hat{p}))$

4.1.3 Three poles out of phase in free space

From sections (4.1.1) and (4.1.2) it has been shown that AVSP-f is able to compute correctly the radiation and cancellation between two monopoles. Smith and Kilham [95] stated that a

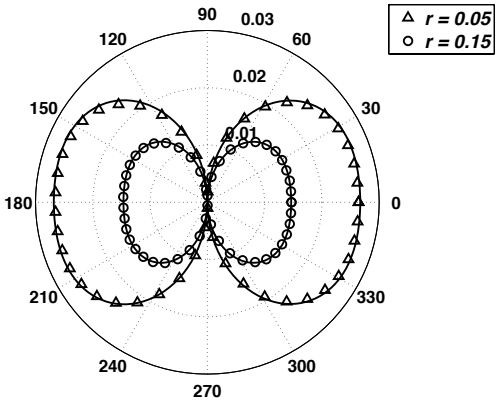

a) Directivity of a dipole
for two different radii.
[—— Analytics, (○△) AVSP-f]

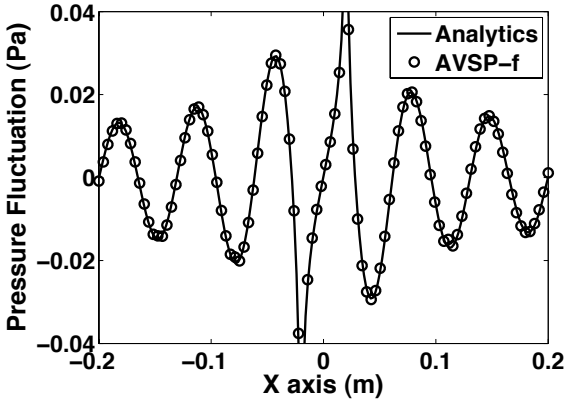

b) Pressure fluctuation
along the horizontal e_1 axis
[—— Analytics, (○) AVSP-f]

Figure 4.7: Analytical solution vs Numerical solution.

turbulent flame is acoustically equivalent to a set of different monopole sources, each of them radiating at different strength, phase and frequencies. Therefore, for a last test of this first validation, it is interesting to evaluate the noise radiation and directivity that results from three monopoles with arbitrary positions and phase shifts. The contribution of a third pole is just added as a third term in Eq. (4.6). After developing, the analytical solution reads

$$\begin{aligned}\hat{p}(\boldsymbol{x},\omega) =& \frac{i}{4c_0^2}\left(\hat{S}_0\delta(y-y_1)e^{-i\phi_1}\right)H_0^2(kr_1)dV_1 + \frac{i}{4c_0^2}\left(\hat{S}_0\delta(y-y_2)e^{-i\phi_2}\right)H_0^2(kr_2)dV_2 \\ &+ \frac{i}{4c_0^2}\left(\hat{S}_0\delta(y-y_3)e^{-i\phi_3}\right)H_0^2(kr_3)dV_3\end{aligned} \tag{4.8}$$

where $\hat{S}_0 = 1E10\ W/m^3s$; $y_1 = [-0.015, 0.015]\ m$, $y_2 = [0.015, 0.015]\ m$ and $y_3 = [0.0, -0.015]\ m$; $\phi_1 = 0\ rad$, $\phi_2 = 1\ rad$ and $\phi_3 = 2\ rad$; $\omega = 2\pi \cdot 5000\ rad/s$. Fig. (4.8) shows the solution given by the code AVSP-f. The reconstruction of the acoustic field at $t_0 = 0$ is evaluated by $p' = |\hat{p}|\cos(arg(\hat{p}))$. This acoustic field is shown in Fig. (4.9). Fig. (4.10) shows that a good agreement is obtained between both analytical and numerical results. The directivity pattern produced by these three monopoles is satisfactorily well recovered.

a) Modulus of Pressure $|\hat{p}|$ b) Argument of pressure $arg(\hat{p})$

Figure 4.8: Outputs of AVSP-f. Three monopoles out of phase

Figure 4.9: Acoustic field produced by three monopoles out of phase. $p' = |\hat{p}| \cos(arg(\hat{p}))$

4.2 The 2D premixed laminar flame

For a second validation of AVSP-f, a two dimensional burner has been chosen. There are three main concerns in the present validation: first, the computation of the flame dynamics through an unsteady CFD method ; second, the post-processing of the CFD results to evaluate the sources of noise; and last but not the least, the consideration of reflecting boundaries (walls, inlet and outlet) in the acoustic code AVSP-f.

The burner, which is based on the LeHelley's burner configuration [33], consists of two coaxial rectangular ducts of different height attached to each other by one of the extremes. The smaller duct acts as the intake whereas the bigger one plays the role of the combustion chamber. The

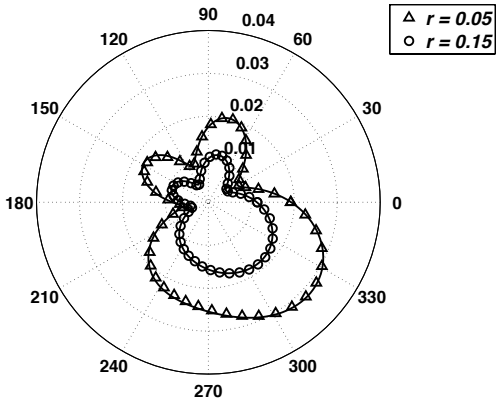

a) Directivity produced by the three poles for two different radii. [—— Analytics, (○△) AVSP-f]

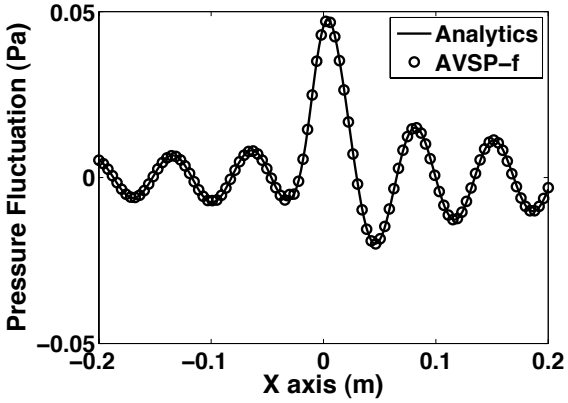

b) Pressure fluctuation along the horizontal e_1 axis [—— Analytics, (○) AVSP-f]

Figure 4.10: Analytical solution vs Numerical solution

premixed gas is a propane air mixture at stochiometric equivalent ratio. The reaction takes place at the dump plane generating a 'V' flame which will be stabilized after some milliseconds. Subsequently, the flame is harmonically perturbed at 500 Hz so that a fluctuation of the heat release rate is produced and hence fluctuations of acoustic pressure. AVSP-f estimates the acoustic distribution in the burner due to the unsteadiness of the heat release.

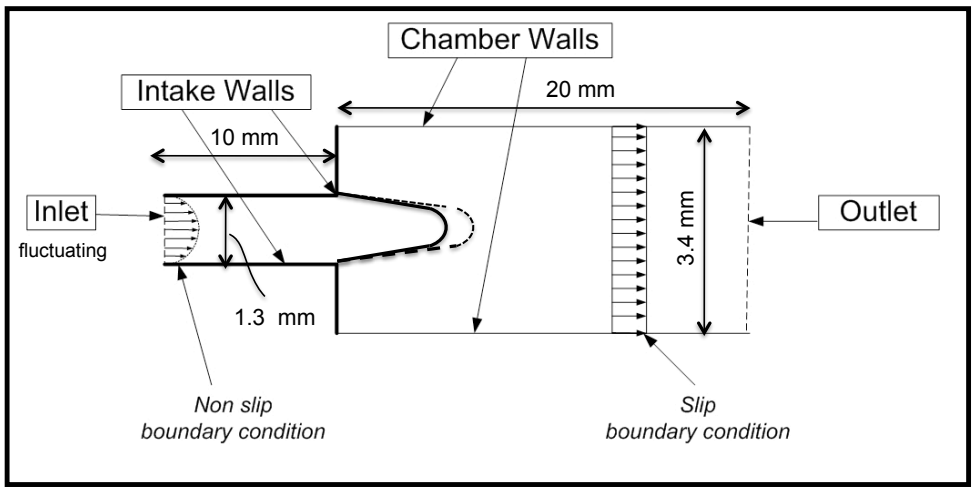

Figure 4.11: The 2D laminar premixed flame burner

4.2.1 CFD computation

An unsteady CFD computation is needed in order to have the quantities required for the posterior determination of the source terms. AVBP [3] is the numerical solver used for the unsteady computation of the laminar premixed flame. In this tool, the full compressible Navier Stokes equations are solved on hybrid (structured and unstructured) grids with second order spatial and temporal accuracy. The inlet mean velocity is equal to 4 m/s which is approximately equivalent to ten times the laminar flame speed of propane at stochiometric equivalent ratio. Two types of boundary conditions are used for treating the walls. The first one, which is applied to the intake, imposes a non-slip boundary condition for the flow while the second one allows the gas to flow tangentially to the chamber walls. Fig. 4.2.1 shows the boundary conditions applied. The outlet boundary condition, which imposes a mean pressure at the outlet, needs a little more of attention. Let us recall that one of the main assumptions of acoustic analogies is to consider the sources of noise to be totally independent of the acoustic field. In order to make this assumption valid, it is of extreme importance to reduce the incoming acoustic waves as much as possible by imposing a non-reflecting boundary condition at the outlet. Note that for this case, the chamber walls are not considered important as reflecting bodies since transversal acoustic waves (normal to chamber walls) are not relevant for the band of frequencies under study.

Boundary conditions in AVBP are based on a method derived by Poinsot and Lele [72] known as NSCBC (Navier-Stokes Characteristic Boundary Conditions). In all characteristic approaches, the main issue is the determination of the amplitudes of waves entering the computational domain. It has been shown that substracting totally the incoming waves (no-reflecting conditions) may induces a drift in the mean flow values. Some reflection must be therefore tolerated in order to stabilize the mean pressure at the outlet [91]. In order to characterize the reflection of a given boundary, it is useful to introduce the reflection coefficient $\hat{R}$. The reflection coefficient $\hat{R}$ is defined as the ratio between the incoming wave $\mathscr{L}_2$ to the outcoming wave $\mathscr{L}_1$. It reads

$$\hat{R} = \mathscr{L}_2 / \mathscr{L}_1 \tag{4.9}$$

A totally non reflecting condition would mean $|\hat{R}| = 0$ whereas a totally reflecting condition would read $|\hat{R}| = 1$. The linear relaxation method (LRM) [74, 91] imposes a proportional relation between the incoming acoustic waves and the difference between the pressure at infinity p_∞ (the target) and the pressure at the outlet of the computational domain p.

$$\mathscr{L}_2 = K(p - p_\infty) \tag{4.10}$$

where the coefficient K stands for the relaxation coefficient. A zero value of K make $\mathscr{L}_2$ vanishing while a big value creates a strong reflection, i.e., a big value of $\mathscr{L}_2$. An expression that relates the reflection coefficient $\hat{R}$ with the relaxation coefficient K has been establihed by Selle

et al.[91].

$$\hat{R} = \frac{1}{1 - i\frac{2\omega}{K}} \tag{4.11}$$

It is interesting to note that high frequency waves (a big value of ω) are less proned to be reflected than low frequency waves. From Eq. (4.11), a cut-off pulsation can be defined as $\omega = K/2$ which corresponds to $f = K/4\pi$. For this specific problem, a satisfactory value of K was found to be equal to 1000 s^{-1} which corresponds to a cut-off frequency around 80 Hz. This value permits a well-posed problem since the mean flow values do not drift away and the reflection conditions are small enough to assure an independence between the flame dynamics and acoustics for frequencies above 80 Hz. It should be noted that for this geometry the first longitudinal acoustic mode is of the order of 10^4 Hz, which is evidently much higher than 80 Hz, so that the outlet boundary condition is indeed virtually non-reflecting for the frequencies of interest. A direct consequence is that the flow reaches a steady state after the transient phase is finished. Figure 4.12 shows the 2D flame once the steady state has been reached.

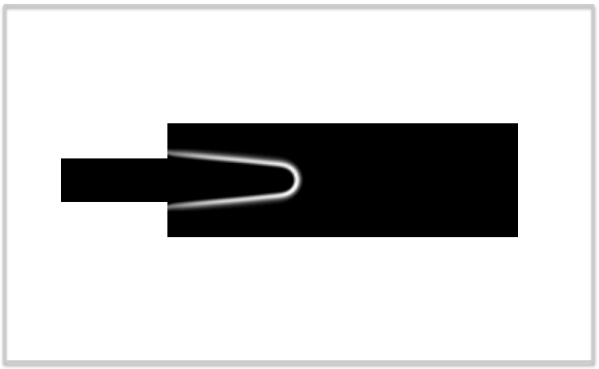

Figure 4.12: 2D premixed laminar flame. Steady state

Once the flame is stable, the inlet velocity is modulated at 500 Hz with an amplitude of $\pm$ 0.4 m/s, which represents 10% of the mean velocity at the intake. In Fig. 4.13, four snapshots are shown which correspond to four instants during one cycle. Table 4.1 shows the main parameters of the CFD computation.

4.2.2 Input data for the acoustic code

The entire CFD computation is carried out in such a way that the Nyquist-Shannon sampling criterion is satisfied. Letting the desired baseband bandwidth be equal to 10000 Hz, a sampling rate of 20000 Hz is necessary, which means a sample time equal to 0.05 ms. Since the perturbation of the integrated heat release is expected to be an harmonic fluctuation that completes

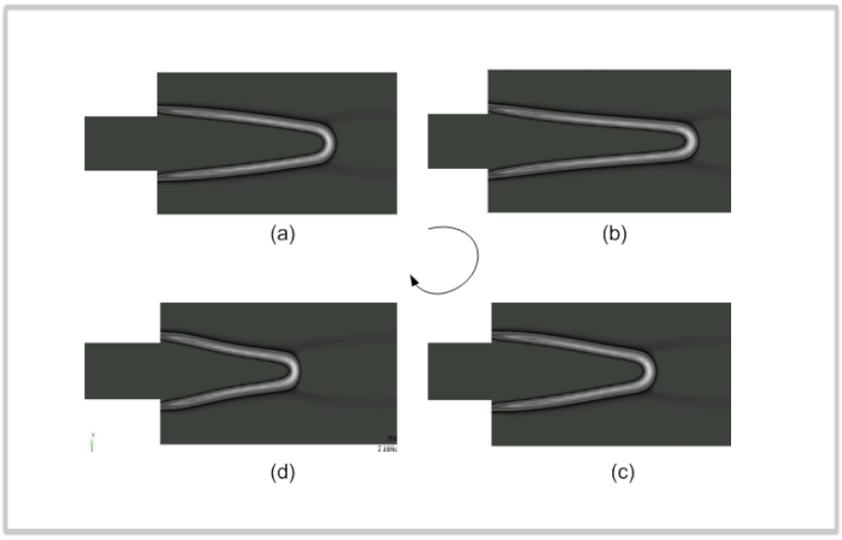

Figure 4.13: 2D premixed laminar flame. Four snapshorts for one cycle. $u'/\bar{u} = 0.1$

Numerical scheme	Lax-Wendroff
$\mathbf{2^{nd}}$ **artificial viscosity**	0.2
$\mathbf{4^{th}}$ **artificial viscosity**	0.05
CFL	0.7
grid type	squares
nodes	31574
$\boldsymbol{P_{inlet}}$	101300 Pa
$\boldsymbol{T_{inlet}}$	300 K

Table 4.1: Main parameters of the CFD computation

one period in 2 ms, a well resolved signal is assured with 40 points per period. Subsequently, the discrete Fourier transform is applied to obtain the heat release rate term as function of the frequency. The source term is then determined by the expression

$$\boxed{\textbf{Source} = -i\omega(\gamma - 1)\hat{\dot{\omega}}_T} \tag{4.12}$$

where the heat capacity ratio γ is also obtained from the CFD computation. In addition to the source term of noise, the mean flow information is given to the acoustic code through the mean sound velocity $\bar{c}$.

Two different types of boundary conditions are used in order to mimic the acoustic behavior of the burner boundaries. Both inlet and walls acoustic response are modeled assuming an acoustic velocity $\hat{u}$ equal to zero. This boundary condition is representative of totally reflecting walls. The outlet is on the contrary characterized by a specific acoustic impedance $\hat{Z}$. This

acoustic impedance is related to the reflection coefficient $\hat{R}$ by

$$\hat{Z} = \frac{\hat{R}+1}{\hat{R}-1} \tag{4.13}$$

while the reflection coefficient $\hat{R}$ is obtained by the relation (4.11).

4.2.3 Results

The exercise of validation, which is illustrated in Fig. 4.14, consists in comparing the pressure field given by AVSP-f to that one obtained directly by the CFD computation performed with the AVBP solver. The discrete Fourier transform is applied to the temporal pressure signals given by the CFD so that they can be compared to the sound pressure spectrum evaluated by the acoustic code. Figure 4.15 shows the Sound Pressure Level SPL predicted by both AVBP and AVSP-f at three different positions downstream the pulsated flame.

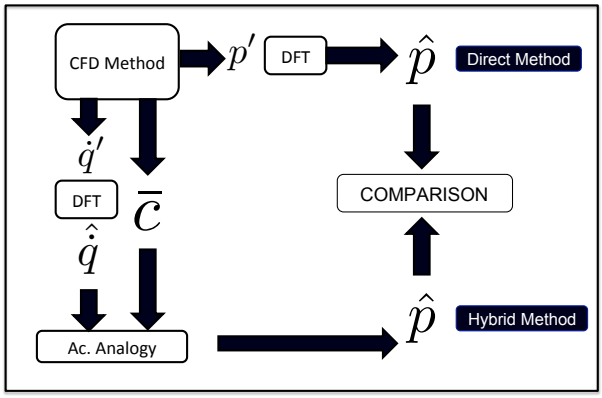

Figure 4.14: Exercise of comparison: CFD method Vs Acoustic solver

A good agreement can be observed in Fig. (4.15). A peak at 500 Hz is seen which represents the frequency at which the flame is excited. Peaks at 1000 and 1500 Hz are also observed. They represent the most significative harmonics of the modulation frequency. A second case is also evaluated. The inlet velocity is now pulsated at $\pm$ 2 m/s (see Fig. 4.16) which corresponds to 50% of the mean velocity at the inlet. The pressure signal obtained by the acoustic code also corresponds very well to the pressure signal given by the CFD computation. Figure 4.17 shows the SPL results.

It is important to emphasize that the acoustic boundary conditions implemented in the acoustic code must correspond to those ones imposed in the CFD simulation if a good match between these two different methods is expected. Several computations (not shown) were made for different values of the impedance $\hat{Z}$ at the outlet. As an example, for $\hat{Z} = 1$ (totally non-reflecting

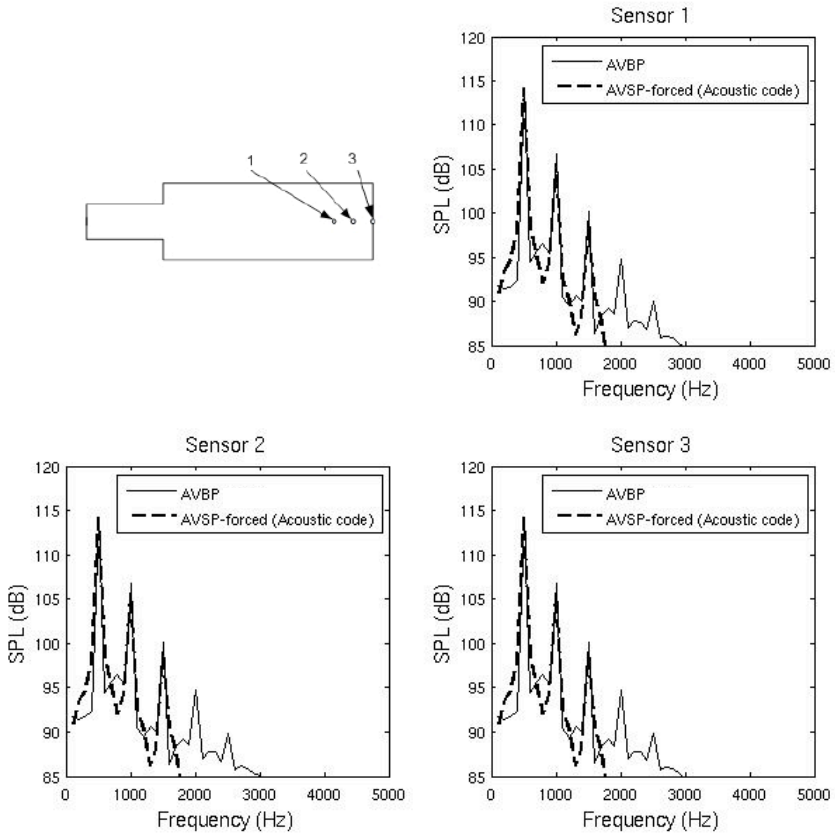

Figure 4.15: 2D premixed laminar flame. Comparison between LES and AVSP-f ($u'/\bar{u} = 0.1$).

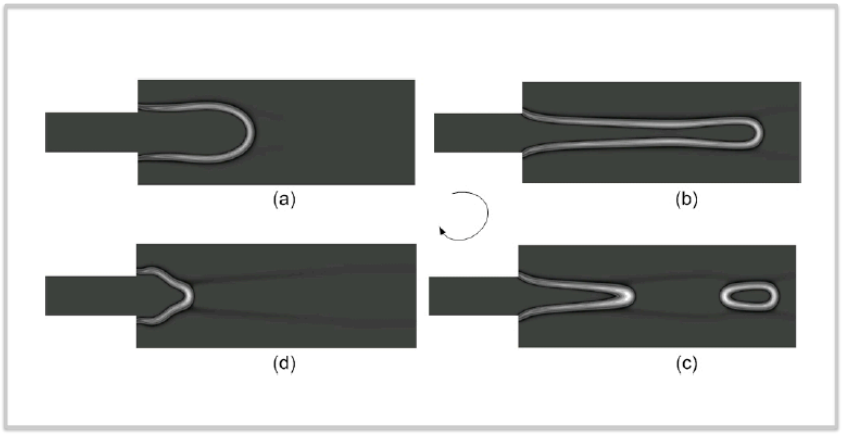

Figure 4.16: 2D premixed laminar flame. Four snapshorts for one cycle. $u'/\bar{u} = 0.5$

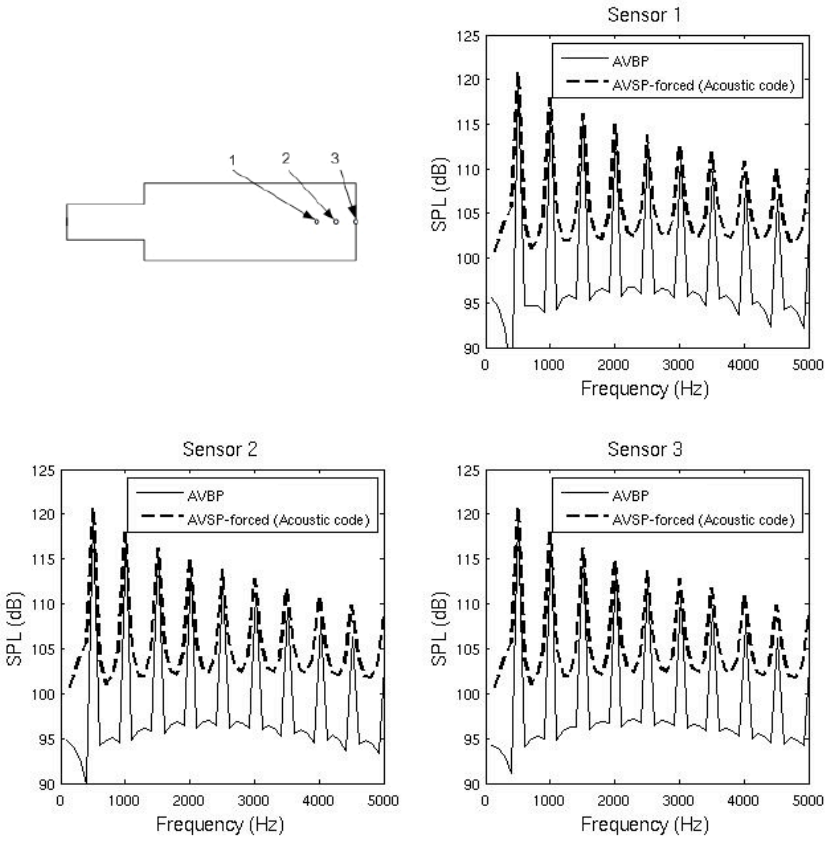

Figure 4.17: 2D premixed laminar flame. Comparison between LES and AVSP-f $(u'/\bar{u} = 0.5)$.

condition) the amplitudes of the acoustic pressure evaluated by AVSP-f are 10% bigger than those computed by the CFD tool.

5

Assessment of combustion noise in a premixed swirled combustor

Contents

5.1 Introduction

The present chapter presents the computation of the noise generated by a confined turbulent flame by both direct and hybrid approaches. Direct computation of noise means computing the field of pressure fluctuation directly from an unsteady CFD method. Concerning confined flames (combustion chambers), LES has been proved to correctly predict hydrodynamic related

fluctuating quantities such as the velocity or the temperature field. On the contrary, acoustic pressure fluctuations, which are much smaller in amplitude, are much more difficult to evaluate and their correct estimation is linked to the order of the numerical scheme and to the degree of resolution of the computational grid. On the other hand, hybrid approaches have not been ever considered to compute combustion noise in confined domains. As a consequence, it is not known yet how appropriate is their use for combustion noise estimation in combustion chambers. There are several conceptual differences between open and confined flames that should be considered regarding this matter. An important one is that in a confined flame there is not such a thing of 'far field pressure'. This means that fluctuations of pressure field are not only composed by acoustics since turbulence, and therefore hydrodynamic fluctuations, might be of considerable importance and, as a consequence, 'contaminate' the acoustic field. Another main concern is the boundary conditions: an open flame is computed considering acoustic waves that propagate outwards the domain and for this purpose the boundaries of the computational domain are treated to be non-reflecting; in a confined flame, acoustic waves produced travel both inwards and outwards. Boundary conditions modeling is therefore expected to be of crucial importance because their acoustic reflection are linked directly to the acoustic field produced. These physical concepts should be taken into account when applying hybrid approaches for confined flames.

5.2 Experimental configuration

Both direct and indirect computations of combustion noise are performed and applied to to swirled premixed combustor (EC2 combustor) carried out in the EM2C laboratory (École Centrale Paris) [43, 44]. The EC2 combustor consists in two geometrically identical stages for air-fuel injection, a premixer and a combustion chamber. Air is fed into each stage through a circular manifold in which a swirler is inserted. This swirler has a hollow cylinder with large lateral openings (see Fig. 5.1a), through which air is injected in the inner premixer channel. Inside these rectangular openings, four injectors (1 mm diameter) deliver gaseous propane perpendicularly to the air flow. This cross-flow configuration enhances fuel-air mixing. The tangential injections create a strong swirl motion in the $D = 30$ mm diameter inner channel, which in turn generate a central recirculation zone at the plenum that stabilizes the flame. The flame is controlled by the fuel-air ratio imposed in each of the two stages and is considered premixed and compact. Note that the LES could consider modeling the lines at each stage of both fuel and air as shown in Fig. 5.1(a). Nevertheless, important computational costs would arise due to the small grid cells that would be necessary to mesh the fuel lines. Since an homogeneous air-fuel mixing is considered to be achieved before arriving to the reacting zone, the fact of meshing fuel lines far upstream from the flame might be totally unnecessary. Therefore the present LES will only consider the air lines (simplified model shown in Fig. 5.1b) in which a premixed mixture with equivalent ratios ϕ_1 and ϕ_2 is injected for each stage.

This configuration features strong combustion instabilities depending on the fuel staging ratio

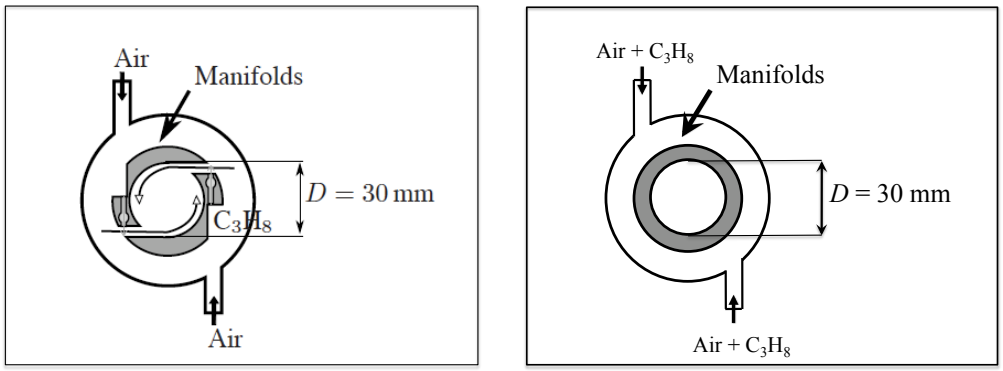

(a) Hollow cylinder - Actual test rig (b) Hollow cylinder simplified for LES

Figure 5.1: Schematic view of a tranversal section through the premixer and circular manifolds.

α, defined as the ratio of the fuel massflow in the furthest stage from the chamber (stage 1) to the total fuel injected massflow.

$$\alpha = \frac{\dot{m}_{f,1}}{\dot{m}_{f,1} + \dot{m}_{f,2}} \tag{5.1}$$

These instabilities are characterized by an important noise radiation due to the intense acoustic levels reached within the chamber and the premixer. The regime in the present study is given in Table 5.1. The gas mixture in the plenum is considered as perfectly premixed with a global equivalence ratio of $\phi_g = 0.832$.

α	$\dot{m}_{air,1}$	$\dot{m}_{f,1}$	$\dot{m}_{air,2}$	$\dot{m}_{f,2}$	ϕ_1	ϕ_2	ϕ_g
14.5 %	20	0.20	20	1.20	0.238	1.428	0.832

Table 5.1: Present operating regime (Mass flow $\dot{m}$ in m^3/h).

The combustion chamber is made of two quartz windows for flame visualizations, and two refractory concrete plates (top and bottom) which can be equipped either with small quartz windows for Particle Image Velocimetry (PIV) laser measurements or with transducer ports for acoustic measurements. The three PIV planes we are comparing with are shown in Fig. 5.2. The combustion chamber and the premixer are also equipped with seven microphones (denoted M1 to M7 in Fig. 5.2) placed at equal distances along the combustor.

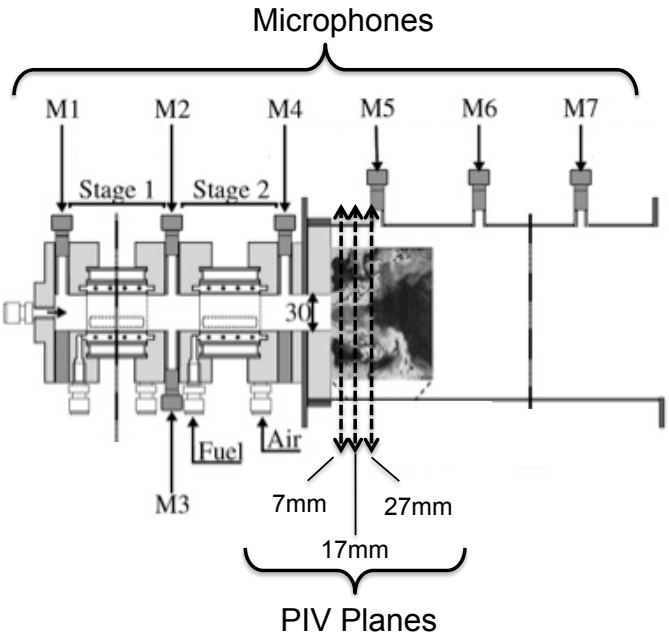

Figure 5.2: Two staged swirled premixed combustor. (Courtesy of École Centrale Paris)

5.3 Combustion noise Analysis

5.3.1 Direct Approach

The AVBP solver, developed at CERFACS, is used for the LES computations [3]. In this tool, the full compressible Navier Stokes equations are solved on hybrid (structured and unstructured) grids with second order spatial and temporal accuracy. Subgrid scale stresses are described by the Smagorinksy model. The flame/turbulence interactions are modeled by the Dynamic Thickened Flame (DTF) model [17]. This combustion model has been used in numerous studies of turbulent combustors [90, 56, 96, 92] in which it has been shown to well predict ignition, blow-off and flash-back of flames as well as acoustic-flame interactions in specific configurations. The spatial discretization in AVBP is based on the finite volume method with a cell-vertex approach, combined to a numerical scheme derived from the Lax-Wendroff scheme. AVBP has been validated/used for a considerable number of configurations.[90, 82, 57]. The main parameters of the LES computation are summarized in table 5.2

Boundary Conditions in AVBP are treated by the Navier Stokes Characteristic Boundary Conditions (NSCBC) method [72]. This method is already a standard technique to control wave crossing the boundaries [74, 42, 91]. It consists in decomposing the variation of flow variables on boundaries into terms due to ingoing and outgoing waves. While walls are always taken as totally reflecting surfaces (no velocity fluctuations normal to the surface are allowed $\rightarrow u' = 0$) with a reflection coefficient $\hat{R} = |\hat{R}|e^{j\theta}$ ($|\hat{R}| = 1$ and $\theta = 0$), the same cannot be stated for inlet

Numerical scheme	Lax-Wendroff
2^{nd} artificial viscosity	0.05
4^{th} artificial viscosity	0.01
LES model	Smagorinsky
Combustion model	Dynamic Thickened Flame

Table 5.2: Main parameters of LES computation

and oulets. Inlets and outlets are characterized by their acoustic impedance $\hat{Z} = \hat{p}/(\bar{\rho}\bar{c}\hat{\boldsymbol{u}} \cdot \boldsymbol{n})$. Following [91] it is possible to relate this acoustic quantity to the NSCBC parameters (see section 4.2.1) by the Eq. (4.11) and (4.13)

$$\hat{R} = \frac{\hat{Z}+1}{\hat{Z}-1} = \frac{1}{1-i\frac{2\omega}{K}} \tag{5.2}$$

in which K is the relaxation coefficient. Classically, outlets to the atmosphere are modeled by zeroing pressure fluctuations $\rightarrow p' = 0$ ($|R| = 1$ and $\theta = \pi$). Another path was followed in the present study, extending the computational domain to some region of the atmosphere after the burner outlet. By doing so, the true impedance of the outlet is implicitely accounted for. On the other hand, the acoustic impedance at the inlets of the EC2 combustor was measured experimentally by Lamraoui [43, 44]. These values were used to characterize the reflection coefficient $\hat{R}$ in the LES performed through the relation (5.2). Similar results were obtained when a simplified acoustic condition ($u' = 0$) at the inlets was applied, proving that acoustic conditions at the inlets are not critical in the present LES study. LES computational grid is shown in Fig. 5.3

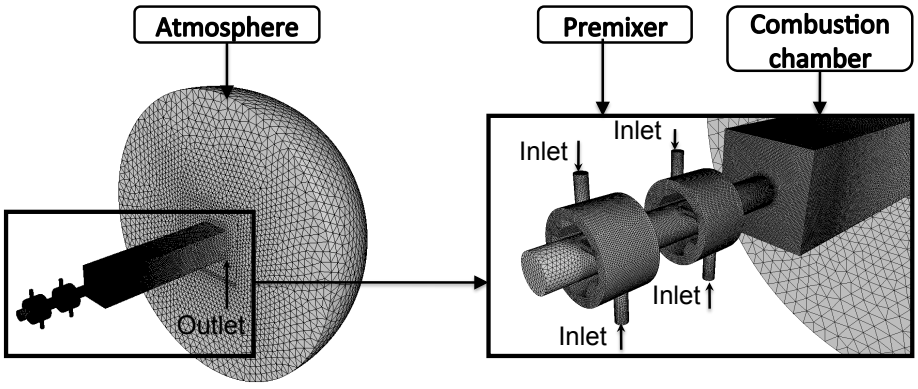

Figure 5.3: Computational grid of EC2 combustor

Two different meshes were used to compute the flow and flame dynamics of the EC2 combustor; their main characteristics are given in table 5.3. The 'coarse' mesh has 3 millions of cells whereas the 'refined' mesh is made of 10 million cells. The quality of the two LES performed

	'coarse' mesh	'refined' mesh
Nodes	706 854	1'887 891
Cells	3'824 053	10' 518 559
Maximum grid size in flame region	~ 1 mm	~ 0.5 mm

Table 5.3: The two computational grids under study

is evaluated through the Pope's criterion [75]. The Smagorinsky filter and the grid resolution for both cases should be sufficient to resolve at least 80 % of the energy remote from the wall. Introducing the resolved (k_f) and the modeled (k_{sgs}) turbulent kinetic energy , the resolved to total kinetic energy reads:

$$Q_{LES} = \frac{k_f}{k_f + k_{sgs}} \tag{5.3}$$

where $k_f = \frac{1}{2}\tilde{u}_i\tilde{u}_i$ and $k_{sgs} = \frac{1}{2}\widetilde{u_i u_i} - \frac{1}{2}\tilde{u}_i\tilde{u}_i = \frac{3}{2}(u'_{sgs})^2$ and $\widetilde{()}$ stands for the LES filter. The subgrid scale velociy is computed from

$$u'_{sgs} = \frac{\nu_t}{C\Delta x} \tag{5.4}$$

where ν_t is the turbulent viscosity, Δ is the filter width and C is a constant estimated as $C \approx 0.12$ in case of isotropic homogeneous turbulence (IHT) or as $C \approx 0.06$ in the case of a turbulent channel. For this case the value of $C \approx 0.12$ was used. Figure 5.4 demonstrates that, for both LES cases, Q_{LES} is greater than 0.8 for almost the entire computational domain excepting regions near walls. The premixer turbulence is however better captured by the 'refined' mesh. It is well known that extremely high computational costs arise when a proper LES on boundary layers is sought. Nevertheless, boundary layers are assumed to little contribute to noise radiation/scattering of turbulent flames. A high resolution in regions near walls is therefore not considered.

Both meshes are found to reproduce the mean PIV very well. This can be observed in Fig. (5.5). Both LES succeed in predicting the central recirculation zone satisfactorily. The LES on the 'refined' mesh is however more accurate for the outer region, particularly for the radial velocity. The fluctuating velocity field is characterized by rms profiles. Figure (5.6) shows that on the 'coarse' mesh a high overprediction of velocity fluctuations is obtained in both axial and radial components. On the fine grid however the LES clearly recovers the experimental velocity fluctuating field.

Acoustics and flame dynamics of the system represented by the heat release are, on the contrary, more difficult to evaluate than the mean and fluctuating velocity fields. The mean value of heat release is similar in both LES and is close to the 40kW experimental thermal power, as

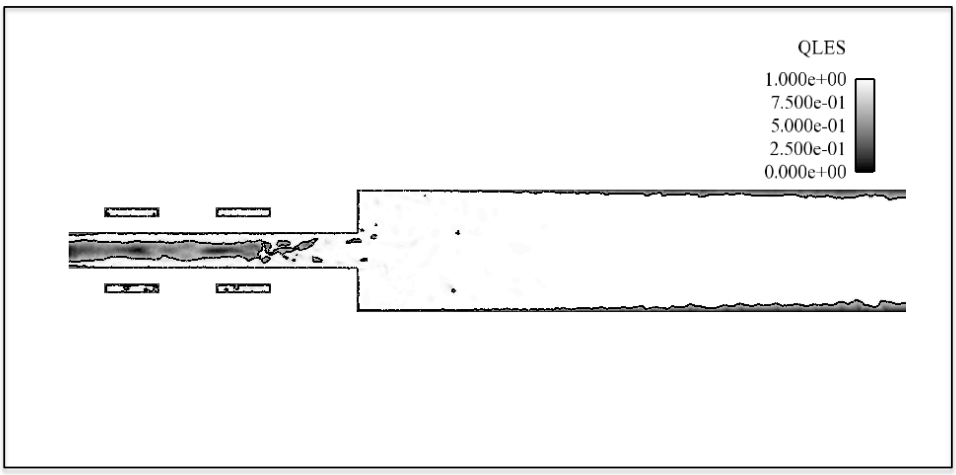

a) LES 3 million Cells

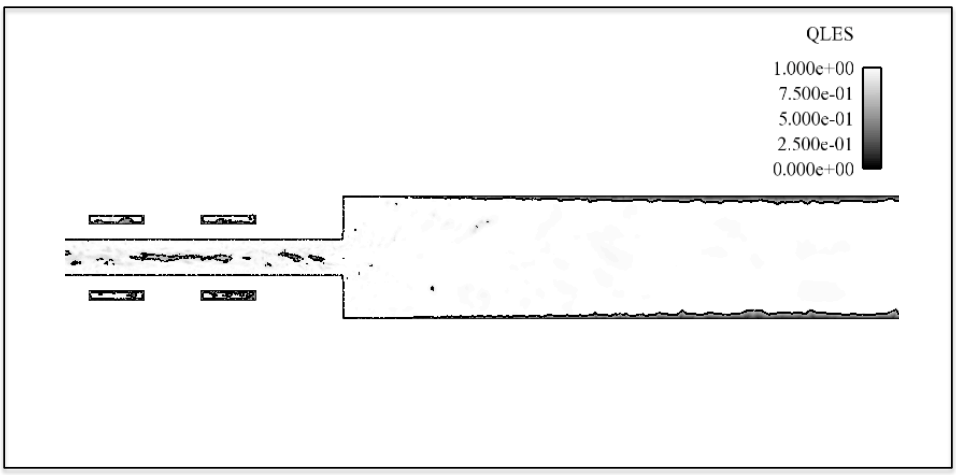

b) LES 10 million Cells

Figure 5.4: Instantaneous Field of Pope's Criterion. The black line stands for the isocontour line $Q_{LES} = 0.8$

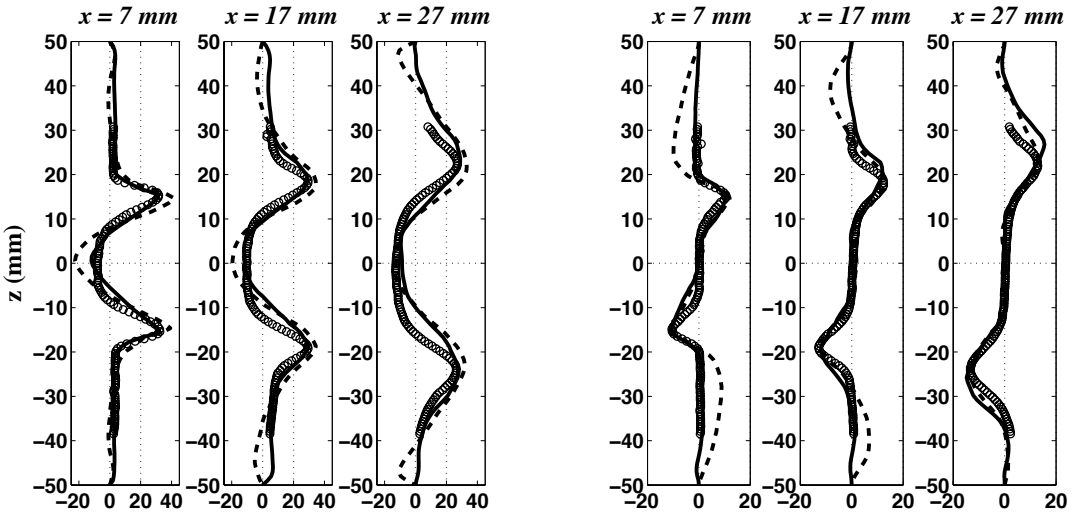

(a) Mean Axial Velocity (m/s) (b) Mean Radial Velocity (m/s)

Figure 5.5: Velocity Profiles: ○ Experimental PIV measurements
– – – LES 3 million cells, —— LES 10 million cells

can be observed in Fig. 5.7(a). Different values in the variations of heat release are however obtained for each LES. Strong and more regular fluctuations of heat release are obtained with the 'coarse' mesh while smaller and less periodic fluctuations are given by the 'refined' mesh computation. It is likely that the coarser mesh does not capture enough small turbulent scales and trigger too large turbulent eddies. These large coherent structures might clearly have an influence on the flame dynamics and thus in the large fluctuations of heat release. The value of the rate of change of heat release integrated over the whole volume of the combustor has also been computed for the two different meshes and is shown in Fig. 5.7(b). On the finer mesh a quieter flame is obtained, considering the smaller values of rate of change of heat release compared to those obtained from the coarse mesh. As a consequence, smaller rms pressure values should be expected on the finer mesh. Acoustics in the chamber is characterized by the Sound Pressure Level (SPL) at a given point rather than rms values of the pressure. Figure 5.8 compares the SPL values at microphone 7 (see the location of *M7* in Fig. 5.2) from the refined and coarse meshes to the experimental measurements. Both LES clearly overestimate the sound levels with a significant improvement with the finer resolution. It is then found that in order to correctly evaluate the dynamics of a flame and the acoustics generated by this one it is not enough to satisfactorily model the fluctuating velocity field as shown in Figs. 5.5 and 5.6. As stated before, computing acoustic pressure fluctuations is very challenging since these values are very small compared to the aerodynamic fields. Several additional phenomena can play an important role and be the (partial) cause of the observed differences with the experimental data.

First, the performed LES assumes a perfect premixed mixture of air and fuel in the reactive

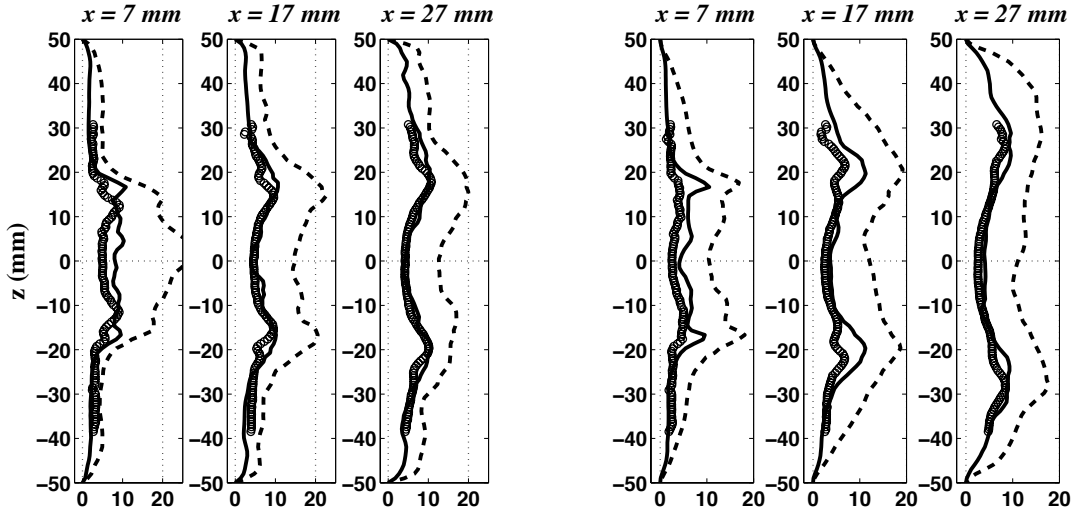

(a) RMS Axial Velocity (m/s) (b) RMS Radial Velocity (m/s)

Figure 5.6: Velocity Profiles: ○ Experimental PIV measurements
– – – LES 3 million cells, —— LES 10 million cells

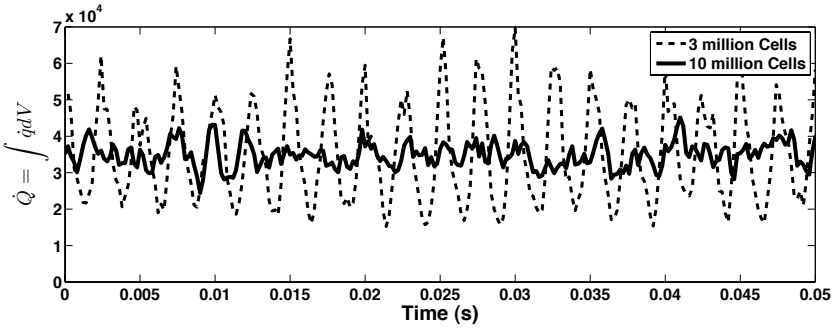

a) Heat release integrated over the entire volume (W)

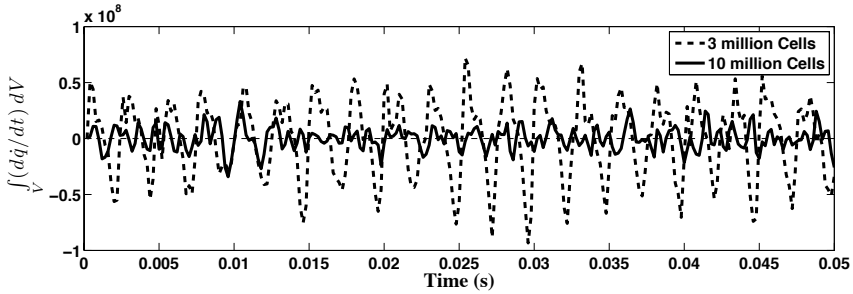

b) Rate of change of heat release integrated over the entire volume (W/s)

Figure 5.7: Heat Release and rate of change of heat release

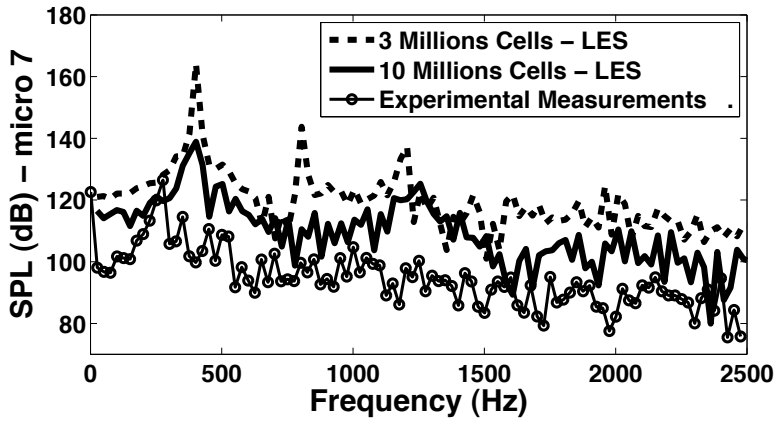

Figure 5.8: Sound Pressure Level

region. This assumption might be a misinterpretation of reality. Small pockets of propane-air presenting an equivalent ratio different for ϕ_g may reach the flame influencing its dynamics and as a consequence the radiated sound. Secondly, perfect adiabatic walls were considered in the present LES. In [92] it was shown that accounting for heat transfer leads to a reduction in the SPL. Some computations, not shown here, were performed considering heat transfer by modeling approximate heat loss coefficients (as done in [92]). No significative changes on the radiated noise were observed. Nevertheless, heat transfer might still be modeled too aproximatively knowing that exact values of heat transfer coefficients are extremely difficult to be obtained experimentally. A proper simulation of conjugate heat transfer including convection, conduction and radiation might be important at some level for noise modeling in turbulent flames, but presently remains too cumbersome. Thirdly, resolution of the computation (mesh refinement and order of the numerical scheme) is clearly significant. High grid resolutions in the reactive region not only means a smaller influence of the combustion model but also to be able to account for the smallest turbulent structures present in the shear layer that might influence the coherence of the bigger scales and thus the global turbulent interaction with the flame. At last but not the least, another explanation lies in the experimental data. Measuring acoustics in a confined combustion chamber is only reliable when acoustic leakages are proved to be controlled. This is, anyway, a difficult task. It has been found by the group in charge of EC2 at EM2C that acoustic leakages are still not totally well managed. As a result, wrong evaluations of pressure fluctuations may arise.

5.3.2 Hybrid approach

Quantities apart from the SPL are considered well estimated from the fine mesh LES and, as a consequence, the last can be taken as an appropriate starting point for the evaluation of the hybrid approach in confined domains. Thus the acoustic outputs from both direct and hybrid

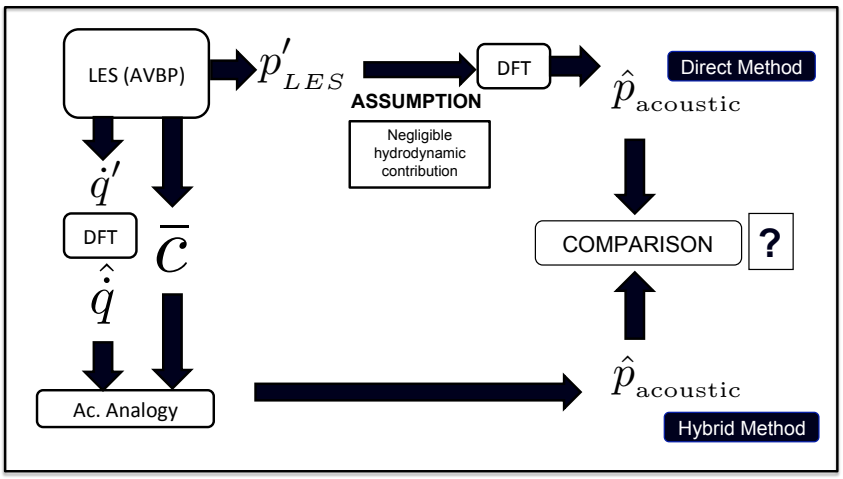

Figure 5.9: Exercise of comparison: Direct Approach Vs Hybrid Approach

approaches are compared for the 10 million cells mesh independently of experimental data. As sketched in Fig. (5.9), hydrodynamic pressure fluctuations are assumed to be small when considering results from the direct approach. Therefore, the acoustic field resulting from the hybrid approach is directly compared to the pressure fluctuation field coming from direct computations.

The hybrid computation is performed in two steps. First, the source of combustion noise is computed by postprocessing the data obtained from the LES computation as seen in Fig. (5.9). The instantaneous heat release is given to the acoustic code in addition to the mean flow information which is contained in the mean sound velocity. The acoustic tool AVSP-f computes the acoustic field throughout the computational domain due to the given noise sources, the mean flow field and the acoustic boundary conditions of the configuration. Figure (5.10) shows one snapshot of the unsteady heat release rate obtained from LES whereas Fig. (5.11) illustrates the mean sound velocity $\bar{c}$ over a longitudinal cut of the EC2 combustor. The source of noise is given to AVSP-f as a function of frequency. The discrete Fourier transform is therefore applied to the temporal sources obtaining as a consequence the modulus $|\hat{S}|$ and the argument $arg(\hat{S})$ for each frequency of interest. Figure 5.12 shows the combustion source for a frequency equal to 377 HZ. As an exercise of visualization, both argument and modulus of the source at 377 Hz are combined so that $S(t)\Big|_{f=377Hz} = |\hat{S}|e^{iarg(\hat{S})}e^{-i\omega t}$ where $\omega = 2\pi \cdot 377\ rad/s$. It is interesting to observe the monopolar behaviour of the combustion source of noise for this frequency, which is the one corresponding to the highest level of pressure fluctuation (see the peak at around 377 Hz in Fig 5.13).

The simplified Phillips equation written in the zero Mach number limit given by Eq. (2.63) is solved in the frequency domain. It consists then in solving the linear system $\mathcal{A}x = b$ (see Eq. 3.61) as many times as the number of desired frequencies f. For this case, the system $\mathcal{A}x = b$

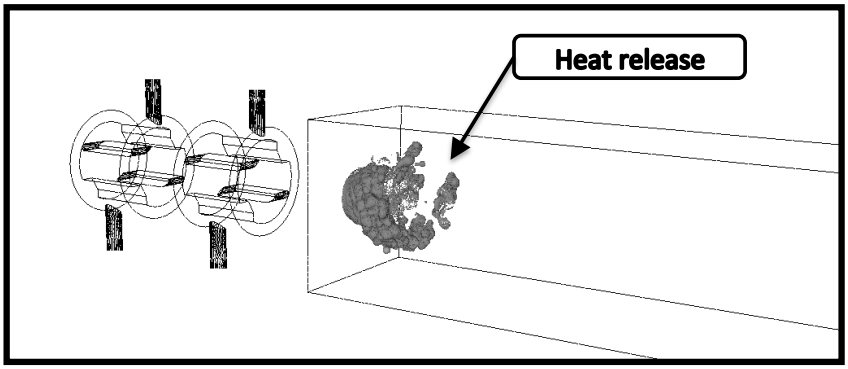

Figure 5.10: Typical iso-surface of the instantaneous unsteady heat release rate $\dot{\omega}_T$

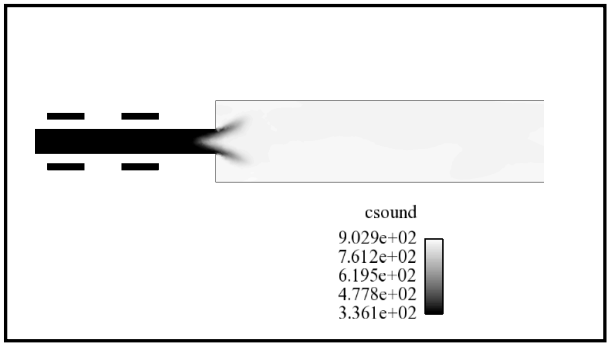

Figure 5.11: Mean sound velocity $\bar{c}$ over a longitudinal plane of the EC2 combustor

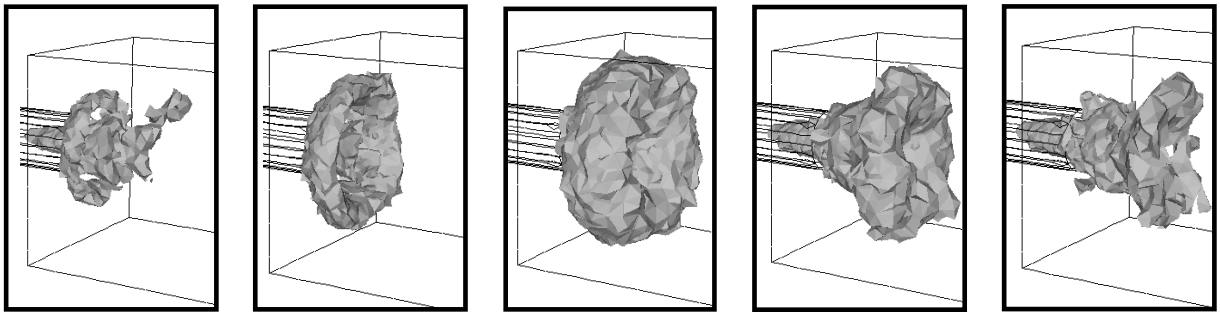

Figure 5.12: The combustion source of noise oscillating at 377 Hz. 5 snapshots during one cycle.

was solved 500 times within a band of frequencies from $25Hz$ to $2500Hz$, with a frequency step of $f = 25Hz$. Overall good agreement is found between the direct and hybrid approaches. Figures 5.13 and 5.14 show the sound pressure levels obtained for microphones 5, 6 and 7 (see the location of $M5$, $M6$, $M7$ in Fig. 5.2).

It is interesting to notice that the hybrid computation manages to recover not only the magnitude of the acoustic pressure over almost all the spectrum, but also the shape of the acoustic

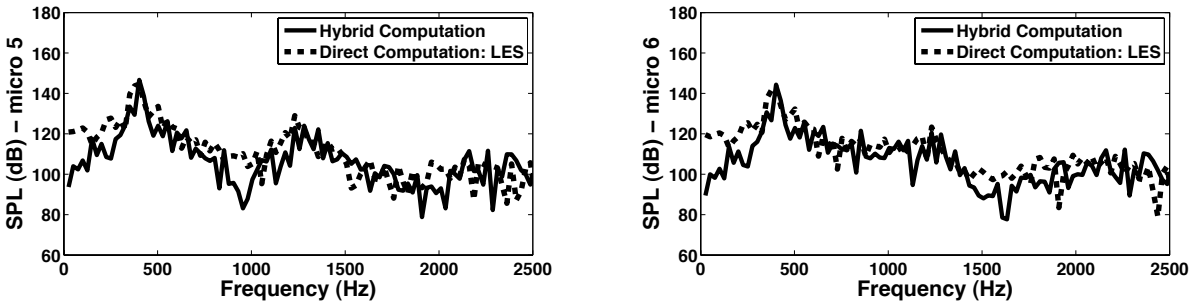

(a) Microphone 5 (b) Microphone 6

Figure 5.13: Sound Pressure Levels from the direct and hybrid approaches

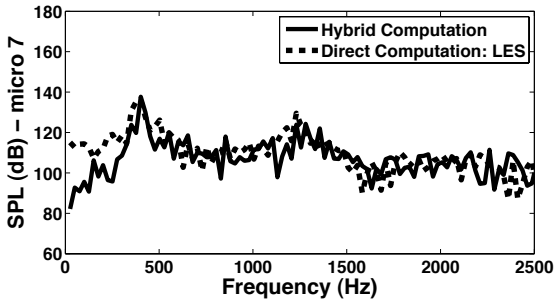

Figure 5.14: Sound Pressure Levels from the direct and hybrid approaches

waves. Figure 5.15 shows the strongest acoustic wave, the quarter wave mode, that resonates at 377 Hz. The pressure fluctuations along the axis of the combustor at different times within a cycle are observed. As both methods yield the same envelope of variations at this frequency, the pressure fluctuation recovered by the direct computation can be seen as almost completely caused by acoustics.

In Fig. 5.13 some zones of the spectrum still show some differences between hybrid and direct computations. Let us focus on the low frequency zone of the spectra before the peak at 377 Hz. At this frequencies it is found that there is a significant hydrodynamic contribution in the direct computation that triggers higher pressure fluctuations. Figure 5.16 shows two interesting situations. The hybrid approach is based on the low Mach number assumption; in other words, the flow is considered stationary. Moreover, no strong gradients of the sound velocity $\bar{c}$ are observed in the premixer region, which means that acoustic waves will propagate through this zone as if a quiescent medium was present. As a result, all acoustic modes of the chamber are excited when computing noise through the hybrid approach. Figure 5.16(a) shows that when considering frequencies close to the first eigen-frequency of the system (240 Hz), the quarter wave mode of the premixer is excited. Fluctuations of different nature are shown in Figure 5.16(b) which illustrates LES results. Although there is a strong coherence of the pressure fluctuations in the chamber region, these fluctuations do not come from acoustics. Moreover, the strong level of turbulence present in the premixer region prevents any important acoustic

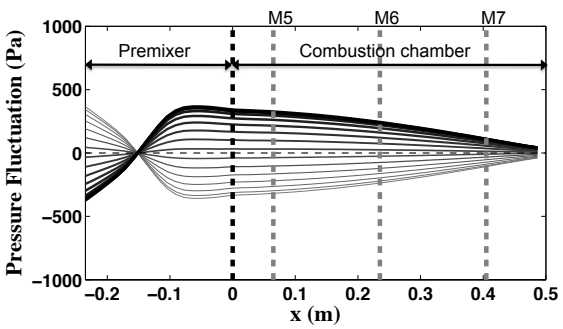

(a) Quarter pressure Wave from Eq. (2.63) Hybrid Computation

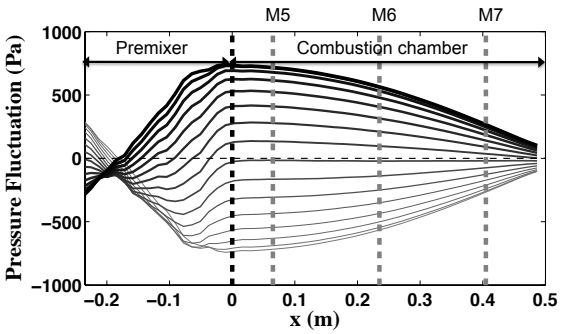

(b) Quarter pressure Wave from LES Direct Computation

Figure 5.15: Longitudinal pressure Waves oscillating at 377 Hz

oscillation to be triggered in this region.

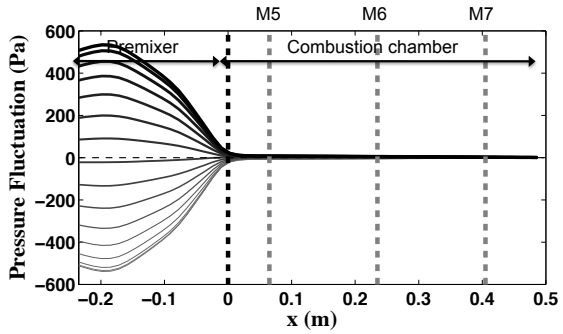

(a) Pressure Wave from Eq. (2.63) Hybrid Computation

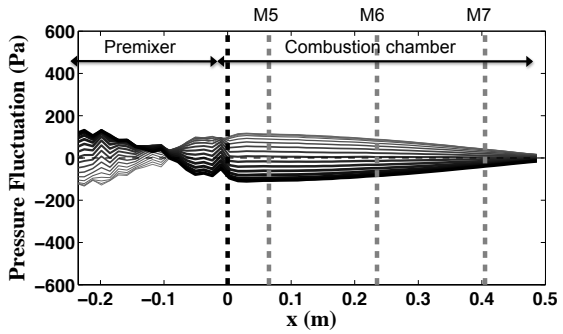

(b) Pressure Wave from LES Direct Computation

Figure 5.16: Longitudinal pressure Waves oscillating at 251 Hz

In Fig. 5.17 two different types of pressure waves are observed at microphone 5 for the direct and hybrid computations in the region around 1000 Hz. Whereas a pure acoustic standing wave is obtained by the hybrid approach, a perturbed pressure wave is obtained in the direct computation results. A pure standing acoustic wave can naturally have an acoustic pressure node. If this pressure node is present close to the region of the measurement device a low value of pressure fluctuation will be obtained. This is what happens for microphone 5 in the zone close to 1000 Hz (Fig. 5.17a). Obviously, when the pressure fluctuations not only contain acoustics but also hydrodynamic perturbations as in the direct computations (Fig. 5.17b), no pressure node can be observed and the resulting SPL is much higher than in the hybrid computation case. Similar conclusions can be drawn at frequencies around 1650 Hz where a pressure node is found close to Microphone 6 (Fig. 5.18).

In order to not have any ambiguity measuring acoustic pressure fluctuations due to the presence of pressure nodes, a more appropriate quantity to evaluate at the microphone positions is

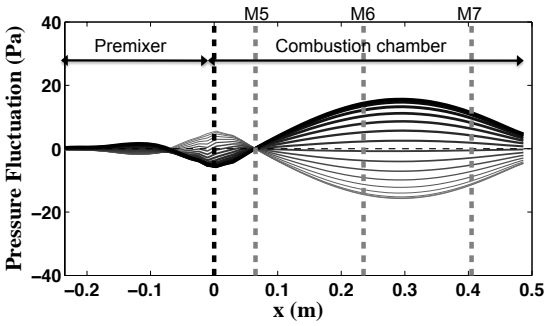

(a) Pressure Wave from Eq. (2.63) Hybrid Computation

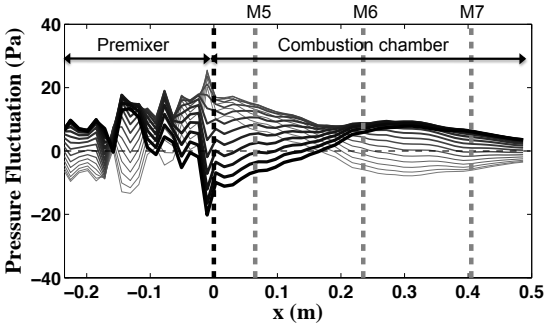

(b) Pressure fluctuation from LES Direct Computation

Figure 5.17: Longitudinal pressure Waves oscillating at 954 Hz

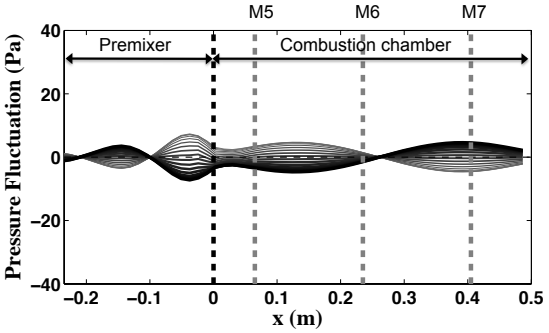

(a) Pressure Wave from Eq. (2.63) Hybrid Computation

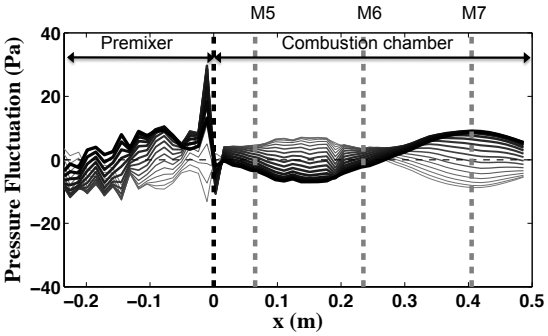

(b) Pressure fluctuation from LES Direct Computation

Figure 5.18: Longitudinal pressure Waves oscillating at 1658 Hz

the acoustic energy. For low Mach number flows, the acoustic energy is defined as [74]

$$E_{ac} = \frac{p'^2}{\bar{\rho}\bar{c}_2} + \bar{\rho}u'^2 \tag{5.5}$$

From the definition of the acoustic energy (Eq. 5.5), it is observed that even though pressure nodes takes place at a given location, the energy contained is different from zero: it is given then by the acoustic velocity which is expected to be maximum at pressure nodes. As a consequence, spectra without strong local minima are obtained. The acoustic energy spectrum for microphones 5, 6 and 7 is shown in Figs. 5.19 and 5.20

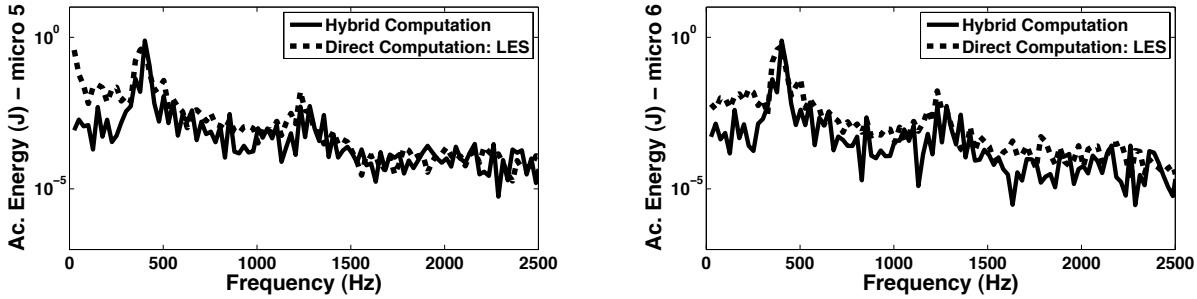

Figure 5.19: Acoustic energy. Direct and hybrid approaches

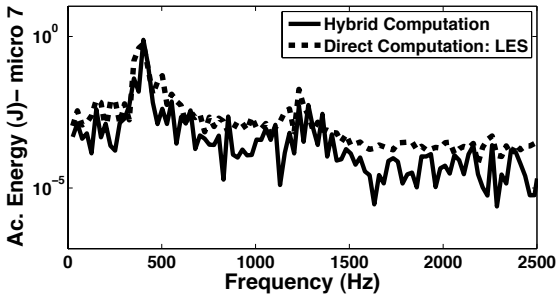

Figure 5.20: Acoustic energy. Direct and hybrid approaches

Although there is an overall good agreement for the three microphones, the energy contain is bigger for the signals coming from the direct approach. This is easily noticed at microphone 7 in Fig. 5.20. In the next, a procedure is exposed so that pure acoustic signals could be retrieved from the LES performed.

5.4 Filtering a LES pressure field to find the corresponding acoustic field

Velocity fluctuations obtained by LES are composed of both hydrodynamics and acoustics

$$u'_{i,LES} = u'_{i,hyd} + u'_{i,ac} \tag{5.6}$$

Appling the operator $\partial/\partial t$ to Eq. (5.6) leads to

$$\frac{\partial u'_{i,LES}}{\partial t} = \frac{\partial u'_{i,hyd}}{\partial t} + \frac{\partial u'_{i,ac}}{\partial t} \tag{5.7}$$

From linear acoustics, the momentum equation is given by

$$\bar{\rho}\frac{\partial u'_{i,ac}}{\partial t} = -\frac{\partial p'_{ac}}{\partial x_i} \tag{5.8}$$

where $\bar{[]}$ and $[]'$ represent respectively the mean and fluctuating flow. Combining Eqs. (5.8) and Eq. (5.7) leads to

$$-\frac{1}{\bar{\rho}}\frac{\partial p'_{ac}}{\partial x_i} + \frac{\partial u'_{i,hyd}}{\partial t} = \frac{\partial u'_{i,LES}}{\partial t} \tag{5.9}$$

Finally the divergence operator to this equation is applied to yield

$$-\frac{\partial}{\partial x_i}\left(\frac{1}{\bar{\rho}}\frac{\partial p'_{ac}}{\partial x_i}\right) + \frac{\partial}{\partial x_i}\left(\frac{\partial u'_{i,hyd}}{\partial t}\right) = \frac{\partial^2 u'_{i,LES}}{\partial x_i \partial t} \tag{5.10}$$

5.4.1 Finding $\frac{\partial \mathbf{u_{i,hyd}}}{\partial \mathbf{x_i}}$

Neglecting viscosity, species diffusion and heat conduction the Navier-Stokes equations for reacting flows read

$$\frac{\partial \rho}{\partial t} + \rho\frac{\partial u_j}{\partial x_j} + u_j\frac{\partial \rho}{\partial x_j} = 0 \tag{5.11}$$

$$\rho\frac{\partial u_i}{\partial t} + \rho u_j\frac{\partial u_i}{\partial x_j} = -\frac{\partial p}{\partial x_i} \tag{5.12}$$

$$\rho c_p\frac{\partial T}{\partial t} + \rho c_p u_j\frac{\partial T}{\partial x_j} = \dot{\omega}_T \tag{5.13}$$

In the low-Mach number approximation, the thermodynamic pressure $\bar{p}$ only depends on tem-

perature. The equation of state is simply

$$\frac{\bar{p}}{r} = K_0 = \rho T \tag{5.14}$$

Replacing Eq. 5.14 in the left hand side of the Eq. (5.13) leads to

$$\rho c_p \frac{\partial K_0/\rho}{\partial t} + \rho c_p u_j \frac{\partial K_0/\rho}{\partial x_j} = \dot{\omega}_T \tag{5.15}$$

Developping Eq. (5.15), and combining it with Eq. (5.11) results in a simplified equation in which density ρ is not anymore present. It reads

$$\frac{\partial u_j}{\partial x_j} = \frac{1}{c_p K_0} \dot{\omega}_T \tag{5.16}$$

This velocity field is supposed to be composed only by hydrodynamics, due to the fact that in the low Mach number model the acoustic wave length is infinitely long and then $\partial u_{ac}/\partial x_j \approx 0$. One can state that the divergence of the fluctuating velocity is

$$\frac{\partial u'_{j,hyd}}{\partial x_j} = \frac{1}{c_p K_0} \dot{\omega}'_T \tag{5.17}$$

5.4.2 Finding the Acoustic Pressure

Injecting Eq. (5.17) into Eq. (5.10) leads to

$$-\frac{\partial}{\partial x_i}\left(\frac{1}{\bar{\rho}}\frac{\partial p'_{ac}}{\partial x_i}\right) = \frac{\partial}{\partial t}\left(\frac{\partial u'_{i,LES}}{\partial x_i} - \frac{\dot{\omega}'_T}{c_p K_0}\right) \tag{5.18}$$

or in the frequency domain

$$\frac{\partial}{\partial x_i}\left(\frac{1}{\bar{\rho}}\frac{\partial \hat{p}_{ac}}{\partial x_i}\right) = i\omega \frac{\partial \hat{u}_{i,LES}}{\partial x_i} - i\omega \frac{\hat{\dot{\omega}}_T}{c_p K_0} \tag{5.19}$$

Finally, multiplying everywhere by $\gamma \bar{p}$

$$\frac{\partial}{\partial x_i}\left(c^2\frac{\partial \hat{p}_{ac}}{\partial x_i}\right) = \underbrace{i\omega\gamma\bar{p}\frac{\partial \hat{u}_{i,LES}}{\partial x_i}}_{T1} - \underbrace{i\omega\frac{\gamma\bar{p}\hat{\omega}_T}{c_p K_0}}_{T2} \tag{5.20}$$

It has been found by the author that the contribution of $T2$ for this case should be neglected to improve the results. As a consequence, Eq. (5.20) simplifies to:

$$\boxed{\mathcal{F}(\hat{p}_{ac}) = \frac{\partial}{\partial x_i}\left(c^2\frac{\partial \hat{p}_{ac}}{\partial x_i}\right) = i\omega\gamma\bar{p}\frac{\partial \hat{u}_{i,LES}}{\partial x_i}} \tag{5.21}$$

5.5 LES Vs Hybrid Results

Figures 5.21 and 5.22 shows the Sound Pressure Level (SPL) given by the solution of Eq. (5.21) (LES 'Filtered'), the hybrid computation and the direct approach for microphones 5, 6 and 7.

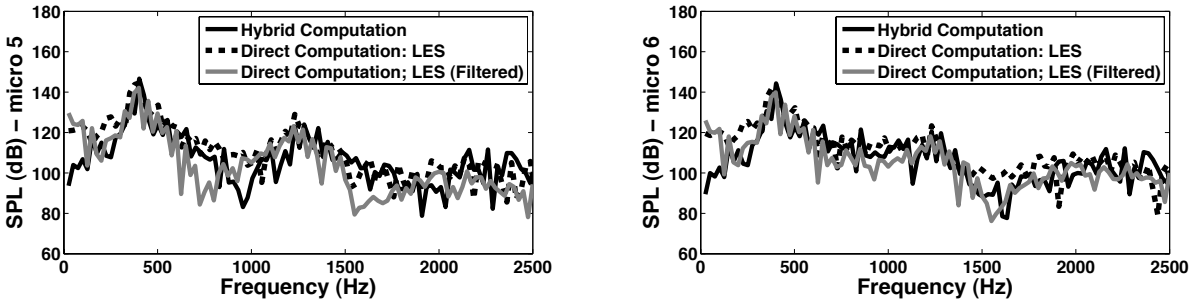

Figure 5.21: Sound Pressure Levels from the direct and hybrid approaches

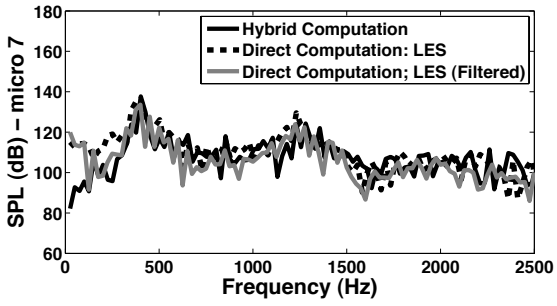

Figure 5.22: Sound Pressure Levels from the direct and hybrid approaches

After extracting the acoustic field from the complete pressure fluctuation field, it is seen that results match pretty well with the values predicted by the hybrid method, especially for microphones 6 and 7. There is a high contain of hydrodynamic fluctuations at low frequencies (before 400 Hz) that has been removed as it can be noted if comparing Figs. 5.16(b) and 5.23(b). The

acoustic field predicted by the hybrid computation is now much closer to that one predicted by the direct method when considering the combustion chamber, as observed from Fig. 5.23.

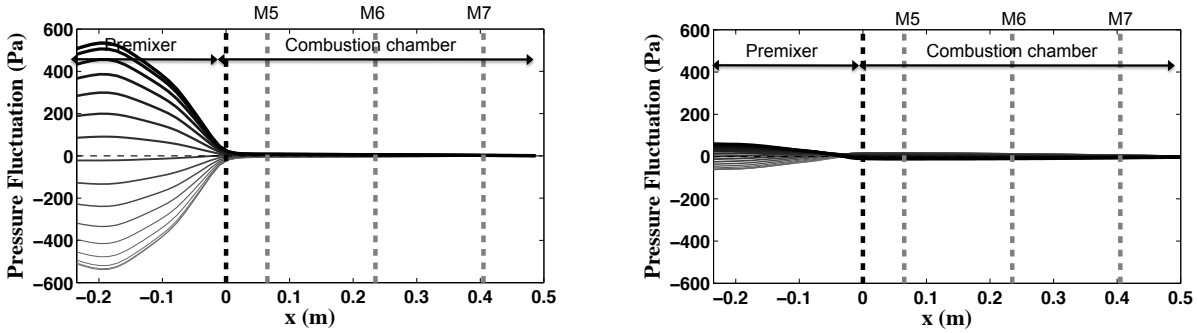

(a) Pressure Wave from Eq. (2.63) Hybrid Computation

(b) Pressure Wave from LES after filtering Direct Computation

Figure 5.23: Longitudinal pressure Waves oscillating at 251 Hz

Considering the pressure wave at 377 Hz (Fig. 5.24), it is observed that it does not change too much after filtering, as can be appreciated by comparing Fig. 5.15(b) with Fig. 5.24(b). As it has been already stated in section 5.3.2, this pressure wave is mainly composed by acoustics since it corresponds to the quarter wave mode of the combustion chamber. The resemblance between hybrid and direct approaches results increases after filtering and is now remarkable.

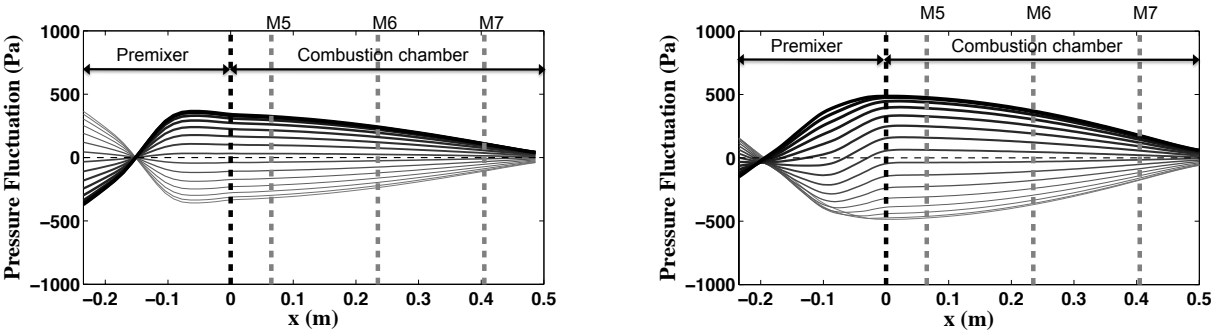

(a) Quarter pressure Wave from Eq. (2.63) Hybrid Computation

(b) Quarter pressure Wave from LES after filtering Direct Computation

Figure 5.24: Longitudinal pressure Waves oscillating at 377 Hz

The local minimum around 1650 Hz shown in the SPL spectrum for microphone 6 (Fig. 5.21b) is well recovered after extracting acoustics from LES. This is due to the fact that once hydrodynamic fluctuation have been extracted, a pressure node close to microphone 6 appears as shown by Fig. 5.26(b). On the contrary, the acoustic signal corresponding to microphone 5 Fig. 5.21(a) presents important differences with respect to the one computed by the hybrid approach. The local minima around 1000 Hz corresponding to the hybrid method is recover at a lower frequency (around 750 Hz) and the pressure node observed in the combustion chamber after extracting hydrodynamics is placed relatively far from that one predicted by the hybrid

approach, as can be observed from Fig. 5.25.

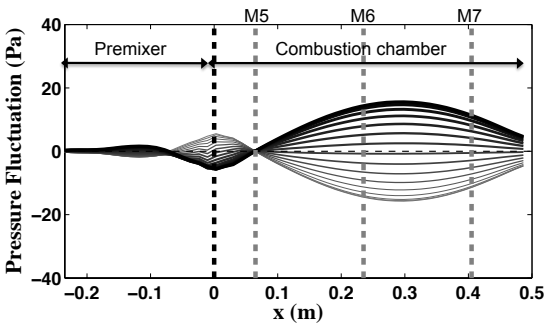

(a) Pressure Wave from Eq. (2.63) Hybrid Computation

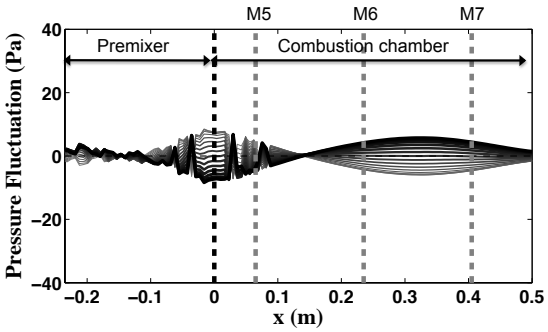

(b) Pressure fluctuation from LES after filtering Direct Computation

Figure 5.25: Longitudinal pressure Waves oscillating at 954 Hz

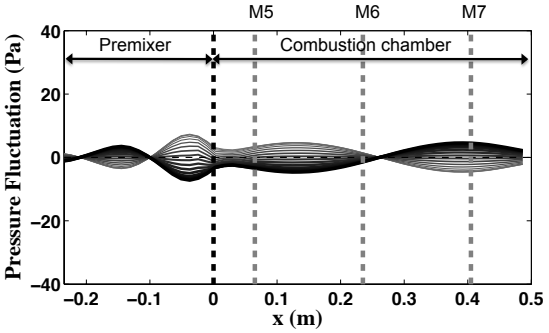

(a) Pressure Wave from Eq. (2.63) Hybrid Computation

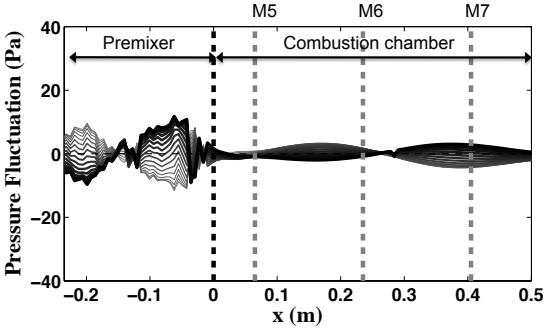

(b) Pressure fluctuation from LES after filtering Direct Computation

Figure 5.26: Longitudinal pressure Waves oscillating at 1658 Hz

Considering now the acoustic energy, it is observed from Figs. 5.27 and 5.28 that the values predicted by the hybrid approach are in a good agreement to that ones computed by LES after extracting the acoustic contain from the complete pressure fluctuations. It is noticeable then that the energy coming from hydrodynamic fluctuations has been removed.

Note that some caution must be taken when computing the Fourier transform of the divergence of the velocity (See T1 Eq. 5.20). If a rectangular window is applied to the temporal signal, a really good correspondance is seen only for frequencies lower than 400 Hz (not shown). On the other hand, if a gaussian window is applied, a good agreement is seen over the entire frequency band, except at a very low frequencies. This is the case for the spectra shown (Figs. 5.21, 5.22, 5.27 and 5.28) where the signal does not capture the good acoustic level before 200 Hz.

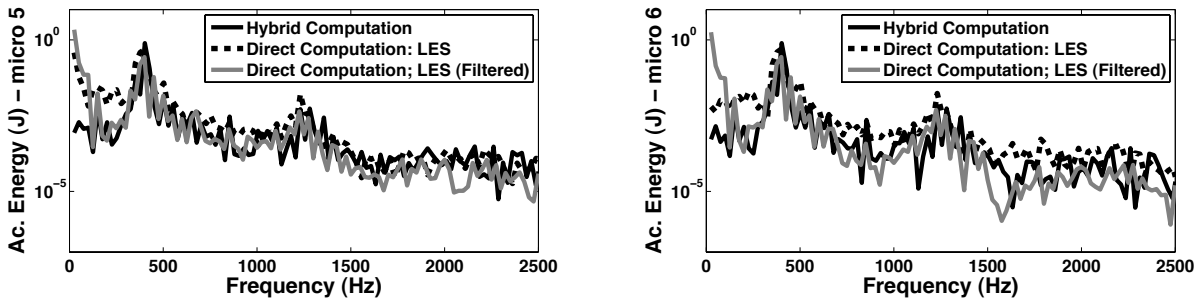

Figure 5.27: Acoustic energy. Direct and hybrid approaches

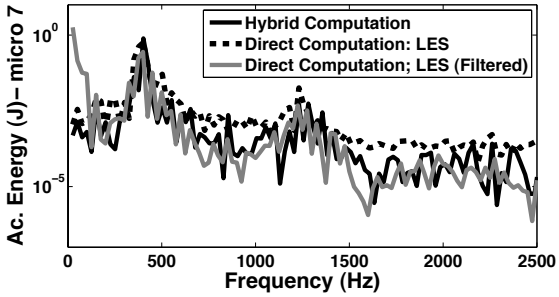

Figure 5.28: Acoustic energy. Direct and hybrid approaches

5.6 Conclusions

Combustion noise of a premixed swirled combustor has been assessed by two different numerical approaches: a direct computation in which the noise produced by the flame is calculated together with the flow and flame dynamics, and a hybrid computation in which the acoustic field is evaluated from the sources of noise in a separate step.

Classical comparisons between mean and fluctuating (rms) velocity fields were performed between two LES on a 'coarse' mesh (3 millions cells) and a 'refined' mesh (10 millions cells), and PIV measurements. Mean velocity fields (axial and radial) were well predicted by both LES cases, whereas only the 'refined' mesh succeed in recovering the proper rms velocity fields. It was then observed that satisfactorily predicting the velocity fluctuating field does not mean to reproduce correct flame dynamics and heat release. On the one hand, the mean heat release corresponding to the experimental thermal power is well captured by both LES. On the other hand, significative differences are found between the two simulations when looking at the shape of the instantaneous heat release and its rate of change. As a consequence, a right estimate of the combustion noise radiation is not reached either. Several phenomena might be the cause of such a misprediction. A lack in numerical resolution can be one possible explanation: computing the small turbulent length scales in the shear flow region might be significant since these eddies might have a non-negligible influence on the flame dynamics and, as a con-

sequence, on the noise prediction. A higher grid resolution in the flame region also decreases the influence of the combustion model, which might have a certain effect when computing the values of rate of change of heat release. Moreover, an accurate prediction of heat transfer might also be a crucial factor, and exact modeling of convection, conduction and radiation might be important in combustion noise modeling.

The output from the hybrid computation is a pure acoustic field due to the turbulent flame. Good agreement is found in almost the entire SPL spectrum when comparing the results of both direct and hybrid computations. Nevertheless, there are still some differences in specific zones of the spectrum. Hybrid computation results only consider pure acoustic waves, and at given frequencies these pure acoustic waves may present acoustic nodes that may take place close to the acoustic sensor position. This leads to a low fluctuation of pressure at this position and hence, to a low value of the SPL spectrum at these frequencies. Moreover, hydrodynamics was proved to be strong at low frequencies and hence, using a LES pressure field to estimate combustion noise is not enough: extracting acoustics from the complete pressure field is essential. A procedure to separate acoustic from hydrodynamics has been proposed. A validation of this procedure is made by comparing the resulting signal to combustion noise predicted by the Hybrid approach.

6

Boundary conditions for low Mach number acoustic codes

Contents

6.1 Introduction

The prediction of combustion instabilities in combustion chambers embedded in complex systems, such as aeronautical engines, is extremely difficult due to all the different phenomena that must be taken into account: the two way interaction between the flame and the most representative turbulent length scales of the reacting and burnt gases, the two way interaction between the flame and the radiated acoustic waves produced by this one, the possible coupling between entropy waves (hot spots generated by the flame) and the acoustic waves produced due to non-homogeneities in the mean flow and evidently the role played by the boundary conditions (inlets, outlets and walls) as surfaces that directly interact with the acoustic, entropy and vortical waves present into the system.

Different strategies have been developed over the years [78, 71, 48, 22, 77] in order to understand the physics of all these interactions and to create methodologies to control or avoid them. In the last recent years, reacting and compressible Large Eddy-Simulation (LES) has shown its capability to study the dynamics of turbulent flames [17, 69, 67, 90, 82, 68, 84]. Due to its intrinsic nature (resolution of the unsteady 3D Navier-Stokes equations) LES is able to predict the interactions between the flame, the turbulent flow and the acoustic modes of the chamber, and for some particular configurations [56] to distinguish between stable and unstable combustion systems. In despite of this, LES remains today very CPU demanding and its use for parametric studies on aeronautical engines design is excluded. In order to overcome this constraint, several methods have been proposed:

1) Navier-Stokes equations are simplified to quasi-1D Linearized Euler equations LEE [64, 5]. This strategy leads to consider only the main fluctuations on the flow (still remaining small in comparison to mean flow values) and the flame which is modeled as a source term. This source term can be coupled to the acoustic field and be responsible for thermo-acoustic instabilities or it can be decoupled and be responsible only for sound generation. Another important characteristic of these methods is that they can also take into account possible couplings of entropy or vorticity with acoustic modes.

2) The three dimensional wave equation is considered and resolved in the frequency domain. The underlying numerical tools, commonly known as Helmholtz solvers, are very useful in order to find the acoustic modes of a real combustor with its geometrical complexity. The influence of the flame dynamics on the acoustic system can also be accounted for. Several studies show their ability to predict combustion instabilities [56, 89, 62] in real combustion chambers. Nevertheless, these methods still present some drawbacks. The wave equation solved does not contain terms of convection, and as a consequence, the mean flow is neglected which can lead to wrong predictions of the propagation speed and wave length which in turn leads to mis-estimations on the resonant frequencies and the grow rates of the acoustic modes. Moreover, entropy and hydrodynamic modes are totally left out of the physics under study, although they play an important role.

The reliability of all these strategies is subjected to the precision at which boundary conditions are modeled. Useful methods have been developed to model the acoustic impedances of inlets/outlets and they have shown to be successful for some particular cases [41]. The general idea is to solve the perturbation equations in a quasi-1D domain which represents the regions either upstream (for the diffuser) or downstream (for the nozzle) of the combustion chamber. Feeding this domain with an incoming acoustic wave, the equivalent impedance can be assessed as soon as the outgoing wave is computed from the perturbation equations. Such a strategy was detailed in [41] in the case of perturbations propagating in an isentropic mean flow. In this chapter, it is generalized to the case where neither the enthalpy nor the entropy or the mean flow are constant.

This chapter is organized as follows. First, the quasi 1D LEE system is presented. Compared to [64], these equations contain additional terms that account for the compression or expansion stages in the system. Second, analytical solutions are derived to systems use to validate quasi 1D LEE numerical tool in three specific cases: isentropic compact nozzles [55], one dimensional flames and one dimensional compressors.

6.2 The quasi 1D Linearized Euler Equations - SNozzle

After applying the quasi 1D approximation, i.e., neglecting the in-plane correlation terms, the quasi-1D LEE for mass, momentum and entropy are written in non-conservative form [64]

$$\frac{\partial \rho}{\partial t} + u\frac{\partial \rho}{\partial x} + \rho\frac{\partial u}{\partial x} + \frac{\rho u}{\mathcal{S}}\frac{\partial \mathcal{S}}{\partial x} = 0 \tag{6.1}$$

$$\rho\frac{\partial u}{\partial t} + \rho u\frac{\partial u}{\partial x} + \frac{\partial p}{\partial x} - \mathcal{F} = 0 \tag{6.2}$$

$$\rho T\frac{\partial s}{\partial t} + \rho T u\frac{\partial s}{\partial x} - \dot{\mathcal{Q}} - \mathcal{W}_k = 0 \tag{6.3}$$

where $\mathcal{S}$, $\dot{\mathcal{Q}}$, $\mathcal{F}$ and $\mathcal{W}_k$ stand for the cross section area, an external energy source, the force added by the compressor, and the work done by the compressor respectively. Except for the mass balance equation which now contains an additional term accounting for the transversal section $\mathcal{S}$, it is observed from Eqs. (6.1) to (6.3) that the quasi 1D LEE system is essentially the 1D restriction of the 3D Euler equations. Considering harmonic perturbations ($\phi' = \hat{\phi}e^{-i\omega t}$), where $\phi(x,t) = \bar{\phi}(x) + \phi'(x,t)$, the quasi 1D LEE system in the frequency domain becomes

$$\left(\frac{\partial \bar{u}}{\partial x} + \bar{u}\frac{\partial}{\partial x} + \frac{\bar{u}}{\mathcal{S}}\frac{\partial \mathcal{S}}{\partial x}\right)\hat{\rho} + \left(\frac{\partial \bar{\rho}}{\partial x} + \bar{\rho}\frac{\partial}{\partial x} + \frac{\bar{\rho}}{\mathcal{S}}\frac{\partial \mathcal{S}}{\partial x}\right)\hat{u} - j\omega\hat{\rho} = 0 \tag{6.4}$$

$$\left(\frac{1}{\bar{\rho}}\frac{\partial \bar{c}^2}{\partial x}+\frac{\bar{u}}{\bar{\rho}}\frac{\partial \bar{u}}{\partial x}+\frac{\bar{c}^2}{\bar{\rho}}\frac{\partial}{\partial x}\right)\hat{\rho}+\left(\frac{\partial \bar{u}}{\partial x}+\bar{u}\frac{\partial}{\partial x}\right)\hat{u}+(\gamma-1)\bar{T}\left(\frac{1}{\bar{p}}\frac{\partial \bar{p}}{\partial x}+\frac{\partial}{\partial x}\right)\hat{s}-\hat{f}-j\omega\hat{u}=0 \quad (6.5)$$

$$\frac{\gamma r\bar{\mathcal{Q}}}{\bar{\rho}\bar{p}}\hat{\rho}+\frac{\partial \bar{s}}{\partial x}\hat{u}+\left(\bar{u}\frac{\partial}{\partial x}+(\gamma-1)\frac{\bar{\mathcal{Q}}}{\bar{p}}\right)\hat{s}-\frac{r}{\bar{p}}\hat{\mathcal{Q}}-\hat{\mathcal{W}}_k-j\omega\hat{s}=0 \quad (6.6)$$

This system of equations can be expressed as an algebraic linear system in the form

$$\mathcal{A}\begin{bmatrix}\hat{\rho}\\ \hat{u}\\ \hat{s}\end{bmatrix}=\begin{bmatrix}0\\ \hat{f}\\ \frac{r}{\bar{p}}\hat{\mathcal{Q}}+\hat{\mathcal{W}}_k\end{bmatrix} \quad (6.7)$$

where

$$\mathcal{A}=\begin{bmatrix}\frac{\partial \bar{u}}{\partial x}+\bar{u}\frac{\partial}{\partial x}+\frac{\bar{u}}{S}\frac{\partial S}{\partial x}-j\omega & \frac{\partial \bar{\rho}}{\partial x}+\bar{\rho}\frac{\partial}{\partial x}+\frac{\bar{\rho}}{S}\frac{\partial S}{\partial x} & 0\\ \frac{1}{\bar{\rho}}\frac{\partial \bar{c}^2}{\partial x}+\frac{\bar{u}}{\bar{\rho}}\frac{\partial \bar{u}}{\partial x}+\frac{\bar{c}^2}{\bar{\rho}}\frac{\partial}{\partial x} & \frac{\partial \bar{u}}{\partial x}+\bar{u}\frac{\partial}{\partial x}-j\omega & (\gamma-1)\bar{T}\left(\frac{1}{\bar{p}}\frac{\partial \bar{p}}{\partial x}+\frac{\partial}{\partial x}\right)\\ \frac{\gamma r\bar{\mathcal{Q}}}{\bar{\rho}\bar{p}} & \frac{\partial \bar{s}}{\partial x} & \bar{u}\frac{\partial}{\partial x}+(\gamma-1)\frac{\bar{\mathcal{Q}}}{\bar{p}}-j\omega\end{bmatrix} \quad (6.8)$$

The Quasi-1D Linearized Euler Equations (Eqs. 6.4, 6.5 and 6.6) are solved by a numerical tool called SNozzle. Within the computational domain, these equations are discretized by finite differences FD with a second order centered scheme. At the inlet, first order FD downwind scheme is applied whereas at the outlet first order FD upwind scheme is used. A staggered grid arrangement (velocity fluctuations stored at the cell edges, density and entropy fluctuations stored at the cell centers) has been used in order to avoid the pressure field to be contaminated by the classical odd-even decoupling phenomenon (reference). The Jacobi preconditioner is used to improve the quality of the matrix $\mathcal{A}$ (Eq. 6.8) and the linear system is solved by inverting the preconditioned matrix through the *LU* factorization.

6.3 The 1D linearized Euler equations for compact systems

In order to validate the numerical too SNozzle, analytical solutions are derived for compact regions where the mean enthalpy or entropy changes. The starting point for this derivation are the 1D Euler equations for mass, momentum and total enthalpy.

$$\frac{\partial \rho}{\partial t} + \frac{\partial}{\partial x}(\rho u) = 0 \tag{6.9}$$

$$\frac{\partial \rho u}{\partial t} + \frac{\partial}{\partial x}(\rho u^2) = -\frac{\partial p}{\partial x} + F \tag{6.10}$$

$$\frac{\partial \rho h_t}{\partial t} + \frac{\partial}{\partial x}(\rho u h_t) = \dot{\mathcal{Q}} + \mathcal{W}_k \tag{6.11}$$

Integrating over the 1D domain between positions x_1 and x_2 results in

$$\begin{aligned} \int_{x_1}^{x_2} \frac{\partial \rho}{\partial t} dx + \int_{x_1}^{x_2} \frac{\partial}{\partial x}(\rho u) dx = 0 \\ \int_{x_1}^{x_2} \frac{\partial \rho}{\partial t} dx + (\rho u)\Big|_{x_1}^{x_2} = 0 \end{aligned} \tag{6.12}$$

$$\begin{aligned} \int_{x_1}^{x_2} \frac{\partial \rho u}{\partial t} dx + \int_{x_1}^{x_2} \frac{\partial}{\partial x}(\rho u^2) dx + \int_{x_1}^{x_2} \frac{\partial p}{\partial x} dx - \int_{x_1}^{x_2} F dx = 0 \\ \int_{x_1}^{x_2} \frac{\partial \rho u}{\partial t} dx + (\rho u^2)\Big|_{x_1}^{x_2} + p\Big|_{x_1}^{x_2} - \mathcal{F} = 0 \end{aligned} \tag{6.13}$$

$$\begin{aligned} \int_{x_1}^{x_2} \frac{\partial \rho h_t}{\partial t} dx + \int_{x_1}^{x_2} \frac{\partial}{\partial x}(\rho u h_t) dx - \int_{x_1}^{x_2} \dot{\mathcal{Q}} dx - \int_{x_1}^{x_2} \mathcal{W}_k dx = 0 \\ \int_{x_1}^{x_2} \frac{\partial \rho h_t}{\partial t} dx + (\rho u h_t)\Big|_{x_1}^{x_2} - \dot{q} - \mathcal{W} = 0 \end{aligned} \tag{6.14}$$

where the following notations have been introduced: $\int \dot{\mathcal{Q}} dx = \dot{q}$, $\int F dx = \mathcal{F}$ and $\int \mathcal{W}_k dx = \mathcal{W}$. After linearizing and recalling that $h_t = c_p T_t$, Eqs. (6.12), (6.13) and (6.14) become

$$\left(\bar{\rho} u' + \rho' \bar{u}\right)\Big|_{x_1}^{x_2} = -\int_{x_1}^{x_2} \frac{\partial \rho'}{\partial t} dx \tag{6.15}$$

$$\left(p' + \rho' \bar{u}^2 + 2\bar{\rho}\bar{u}u'\right)\Big|_{x_1}^{x_2} - \mathcal{F}' = -\int_{x_1}^{x_2} \frac{\partial}{\partial t}\left(\bar{\rho} u' + \rho' \bar{u}\right) dx \tag{6.16}$$

$$\left[c_p \bar{T}_t(\bar{\rho} u' + \rho' \bar{u}) + \bar{\rho}\bar{u}(c_p T' + \bar{u}u')\right]\Big|_{x_1}^{x_2} - \dot{q}' - \mathcal{W}' = -\int_{x_1}^{x_2} \frac{\partial}{\partial t}\left[\rho' c_p \bar{T}_t + \bar{\rho}\left(c_p T' + \bar{u}u'\right)\right] dx \tag{6.17}$$

Considering now harmonic oscillations ($\phi' = \hat{\phi} e^{-i\omega t}$) leads to:

$$(\bar{\rho}\hat{u} + \hat{\rho}\bar{u}) \Big|_{x_1}^{x_2} = \boldsymbol{i}\omega \int_{x_1}^{x_2} \hat{\rho} dx \tag{6.18}$$

$$\left(\hat{p} + \hat{\rho}\bar{u}^2 + 2\bar{\rho}\bar{u}\hat{u}\right) \Big|_{x_1}^{x_2} - \hat{\mathcal{F}} = \boldsymbol{i}\omega \int_{x_1}^{x_2} \left(\bar{\rho}\hat{u} + \hat{\rho}\bar{u}\right) dx \tag{6.19}$$

$$\left[c_p \bar{T}_t(\bar{\rho}\hat{u} + \rho'\bar{u}) + \bar{\rho}\bar{u}(c_p\hat{T} + \bar{u}\hat{u})\right] \Big|_{x_1}^{x_2} - \hat{\dot{q}} - \hat{\mathcal{W}} = \boldsymbol{i}\omega \int_{x_1}^{x_2} \left[\hat{\rho} c_p \bar{T}_t + \bar{\rho}\left(c_p\hat{T} + \bar{u}\hat{u}\right)\right] dx \tag{6.20}$$

The contribution of the RHS terms on the above equations goes to zero for compact regions ($x_1 \to x_2$). Equations (6.18), (6.19) and (6.20) are then simplified to

$$\boxed{\bar{\rho}_1\hat{u}_1 + \hat{\rho}_1\bar{u}_1 = \bar{\rho}_2\hat{u}_2 + \hat{\rho}_2\bar{u}_2} \tag{6.21}$$

$$\boxed{\hat{p}_1 + \hat{\rho}_1\bar{u}_1^2 + 2\bar{\rho}_1\bar{u}_1\hat{u}_1 + \hat{\mathcal{F}} = \hat{p}_2 + \hat{\rho}_2\bar{u}_2^2 + 2\bar{\rho}_2\bar{u}_2\hat{u}_2} \tag{6.22}$$

$$\boxed{c_p\bar{T}_{t1}(\bar{\rho}_1\hat{u}_1 + \hat{\rho}_1\bar{u}_1) + \bar{\rho}_1\bar{u}_1(c_p\hat{T}_1 + \bar{u}_1\hat{u}_1) + \hat{\dot{q}} + \hat{\mathcal{W}} = c_p\bar{T}_{t2}(\bar{\rho}_2\hat{u}_2 + \hat{\rho}_2\bar{u}_2) + \bar{\rho}_2\bar{u}_2(c_p\hat{T}_2 + \bar{u}_2\hat{u}_2)} \tag{6.23}$$

where the indices 1 and 2 denote the regions upstream or downstream of any infinitely thin compact element; $\hat{\dot{q}}$, $\hat{\mathcal{F}}$ and $\hat{\mathcal{W}}$ being the total heat, force and work associated to this element. Equations (6.21) - (6.23) generalize the results of Dowling [22] to the case where the compact interface between states 1 and 2 generates a force $\hat{\mathcal{F}}$ and the associated work $\hat{\mathcal{W}}$.

6.3.1 The transmitted and reflected waves

In the frequency domain, acoustic and entropy waves $\hat{w}$ are defined by their amplitude $|\hat{w}|$ and phase ϕ, so that $\hat{w} = |\hat{w}|e^{i\phi}$. They read [55]

$$\hat{w}^+ = \frac{\hat{p}}{\gamma\bar{p}} + \frac{\hat{u}}{\bar{c}} = |\hat{w}^+| e^{\boldsymbol{i}\omega x/\bar{c}(1+\bar{\mathcal{M}})} \tag{6.24}$$

$$\hat{w}^- = \frac{\hat{p}}{\gamma\bar{p}} - \frac{\hat{u}}{\bar{c}} = |\hat{w}^-| e^{-\boldsymbol{i}\omega x/\bar{c}(1-\bar{\mathcal{M}})} \tag{6.25}$$

$$\hat{w}^S = \frac{\hat{p}}{\gamma\bar{p}} - \frac{\hat{\rho}}{\bar{\rho}} = |\hat{w}^S| e^{\boldsymbol{i}\omega x/\bar{u}} \tag{6.26}$$

where $\hat{w}^+$ and $\hat{w}^-$ represent the acoustic waves propagating respectively in the direction of the flow at speed $(\bar{u}+\bar{c})$, and against the flow at speed $(\bar{c}-\bar{u})$. $\hat{w}^S$ stands for the entropy wave that is convected at the mean flow velocity $(\bar{u})$.

The compact assumption is realistic when the length of the system L is small if compared to the respective wavelength λ. When considering acoustics in nozzles, it is shown in [41] that this assumption is valid nozzles for frequencies up to 700 Hz, which is already an important bandwidth. When a wave passes through a compact domain, it is assumed then that only its amplitude changes. The phase, on the contrary remains constant. This can be easier understood from Fig. (6.1).

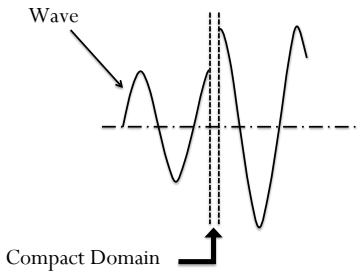

Figure 6.1: A compact nozzle acting on a wave

As a result, the compact assumption consists simply in expressing all fluctuating quantities as quasi-stationary ($\omega \approx 0$). Pressure, velocity and entropy fluctuations can be defined then as function only of their amplitudes

$$\frac{\hat{p}}{\gamma\bar{p}} = \frac{1}{2}\hat{w}^+ + \frac{1}{2}\hat{w}^- \approx \frac{1}{2}|\hat{w}^+| + \frac{1}{2}|\hat{w}^-| \tag{6.27}$$

$$\frac{\hat{u}}{\bar{c}} = \frac{1}{2}\hat{w}^+ - \frac{1}{2}\hat{w}^- \approx \frac{1}{2}|\hat{w}^+| - \frac{1}{2}|\hat{w}^-| \tag{6.28}$$

$$\frac{\hat{s}}{c_p} = \hat{w}^S \approx |\hat{w}^S| \tag{6.29}$$

The reflection R and transmission T coefficients are now defined. The coefficient R_{AA} is the reflection coefficient that measures the amplitude of the outgoing acoustic wave w_1^- with respect to an incoming wave w_1^+ when it is assured that no incoming entropy waves are present $\hat{w}_1^S = 0$. R_{SA} is also a reflection coefficient, but instead of R_{AA}, relates the amplitude of an outgoing acoustic wave w_1^- with respect to an incoming entropy wave $\hat{w}_1^S$. In this case, no incoming acoustic waves are present $\hat{w}_1^+ = 0$. The transmitted waves T are defined in a similar way. This definition is shown in table 6.1. All the possible waves $\hat{w}$ that can appear in a 1D system are shown in Fig. (6.2)

Six other coefficients are now defined, which are helpful to express Eqs. (6.21), (6.22) and (6.23)

R_{AA}	$\rightarrow$	$\hat{w}_1^-/\hat{w}_1^+$	$\rightarrow$	with	$\hat{w}_1^S = 0$
R_{SA}	$\rightarrow$	$\hat{w}_1^-/\hat{w}_1^S$	$\rightarrow$	with	$\hat{w}_1^+ = 0$
T_{AA}	$\rightarrow$	$\hat{w}_2^+/\hat{w}_1^+$	$\rightarrow$	with	$\hat{w}_1^S = 0$
T_{SA}	$\rightarrow$	$\hat{w}_2^+/\hat{w}_1^S$	$\rightarrow$	with	$\hat{w}_1^+ = 0$
T_{AS}	$\rightarrow$	$\hat{w}_2^S/\hat{w}_1^+$	$\rightarrow$	with	$\hat{w}_1^S = 0$

Table 6.1: Wave coefficients definition

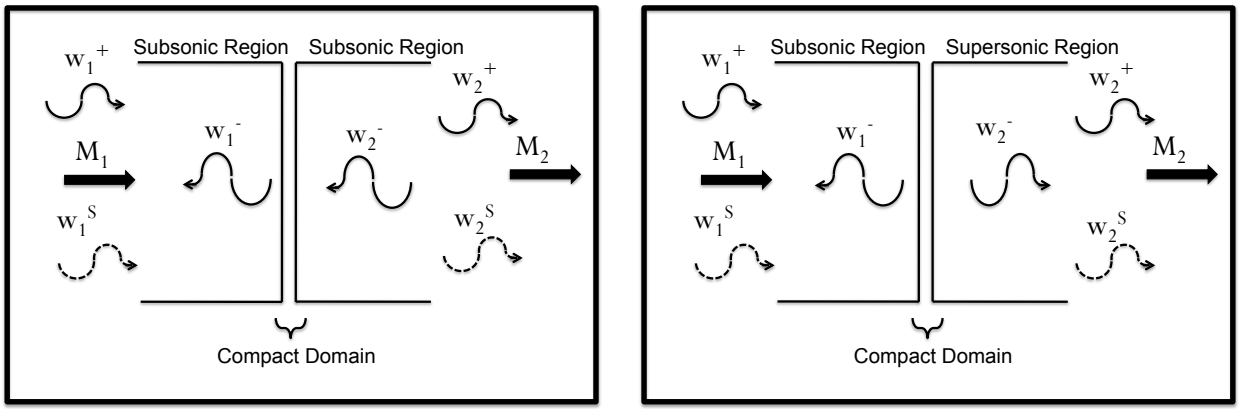

(a) (b)

Figure 6.2: Some possible configurations under the compact assumption

as function principally of the mach number $\bar{\mathcal{M}} = \bar{u}/\bar{c}$.

$$\boxed{A_1 = \frac{\gamma\hat{p}}{2}|\hat{w}_1^+|, \quad B_1 = \frac{\gamma\hat{p}}{2}|\hat{w}_1^-|, \quad A_2 = \frac{\gamma\hat{p}}{2}|\hat{w}_2^+|, \quad B_2 = \frac{\gamma\hat{p}}{2}|\hat{w}_2^-|, \quad E_1 = c_p|\hat{w}_1^S|, \quad E_2 = c_p|\hat{w}_2^S|} \tag{6.30}$$

Here A and B have (Pa) units while E has (kJ/kgK) units. Considering also a perfect gas $\frac{\hat{T}}{\bar{T}} = \left(\frac{\hat{p}}{\bar{p}} - \frac{\hat{\rho}}{\bar{\rho}}\right)$, Eqs. (6.21) to (6.23), under the compact assumption, become

$$\boxed{\begin{aligned} &A_1(1+\bar{\mathcal{M}}_1)/\bar{c}_1 - B_1(1-\bar{\mathcal{M}}_1)/\bar{c}_1 - \rho_1\bar{c}_1\bar{\mathcal{M}}_1E_1/c_p = \\ &A_2(1+\bar{\mathcal{M}}_2)/\bar{c}_2 - B_2(1-\bar{\mathcal{M}}_2)/\bar{c}_2 - \rho_2\bar{c}_2\bar{\mathcal{M}}_2E_2/c_p \end{aligned}} \tag{6.31}$$

$$\boxed{\begin{aligned} &(1+\bar{\mathcal{M}}_1)^2A_1 + (1-\bar{\mathcal{M}}_1)^2B_1 - \rho_1\bar{c}_1^2\bar{\mathcal{M}}_1^2E_1/c_p + \hat{\mathcal{F}} = \\ &(1+\bar{\mathcal{M}}_1)^2A_2 + (1-\bar{\mathcal{M}}_2)^2B_2 - \rho_2\bar{c}_2^2\bar{\mathcal{M}}_2^2E_2/c_p \end{aligned}} \tag{6.32}$$

$$\boxed{\begin{aligned} &(1+\bar{\mathcal{M}}_1)a_1\bar{c}_1A_1 + (1-\bar{\mathcal{M}}_1)a_2\bar{c}_1B_1 - \rho_1\bar{c}_1^3\bar{\mathcal{M}}_1^3E_1/2c_p + \hat{\mathcal{W}}/\bar{c}_1 + \hat{\dot{q}}/\bar{c}_1 = \\ &(1+\bar{\mathcal{M}}_2)a_3\bar{c}_2A_2 + (1-\bar{\mathcal{M}}_2)a_4\bar{c}_1B_2 - \rho_2\bar{c}_2^3\bar{\mathcal{M}}_2^3E_2/2c_p \end{aligned}} \tag{6.33}$$

with $a_1 = \bar{\mathcal{M}}_1 + \frac{1}{2}\bar{\mathcal{M}}_1^2 + \frac{1}{\gamma-1}$, $a_2 = \bar{\mathcal{M}}_1 - \frac{1}{2}\bar{\mathcal{M}}_1^2 - \frac{1}{\gamma-1}$ and $a_3 = \bar{\mathcal{M}}_2 + \frac{1}{2}\bar{\mathcal{M}}_2^2 + \frac{1}{\gamma-1}$. These equations (6.31, 6.32 and 6.33) are solved for three unknowns out of six: A_1, A_2, B_1, B_2, E_1 and E_2. As a consequence, three of these six coefficients must be imposed to the problem.

6.4 Transmitted and reflected acoustic waves in isentropic nozzles

As already stated in the introductory part of this section, determining appropriate acoustic boundary conditions for combustion chambers is crucial in order to correctly predict combustion instabilities. These acoustic boundary conditions depend on the mean flow either upstream (Compressors) or downstream (Turbines). As a first step, it is useful to consider the mean flow in these regions as isentropic ($\hat{W}$, $\hat{\dot{\mathcal{Q}}} = 0$) and isenthalpic ($\hat{F}$) $= 0$. This means that the combustion chamber is only surrounded by perfect diffusers and nozzles.

The unchocked Nozzle

A subsonic system need to be acoustically constrained both at the inlet and at the outlet. In order to acoustically characterize the nozzle independently from boundary conditions, the outlet is fixed as totally non-reflecting ($w_2^- = 0 \rightarrow E_2 = 0$). Eqs. (6.31) and (6.33) are re-arranged to obtain the following general expressions [55]

$$R_{AA} = B_1/A_1 = \left(\frac{\bar{\mathcal{M}}_1 - \bar{\mathcal{M}}_2}{\bar{\mathcal{M}}_1 + \bar{\mathcal{M}}_2}\right)\left(\frac{\bar{\mathcal{M}}_1 + 1}{\bar{\mathcal{M}}_1 - 1}\right)\left(\frac{1 - \frac{1}{2}(\gamma-1)\bar{\mathcal{M}}_1\bar{\mathcal{M}}_2}{1 + \frac{1}{2}(\gamma-1)\bar{\mathcal{M}}_1\bar{\mathcal{M}}_2}\right) \tag{6.34}$$

$$R_{SA} = B_1/E_1 = \left(\frac{\bar{\mathcal{M}}_2 - \bar{\mathcal{M}}_1}{1 - \bar{\mathcal{M}}_1}\right)\left(\frac{\bar{\mathcal{M}}_1}{1 + \frac{1}{2}(\gamma-1)\bar{\mathcal{M}}_1\bar{\mathcal{M}}_2}\right) \tag{6.35}$$

$$T_{AA} = A_1/A_2\left(\frac{2\bar{\mathcal{M}}_2}{1 + \bar{\mathcal{M}}_2}\right)\left(\frac{1 + \bar{\mathcal{M}}_1}{\bar{\mathcal{M}}_1 + \bar{\mathcal{M}}_2}\right)\left(\frac{1 + \frac{1}{2}(\gamma-1)\bar{\mathcal{M}}_2^2}{1 + \frac{1}{2}(\gamma-1)\bar{\mathcal{M}}_1\bar{\mathcal{M}}_2}\right) \tag{6.36}$$

$$T_{SA} = E_1/A_2\left(\frac{\bar{\mathcal{M}}_2 - \bar{\mathcal{M}}_1}{1 + \bar{\mathcal{M}}_2}\right)\left(\frac{\frac{1}{2}\bar{\mathcal{M}}_2}{1 + \frac{1}{2}(\gamma-1)\bar{\mathcal{M}}_1\bar{\mathcal{M}}_2}\right) \tag{6.37}$$

The chocked Nozzle

The mass flow through a chocked nozzle is constrained by

$$\dot{m} = \frac{p_{t,1}}{\sqrt{\gamma t T_{t,1}}} A_{cr} \gamma \left(\frac{\gamma + 1}{2} \right)^{-\frac{\gamma+1}{2(\gamma-1)}} \tag{6.38}$$

Derivating the logarithm of Eq. (6.38) results in a simple expression [41]

$$\frac{\hat{u}_1}{\bar{c}_1} - \frac{\gamma}{2} \mathcal{M}_1 \left(\frac{\hat{p}_1}{\gamma \bar{p}_1} + \frac{1}{2} \bar{\mathcal{M}}_1 \frac{\hat{\rho}_1}{\bar{\rho}_1} \right) = 0 \tag{6.39}$$

which if combined with the expression of waves (section 6.3.1) results in

$$R_{AA} = \frac{1 - \frac{1}{2}(\gamma - 1)\bar{\mathcal{M}}_1}{1 + \frac{1}{2}(\gamma - 1)\bar{\mathcal{M}}_1} \tag{6.40}$$

$$R_{SA} = \frac{\frac{1}{2}\bar{\mathcal{M}}_1}{1 + \frac{1}{2}(\gamma - 1)\bar{\mathcal{M}}_1} \tag{6.41}$$

$$T_{AA} = \frac{1 + \frac{1}{2}(\gamma - 1)\bar{\mathcal{M}}_2}{1 + \frac{1}{2}(\gamma - 1)\bar{\mathcal{M}}_1} \tag{6.42}$$

$$T_{SA} = \frac{\frac{1}{2}(\bar{\mathcal{M}}_2 - \bar{\mathcal{M}}_1)}{1 + \frac{1}{2}(\gamma - 1)\bar{\mathcal{M}}_1} \tag{6.43}$$

It is important to emphasize here that since the nozzle is chocked, the flow after the throat is supersonic. As a consequence acoustic waves should not be imposed at the outlet of the computational domain. Doing so would result in an ill-posed problem.

6.4.1 Acoustic Response of Chocked and Unchocked Nozzles

As stated before, the compact assumption is very useful to study the acoustic response of a nozzle when the acoustic wave length λ is much larger than the nozzle length. When acoustic and entropy disturbances fluctuate at large frequencies, the jump conditions showed previously become unsuited since they do not account for phase changes across the nozzle. In order to study the influence of 'non-compactness' different methods are found in the literature [12, 59, 55]. In [55] it is stated that the main influence of the nozzle finiteness is to alter the phase between the two wave trains. This can be modeled by considering that the mean flow velocity changes linearly through the nozzle. Nevertheless, this assumption is too restrictive for real systems. For reliable computations, it is then mandatory to resolve the mean flow in the nozzle. If non-linear acoustics and complex geometries are considered, the only possibility would be to resolve the complete set of Euler equations in the time domain. Nevertheless, three dimensional Euler computations are computational expensive and the consideration of non-linearities is not always necessary. If a three dimensional nozzle can be seen as axysymmetric and planar waves

are expected, an approximate yet accurate method to study the acoustics of such a system is to resolve the quasi-one dimensional and Linearized Euler Equations (section 6.2).

Two different nozzle configurations are studied. They are shown in Figure (6.3) and the mean flow and geometrical parameters are given in table (6.2).

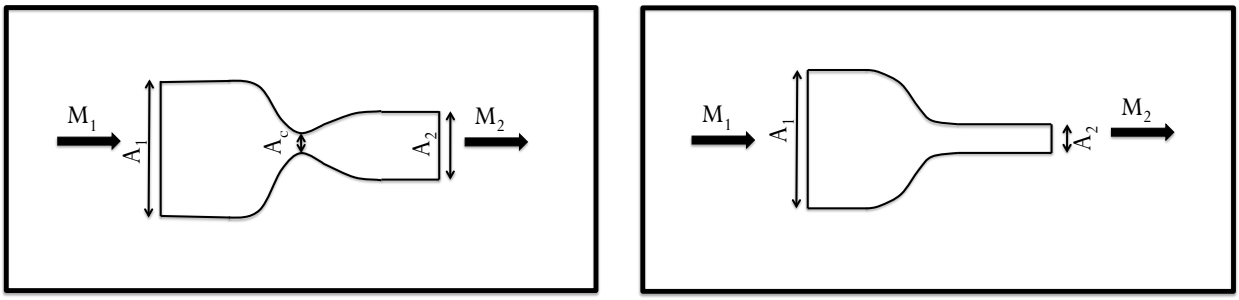

(a) (b)

Figure 6.3: Chocked and Unchocked configurations studied

	Unchocked Case	**Chocked Case**
A_1/A_c	5.651	5.873
A_2/A_c	1.000	1.032
$\mathcal{M}_2$	0.8	1.2
$\mathcal{M}_1$	0.1	
T_1	1300K	
P_1	800 kPa	

Table 6.2: Mean flow inlet conditions and geometrical parameters

In order to test the reliability of the SNozzle tool (see section 6.2), the results given by this solver are compared to those obtained by solving the complete set of Euler Equations using the LES AVBP solver. Besides, they are compared to the analytical results obtained under the compact assumption. More precisely, the following approaches are compared in what follows:

- **Analytics:** The acoustic parameters $R_{AA}, R_{SA}, T_{AA}, T_{SA}$ are computed through the relations proposed by Marble & Candel [55]. Equations (6.34) to (6.37), and (6.40) to (6.43) are then used.
- **Quasi-1D LEE (SNozzle):** The inlet Mach number $\bar{\mathcal{M}}_1$, temperature $\bar{T}_1$ and pressure $\bar{P}_1$ are given as inputs to SNozzle as well as the geometry (x coordinate and section area $\mathcal{S}$). The outlet is taken as totally non reflecting ($w_2^- = 0$), whereas at the inlet either w_1^+ or w^S are imposed. Two thousand points are used for both geometries.
- **The 3D Euler Equations (AVBP):** The LES solver AVBP (see section 5.3.1) is used, in which the viscous terms of the Navier Stokes equations have been neglected. Care has

to be taken specially with the use of the inlet boundary condition, since it must impose both the mean flow and either the entropy or acoustic wave [37]. Therefore, the inlet must be non reflecting so that the reflected w_1^- be completely evacuated. The mesh is composed of sixty thousand nodes which is equivalent to the two thousand nodes mesh for the Quasi-1D LEE solver.

6.4.2 Results

The value of both transmission and reflection coefficients are shown in Fig. (7.4). They are plotted against the non-dimensional frequency $\Omega = \omega l_n / \bar{c}_1$ where ω is the angular frequency, l_n the length of the nozzle and $\bar{c}_1$ the speed of sound at the inlet. It is observed that analytical results are well suited when considering small frequencies ($\Omega \rightarrow 0$). Both numerical tools converge to Marble & Candel expressions when $\lambda \gg l_n$ for all coefficients, excepting R_{SA} where the AVBP solver, which solves the 3D Euler equations, fails to reproduce the analytical value. Despite our efforts, no definite explanation was found for this result, even if artificial viscosity and lack of grid refinements seem to be good candidates for explaining such errors. Note however that the error is for the R_{SA} coefficient which is always the smallest one.

At small frequencies, it is observed that the main influence of a chocked nozzle is the increase of noise ($\hat{w}_2^+ \nearrow$) due to entropy waves, as already stated in [47]. This can be seen in the value of T_{SA} ($\hat{w}_2^+ / \hat{w}_1^S$) which is twice larger when the nozzle is chocked. The reflected wave $\hat{w}_1^-$ increases also but to a less extend. On the other hand, the acoustic response of the nozzle due to an incoming acoustic wave remains quite similar (T_{AA} and R_{AA}) for both unchocked and chocked configurations.

When the reduced frequency increases, the value of the acoustic coefficients starts to move away smoothly from the analytical results. Up to $\Omega \approx 2$ results given by both numerical solvers can be considered similar. At higher frequencies, the 3D Euler solver curves representing T_{AA} and R_{AA} start to decrease faster, the largest differences appearing for R_{AA} and the unchocked case. This is due to the numerical scheme used in the 3D Euler solver, which appears to be dissipative for small length waves. Recall that the mesh is kept unchanged when Ω increases so that numerical errors increase. On the other hand, a higher spatial resolution is considered in the quasi-1D LEE solver (2000 cells) and the corresponding results are virtually free of numerical errors (it has been checked that grid convergence is reached for the results displayed).

6.5 When entropy does not remain constant through a duct

In the previous section the influence of the inlet/outlet Mach number $\bar{\mathcal{M}}$ on the transmitted and reflected waves was studied in isentropic nozzles. The aim of this section is not anymore to

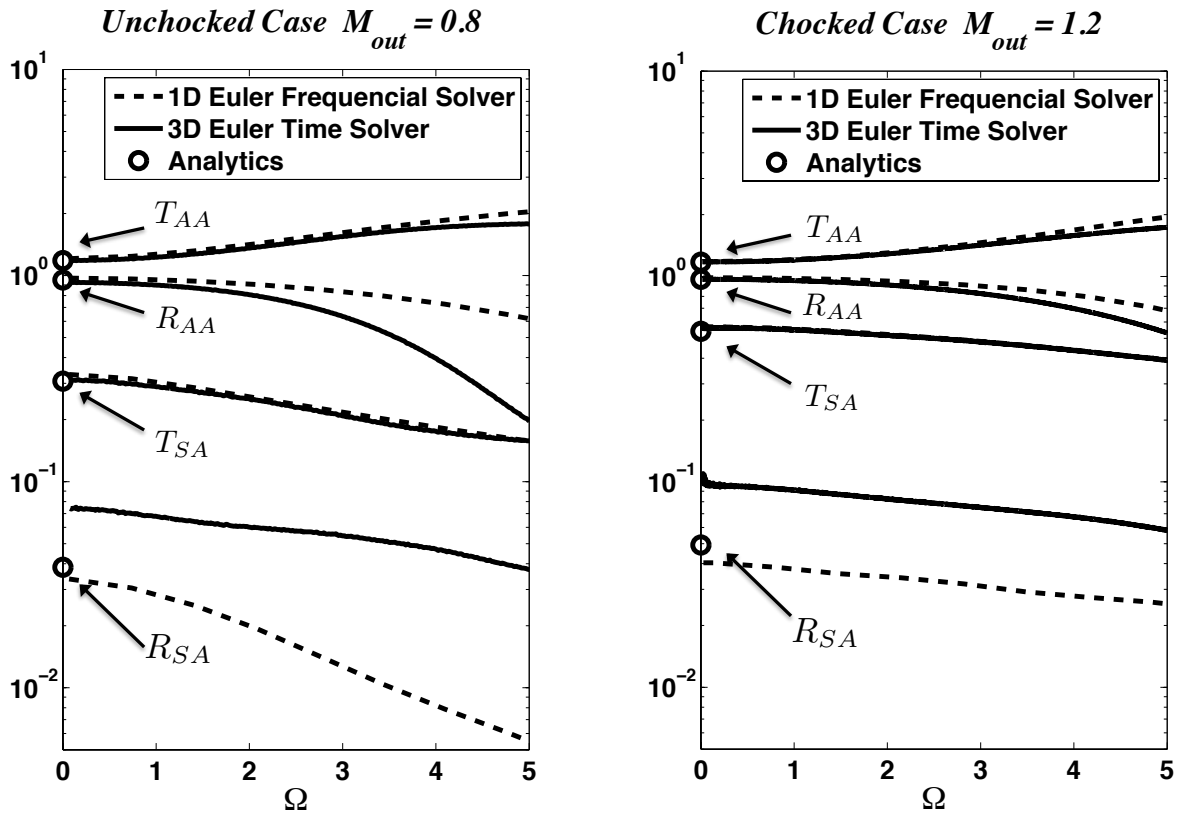

(a) (b)

Figure 6.4: Reflection and Transmission coefficients for both unchocked and chocked cases

evaluate the acoustic response of a system due to changes in the mean flow caused by section variations, but to study the influence of an entropy variation on the acoustics of a given system. As a result, a thin one-dimensional flame will be considered. This flame, which is characterized by a mean entropy jump, is located at the middle of a constant section duct (Fig.6.5). An incoming acoustic wave w_1^+ is imposed at the inlet and the acoustic reflected wave w_1^- generated by the flame is evaluated. In addition, the acoustic transmitted wave w_2^+ and the entropy wave w_2^S created after the entropy jump are also computed. This study will be carried out both analytically (Eqs. 6.31, 6.32 and 6.33) and numerically by resolving the LEE system thanks to the SNozzle tool (section 6.2).

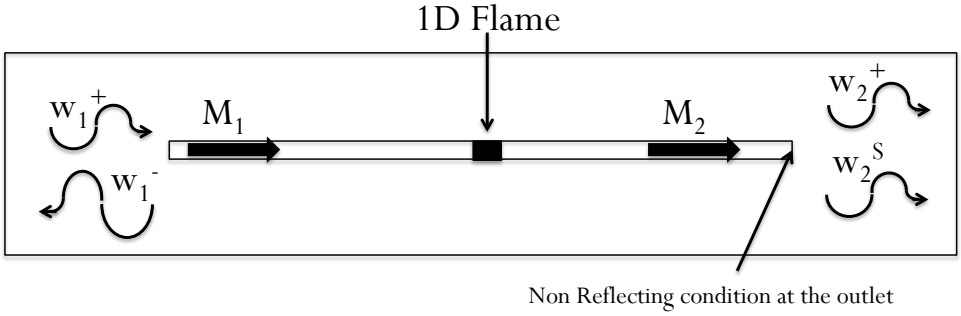

Figure 6.5: 1D Flame

6.5.1 Analytic Solution : Building the linear system of equations

After having neglected B_2 and E_1, the sources due to the presence of a compressor $\hat{\mathcal{F}}$ and $\hat{\mathcal{W}}$, and the unsteady source of energy $\hat{\dot{q}}$ the system of equations to resolve become

$$(1+\bar{\mathcal{M}}_1)/\bar{c}_1 A_1 - (1-\bar{\mathcal{M}}_1)/\bar{c}_1 B_1 = (1+\bar{\mathcal{M}}_2)/\bar{c}_2 A_2 - \rho_2 \bar{c}_2 \bar{\mathcal{M}}_2 E_2/c_p \tag{6.44}$$

$$(1+\bar{\mathcal{M}}_1)^2 A_1 + (1-\bar{\mathcal{M}}_1)^2 B_1 = (1+\bar{\mathcal{M}}_2)^2 A_2 - \rho_2 \bar{c}_2^2 \bar{\mathcal{M}}_2^2 E_2/c_p \tag{6.45}$$

$$(1+\bar{\mathcal{M}}_1) a_1 \bar{c}_1 A_1 + (1-\bar{\mathcal{M}}_1) a_2 \bar{c}_1 B_1 = (1+\bar{\mathcal{M}}_2) a_3 \bar{c}_2 A_2 - \rho_2 \bar{c}_2^3 \bar{\mathcal{M}}_2^3 E_2/2c_p \tag{6.46}$$

with $a_1 = \bar{\mathcal{M}}_1 + \frac{1}{2}\bar{\mathcal{M}}_1^2 + \frac{1}{\gamma-1}$, $a_2 = \bar{\mathcal{M}}_1 - \frac{1}{2}\bar{\mathcal{M}}_1^2 - \frac{1}{\gamma-1}$ and $a_3 = \bar{\mathcal{M}}_2 + \frac{1}{2}\bar{\mathcal{M}}_2^2 + \frac{1}{\gamma-1}$. These equations (6.44, 6.45 and A.1) are resolved for three unknowns: B_1, A_2 and E_2. The coefficient A_1 is the amplitude of the forced acoustic wave and must be given as an input to the problem. Note that for this particular case $\hat{\dot{q}}$ was set to zero. This term could be also model as $\hat{\dot{q}} = c_p(\bar{T}_{t2} - \bar{T}_{t1})(\bar{\rho}_1 \hat{u}_1 + \hat{\rho}_1 \bar{u}_1)$ as done in [22].

6.5.2 The mean flow in SNozzle

Before performing any analysis on fluctuating quantities, it is necessary to define the baseline flow of the 1D Flame configuration. The1D flame is considered to produce a jump of temperature at $x = 0$. This temperature jump must be as smooth as possible so that gradients of all related quantities are properly computed. The temperature profile, shown in Fig. 6.6(a) is built from an hyperbolic tangent function. The mean value of the entropy $\bar{s}$ is function of the mean density $\bar{\rho}$ and the mean temperature $\bar{T}$. It reads

$$\bar{s} = c_v \ln \left[\frac{R\bar{T}}{\bar{\rho}^{\gamma-1}} \right] \tag{6.47}$$

Along this study the perturbations of the heat release $\hat{\dot{q}}(t) = 0$ are neglected. Nevertheless a profile of the mean heat release $\bar{\dot{q}}$ is present and defined as

$$\bar{\dot{q}} = \frac{\bar{P}\bar{u}}{r} \frac{\partial \bar{s}}{\partial x} \tag{6.48}$$

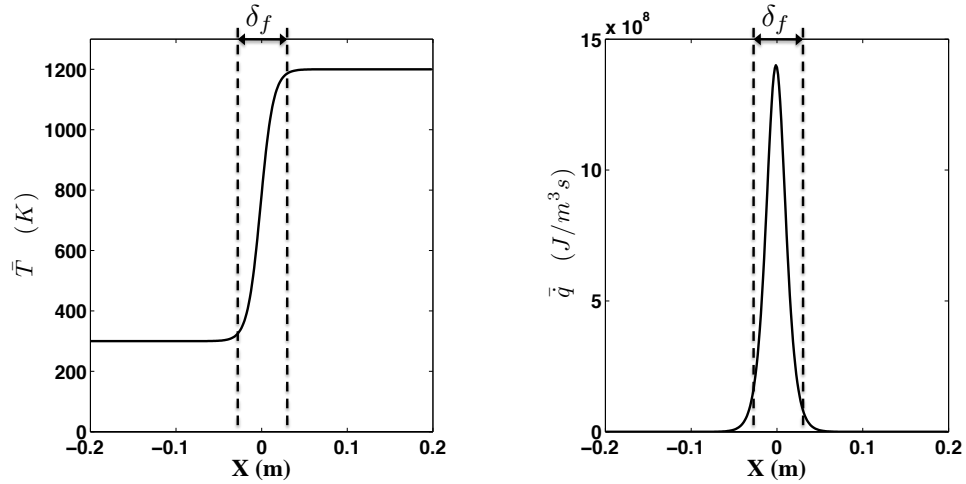

(a) Mean Temperature (b) Mean Heat Release

Figure 6.6: Typical Profiles

The mean quantities $\bar{u}$, $\bar{\rho}$ and $\bar{p}$ are obtained in such a way that the Euler equations for steady flows are satisfied. Figures 6.6, 6.7 and 6.8 show the mean profiles of heat release, pressure, velocity, density and the Mach number for the case in which $\mathcal{M}_1 = 0.1$.

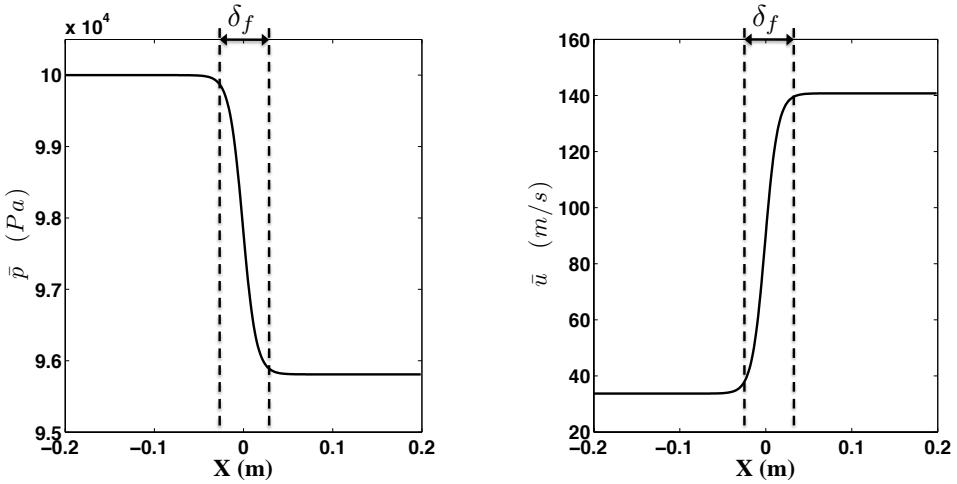

(a) Mean pressure (b) Mean velocity

Figure 6.7: Typical Profiles

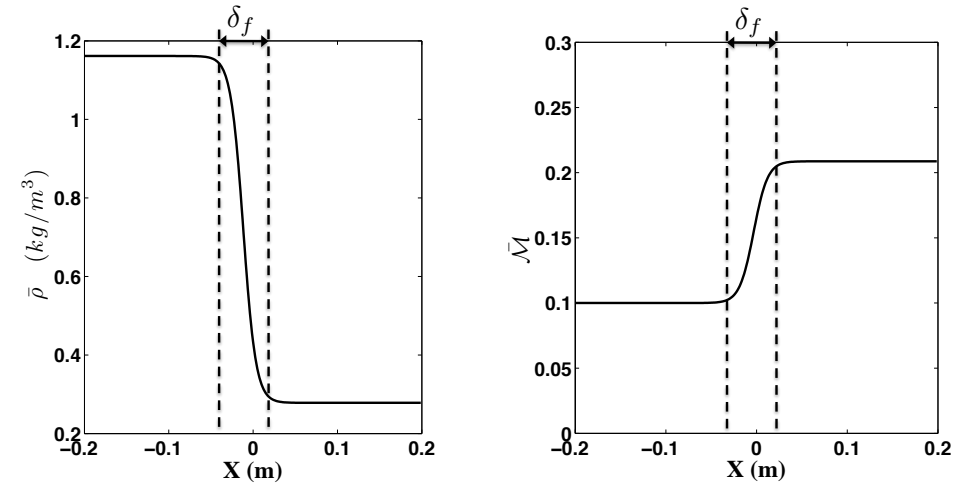

(a) Mean density (b) Mean Mach number

Figure 6.8: Typical Profiles

6.5.3 Results

The 1D Flame system is considered compact since the flame thickness δ_f remains small for all the acoustic wave lengths λ studied. For this reason, the present analysis focuses mainly on the effects of both the inflow Mach Number $\bar{\mathcal{M}}_1$ and the temperature jump ($\bar{T}_2/\bar{T}_1$).

Figure (6.9) shows the values of the coefficients R_{AA}, T_{AA} and T_{AS} (see table 6.1) obtained by both the analytical and the LEE approaches for two different values of $\bar{T}_2/\bar{T}_1$.

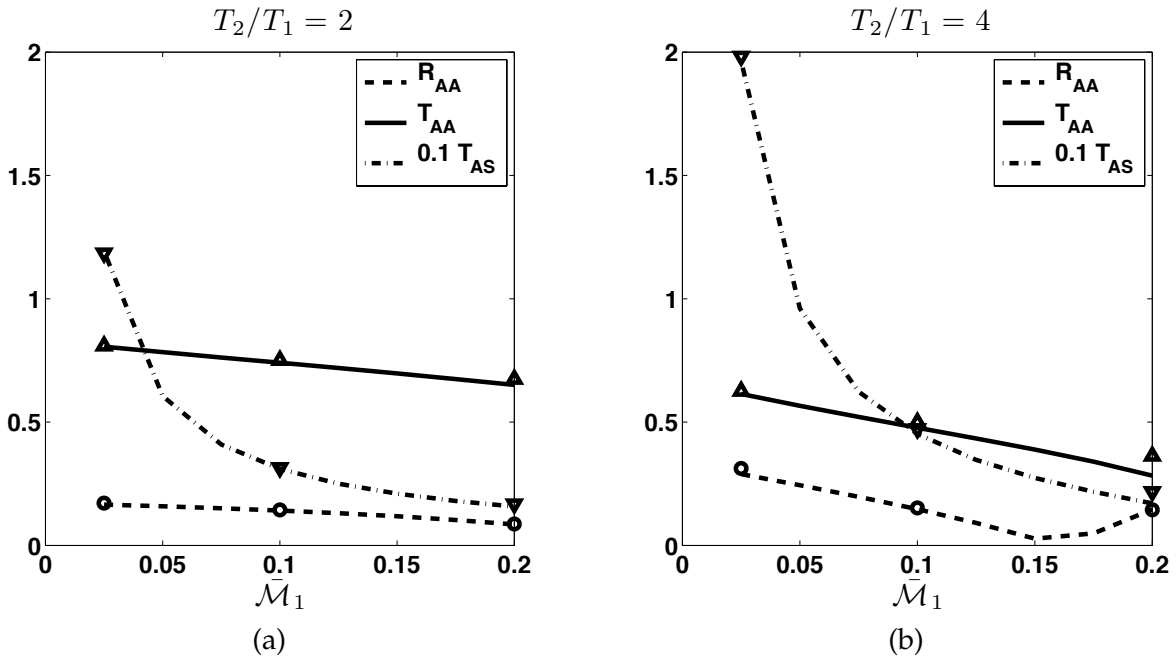

Figure 6.9: 1D Flame - Entropy Jump Case. Lines correspond to analytical solutions. Symbols ($\triangle$,$\triangledown$,$\circ$) represent SNozzle solutions

.

Good agreement is found between analytical solutions and SNozzle results. It is observed that the lower the inflow Mach number $\bar{\mathcal{M}}_1$, the bigger the amplitude of all the waves w_1^-,w_2^+ and w_2^S. The temperature jump T_2/T_1 has a strong but opposite effect on both transmitted acoustic wave and generated entropy wave. A high value of T_2/T_1 generates a high amplitude entropy wave. On the other hand, this high value of T_2/T_1 creates a reduction of the amplitude of the transmitted acoustic wave so that the energy of the fluctuations is conserved through the flame [64].

6.6 Transmitted and Reflected Waves through an ideal Compressor: the enthalpy jump case

In the previous two sections, the focus was on the acoustic response of ducts due to:

- a change in the mean flow due to variations of section area: the nozzle case.
- a change in the mean flow due to an entropy jump : the 1D flame case.

The purpose of this section is to focus on the acoustic response of a system when the changes in the mean flow are due to enthalpy jumps. The case to study here is then an ideal compressor. The first step when modeling a compressor is to consider it as an isentropic element that creates a difference in both the total pressure and the kinetic energy in the flow, i.e., an element that exerts a work on the flow by changing its total enthalpy. The case considers a constant section duct (as in the 1D flame case) with a jump of total enthalpy at the middle. This is represented in Fig. (6.10)

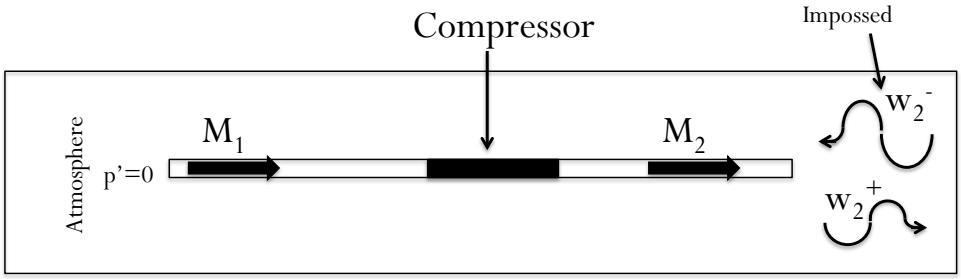

Figure 6.10: compressor

In this configuration an upstream acoustic wave w_2^- is imposed at the outlet while a Dirichlet acoustic condition is imposed at the inlet ($p' = 0$). This analytical/numerical setup is a crude representation of the inlet air circuit and compressor of an aeronautical engine. The acoustic waves, produced in the combustion chamber, travel upstream through the compressor until reaching the atmosphere which is considered as a totally reflecting acoustic condition ($p' = 0$ $\rightarrow R = 1$ with a phase $\phi = \pi$). As done before, this study is carried out both analytically and numerically (SNozzle).

6.6.1 Building the linear system of equations for the analytical solution

Equation (6.22) is the momentum equation of the 1D LEE for compact systems. The influence of the compressor into the system is accounted by the term $\hat{\mathcal{F}}$. Nevertheless, the most practical characterization of a compressor in a 1D system is simply by its total pressure ratio

$\pi_c = p_{t,2}/p_{t,1}$ where the indices [1] and [2] represent the flow upstream and downstream of the compressor respectively. It is then useful to redefine Eq. (6.13) as function of the parameter π_c.

$$\mathcal{F} = (\rho u^2)\Big|_1^2 + p\Big|_1^2 + \int_{x_1}^{x_2} \frac{\partial}{\partial t}(\rho u)\, dx \tag{6.49}$$

$$\mathcal{F} = \Delta p_t + \Delta e_k + \int_{x_1}^{x_2} \frac{\partial}{\partial t}(\rho u)\, dx \tag{6.50}$$

where $p_t = p + \rho u^2/2$ and $e_k = \rho u^2/2$. From Eq. (6.50) it is observed that the compressor $\mathcal{F}$ acts as an element that exerts a change in the total pressure p_t of the flow as well as in its fluctuating kinetic energy e_k. The parameter π_c is now inserted into the expression leading to

$$\mathcal{F} = p_{t1}(\pi_c - 1) + \Delta e_k + \int_{x_1}^{x_2} \frac{\partial}{\partial t}(\rho u)\, dx \tag{6.51}$$

Equation (6.51) is now linearized and expressed in the frequency domain. It yields

$$\widehat{\mathcal{F}} = \bar{p}_t \hat{\pi}_c + \hat{p}_{t,1}(\bar{\pi}_c - 1) + \Delta \hat{e}_k - \boldsymbol{i}\omega \int_{x_1}^{x_2} (\bar{\rho}\hat{u} + \hat{u}\hat{\rho})\, dx \tag{6.52}$$

where $\hat{e}_k = \hat{\rho}\bar{u}^2/2 + \bar{\rho}\bar{u}\hat{u}$ and $\hat{p}_t = \hat{p} + \hat{\rho}\bar{u}^2/2 + \bar{\rho}\bar{u}\hat{u}$. For a compact system the integral can be neglected and Eq. (6.52) results in

$$\hat{\mathcal{F}} = \bar{p}_t \hat{\pi}_c + \hat{p}_{t,1}(\bar{\pi}_c - 1) + \Delta \hat{e}_k \tag{6.53}$$

In Appendix A, it is shown that π_c' is a complex term that depends mainly on the mean and fluctuation value of the enthalpy both upstream and downstream of the compressor. Neglecting this term might be an strong assumption. The conditions of a compressor such that $\pi_c' \approx 0$ are discussed in Appendix A. Nevertheless, it is practical as a first approximation and it is useful to see the influence of the mean value of the total pressure ratio $\bar{\pi}_c$. After this assumption, the momentum equation (Eq. 6.22) becomes

$$\hat{p}_{t,1}\bar{\pi}_c = \hat{p}_{t,2} \tag{6.54}$$

Finally, the system of equations to resolve is expressed as function of the Mach Number $\bar{\mathcal{M}}$. The continuity equation (Eq. 6.31) and the momentum equation (Eq. 6.54) read

$$(1+\bar{\mathcal{M}}_1)/\bar{c}_1 A_1 - (1-\bar{M}_1)/\bar{c}_1 B_1 = (1+\bar{\mathcal{M}}_2)/\bar{c}_2 A_2 - (1-\bar{\mathcal{M}}_2)/\bar{c}_2 B_2 \tag{6.55}$$

$$\bar{\pi}_c b_1 A_1 + \bar{\pi}_c b_2 B_1 = b_3 A_2 + b_4 B_2 \tag{6.56}$$

with $b_1 = \left(1+0.5\bar{\mathcal{M}}_1^2+\bar{\mathcal{M}}_1\right)$, $b_2 = \left(1+0.5\bar{\mathcal{M}}_1^2-\bar{\mathcal{M}}_1\right)$, $b_3 = \left(1+0.5\bar{\mathcal{M}}_2^2+\bar{\mathcal{M}}_2\right)$ and $b_4 = \left(1+0.5\bar{\mathcal{M}}_2^2-\bar{\mathcal{M}}_2\right)$

In addition the acoustic condition at the inlet ($\hat{p}=0$) must be taken into account. This is done simple by doing $A_1 = B_1 e^{i\pi} = -B_1$. The coefficient B_2 which is related to the forced wave at the outlet must be given by the user. The system is resolved then to find the values of A_1, B_1 and A_2.

6.6.2 The mean flow in SNozzle

The main effect of a compressor is to add energy to the flow by increasing its total pressure $\bar{p}_t$. A typical profile of $\bar{p}_t$ corresponding to a compressor of thickness δ_c is shown in Fig. 6.11(a). This jump of total pressure is built from the following hyperbolic tangent function

$$\bar{p}_t = \bar{p}_{t1} + 0.5\bar{p}_{t1}\left(\bar{\pi}_c - 1\right)\left[1+\tanh\left(\frac{k(x-x_m)}{x_m - x_{ups}}\right)\right] \tag{6.57}$$

which satisfies the isentropic expression:

$$\bar{\pi}_c = \frac{\bar{p}_{t2}}{\bar{p}_{t1}} = \left(\frac{\bar{T}_{t2}}{\bar{T}_{t1}}\right)^{\gamma/(\gamma-1)} \tag{6.58}$$

The subindices [1] [2] stand for upstream and downstream of the compressor respectively. The Mach number profile $\bar{\mathcal{M}}$ for the case in which $\bar{\mathcal{M}}_2 = 0.025$ is shown in Fig. 6.11(b).

All mean quantities satisfy the Euler equations for steady and isentropic flows. Mean profiles of pressure, velocity, density and temperature are shown in Figs. 6.12 and 6.13 for the case in which $\bar{\pi}_c = 2$ and $\bar{\mathcal{M}}_2 = 0.025$.

6.6.3 Introducing π_c in the momentum equation

Let us recall the momentum equation of the Quasi-1D LEE system. It reads

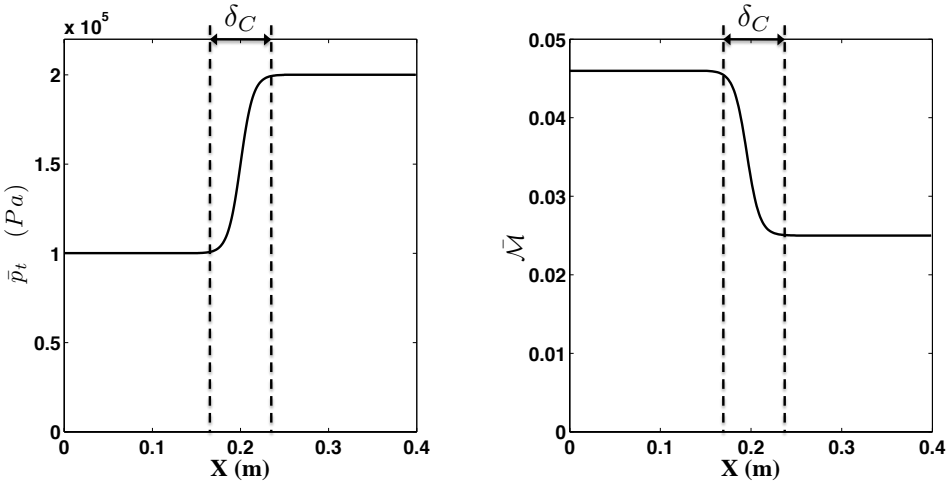

(a) Total Pressure $\bar{p}_t$. $\bar{\pi}_c = 2$ (b) Mach number $\bar{\mathcal{M}}$

Figure 6.11: Mean Flow. Typical Profiles

.

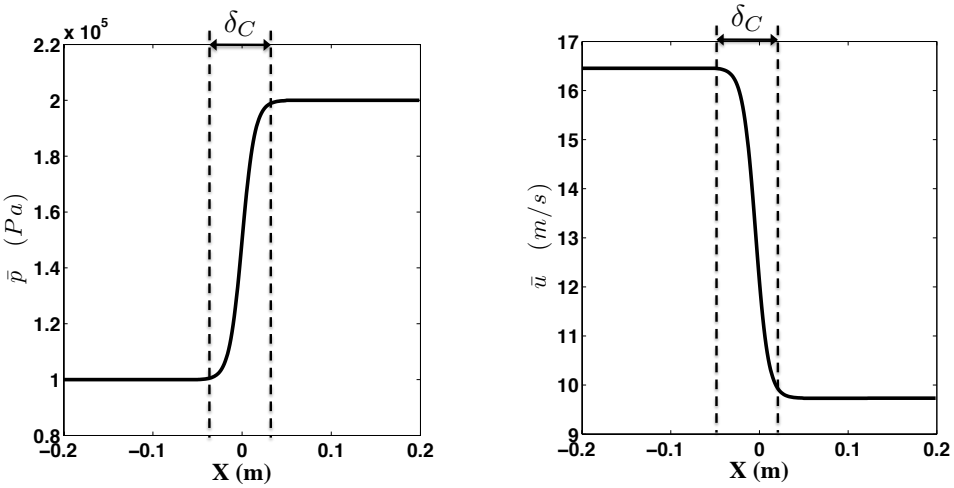

(a) Mean pressure (b) Mean velocity

Figure 6.12: Typical Profiles

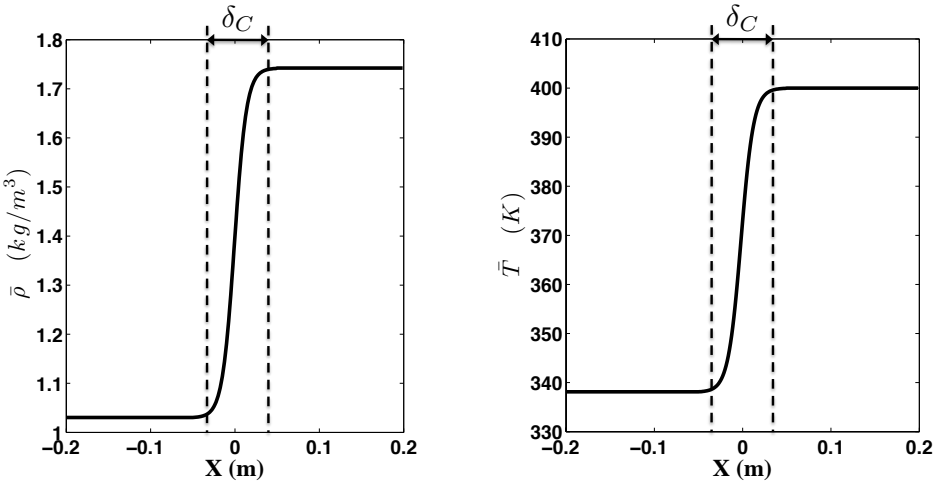

(a) Mean density (b) Mean temperature

Figure 6.13: Typical Profiles

$$\left(\frac{1}{\bar{\rho}}\frac{\partial \bar{c}^2}{\partial x}+\frac{\bar{u}}{\bar{\rho}}\frac{\partial \bar{u}}{\partial x}+\frac{\bar{c}^2}{\bar{\rho}}\frac{\partial}{\partial x}\right)\hat{\rho}+\left(\frac{\partial \bar{u}}{\partial x}+\bar{u}\frac{\partial}{\partial x}\right)\hat{u}+(\gamma-1)\bar{T}\left(\frac{1}{\bar{p}}\frac{\partial \bar{p}}{\partial x}+\frac{\partial}{\partial x}\right)\hat{s}-j\omega\hat{u}-\widehat{F}=0 \quad (6.59)$$

From Eq. (6.13), it is known that $\mathcal{F}(x)=\int F\,dx$, or in other words $F=\frac{\partial \mathcal{F}}{\partial x}$, where $\mathcal{F}$ is given by Eq. (6.52). Since in the Quasi-1D LEE $\mathcal{F}$ is function of x, Eq. (6.50) can be re-stated as

$$\mathcal{F}(x)=\Delta p_t+\Delta e_k+\int\frac{\partial}{\partial t}\left(\rho(x)u(x)\right)dx \quad (6.60)$$

$$\mathcal{F}(x)=p_t(x)-p_{t,1}+e_k(x)-e_{k,1}+\int\frac{\partial}{\partial t}\left(\rho(x)u(x)\right)dx \quad (6.61)$$

$$F(x)=\frac{\partial}{\partial x}\left[p_t(x)+e_k(x)\right]+\frac{\partial}{\partial t}\left[\rho(x)u(x)\right] \quad (6.62)$$

In seek of readiness, the argument (x) is dropped. Linearizing and considering harmonic oscillations:

$$\hat{F}=\frac{\partial \hat{p}_t}{\partial x}+\frac{\partial}{\partial x}\left(\bar{\rho}\bar{u}\hat{u}+\frac{1}{2}\hat{\rho}\bar{u}^2\right)-i\omega\left(\bar{\rho}\hat{u}+\hat{\rho}\bar{u}\right) \quad (6.63)$$

In order to allow a fair comparison with the analytical solution (section 6.6.1), it is necessary that the computation is made in such a way that $\pi_c'=0$. This means that

$$\frac{\hat{p}_t}{\hat{p}_{t,1}} = \frac{\bar{p}_t}{\bar{p}_{t,1}} \quad \text{thus} \quad \frac{\partial \hat{p}_t}{\partial x} = \frac{\hat{p}_{t,1}}{\bar{p}_{t,1}} \frac{\partial \bar{p}_t}{\partial x} \tag{6.64}$$

The profile of $\hat{p}_t$ is given by a smooth hyperbolic tangent relation as seen in Fig. 6.14. From Eq. (6.64), the $(\partial \hat{p}_t / \partial x)$ term in Eq. (6.63) must be written as

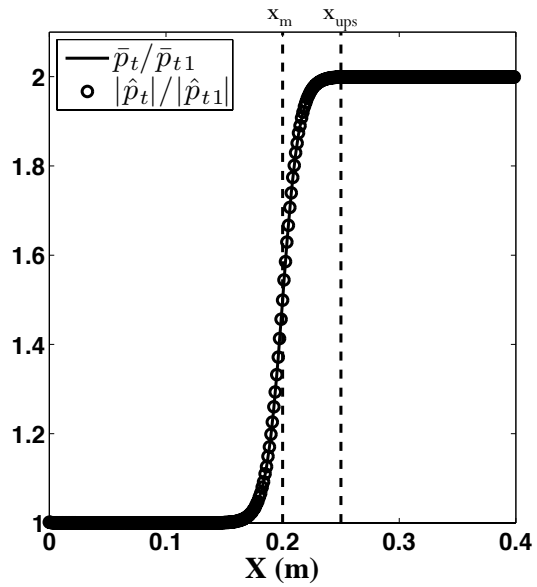

Figure 6.14: Mean and Fluctuation profiles of total pressure

$$\frac{\partial \hat{p}_t}{\partial x} = \hat{p}_{t1} f(x, \bar{\pi}_c) \quad \text{with} \tag{6.65}$$

$$f(x, \pi_c) = 0.5\,(\bar{\pi}_c - 1) \left[1 - \tanh^2\left(\frac{k(x - x_m)}{x_m - x_{ups}}\right)\right] \left[\frac{k}{x_m - x_{ups}}\right] \tag{6.66}$$

6.6.4 Results

Two different cases are considered, corresponding to two different values of $\pi_c = \bar{p}_{t2}/\bar{p}_{t1}$. The value of the reflection coefficient $R = w_2^+ / w_2^-$ is computed by using both the analytical and the numerical approach (SNozzle). In order to observe the influence of the forcing frequency on the values of R, results are plotted as a function of an adimensional frequency.

$$\Omega = fL/\bar{c}_2 \tag{6.67}$$

where L represents the length of the compressor and $\bar{c}_2$ the velocity of sound at the outlet. The

values of R computed by SNozzle match the values of R given analytically when the length wave is extremely large compared to L ($\Omega \approx 0$). This is shown in Figs (6.15) and (6.16) .

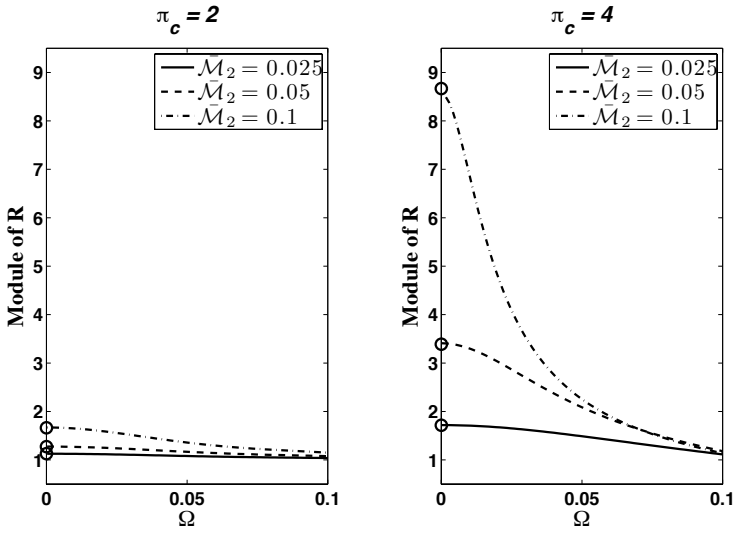

(a) (b)

Figure 6.15: Modulus of the Reflection Coefficient. Lines represent SNozzle solutions. Symbols (○) stands for Analytical results

.

From Fig. (6.15) it is observed that, for a given $\bar{\pi}_c$, lower values of $\bar{\mathcal{M}}_2$ lead to smaller values of $|R|$. For high values of $\bar{\pi}_c$, the magnitude or the reflection coefficient increases significantly mainly for low forcing frequencies. It should be clear then that the inclusion of an enthalpy jump is crucial for the estimation of acoustic boundaries to impose at the edge of a combustion chamber within an aeronautical engine.

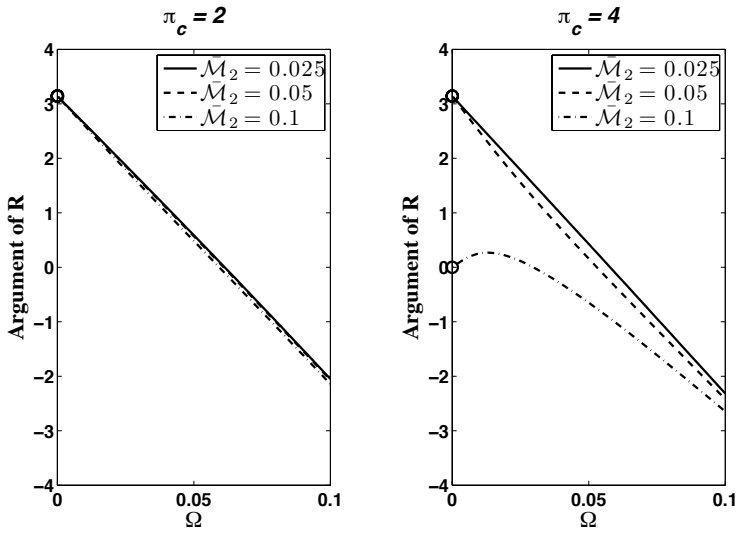

(a) (b)

Figure 6.16: Argument of the Reflection Coefficient. Lines represent SNozzle solutions. Symbols (○) stands for Analytical results

.

7

Computation of the Reflection Coefficient on the Inlet air circuit of an Helicopter combustor chamber

Contents

7.1 Motivation

The numerical tool described in Chapter 6 can be used to compute the equivalent impedance of any airline with compressor or turbine. It is applied in this chapter to an actual aeroengine which is know from experiments to oscillate at 250 Hz for certain operating conditions. Combustion instabilities emerge due to a coupling between the unsteady heat released by the flame and the acoustic field of the chamber. In order to characterize this unstable mode, it is important to know whether it corresponds to an acoustic mode of the combustor. For this purpose, a Helmholtz solver [56, 89, 62] is used to compute the different acoustic modes of this system. At

first, simplified acoustic boundary conditions are imposed at both inlet and outlet (u'=0). They can be considered as fully reflecting conditions as if they were a rigid wall. In a second step, the impedance computed by the SNozzle tool for the inlet of the combustion chamber is used instead of the simple $u' = 0$ condition.

When the simple condition (u'=0) is used, the Helmholtz solver computes an acoustic mode around 500Hz which is considered a value far from what is observed in experiments. It is well known that the resonant modes of a system are fully dependent on the acoustic boundary conditions used [56]. A viewpoint often put forward is that the bad prediction of the resonant frequency by the Helmholtz solver is probably due to the crude treatment of acoustics at both the inlet and the outlet. In the combustion chamber studied, the flow is shocked at the outlet. In this case, and for low frequencies, it is known that the reflection coefficient can be considered close to that of a rigid wall. On the other hand, the same cannot be stated for the Inlet. Acoustic properties of the combustion chamber inlet are fully dependent on the upstream configuration of the combustor. The question that is investigated in this chapter is then to know whether using a more accurate description of the inlet impedance leads to large changes in the mode computed by the Helmholtz solver, hopefully in better agreement with the experiments. This exercise also serves as an illustration of the capability of the SNozzle tool to represent complex intakes.

Aeronautical engines are complex systems in which the combustion chamber is present just in a tiny region after the compressor stages. From the point of view of the combustor, the upstream region is then composed by several compression stages in which acoustics depends on enthalpy jumps (compressors), the intake acoustic condition (usually related to the atmosphere) and the geometry of the entire system. Figure (7.1) shows the intake duct of a typical helicopter combustor.

SNozzle has been developed for computing the acoustic response of a quasi-1D system due to an acoustic perturbation. This numerical tool considers non-negligible Mach Numbers as well as total pressure jumps in the mean flow. SNozzle is then considered appropriate to evaluate the acoustic impedance at a specific transversal plane of systems such as of the present aeronautical airline. Once the acoustic impedance is evaluated, this acoustic condition can be imposed in the Helmholtz solver. Resonant frequencies closer to the experimental measurements are expected. Insignificant changes in the computed mode would support the idea that the disagreement between the computed and observed mode is not due to errors in the inlet impedance description.

7.2 Mean parameters of the Intake Duct

SNozzle needs two thermodynamical parameters (Temperature and Pressure) , the Mach number at the outlet (see Fig. 7.1) and the Section Area as a function of the curvilinear axis (Fig. 7.2). The position and the total pressure jump due to the compressors is also needed in order to

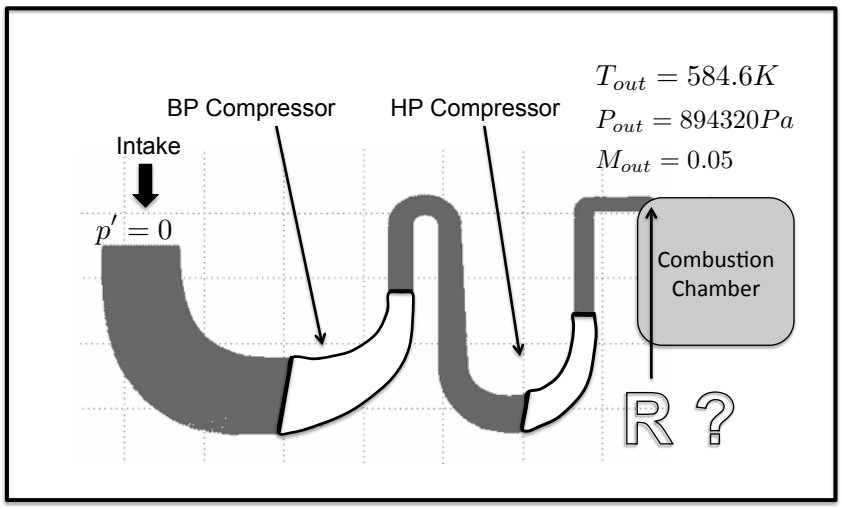

Figure 7.1: Airline Configuration

characterize the mean flow.

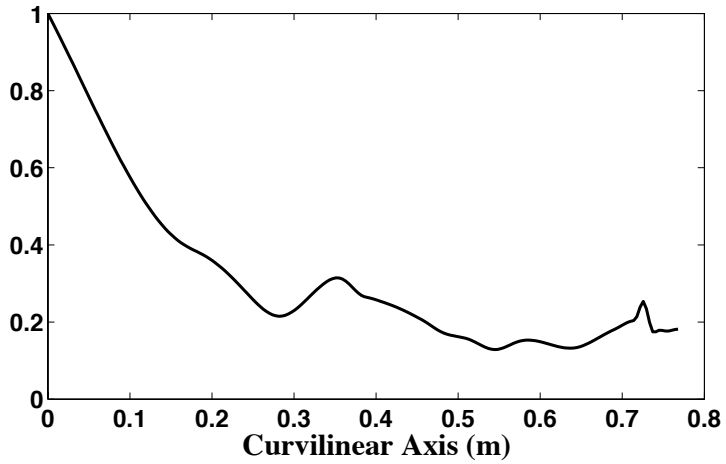

Figure 7.2: Adimensional section area of the aeroengine airline

Figure (7.3) show the mean field of total pressure and total temperature computed by SNozzle. In real engines, this pressure jump is not performed isentropically. As a consequence the evaluation of a polytropic coefficient η_p is essential.

$$\frac{\bar{p}_{t2}}{\bar{p}_{t1}} = \left(\frac{\bar{T}_{t2}}{\bar{T}_{t1}}\right)^{\gamma\eta_p/(\gamma-1)} \tag{7.1}$$

In the present helicopter system, this coefficient is close to 0.87 for the first compressor stage and $\eta_p = 0.9$ for the second one. The mean field can be, as a result, be modeled properly in the computational analysis. This is shown in Fig. 7.3.

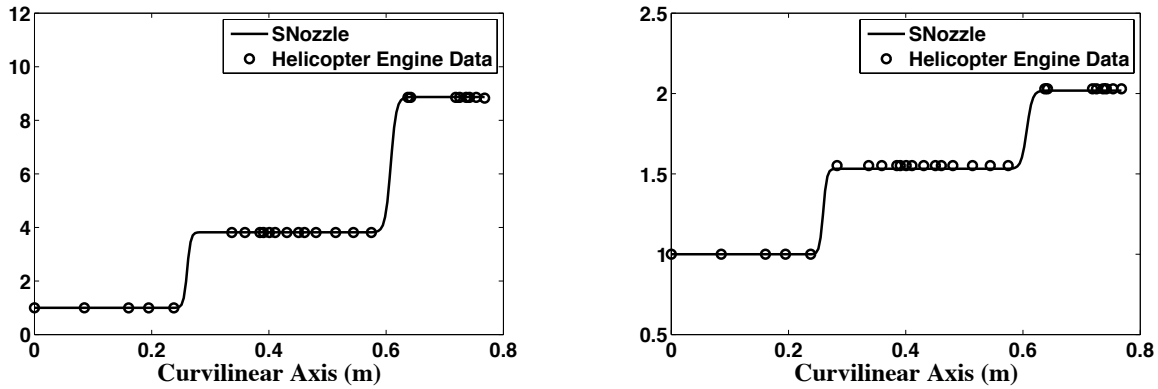

a) Normalized Total Pressure b) Normalized Total Temperature

Figure 7.3: Total Pressure and Total Temperature profiles

7.3 Acoustic Evaluation

The reflection coefficient $R = w_2^+ / w_2^-$ is computed for the outlet section of the intake duct which corresponds to the inlet of the helicopter combustion chamber. It is evaluated for two different cases:

- **CASE A → Airline with total pressure jump:** The Evaluation of acoustics is done for the geometry including the compressors. It means that a total pressure jump is imposed to the mean flow.

- **CASE B → Airline without total pressure jump:** In order to assess the actual influence of the compressors on the acoustics of the system, the acoustic response of the intake is done without any total pressure jump. In fact, this is how the reflection coefficient was used to be computed [41] before the development of the Snozzle tool.

It is noticeable that the presence of the compressors increases the amplitude of the reflected wave (Fig. 7.4 a). When no total pressure jump is imposed, the amplitude of the reflected wave is similar to the forced one, while is twice as large when the work done by the compressor is accounted for. The phase of R (Fig. 7.4 b) also changes when the compressors are added to the system.

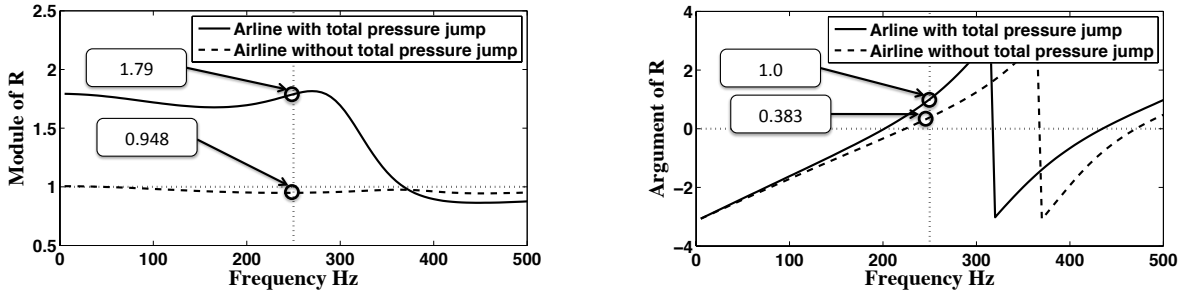

(a) (b)

Figure 7.4: Reflection Coefficient

7.4 Helmholtz Solver Computation

AVSP [56, 89, 62] is the Helmholtz solver used to find the acoustic modes of the aero-engine of interest. The acoustic information given to AVSP for describing the boundary conditions is expressed in terms of the acoustic admittance Y at the inlet of the chamber. It is related to the reflection coefficient as follows

$$Y = \frac{R-1}{R+1} \tag{7.2}$$

and its evolution with frequency is diplayed in Fig. 7.5

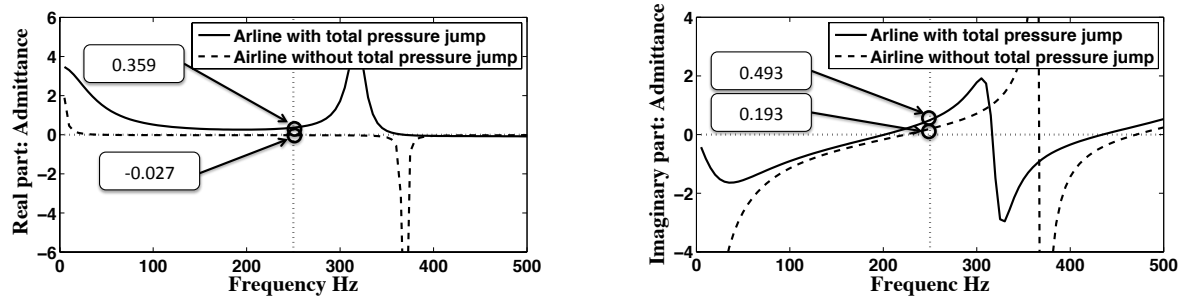

Figure 7.5: Acoustic Admittance

AVSP computes the resonant modes of the combustor accounting for these values of Y. Table 7.1 displays the frequency of the first computed eigenmode.

From table 7.1, it is clear that no variations are found on the resonant frequency of the aero-engine. This frequency corresponds to 508 Hz which also the one when the Neumann condition $u' = 0$ is applied at the inlet. The Modulus and the Argument of the pressure are displayed in Fig. 7.6.

It is interesting then to analyze in which cases, the compressor would change the resonant

INLET B.C	Eigen-frequency (real part)	Eigen-frequency IM (imaginary part)
$u' = 0$	507.9 Hz	-2.3 Hz
Airline with total pressure jump	508.8 Hz	-4.4Hz
Airline without total pressure jump	508.5 Hz	-4.6 Hz

Table 7.1: Eigen-Frequencies found by AVSP. Ardiden Combustor

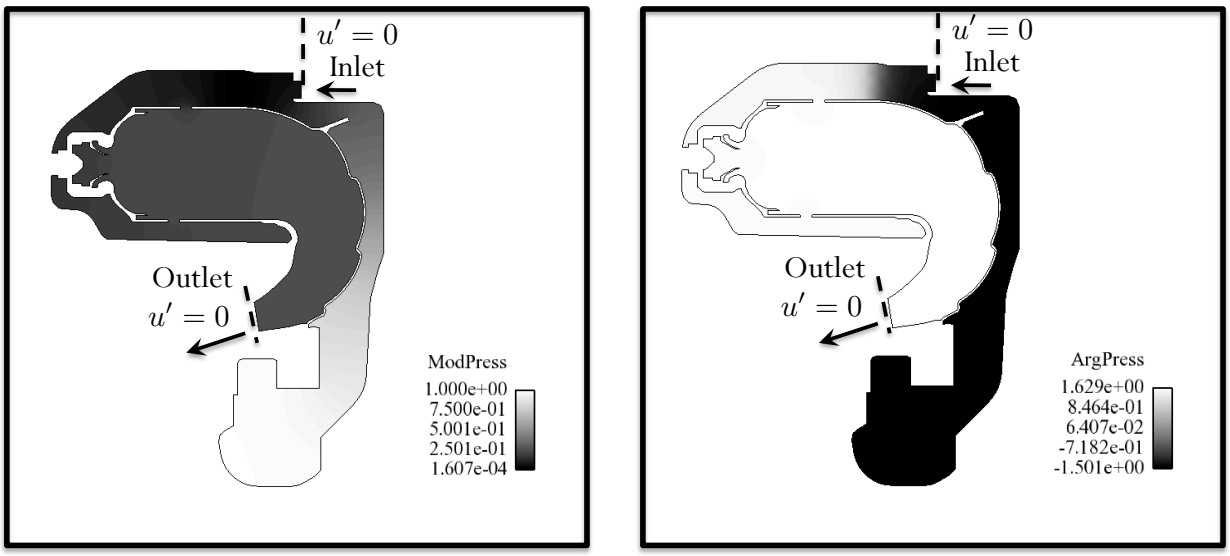

(a) (b)

Figure 7.6: Acoustic Mode of the Aeroengine combustor. 507.9 Hz

frequency of the combustor. Figure 7.7 shows the correspondance between $|R|$,$Arg(R)$ respect to $real(Y), imag(Y)$. The Neumann Condition $u' = 0$ corresponds to a case in which $|R| = 1$ and $Arg(R) = 0$, which in turn is equivalent to $real(Y) = 0$ and $imag(R) = 0$.

Changing the phase of R while maintaining $|R| = 1$ is equivalent to change $imag(Y)$ while keeping $real(Y) = 0$. On other hand, if $Arg(R)$ is fixed to zero but $|R|$ changes, it corresponds to a variation of $real(Y)$ maintaining $imag(Y) = 0$. By doing so, it is possible to compute the correspondant resonant frequencies for the following hypothetical and extreme cases:

- The compressor does not change the phase of the acoustic waves but only their amplitude ratio, i.e., $Arg(R) = 0$ and $|R|$ varies from 0.1 to 1000.
- The compressor does not change the amplitude of the waves but only produce a phase shift, i.e., $|R| = 1$ and $Arg(R)$ varies from $-\pi$ to π.

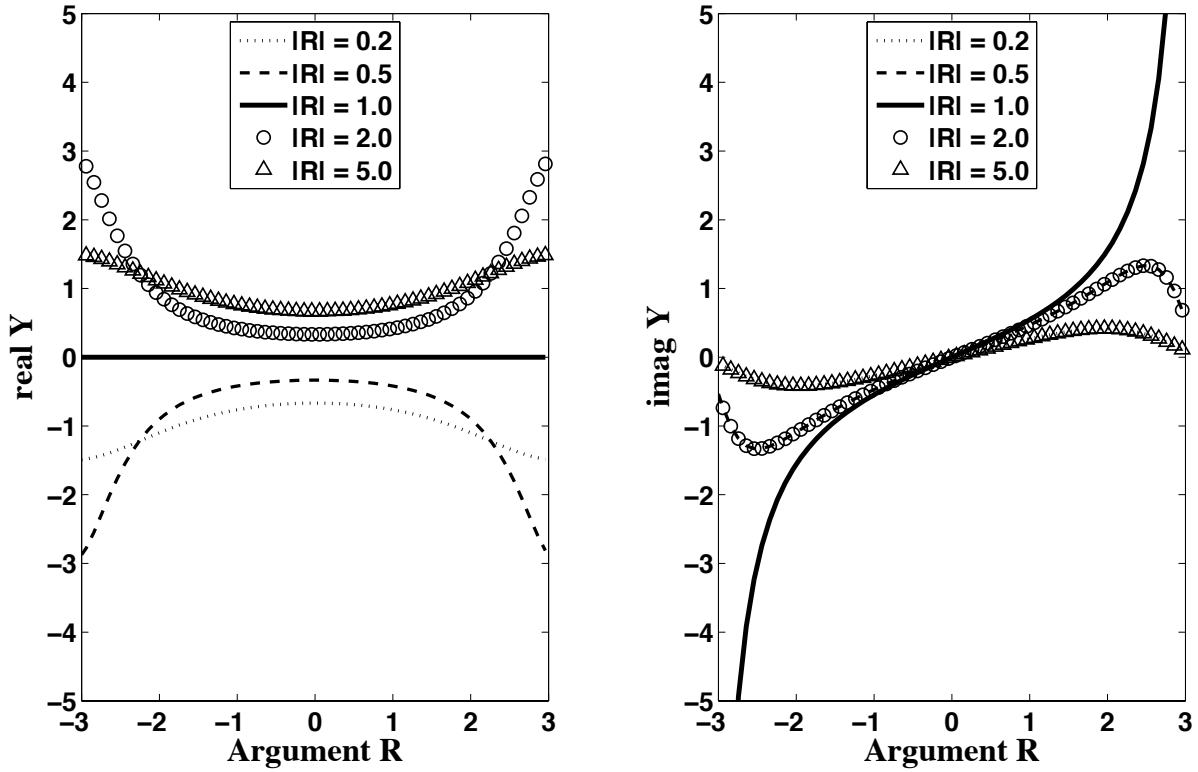

(a) (b)

Figure 7.7: Admittance Vs Reflection Coefficient

From Fig. 7.8 it is understood that a considerable variation is produced on the resonant frequency when the phase is shift at the inlet of the combustor. This Frequency can vary by

$100Hz$ when modifying the phase from $-\pi$ to π. On the contrary, varying the modulus of the reflection coefficient $|R|$ does not imply a significative change in the Eigen-Frequency of the combustor. Given the very large variations of $|R|$ and $arg(R)$ considered in Fig. 7.8, the results also demonstrate that the large disagreement between the computed (500 Hz) and observed (250 Hz) mode for this combustion chamber cannot be only due to a wrong representation of the inlet impedance. The results obtained from SNozzle and reported in table 7.1 suggest that improving the inlet condition has in fact no effect on the result.

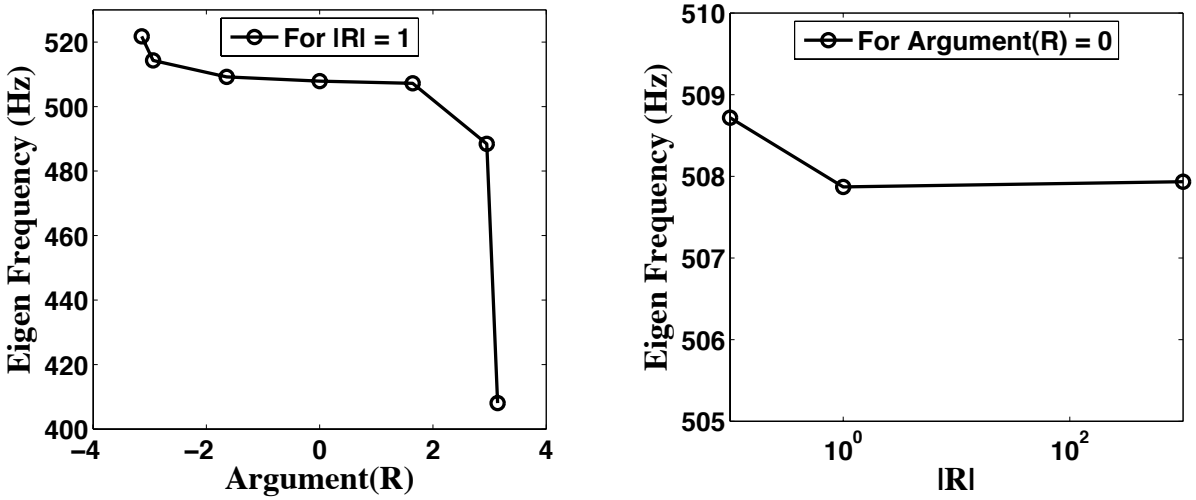

(a) (b)

Figure 7.8: Eigen Frequency Vs Reflection Coefficient

7.5 Conclusions

The approach used to model the compressor as an element that perturbs the acoustics of the airline might be still too approximative. The inclusion of $\pi_c' \neq 0$ into the compressor acoustic model might contribute to a stronger variation on both $|R|$ and $Arg(R)$ at the inlet of the combustor. Nevertheless, it has been seen that the lowest possible eigen-frequency in the Aero-engine combustor corresponds to a value around 410 Hz, which is still too far from what is found in experiments: 250 Hz.

It is highly probable then that the resonant frequency found experimentally does not correspond to an acoustic mode of the combustor. This frequency might be linked instead to a combustion instability known as 'rumble', which is due to a coupling between entropy waves convected at the mean flow and the acoustic waves generated at the high pressure distributor. In order to verify if this instability mechanism is present, it is necessary to use an acoustic code that accounts for the presence of a mean flow. i.e., to consider the complete set of Linearized Euler Equations instead of the Helmholtz equation.

Bibliography

[1] AGARWAL, A., MORRIS, P. J., AND MANI, R. Calculation of sound propagation in nonuniform flows: suppression of instability waves. *AIAA Journal 42* (2004), 80–88.

[2] ARNOLDI, W. The principle of minimized iteration in the solution of the matrix eigenproblem. *Quart. Appl. Math. 9* (1951), 17–29.

[3] AVBP. Avbp code: www.cerfacs.fr/cfd/avbp_code.php and www.cerfacs.fr/cfd/cfdpublications.html.

[4] BAILLY, C., BOGEY, C., AND CANDEL, S. Modelling of sound generation by turbulent reacting flows. *International Journal of Aeroacoustics 9* (2009), 461–489.

[5] BAILLY, C., AND JUVAND, D. Numerical solution of acoustic propagation problems using linearized euler equations. *AIAA Journal 38* (2000), 22–29.

[6] BAILLY, C., AND JUVÉ, D. A stochastic approach to compute subsonic noise using linearized euler's equation. *AIAA Journal* (1999).

[7] BÉCHARA, W., BAILLY, C., LAFON, P., AND CANDEL, S. Stochastic approach to noise modeling for free turbulent flows. *AIAA Journal 32*, 3 (1994), 455–463.

[8] BODONY, D. J., AND LELE, S. K. On the current status of jet noise predictions using large-eddy simulation. *AIAA Journal 46* (2008), 364–380.

[9] BRAGG, S. Combustion noise. *J. Inst. of Fuel 36* (1963), 12–16.

[10] BUI, T. P., SCHRÖDER, W., AND MEINKE, M. Acoustic perturbation equations for reacting flows to compute combustion noise. *International Journal of Aeroacoustics 6* (2007), 335–355.

[11] BUTLER, T. D., AND O'ROURKE, P. J. A numerical method for two-dimensional unsteady reacting flows. In *16th Symp. (Int.) on Combustion* (1977), The Combustion Institute, pp. 1503–1515.

[12] CANDEL, S. *Analytical Studies of Some Acoustic Problems of Jet Engines*. PhD thesis, California Institute of Technology, Pasadena, California, 1972.

[13] CANDEL, S., DUROX, D., DUCRUIX, S., BIRBAUD, A. L., AND NOIRAY, N. Flame dynamics and combustion noise: progress and challenges. *International Journal of Aeroacoustics 8* (2009), 1–56.

[14] CHIU, H. . H., AND SUMMERFIELD, M. Theory of combustion noise. *Acta Astronautica 1* (1974), 967–984.

[15] CHRISTOPHE, J., AND MOREAU, S. Les of the trailing-edge flow and noise of a controlled-diffusion airfoil at high angle of attack. In *Proceedings of the Summer Program 2008* (Center for Turbulence Research, NASA AMES, Stanford University, USA, 2008), pp. 1–12.

[16] CLAVIN, P., AND SIGGIA, E. D. Turbulent premixed flames and sound generation. *Combust. Sci. Tech. 78* (1991), 147–155.

[17] COLIN, O., DUCROS, F., VEYNANTE, D., AND POINSOT, T. A thickened flame model for large eddy simulations of turbulent premixed combustion. *Phys. Fluids 12*, 7 (2000), 1843–1863.

[18] CROCCO, L. Aspects of combustion instability in liquid propellant rocket motors. part i. *J. American Rocket Society 21* (1951), 163–178.

[19] CROCCO, L. Aspects of combustion instability in liquid propellant rocket motors. part ii. *J. American Rocket Society 22* (1952), 77–16.

[20] CURLE, N. The influence of solid boundaries upon aerodynamic sound. *Proc. R. Soc. Lond. Series A* (1955).

[21] DI MARE, F., JONES, W., AND MENZIES, K. Large-eddy simulation of a model gas turbine combustor. *Combust. Flame 137* (2004), 278–294.

[22] DOWLING, A. P. The calculation of thermoacoustic oscillations. *J. Sound Vib. 180*, 4 (1995), 557–581.

[23] ECKSTEIN, J., FREITAG, E., HIRSCH, C., AND SATTELMAYER, T. Experimental study on the role of entropy waves on low-frequency oscillations for a diffusion burner. In *Asme Turbo Expo.* (Viena, Austria, 2004).

[24] EWERT, R., MEINKE, M., AND SCHRÖDER, W. Aeroacoustic source terms for the linearized euler equations. *AIAA Journal* (2000), 2000–2046.

[25] EWERT, R., MEINKE, M., AND SCHRÖDER, W. Comparison of source term formulations for a hybrid cfd/caa method. *AIAA Journal* (2001), 2001–2200.

[26] EWERT, R., AND SCHRÖDER, W. Acoustic perturbation equations based on flow decomposition via source filtering. *J. Comput. Phys. 188* (2003), 365–398.

[27] FARASSAT, F. Linear acoustics formulas for calculation of rotating blade noise. *AIAA Journal 19*, 9 (1981), 1122–1130.

[28] FLEMMING, F., SADIKI, A., AND JANICKA, J. Investigation of combustion noise using a les/caa hybrid approach. In *Proc. Combust. Inst.* (2007), vol. 31, pp. 3189–3196.

[29] FRAYSSÉ, V., AND ET AL. A set of gmres routines for real and complex arithmetics on high performance computers. Tech. rep., CERFACS, 2003.

[30] FRAYSSÉ, V., GIRAUD, L., AND GRATTON, S. A set of flexible gmres routines for real and complex arithmetics on high performance computers. Tech. rep., CERFACS, 2007.

[31] GOLDSTEIN, M. E. *Aeroacoustics*. McGraw-Hill, New York, 1976.

[32] HASSAN, H. Scaling of combustion generated noise. *J. Fluid Mech. 49* (1974), 445–453.

[33] HELLEY, P. L. *Etude théorique et expérimentale des intabilités de combustion et de leur contrôle dans un bruleur laminaire prémélangé*. PhD thesis, Ecole Centrale Paris, 1994.

[34] HURLE, I. R., PRICE, R. B., SUDGEN, T. M., AND THOMAS, A. Sound emission from open turbulent premixed flames. *Proc. R. Soc. Lond. 303* (1968), 409–427.

[35] ICAO. Growth air traffic projected to continue to 2025: www.icao.int/icao/en/nr/2007/pio200708_e.pdf, 2007.

[36] IHME, M., PITSCH, H., AND BODONY, H. Radiation of noise in turbulent flames. *Proc. Combust. Inst. 32* (2009), 1545–1554.

[37] KAUFMANN, A., NICOUD, F., AND POINSOT, T. Flow forcing techniques for numerical simulation of combustion instabilities. *Combust. Flame 131* (2002), 371–385.

[38] KLEIN, S. A. *On the acoustics of turbulent non-premixed flames*. PhD thesis, Universit de Twente, 2000.

[39] KOTAKE, S. On combustion noise related to chemical reactions. *J. Sound Vib. 42* (1975), 399–410.

[40] KOTAKE, S., AND HATTA, K. On the noise of diffusion flames. *Japan Society of Mechanical Engineers Journal* (1965), 211–219.

[41] LAMARQUE, N., AND POINSOT, T. Boundary conditions fo acoustic eigenmode computations in gas turbine combustion chambers. *AIAA Journal 46*, 9 (2008), 2282–2292.

[42] LAMARQUE, N., PORTA, M., NICOUD, F., AND POINSOT, T. On the stability and dissipation of wall boundary conditions for compressible flows. *Int. J. Numer. Meth. Fluids 62* (2010), 1134–1154.

[43] LAMRAOUI, A., AND ET AL. Acoustic reconstruction of the fuel and air feeding line impedances in a swirled burner during combustion instabilities. In *3rd European Conference for Aerospace Sciences EUCASS* (2009).

[44] LAMRAOUI, A., RICHECOEUR, F., SCHULLER, T., AND DUCRUIX, S. Methodology for on the fly acoustic characterization of the feedings lines impedances in a turbulent swirled combustor. In *Proceedings of ASME Turbo Expo 2010: Power for Land, Sea and Air* (2010).

[45] LAWSON, C. L., AND HANSON, R. J. *Solving Least Squares Problems*. SIAM Classics in Applied Mechanics, 1974.

[46] LEROYER, P. Airside study of charles de gaulle airport. Tech. rep., Airside Organization. Traffic Growth and Risks of Congestion. MIT, 2004.

[47] LEYKO, M., NICOUD, F., AND POINSOT, T. Comparison of direct and indirect combustion noise mechanisms in a model combustor. *AIAA Journal 47*, 11 (2009), 2709–2716.

[48] LIEUWEN, T., AND YANG, V. Combustion instabilities in gas turbine engines. operational experience, fundamental mechanisms and modeling. In *Prog. in Astronautics and Aeronautics AIAA* (2005), vol. 210.

[49] LIEUWEN, T., AND ZINN, B. T. The role of equivalence ratio oscillations in driving combustion instabilities in low nox gas turbines. *Proc. Combust. Inst. 27* (1998), 1809–1816.

[50] LIGHTHILL, M. J. On sound generated aerodynamically: I. general theory. *Proc. R. Soc. Lond. 211*, 1107 (1952), 564–587.

[51] LIGHTHILL, M. J. On sound generated aerodynamically: Ii. turbulence as a source of sound. *Proc. R. Soc. Lond. 222* (1954), 1–32.

[52] LILLEY, G. M. The generation and radiation of supersonic jet noise vol iv - theory of turbulence generated jet noise, noise radiation from upstream sources, and combustion noise. part ii: Generation of sound in a mixing region. Afapl-tr-72-53, Air Force Aero Propulsion Laboratory, 1972.

[53] LILLEY, G. M. On the noise from jets. Agard cp-131, 1974.

[54] LYRINTZIS, A. S. Integral acoustic methods: From the (cfd) near-field to the (acoustic) far-field. *International Journal of Aeroacoustics 2* (2003), 95–128.

[55] MARBLE, F. E., AND CANDEL, S. Acoustic disturbances from gas nonuniformities convected through a nozzle. *J. Sound Vib. 55* (1977), 225–243.

[56] MARTIN, C., BENOIT, L., SOMMERER, Y., NICOUD, F., AND POINSOT, T. Les and acoustic analysis of combustion instability in a staged turbulent swirled combustor. *AIAA Journal 44*, 4 (2006), 741–750.

[57] MENDEZ, S., AND NICOUD, F. Large eddy simulation of a bi-periodic turbulent flow with effusion. *J. Fluid Mech. 598* (2008), 27–65.

[58] MILLER, N. P., REINDEL, E. M., AND HORONJEFF, R. D. *Aircraft and airport noise prediction and control*. Handbook of Noise and Vibration Control. Malcolm J. Crocker, 2007.

[59] MOASE, W., BREAR, M., AND MANZIE, C. The forced response of chocked nozzles and supersonic diffusers. *J. Fluid Mech.* (2007).

[60] MOREAU, S., AND ROGER, M. Effect of airfoil aerodynamic loading on trailing-edge noise sources. *AIAA Journal 43*, 1 (2005), 41–52.

[61] MORFEY, C. L. Amplification of aerodynamic noise by convected flow inhomogeneities. *J. Sound Vib. 31* (1973), 391–397.

[62] NICOUD, F., BENOIT, L., AND SENSIAU, C. Acoustic modes in combustors with complex impedances and multidimensional active flames. *AIAA Journal 45* (2007), 426–441.

[63] NICOUD, F., AND POINSOT, T. Thermoacoustic instabilities: should the rayleigh criterion be extended to include entropy changes ? *Combust. Flame 142* (2005), 153–159.

[64] NICOUD, F., AND WIECZOREK, K. About the zero mach number assumption in the calculation of thermoacoustic instabilities. *International Journal of Spray and Combustion Dynamics 1* (2009), 67–112.

[65] OBERAI, A., ROKNALDIN, F., AND HUGHES, T. Computation of trailing-edge noise due to turbulent flow over an airfol. *AIAA Journal 40* (2002), 2206–2216.

[66] PHILLIPS, O. M. On the generation of sound by supersonic turbulent shear layers. *J. Fluid Mech. 9* (1960), 1–28.

[67] PIERCE, C. D., AND MOIN, P. Progress-variable approach for large eddy simulation of non-premixed turbulent combustion. *J. Fluid Mech. 504* (2004), 73–97.

[68] PITSCH, H. Large eddy simulation of turbulent combustion. *Ann. Rev. Fluid Mech. 38* (2006), 453–482.

[69] PITSCH, H., AND DE LA GENESTE, L. D. Large eddy simulation of premixed turbulent combustion using a level-set approach. *Proc. Combust. Inst. 29* (2002), 2001–2008.

[70] PITSCH, H., AND STEINER, H. Large eddy simulation of a turbulent piloted methane/air diffusion flame (sandia flame d). *Phys. Fluids 12* (2000), 2541–2554.

[71] POINSOT, T., AND CANDEL, S. Interactions between acoustics and combustion. In *Acoustics 88.* (1988).

[72] POINSOT, T., AND LELE, S. Boundary conditions for direct simulation of compressible viscous flows. *J. Comput. Phys. 101*, 1 (1992), 104–129.

[73] POINSOT, T., TROUVÉ, A., VEYNANTE, D., CANDEL, S., AND ESPOSITO, E. Vortex driven acoustically coupled combustion instabilities. *J. Fluid Mech. 177* (1987), 265–292.

[74] POINSOT, T., AND VEYNANTE, D. *Theoretical and numerical combustion*. R. T. Edwards, 2005.

[75] POPE, S. B. *Turbulent Flows*. Cambridge University Press., Cambridge, UK, 2000.

[76] PRICE, R., HURLE, I., AND SUDGEN, T. Optical studies of the generation of noise in turbulent flames. In *Twelf Symposium (International) on combustion.* (Pittsburg, 1968), The Combustion Institute,, pp. 1093–1102.

[77] RAO, P., AND MORRIS, P. Use of finite element methods in frequency domain aeroacoustics. *AIAA Journal 44* (2006), 1643–1652.

[78] RAYLEIGH, L. The explanation of certain acoustic phenomena. *Nature July 18* (1878), 319–321.

[79] ROGALLO, R. S., AND MOIN, P. Numerical simulation of turbulent flows. *Ann. Rev. Fluid Mech. 16* (1984), 99–137.

[80] ROGER, M. Aeroacoustics of wall-bounded flows. In *Lecture Series. March 9-13* (2009), Von Karman Institute for Fluid Dynamics.

[81] ROGERS, D. E., AND MARBLE, F. E. A mechanism for high frequency oscillations in ramjet combustors and afterburners. *Jet Propulsion 26* (1956), 456–462.

[82] ROUX, S., LARTIGUE, G., POINSOT, T., MEIER, U., AND BÉRAT, C. Studies of mean and unsteady flow in a swirled combustor using experiments, acoustic analysis and large-eddy simulations. *Combust. Flame 141* (2005), 40–54.

[83] SAAD, Y., AND SCHULTZ, M. Gmres: A generalized minimal residual algorithm for solving nonsymmetric linear systems. *SIAM J. Sci. Stat. Comput. 7*, 3 (1986), 856–869.

[84] SCHMITT, P., POINSOT, T., SCHUERMANS, B., AND GEIGLE, K. Large eddy simulation and experimental study of heat transfer, nitric oxide emissions and combustion instability in a swirled turbulent high pressure burner. *J. Fluid Mech. 570* (17-46), 17–46.

[85] SCHRAM, C. A boundary element extension of curle's analogy for non-compact geometries at low-mach numbers. *J. Sound Vib. 322*, 264-281 (200).

[86] SCHULLER, T. *Mécanismes de Couplage dans les Interactions Acoustique-Combustion*. Phd thesis, Ecole Centrale de Paris, 2003.

[87] SEARBY, G., AND ROCHWERGER, D. A parametric acoustic instability in premixed flames. *J. Fluid Mech. 231* (1991), 529–543.

[88] SELLE, L. *Simulation aux grandes échelles des interactions flamme-acoustique dans un écoulement vrillé*. Phd thesis, INP Toulouse, 2004.

[89] SELLE, L., BENOIT, L., POINSOT, T., NICOUD, F., AND KREBS, W. Joint use of compressible large-eddy simulation and helmholtz solvers for the analysis of rotating modes in an industrial swirled burner. *Combust. Flame 145*, 1-2 (2006), 194–205.

[90] SELLE, L., LARTIGUE, G., POINSOT, T., KOCH, R., SCHILDMACHER, K. U., KREBS, W., PRADE, B., KAUFMANN, P., AND VEYNANTE, D. Compressible large-eddy simulation of turbulent combustion in complex geometry on unstructured meshes. *Combust. Flame 137*, 4 (2004), 489–505.

[91] SELLE, L., NICOUD, F., AND POINSOT, T. The actual impedance of non-reflecting boundary conditions: implications for the computation of resonators. *AIAA Journal 42*, 5 (2004), 958–964.

[92] SENGISSEN, A. X., KAMPEN, J. F. V., HULS, R. A., STOFFELS, G. G. M., KOK, J. B. W., AND POINSOT, T. Les and experimental studies of cold and reacting flow in a swirled partially premixed burner with and without fuel modulation. *Combust. Flame 150* (2007), 40–53.

[93] SENSIAU, C. *Simulations numériques des instabilités thermoacoustiques dans les chambres de combustion annulaires*. PhD thesis, Université Montpellier II, 2008.

[94] SMITH, M. J. T. *Aircraft noise*. Cambridge University Press. Cambridge, UK, 1989.

[95] SMITH, T. J. B., AND KILHAM, J. K. Noise generation by open turbulent flames. *J. Acous. Soc. Am. 35*, 5 (1963), 715–724.

[96] SOMMERER, Y., GALLEY, D., POINSOT, T., DUCRUIX, S., LACAS, F., AND VEYNANTE, D. Large eddy simulation and experimental study of flashback and blow-off in a lean partially premixed swirled burner. *J. Turb. 5* (2004).

[97] STAUFER, M., SCHWARZ, A., AND JANICKA, J. On the simulation of premixed flames and coupling of large-eddy simulation with computational aeroacoustics. *Acta Acustica united with Acustica 95* (2009), 409–417.

[98] STRAHLE, W. C. On combustion generated noise. *J. Fluid Mech. 49* (1971), 399–414.

[99] STRAHLE, W. C. Some results in combustion generated noise. *J. Sound Vib. 23*, 1 (1972), 113–125.

[100] THOMAS, A., AND WILLIAMS, G. Flame noise: sound emission from spark-ignited bubbles of combustible gas. *Proc. R. Soc. Lond. 294* (1966), 449–466.

[101] TREFETHEN, L. N., AND BAU, D. *Numerical linear algebra*. Society for Industrial and Applied Mathematics SIAM., Philadelphia, United States of America, 1997.

[102] VAN KAMPEN, J. *Acoustic pressure oscillation induced by confined turbulent premixed natural gas flames*. PhD thesis, University of Twente, 2006.

[103] WANG, M., MOREAU, S., IACCARISNO, G., AND ROGER, M. Les prediction of wall-pressure fluctuations and noise of a low-speed airfoil. *International Journal of Aeroacoustics 3* (2009).

[104] WHO. Adverse health effects of noise: www.who.int/docstore/peh/noise/guidelines2.html, 1999.

[105] WILLIAMS, F. A. *Combustion Theory*. The Benjamin/Cummings Publishing Company, Menlo Park, CA, 1985.

[106] WILLIAMS, J. E. F., AND HAWKINGS, D. L. Sound generated by turbulence and surfaces in arbitrary motion. *Philosophical Transactions of the Royal Society of London A264* (1969), 321–342.

A

About the $\pi'_c = 0$ assumption

A.1 When is π'_T equal to zero?

Let us recall the equation of conservation of the total energy through a compressor. It is defined as

$$\rho_1 u_1 h_{t,1} + \mathcal{W} = \rho_2 u_2 h_{t,2} \tag{A.1}$$

where $\mathcal{W}$ is the work done by the compressor. This equation can be also written as

$$\pi_T \rho_1 u_1 h_{t,1} = \rho_2 u_2 h_{t,2} \tag{A.2}$$

where π_T is the total enthalpy ratio between the upstream and downstream flow. Equation (A.1) can be re-written as

$$\rho_1 u_1 h_{t,1} + \rho_1 u_1 \Delta h_t = \rho_2 u_2 h_{t,2} \tag{A.3}$$

where $\Delta h_t = \Delta(U v_\theta)$ is related to the conservation of the rothalpy (see Fig. A.1)

$$I = h_{t,1} - U_1 v_{\theta_1} = h_{t,2} - U_2 v_{\theta_2} \tag{A.4}$$

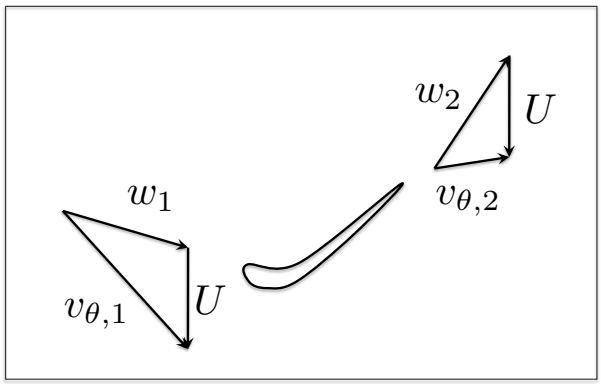

Figure A.1: Velocity triangles

Considering now $U_1 = U_2 = U$ for an axial compressor and $\rho_1 u_1 = \rho_2 u_2$ due to mass conservation, it is possible to express W_c as function of U and v_θ,

$$\frac{\mathcal{W}}{\rho_1 u_1} = h_{t,2} - h_{t,1} = U(v_{\theta,2} - v_{\theta,1}) \tag{A.5}$$

and introducing now π_T

$$h_{t,1}(\pi_T - 1) = U(v_{\theta,2} - v_{\theta,1}) \tag{A.6}$$

Let us now define a parameter $\zeta = \frac{U v_\theta}{h_t}$. The variable π_T is then expressed as

$$h_{t,1}(\pi_T - 1) = \zeta_1 h_{t,1} - \zeta_2 h_{t,2} = \zeta_1 h_{t,1} - \zeta_2 \pi_T h_{t,1} \tag{A.7}$$

$$(\pi_T - 1) = \zeta_1 - \zeta_2 \pi_T \tag{A.8}$$

Finally, resolving for π_T, it yields

$$\pi_T = \frac{\zeta_1 + 1}{\zeta_2 + 1} \tag{A.9}$$

Applying the differential of the logarithm to Eq. (A.9) results in

$$\frac{\pi_T'}{\bar{\pi}_T} = \frac{\zeta_1'}{\bar{\zeta}_1 + 1} - \frac{\zeta_2'}{\bar{\zeta}_2 + 1} \tag{A.10}$$

The fractional variation of ζ can in turn be found. It yields

$$\frac{\zeta'}{\bar{\zeta}} = \frac{v'_\theta}{\bar{v}_\theta} - \frac{h'_t}{\bar{h}_t} \tag{A.11}$$

From Eq. (A.10), it is then possible to state that $\pi'_T = 0$ if both ζ'_1 and ζ'_2 are zero, or if $\frac{\zeta'_1}{\bar{\zeta}_1+1} = \frac{\zeta'_2}{\bar{\zeta}_2+1}$ which is equivalent to

$$\zeta'_1 = \bar{\pi}_T \zeta'_2 \tag{A.12}$$

$$\left(\frac{v'_{\theta,1}}{v_{\bar{\theta},1}} - \frac{h'_{t,1}}{\bar{h}_{t,1}}\right)\bar{\zeta}_1 = \bar{\pi}_T \left(\frac{v'_{\theta,2}}{v_{\bar{\theta},2}} - \frac{h'_{t,2}}{\bar{h}_{t,2}}\right)\bar{\zeta}_2 \tag{A.13}$$

$$\left(\frac{v'_{\theta,1}}{v_{\bar{\theta},1}} - \frac{h'_{t,1}}{\bar{h}_{t,1}}\right)\frac{\bar{v}_{\theta,1}}{\bar{h}_{t,1}} = \bar{\pi}_T \left(\frac{v'_{\theta,2}}{v_{\bar{\theta},2}} - \frac{h'_{t,2}}{\bar{h}_{t,2}}\right)\frac{\bar{v}_{\theta,2}}{\bar{h}_{t,2}} \tag{A.14}$$

This relation can be splitted. Therefore π'_T is zero if both

$$\frac{v'_{\theta,1}}{\bar{v}_{\theta,1}}\frac{\bar{v}_{\theta,1}}{\bar{h}_{t,1}} = \bar{\pi}_T \frac{v'_{\theta,2}}{\bar{v}_{\theta,2}}\frac{\bar{v}_{\theta,2}}{\bar{h}_{t,2}} \tag{A.15}$$

and

$$\frac{h'_{t,1}}{\bar{h}_{t,1}}\frac{\bar{v}_{\theta,1}}{\bar{h}_{t,1}} = \bar{\pi}_T \frac{h'_{t,2}}{\bar{h}_{t,2}}\frac{\bar{v}_{\theta,2}}{\bar{h}_{t,2}} \tag{A.16}$$

or if

$$\frac{v'_{\theta,1}}{v_{\bar{\theta},1}} = \frac{h'_{t,1}}{\bar{h}_{t,1}} \quad \text{or} \quad \frac{v'_{\theta,2}}{v_{\bar{\theta},2}} = \frac{h'_{t,2}}{\bar{h}_{t,2}} \tag{A.17}$$

Equations (A.15) and (A.16) can be simplified in Eqs. (A.18) and (A.19) respectively. It results in

$$v'_{\theta,1} = v'_{\theta,2} \tag{A.18}$$

and

$$\bar{\pi}_T h'_{t,1} \bar{v}_{\theta,1} = h'_{t,2} \bar{v}_{\theta,2} \tag{A.19}$$

Summarizing, the fluctuation of the parameter π'_T can be neglected if

$$\boxed{v'_{\theta,1} = v'_{\theta,2} \quad \text{and} \quad \bar{\pi}_T h'_{t,1} \bar{v}_{\theta,1} = h'_{t,2} \bar{v}_{\theta,2}} \tag{A.20}$$

or

$$\boxed{\frac{v'_{\theta,1}}{\bar{v_{\theta,1}}} = \frac{h'_{t,1}}{\bar{h}_{t,1}} \quad \text{or} \quad \frac{v'_{\theta,2}}{\bar{v_{\theta,2}}} = \frac{h'_{t,2}}{\bar{h}_{t,2}}} \tag{A.21}$$

The parameter π_T is related to the total pressure ratio π_c as $\pi_T = \pi_c^{(\gamma-1)/\gamma}$. The fractional variation of π_c is written.

$$\frac{\pi'_T}{\bar{\pi}_T} = \frac{\gamma - 1}{\gamma} \frac{\pi'_c}{\bar{\pi}_c} \tag{A.22}$$

It is observed then that making $\pi'_T = 0$ is equivalent to make $\pi'_c = 0$, which is a **clear simplification** for the definition of the differential equation of momentum in SNozzle. Indeed, doing $\pi'_c = 0$ means that $p'_{t,2}/p'_{t,1} = \bar{\pi}_c$

B

Publications

In this appendix two publications are shown. They were realized during the work on this Ph.D.

Assessment of combustion noise in a premixed swirled combustor via Large-eddy simulation

Silva, C., Leyko, M., Nicoud, F., and Moreau, S.

Computers & *Fluids*, accepted (2010)

This article shows the computation of noise in a premixed swirled combustor by both direct and hybrid approaches. The direct approach is performed by a LES solver (AVBP) while the hybrid approach is carried out by an acoustic solver (AVSP-f) developed during this thesis. Results coming from both approaches are compared and discussed.

Extracting the acoustic pressure field from Large-eddy simulation of confined reactive flows

Silva, C., Nicoud, F., and Moreau, S.

in *16th AIAA/CEAS Aeroacoustics.* Stockholm, Sweden (2010)

Based on the previous work, it has been realized that it is not appropriate to directly compare the pressure fluctuations coming from LES and those coming from the acoustic solver when computing noise in a confined domain: hydrodynamic pressure fluctuations must be removed from the pressure field so that a proper acoustic field is obtained. A method to extract the acoustic field from the entire pressure field given by LES is proposed.

Assessment of combustion noise in a premixed swirled combustor via Large-eddy simulation

Camilo F. Silva* and Matthieu Leyko †
CERFACS, 31057 Toulouse, France
Franck Nicoud ‡
Université Montpellier II, 34095 Montpellier, France
Stéphane Moreau §
Université Sherbrooke, 2500, boul. de l'Université Sherbrooke (Québec), Canada J1K 2R1

Abstract

Today, much of the current effort in combustion noise is the development of efficient numerical tools to calculate the noise radiated by flames. Although unsteady CFD methods such as LES or DNS can directly provide the acoustic field radiated by noise sources, this evaluation is limited to small domains due to high computational costs. Hybrid methods have been developed to overcome this limitation. In these schemes, the noise sources are decoupled from the radiated sound. The sources are still calculated by DNS or LES codes whereas the radiated sound is evaluated by acoustic codes using an acoustic analogy.

In the present paper the assessment of combustion noise is conducted by both direct (LES) and hybrid computations in a premixed swirled combustor. Some comparisons of the sound pressure levels resulting from both approaches are shown, and the main differences between the two methods are explained.

keywords: combustion noise, acoustic analogy, direct computation, hybrid computation.

1 Introduction

Today Large Eddy Simulation (LES) has become an important tool for the simulation and post-processing analysis of turbulent flows. It offers the best promise in the foreseeable future for the estimation of noise from flows at Reynolds Numbers of interest in both open and closed systems. In aeroacoustics, LES plays an important role in the study of aerodynamical generated noise of numerous practical cases that range from air jets, high-lift devices or landing gears in an aircraft to the rear-view mirror of a car or the blades of a wind turbine [1, 2]. On the contrary, thermoacoustics is less understood than aeroacoustics. This is caused by additional physical phenomena implied such as the addition of unsteady heat release to the turbulent flow. Yet, LES has been successfully applied to partially premixed and non-premixed open flames [3, 4, 5] as well as to more complex cases such as gas turbine combustors. [6]

*Corresponding author. Ph.D. Student, CFD Team, 42, Av. Gaspard Coriolis; silva@cerfacs.fr. Tel: (33).(0)5.61.19.31.10
†Ph.D. Student, CFD Team, 42, Av. Gaspard Coriolis; leyko@cerfacs.fr
‡Professor, Université Montpellier II, I3M - CNRS UMR 5149 - CC51, franck.nicoud@univ-montp2.fr
§Professor, GAUS, Mechanical Engineering Department, Université de Sherbrooke, stephane.moreau@usherbrooke.ca.

Computational techniques for the estimation of sound can be classified into two broad categories: direct computations and indirect, or hybrid, computations. LES is present in both categories. Direct computations resolve the flow field together with the sound radiation. A compressible LES code is therefore required in addition to high-resolution numerical schemes in order to minimize both dispersion and dissipation. Moreover, the computational domain must be large enough to include the sources of noise as well as part of the acoustic near field [7]. Very expensive computational costs can arise since hydrodynamic and acoustic scales differ by a large amount in typical applications where the Mach number is moderate. This is even more severe when dealing with thermoacoustics since the transport equation of each species must be considered in order to solve the problem of compressible multicomponent reactive flows.

In hybrid approaches, the computation of sound is made in two different steps. The sources of noise are modeled first, which requires a proper estimation of the flow and the flame dynamic properties. These sources are assumed independent of any acoustic quantity. The far field acoustic radiation is then predicted from the different noise sources. Acoustic propagation is calculated based on equations relevant to acoustic phenomena. The derivation of a wave equation governing sound propagation in an arbitrary mean flow (and therefore accounting for mean flow-acoustic interactions) remains a difficult and controversial task in aeroacoustics [8]. Since the sources of noise and the acoustic radiation are computed separately, the computational effort is less critical than in direct sound computations. The sources of noise can be computed by numerical codes with lower-resolution schemes provided that numerical dissipation is carefully controlled [9] and that the acoustic source formulations fulfill true radiation characteristics (dipole, quadripole, etc). Regarding thermoacoustics, and more specifically combustion noise, it has been established that turbulent flames behave like low frequency monopoles [10]. After the different sources have been computed, the sound radiation, due to these sources, is evaluated by solving the wave operator coming from an acoustic analogy equation [4, 5, 11]. Notably, Strahle's formulation of Lighthill's analogy [12] [13] which takes into account the conservation equation of multicomponent reacting flows and Phillips' analogy [14]. Alternative methods include the Linearized Euler equations or its APE formulation [15, 16]. Acoustic analogies are satisfactory for open systems, i.e. when the acoustic fluctuations produced by the source propagate to the infinite and anechoic far-field. Moreover, in these cases, it is relatively easy to distinguish pure acoustics from hydrodynamic pressure fluctuations in the region of interest (farfield): hydrodynamic pressure fluctuations are negligible in the far field since they typically decay at least as the inverse third power of the distance to the sources [17]. Less is known about aeroacoustics in confined domains where acoustic and hydroynamic pressure fluctuations are both present. Interesting developments have been done to account for turbulence-body interaction [18, 19] . More recently, Schram used a modified Curle's analogy combined with a boundary element method (BEM) for evaluating the acoustic field produced by a non-compact turbulent source in a confined domain[20].

In the field of thermo-acoustics, it seems that no significative work has been done for evaluating the noise produced by confined flames using hybrid approaches. In reactive flows, confined systems might present an important interaction between the flame, the turbulent flow and the walls of the system. However if this interaction is not strongly present, the flame can be assumed independent of the acoustic field generated and acoustic analogies should apply. The general objective of this study is therefore to investigate whether acoustic analogies might be considered for the evaluation of noise in such confined domains.

2 Combustion noise through Phillips' analogy

The first attempt to include inhomogeneities of the mean flow into the acoustic wave operator is due to Phillips [21] who derived the following expression:

$$\frac{d^2\pi}{dt^2} - \frac{\partial}{\partial x_i}\left(c^2\frac{\partial \pi}{\partial x_i}\right) = \frac{\partial u_i}{\partial x_j}\frac{\partial u_j}{\partial x_i} + \frac{d}{dt}\left(\frac{\gamma-1}{\rho c^2}\dot{\omega}_T\right) + \frac{d}{dt}\left[\frac{\gamma-1}{\rho c^2}\left(\nabla\cdot(\lambda\nabla T) - \rho\sum_k Y_k c_{p,k}\mathbf{v}_k\cdot\nabla T + \tau:\nabla\mathbf{u}\right)\right] - \frac{\partial}{\partial x_i}\left(\frac{1}{\rho}\frac{\partial \tau_{ij}}{\partial x_j}\right) + \frac{d^2}{dt^2}(\ln r) \tag{1}$$

where π is a function of the logarithm of the pressure $\pi = (1/\gamma)\ln(p/p_\infty)$. The first term in the RHS is related to the noise created by turbulence. The second term is the monopole source of noise due to the unsteady heat release induced by the flame. The third one is linked to the noise produced by molecular transport whereas the gradient of the viscous tensor appears in the fourth term. Finally, the last term is known as the non-isomolar combustion source of noise.

In order to simplify this equation, one may consider different realistic assumptions in order to evaluate the acoustics for low mach number reactive systems [22]. Therefore, it is stated that

- The pressure level of the oscillations are small compared to the local mean pressure. $p'/p_0 \ll 1$.
- The system is nearly isobaric so that $p_0 \approx const.$
- The mean flow is small so that the convective terms in the equation are negligible.

As a consequence, the acoustic wave equation for low mach number reacting flows reads

$$\nabla\cdot(c_0^2\nabla p') - \frac{\partial^2 p'}{\partial t^2} = -(\gamma-1)\frac{\partial \dot{q}'}{\partial t} - \gamma p_0 \nabla\boldsymbol{v} : \nabla\boldsymbol{v} + \frac{\gamma p_0}{W_0}\frac{\partial^2 W'}{\partial t^2} \tag{2}$$

where c_0, p, γ, $\dot{q}$, $\boldsymbol{v}$, W represent the speed of sound, the pressure, heat capacity ratio, the heat release rate, the velocity vector and the mixture molar weight respectively. The symbols $()_0$ and $()'$ define mean and fluctuating quantities respectively. As it can be noticed in the left hand side of Eq. 2, the speed of sound c is placed inside the divergence operator. This ensures to capture acoustic fluctuations with strong variations of the mean temperature as it occurs close to the flame front.

In the combustion case exposed in this paper, the non-isomolar combustion noise does not play an important role since the reactant mixtures are highly diluted in nitrogen. Further on, the aerodynamic source of noise is considered small with respect to the noise source associated with the perturbation of the heat release rate [23]. The inhomogeneous wave equation then reduces to

$$\boxed{\nabla\cdot(c_0^2\nabla p') - \frac{\partial^2 p'}{\partial t^2} = -(\gamma-1)\frac{\partial \dot{q}'}{\partial t}} \tag{3}$$

3 Description of the acoustic Tool

Under harmonic oscillation assumptions, the pressure fluctuation p' and the heat fluctuation $\dot{q}'$ are expressed as follows [24]:

$$p'(\overrightarrow{x},t) = \Re(\hat{p}(\overrightarrow{x})e^{-i\omega t}) \tag{4}$$

$$\dot{q}'(\overrightarrow{x},t) = \Re(\hat{\dot{q}}(\overrightarrow{x})e^{-i\omega t}) \tag{5}$$

where $\omega = 2\pi f$. The quantities $\hat{p}$ and $\hat{\dot{q}}$ are complex amplitudes which depend on space only and are related by the so called Helmholtz equation :

$$\begin{cases} \nabla \cdot c_0^2 \nabla \hat{p} + \omega^2 \hat{p} = i\omega(\gamma - 1)\hat{\dot{q}} & \text{in } \Omega \\ + \text{ Boundary Conditions} & \text{on } \Gamma \end{cases} \tag{6}$$

When solving eq. 6 for pressure, the combustion term $\hat{\dot{q}}$ must be either known or modeled. If thermoacoustic eigen modes are sought for, $\hat{\dot{q}}$ is considered as a function of the acoustic pressure at some reference position, $\hat{\dot{q}} = \hat{\dot{q}}_{amp}(\hat{p}, \omega)$ so that eq. 6 is an eigenvalue problem which must be solved by using dedicated numerical methods [25]. On the contrary, when dealing with combustion noise the flame is considered as an autonomous acoustic source that generates combustion noise and $\hat{\dot{q}}$ reduces to a fixed forcing term:

$$\begin{cases} \nabla \cdot c^2 \nabla \hat{p} + \omega^2 \hat{p} = i\omega(\gamma - 1)\hat{\dot{q}}_{noise}(\omega) \\ + \text{ Boundary Conditions} \end{cases} \tag{7}$$

For Eq. 7 the mathematical problem to solve is a linear system:

$$\underbrace{\mathcal{A}}_{\nabla \cdot c^2 \nabla + \omega^2 I} \underbrace{x}_{\hat{p}} = \underbrace{b}_{i\omega(\gamma-1)\hat{\dot{q}}_{noise}} \tag{8}$$

This Linear system is solved by the Generalized Minimum REsidual (GMRES) method. This algorithm was chosen mainly due to its portability, simplicity, flexibility and efficiency . GMRES solves large, sparse and non Hermitian linear systems and belongs to the class of Krylov based iterative methods. This is an important feature that allows using only Matrix-vector products when solving Eq. 8, instead of storing the full matrix $\mathcal{A}$.

The present numerical tool uses a CERFACS implementation of the GMRES algorithm for both real and complex, single and double precision arithmetics suitable for serial, shared memory and distributed memory computers [26].

4 Experimental Configuration

Both direct and indirect computations of combustion noise using the above methodology are assessed by comparing with the experiment in a swirled premixed combustor (EC2 combustor) carried out in the laboratory EM2C (École Centrale Paris) [27][28]. The EC2 combustor consists in two geometrically indentical stages for air-fuel injection, a premixer and a combustion chamber. Air is fed into each stage through a circular manifold in which a swirler is inserted. This swirler has a hollow cylinder with large lateral openings (see Fig. 1a), through which air is injected in the inner premixer channel. Inside these rectangular openings, four injectors (1 mm diameter) deliver gaseous propane perpendicularly to the air flow. This cross-flow configuration enhances fuel-air mixing. The tangential injections create a strong

swirl motion in the $D = 30$ mm diameter inner channel, which in turn generate a central recirculation zone at the plenum that stabilizes the flame. The flame is controlled by the fuel-air ratio imposed in each of the two stages and is considered premixed and compact. Note that the LES could consider modeling the lines at each stage of both fuel and air as shown in Fig. 1(a). Nevertheless, important computational costs would arise due to the small grid cells that would be necessary to mesh the fuel lines. Since an homogeneous air-fuel mixing is considered to be achieved before arriving to the reacting zone, the fact of meshing fuel lines far upstream from the flame might be totally unnecesary. Therefore the present LES will only consider the air lines (simplified model shown in Fig. 1b) in which already a premixed mixture with equivalent ratios $\phi_1 - \phi_2$ is accounted for each stage repectively.

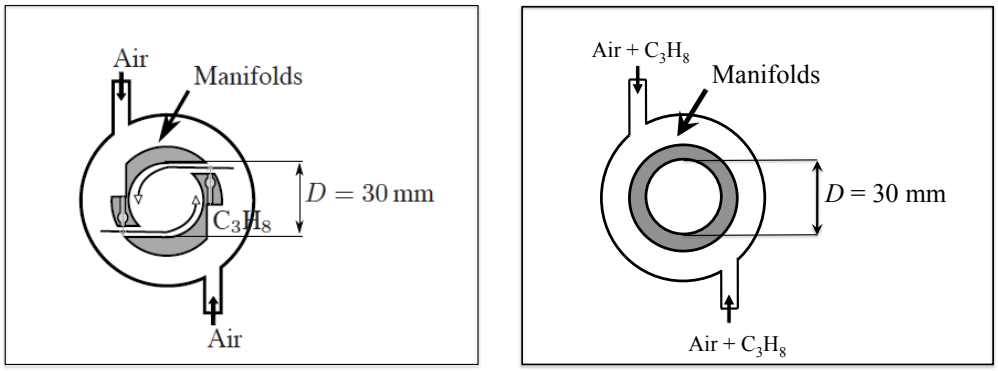

(a) Hollow cylinder - Actual test rig (b) Hollow cylinder simplified for LES

Figure 1: Schematic view of a tranversal section through the premixer and circular manifolds.

This configuration features strong combustion instabilities depending on the fuel staging ratio α, defined as the ratio of the fuel massflow in the furthest stage from the chamber (stage 1) to the total fuel injected massflow.

$$\alpha = \frac{\dot{m}_{f,1}}{\dot{m}_{f,1} + \dot{m}_{f,2}} \tag{9}$$

These instabilities are characterized by an important noise radiation due to the intense acoustic levels reached within the chamber and the premixer. The regime in the present study is given in Table 1. The gas mixture in the plenum is considered as perfectly premixed with a global equivalence ratio of $\phi_g = 0.832$.

α	$\dot{m}_{air,1}$	$\dot{m}_{f,1}$	$\dot{m}_{air,2}$	$\dot{m}_{f,2}$	ϕ_1	ϕ_2	ϕ_g
14.5 %	20	0.20	20	1.20	0.238	1.428	0.832

Table 1: Present operating regime (Mass flow $\dot{m}$ in m^3/h).

The combustion chamber is made of two quartz windows for flame visualizations, and two refractory concrete plates (top and bottom) which can be equipped either with small quartz windows for Particle Image Velocimetry (PIV) laser measurements or with transducer ports for acoustic measurements. The three PIV planes we are comparing with are shown in Fig. 2. The combustion chamber and the premixer are also equipped with seven microphones (denoted M1 to M7 in Fig. 2) placed at equal distances along the combustor.

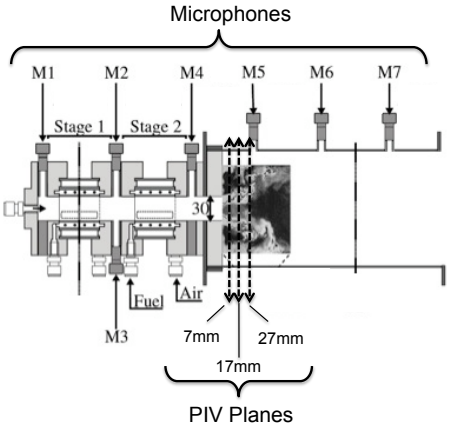

Figure 2: Two staged swirled premixed combustor. (Courtesy of École Centrale Paris)

5 Combustion noise Analysis

5.1 Direct Approach

AVBP, developed by CERFACS, is the parallel solver used for the LES computations [29]. In this code, the full compressible Navier Stokes equations are solved on hybrid (structured and unstructured) grids with second order spatial and temporal accuracy. Subgrid scale stresses are described by the Smagorinksy model. The flame/turbulence interactions are modeled by the Dynamic Thickened Flame (DTF) model [30]. This combustion model has been used in numerous studies of turbulent combustors [31][39][40][41] in which it has been shown to well predict ignition, blow-off and flash-back of flames as well as acoustic-flame interactions in specific configurations. The spatial discretization in AVBP is based on the finite volume method with a cell-vertex approach, combined to a numerical scheme derived from the Lax-Wendroff scheme. AVBP has been validated/used for a considerable number of configurations.[31, 32, 33]

Boundary Conditions in AVBP are treated by the Navier Stokes Characteristic Boundary Conditions (NSCBC) method [34]. This method is already an standard technique to control wave crossing the boundaries [35][36][37]. It consists in decomposing the variation of flow variables on boundaries into terms due to ingoing and outgoing waves. While walls are always taken as totally reflecting surfaces (no velocity fluctuations normal to the surface are allowed $\rightarrow u' = 0$) with a reflection coefficient $R = |R|e^{j\theta}$ ($|R| = 1$ and $\theta = 0$), the same cannot be stated for inlet and oulets. Acoustics of both inlets and outlets is characterized by their acoustic impedance $Z = p'/(\rho_0 c_0 \vec{u}' \cdot \vec{n})$. Following [37] it is possible to relate this acoustic quantity to the NSCBC parameters and is therefore straighforward to consider in the LES. This procedure was carried out with experimental data provided in [27][28]. Similar results were obtained when simplified acoustic conditions ($u' = 0$) were applied, proving that acoustic conditions at the inlets are not critical in the present LES study. Classically, outlets to the atmosphere are considered restrictive to pressure fluctuations $\rightarrow p' = 0$ ($|R| = 1$ and $\theta = \pi$). It is though preferred to extend the computational domain to some region of the atmosphere after the burner outlet. By doing so, the true impedance of the outlet is implicitely accounted for.

Two different meshes were used to compute the flow and flame dynamics of the EC2 combustor. The 'coarse' mesh has 3 millions of cells whereas the 'refined' mesh is made of 10 million cells. The quality of the two LES performed is evaluated through Pope's criterion [38]. The smagorinsky filter and the grid resolution for both cases should be sufficient to resolve at least 80 % of the energy remote from the

wall. The ratio of the resolved turbulent kinetic energy k_f with respect to the modeled turbulent kinetic energy k_{sgs} is then quantified.

$$Q_{LES} = \frac{k_f}{k_f + k_{sgs}} \tag{10}$$

where $k_f = \frac{1}{2}\tilde{u}_i\tilde{u}_j$ and $k_{sgs} = \frac{1}{2}\widetilde{u_i u_j} - \frac{1}{2}\tilde{u}_i\tilde{u}_j = \frac{3}{2}(u'_{sgs})^2$ and $\widetilde{()}$ stands for the LES filter. Figure 3 demonstrates that, for both LES cases, Q_{LES} is greater than 0.8 for almost the entire computational domain excepting regions near walls. The premixer turbulence is however better captured by the 'refined' mesh. It is well known that extremely high computational costs arise when a proper LES on boundary layers is sought. Nevertheless, boundary layers are assumed to little contribute to noise radiaton/scattering of turbulent flames. A high resolution in regions near walls is therefore not considered.

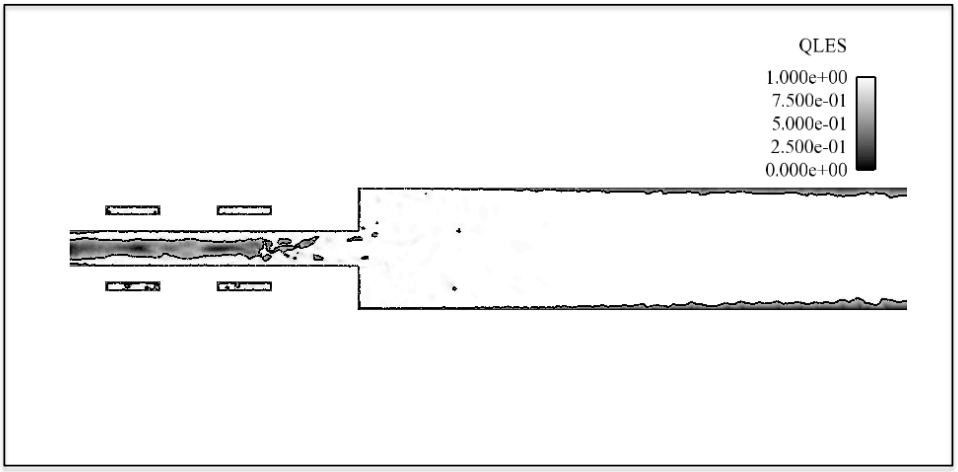

a) LES 3 million Cells

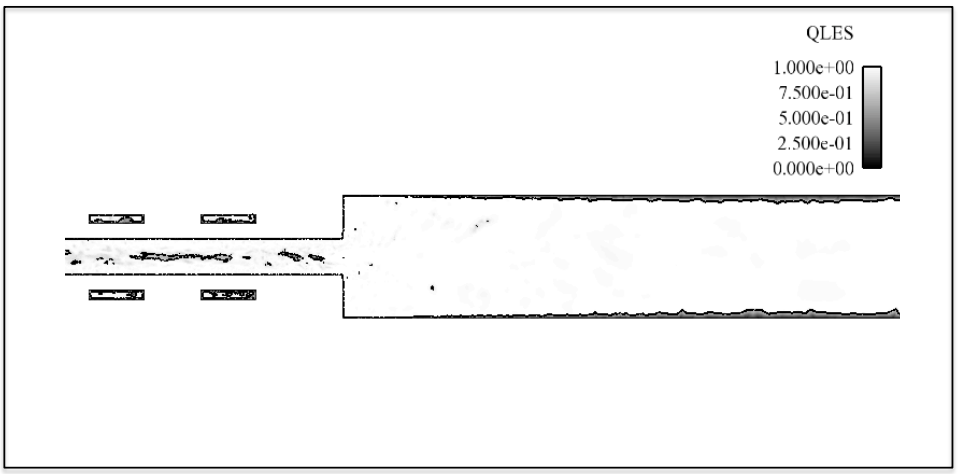

b) LES 10 million Cells

Figure 3: Instantaneous Field of Pope's Criterion. The black line stands for the isocontour line $Q_{LES} = 0.8$

Both meshes are found to reproduce the mean PIV very well. This can be observed in Fig. 4. Both

LES succeed in predicting the central recirculation zone satisfactorily. The LES on the 'refined' mesh is however more accurate for the outer region, particularly for the radial velocity. The fluctuating velocity field is characterized by rms profiles. Figure 5 shows that on the 'coarse' mesh a high overprediction of velocity fluctuations is obtained in both axial and radial components. On the fine grid however the LES clearly recovers the experimental velocity fluctuating field.

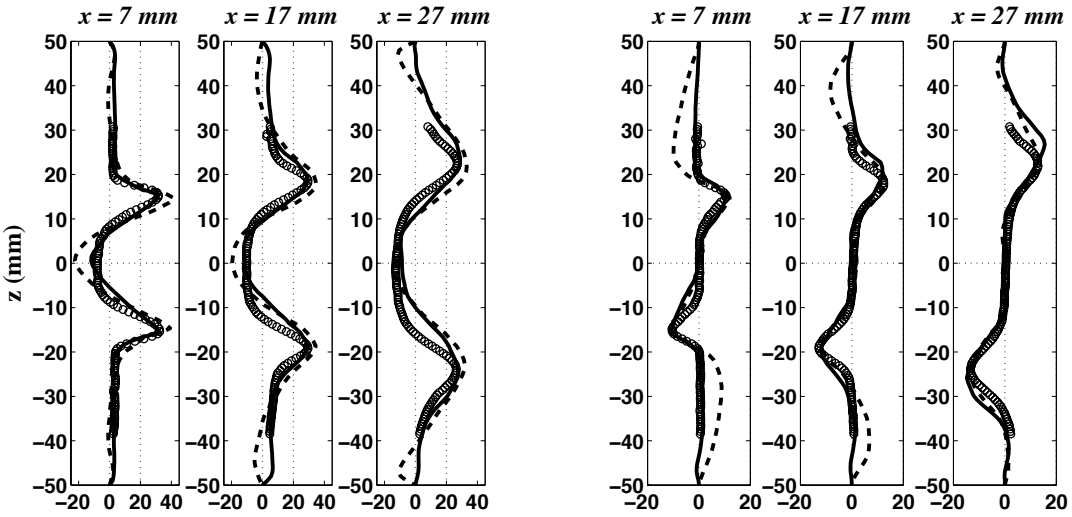

(a) Mean Axial Velocity (m/s) (b) Mean Radial Velocity (m/s)

Figure 4: Velocity Profiles: ∘ Experimental PIV measurements
− − − LES 3 million cells, ——— LES 10 million cells

Acoustics and flame dynamics of the system represented by the heat release are, on the contrary, more difficult to evaluate than the mean and fluctuating velocity field. The mean value of heat release is similar in both LES and is close to the 40kW experimental thermal power, as can be observed in Fig. 6(a). Different values in the variations of heat release are however obtained for each LES. Strong and more regular fluctuations of heat release are obtained with the 'coarse' mesh while smaller and less periodic fluctuations are given by the 'refined' mesh computation. It is likely that the coarser mesh does not capture enough small turbulent scales and trigger too large turbulent eddies. These large coherent structures might clearly have an influence on the flame dynamics and thus in the large fluctuations of heat release. The value of the rate of change of heat release integrated over the whole volume of the combustor has also been computed for the two different meshes and is shown in Fig. 6(b). On the finer mesh a quieter flame is modeled, considering the smaller values of rate of change of heat release compared to those obtained from the coarse mesh. As a consequence, smaller rms pressure values should be expected on the finer mesh. Acoustics in the chamber is rather characterized by the Sound Pressure Level (SPL) at a given point than rms values of the pressure. Figure 7 compares the SPL values at the microphone 7 (see the location of $M7$ in Fig. 2) of the computations on the refined and coarse meshes to the experimental measurements. Both LES clearly overestimate the sound levels with a significant improve on the finer. It is then found that in order to correctly evaluate the dynamics of a flame and the acoustics generated by this one it is not enough to satisfactorily model the fluctuating velocity field as shown in Figs. 4 and 5. As stated before, computing acoustic pressure fluctuations is very challenging since these values are very small compared to the aerodynamic fields. Several additional phenomena can play an important role.

First, the performed LES assume a perfect premixed mixture of air and fuel in the reactive region. This

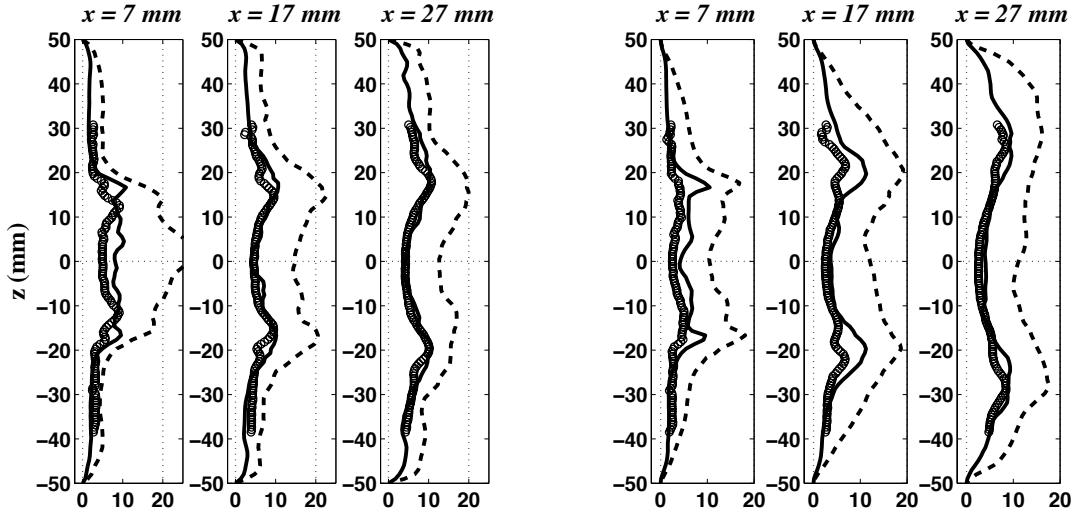

(a) RMS Axial Velocity (m/s) (b) RMS Radial Velocity (m/s)

Figure 5: Velocity Profiles: ∘ Experimental PIV measurements
− − − LES 3 million cells, ——— LES 10 million cells

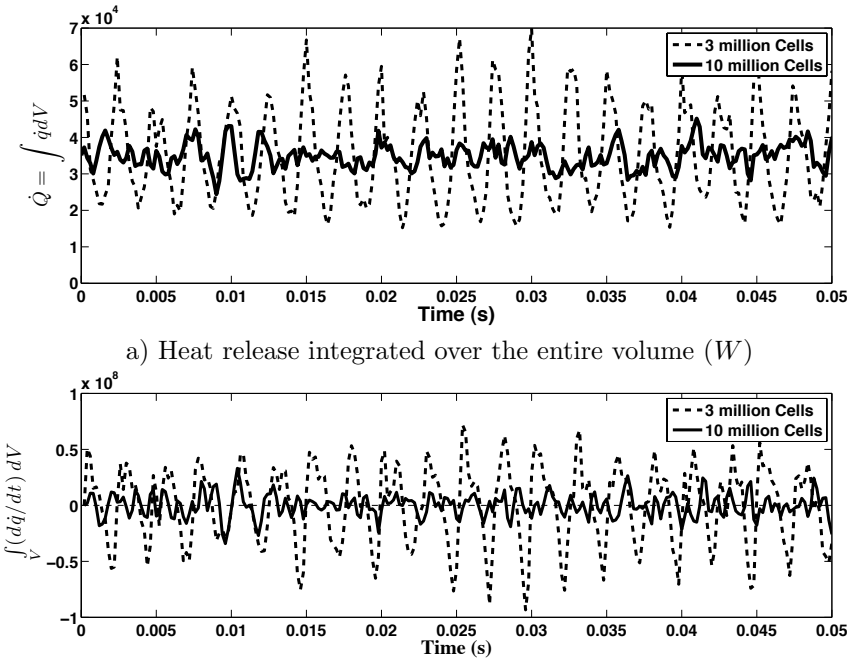

a) Heat release integrated over the entire volume (W)

b) Rate of change of heat release integrated over the entire volume (W/s)

Figure 6: Heat Release and rate of change of heat release

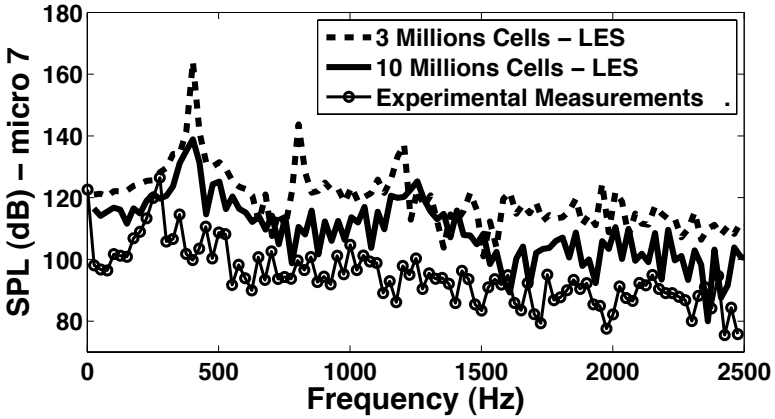

Figure 7: Sound Pressure Level

assumption might be a misinterpretation of reality. Small pockets of propane-air presenting an equivalent ratio different for ϕ_g may reach the flame influencing its dynamics and as a consequence the radiated sound. Secondly, perfect adiabatic walls were considered in the present LES. In [41] it was shown that accounting for heat transfer leads to a reduction in the SPL. Some computations, not shown here, were performed considering heat transfer by modeling approximate heat loss coefficients (as done in [41]). No significative changes on the radiated noise were observed. Nevertheless, heat transfer might still be modeled too aproximatively knowing that exact values of heat transfer coefficients are extremely difficult to be obtained experimentally. A proper simulation of conjugate heat transfer including convection, conduction and radiation might be important at some level for noise modeling in turbulent flames, but presently remains too cumbersome. Thirdly, resolution of the computation (mesh refinement and order of the numerical scheme) is clearly significant. High grid resolutions in the reactive region not only means a smaller influence of the combustion model but also to be able to account for the smallest turbulent structures present in the shear layer that might influence the coherence of the bigger scales and thus the global turbulent interaction with the flame. At last but not the least, another explanation lies in the experimental data. Measuring acoustics in a confined combustion chamber is only reliable when acoustic leakages are proved to be controlled. This is, anyway, a difficult task. It has been found by the concerned EC2 experimentalists that acoustic leakages are still not totally well managed. As a result, wrong evaluations of pressure fluctuations may arise.

5.2 Hybrid approach

The acoustic outputs from both direct and hybrid approaches are compared for the 10 million cells mesh independently of experimental data. As sketched in Fig. 8, hydrodynamic pressure fluctuations are assumed to be small when considering results from the direct approach. Therefore, the acoustic field resulting from the hybrid approach is directly compared to the pressure fluctuation field coming from direct computations.

The hybrid computation accounts for two steps. First, the source of combustion noise is computed by postprocessing the data obtained from the LES computation (instantaneous heat release rate in addition to mean flow parameters taken from the 10 million cells numerical results). Secondly, the simplified Phillips equation written in the zero Mach number limit given by Eq. 7 is solved in the frequency domain.

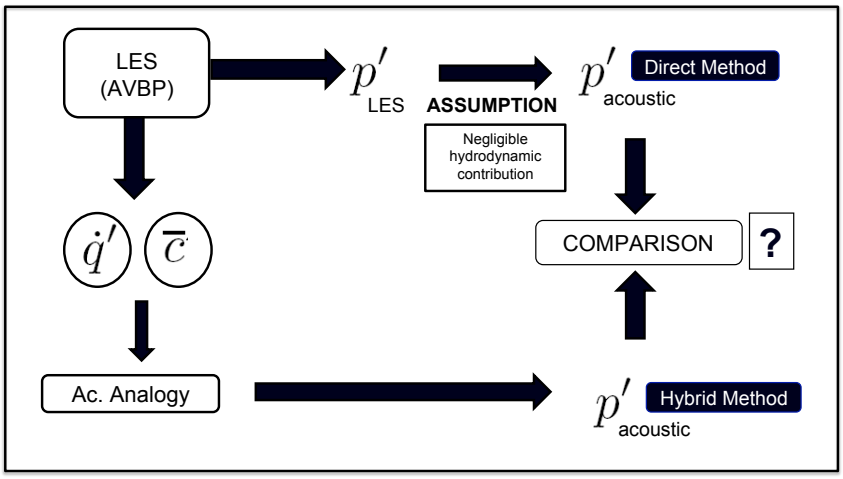

Figure 8: Exercise of comparison: Direct Approach Vs Hybrid Approach

Overall good agreement is found between both direct and hybrid approaches in Fig. 9 which shows the sound pressure levels obtained by microphones 5 and 7 (see the location of $M5$, $M7$ in Fig. 1).

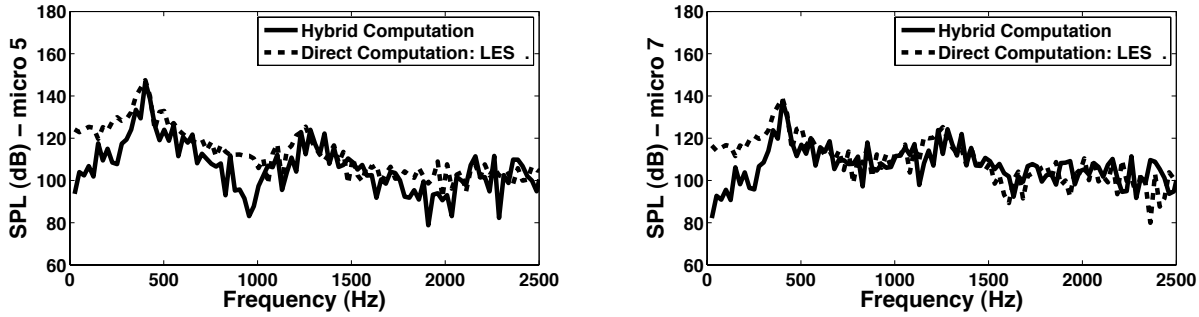

(a) Microphone 5 (b) Microphone 7

Figure 9: Sound Pressure Levels from the direct and hybrid approaches

It is interesting to notice that the hybrid computation manages to recover not only the magnitude of the acoustic pressure over almost all the spectrum, but also the shape of the acoustic waves. Figure 10 shows the strongest acoustic wave, the quarter wave mode, that resonates at 377 Hz. The pressure fluctuations along the axis of the combustor at different times within a cycle are observed. As both methods yield the same envelope of variations at this frequency, the pressure fluctuation recovered by the direct computation can be seen as almost completely caused by acoustics.

In Fig. 9 some zones of the spectrum still show important gaps between hybrid and direct computations. For example in Fig. 11 two different types of pressure waves are observed at microphone 5 for the direct and hybrid computations in the region around 1000 Hz. Whereas a pure acoustic standing wave is obtained by the hybrid approach, a perturbed pressure wave is obtained in the direct computation results. A pure standing acoustic wave can naturally have an acoustic pressure node. If this pressure node is present close to the region of the measurement device a low value of pressure fluctuation will be obtained. This is what happens for microphone 5 in the zone close to 1000 Hz (fig. 11a). Obviously, when the pressure fluctuations not only contain acoustics but also hydrodynamic perturbations as in the

direct computations (Fig. 11b), no pressure node can be observed and the resulting SPL is much higher than in the hybrid computation case. Similar conclusions can be drawn at very low frequencies (before the peak at 377 Hz) where the significant hydrodynamic contribution in the direct computation triggers higher pressure fluctuations.

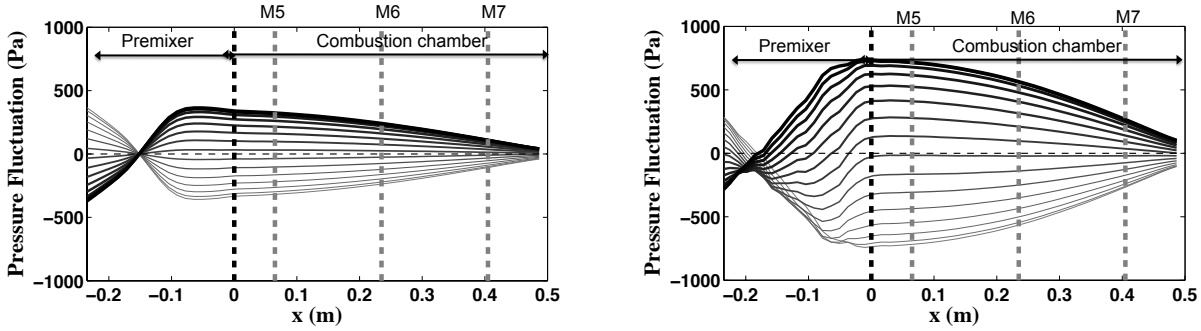

(a) Quarter pressure Wave from eq. 8 Hybrid Computation

(b) Quarter pressure Wave from LES Direct Computation

Figure 10: Longitudinal pressure Waves oscillating at 377 Hz

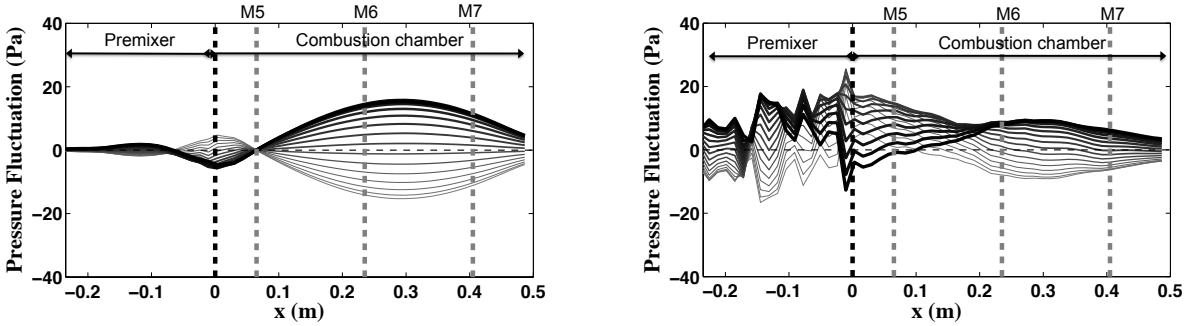

(a) Pressure Wave from eq. 8 Hybrid Computation

(b) Pressure fluctuation from LES Direct Computation

Figure 11: Longitudinal pressure Waves oscillating at 954 Hz

6 Conclusions

Combustion noise of a premixed swirled combustor has been assessed by two different numerical approaches: a direct computation in which the noise produced by the flame is calculated together with the flow and flame dynamics, and a hybrid computation in which the acoustic field is evaluated from the sources of noise in a separate step.

Classical comparisons between mean and fluctuating (rms) velocity fields were performed between two LES on a 'coarse' mesh grid (3 million cells) and a 'refined' mesh grid (10 million cells), and PIV measurements. Mean velocity fields (axial and radial) were well predicted by both LES cases, whereas only the 'refined' mesh succeed in recovering the proper rms velocity fields. It was then observed that satisfactorily predicting the velocity fluctuating field does not mean to reproduce correct flame dynamics and heat release. On the one hand, the mean heat release corresponding to the experimental thermal

power is well captured by both LES. On the other hand, significative differences are found between the two simulations on the shape of the instantaneous heat release and its rate of change. As a consequence, a right estimate of the combustion noise radiation is not yet well obtained. Several phenomena might be the cause of such a misprediction. A lack in numerical resolution can be one possible explanation: computing the small turbulent length scales in the shear flow region might be significant since these eddies might have a non-negligible influence on the flame dynamics and, as a consequence, on the noise prediction simulations. A higher grid resolution in the flame region also decreases the influence of the combustion model, which might have a certain effect when computing the values of rate of change of heat release. Moreover, an accurate prediction of heat transfer might also be a crucial factor, and exact modeling of convection, conduction and radiation might be important in combustion noise modeling.

The output from the hybrid computation is a pure acoustic field due to the turbulent flame. Good agreement is found in almost the entire SPL spectrum when comparing the results of both direct and hybrid computations. Nevertheless, there are still some differences in specific zones of the spectrum. Hybrid computation results only consider pure acoustic waves, and at given frequencies these pure acoustic waves may present acoustic nodes that may take place close to the acoustic sensor position. This leads to a low fluctuation of pressure at this position and hence, to a low value of the SPL spectrum at these frequencies. At low frequencies, the pressure fluctuations coming from the direct approach are most likely caused not only by acoustics but also by hydrodynamic fluctuations which then leads to higher sound pressure levels than the hybrid approach.

Acknowledgments

This work was supported by the Fondation de Recherche pour l'aéronautique et l'espace (FRAE) through the BRUCO project. The authors also gratefully acknowledge the Centre Informatique National de l'Enseignement Supérior (CINES) for giving access to parallel computers and École Centrale Paris for the interesting discussions and experimental data. An special recognition is also given to Ammar Lamraoui of the laboratory EM2C (École Centrale Paris) for the efforts done in measuring the acoustic impedance of all fuel-air inlets on the EC2 combustion chamber.

References

[1] A. Oberai, F. Roknaldin and T. Hughes "Computation of trailing-edge noise due to turbulent flow over an airfoil" AIAA Journal, **40** 2206 - 2216 (2002).

[2] D.J. Bodony and S. K. Lele "On the current status of jet noise predictions using Large-Eddy Simulation" AIAA Journal, **46** 364 - 380 (2008).

[3] H. Pitsch and H. Steiner, "Large-Eddy Simulation of a turbulent piloted methane/air diffusion flame (Sandia flame D)" Phys. Fluids , **12**, 2541-2554 (2000).

[4] F. Flemming, A. Sadiki and J. Janicka "Investigation of combustion noise using a LES/CAA hybrid approach" Proc. of the Combustion Institute, **31**, 3189-3196 (2007).

[5] M. Ihme, H. Pitsch and H. Bodony "Radiation of noise in turbulent flames" Proc. of the Combustion Institute, **32**, 1545-1554 (2009).

[6] F. di Mare, W. Jones and K. Menzies "Large-Eddy Simulation of a model gas turbine combustor" Combust. Flame, **137**, 278-294 (2004).

[7] A. S. Lyrintzis "Integral acoustic methods: From the (cfd) near-field to the (acoustic) far-field" Int. J. Aeroacoustics, **2**, 95-128 (2003).

[8] C. Bailly, C. Bogey and S. Candel "Modelling of sound generation by turbulent reacting flows" Int. J. Aeroacoustics **9**, 461-489 (2009).

[9] M. Wang, S. Moreau G. Iaccarisno and M. Roger "LES prediction of wall-pressure fluctuations and noise of a low-speed airfoil" Int. J. Aeroacoustics, **3** (2009).

[10] S. Bragg "Combustion noise" J. Inst. of Fuel, **36** 12-16 (1963).

[11] M. Staufer, A. Schwarz and J. Janicka "On the simulation of premixed flames and coupling of Large-Eddy Simulation with computational aeroacoustics" Acta Acustica united with Acustica, **95** 409-417 (2009).

[12] M. J. Lighthill "On sound generated aerodynamically: I. General theory" Proc. R. Soc. London Ser. A, **222** 1 - 32 (1954).

[13] W. C. Strahle "On Combustion Generated Noise" J. Fluid Mech., **49** 399 - 414 (1971).

[14] S. Kotake "On combustion noise related to chemical reactions" J. Sound Vibration, **42** 399-410 (1975).

[15] R. Ewert and W. Schröder. "Acoustic perturbation equations based on flow decomposition via source filtering" J. Comput. Phys., **188** 365 - 398 (2003).

[16] C. Bailly and D. Juvand "Numerical solution of acoustic propagation problems using Linearized Euler Equations" AIAA Journal, **38** 22 - 29 (2000).

[17] M. Roger "Aeroacoustics of wall-bounded flows" Von Karman Institute For Fluid Dynamics. Lecture Series. March 9-13 (2009).

[18] N. Curle "The influence of solid boundaries upon aerodynamic sound" Proc. R. Soc. London Ser. A 231, (1955).

[19] H.G. Davies, J.E. Ffowcs Williams "Aerodynamic sound generation in a pipe" J. Sound Vibration, **161** 2 (1981).

[20] C. Schram "A boundary element extension of Curle's analogy for non-compact geometries at low-Mach numbers" J. Sound Vibration, **322** 264-281 (2009).

[21] O. M. Phillips "On the generation of sound by supersonic turbulent shear layers" J. Fluid Mech., **9** 1-28 (1960).

[22] F. Williams "Combustion theory" The Benjamin/Cummings Publishing Company (1985)

[23] H. Hassan "Scaling of combustion-generated noise" J. Fluid Mech., **49** 445-453 (1974).

[24] A. Pierce "Acoustics. An introduction to its physical principles and applications" The Acoustical Society of America. (1994).

[25] F. Nicoud, L. Benoit and C. Sensiau "Acoustic modes in combustors with complex impedances and multidimensional active flames" AIAA Journal, **45** 426-441 (2007).

[26] V. Frayssé, L. Giraud, S. Gratton and J. Langou "A Set of GMRES routines fo real and complex arithmetics on high performance computers." CERFACS Technical Report, (2003).

[27] A. Lamraoui et al. "Acoustic reconstruction of the fuel and air feeding line impedances in a swirled burner during combustion instabilites" In *3rd European Conference for Aerospace Sciences EUCASS* (2009).

[28] A. Lamraoui, F. Richecoeur, T. Schuller and S. Ducruix "Methodology for on the fly acoustic characterization of the feeding lines impedances in a turbulent swirled combustor" In *Proceedings of ASME Turbo Expo 2010: Power for Land, Sea and Air* (2010).

[29] AVBP Code: *http://www.cerfacs.fr/4-26334-The-AVBP-code.php* and *http://www.cerfacs.fr/4-25719-Publications.php*, (2010)

[30] O. Colin, F. Ducros, D. Veynante and T. Poinsot "A thickened flame model for large eddy simulations of turbulent premixed combustion" Phys. Fluids **12**, 1843-1863 (2000)

[31] L. Selle, G. Lartigue, T. Poinsot, R. Koch, K.-U. Schildmacher, W. Krebs, B. Prade, P. Kaufmann and D. Veynante "Compressible Large-Eddy Simulation of turbulent combustion in complex geometry on unstructured meshes" Combust. Flame. **137**, 4, 489-505 (2004)

[32] S. Roux, G. Lartigue, T. Poinsot, U. Meier and C. Bérat "Studies of mean and unsteady flow in a swirled combustor using experiments, acoustic analysis and Large-Eddy Simulations" Combust. Flame. **141**, 40-54 (2005)

[33] S. Mendez and F. Nicoud "Large eddy simulation of a bi-periodic turbulent flow with effusion" J. Fluid Mech., **46**, 2623-2633 (2008)

[34] T. Poinsot and S. Lele "Boundary Conditions for Direct Simulation of Compressible Viscous Flows" J. Comput. Phys. , **101** 104-129 (1992).

[35] T. Poinsot and D. Veynante "Theoretical and Numerical Combustion" R.T. Edwards. (2005)

[36] N. Lamarque, M. Porta, F. Nicoud, and T. Poinsot. "On the stability and dissipation of wall boundary conditions for compressible flows" International Journal for Numerical Methods in Fluids, **62** 1134-1154 (2010).

[37] L. Selle, F. Nicoud, and T. Poinsot "The actual impedance of non-reflecting boundary conditions: implications for the computation of resonators" AIAA Journal, **42** 958-964 (2004).

[38] S. Pope "Turbulent Flows" Cambridge University Press. Cambridge, USA (2000)

[39] C. Martin, L. Benoit, Y. Sommerer, F. Nicoud and T. Poinsot "LES and acoustic analysis of combustion instability in a staged turbulent swirled combustor" AIAA Journal, **44** 741-750 (2006).

[40] Y. Sommerer, D. Galley, T. Poinsot, S. Ducruix, F. Lacas, and D. Veynante "Large eddy simulation and experimental study of flashback and blow-off in a lean partially premixed swirled burner" Journal of Turbulence, **5** -37 (2004).

[41] A.X. Sengissen, J.F. Kampen, R.A. Huls, G.G.M. Stoffels, J.B.W. Kok and T.J. Poinsot "LES and experimental studies of cold and reacting flow in a swirled partially premixed burner with and without fuel modulation" Combust. Flame. **150** 40-53 (2007)

Extracting the Acoustic pressure field from Large Eddy Simulation of confined reactive flows

Camilo F. Silva*
CERFACS, 31057 Toulouse, France
Franck Nicoud †
Université Montpellier II, 34095 Montpellier, France
Stéphane Moreau ‡
Université Sherbrooke, 2500, boul. de l'Université Sherbrooke (Québec), Canada J1K 2R1

Today, much of the current effort in the field of combustion noise is the development of efficient numerical tools to calculate the noise radiated by flames. Although unsteady CFD methods such as LES or DNS can directly provide the acoustic field radiated by noise sources, this evaluation is limited to small domains due to high computational costs. Hybrid methods have been developed to overcome this limitation. In these schemes, the noise sources are decoupled from the radiated sound. The sources are still calculated by DNS or LES codes whereas the radiated sound is evaluated by acoustic codes.

These two approaches (direct and hybrid) have been widely used to assess combustion noise radiated by open flames. On the contrary, not significative work has been done for evaluating noise radiated by confined flames. Moreover, several problems can arise when attempting to compare direct to hybrid methods results from confined combustors. While almost a pure acoustic pressure field is obtained from direct computations when considering an open flame, for confined flames this statement does not hold: hydrodynamic pressure fluctuations play an important role. In the present paper the assessment of combustion noise is conducted by both direct (LES) and hybrid computations in a premixed swirled combustor. A method to extract the acoustic field from the entire pressure field given by LES is proposed.

keywords: combustion noise, acoustic analogy, direct computations, hybrid computations.

I. Introduction

Large Eddy Simulation (LES) has become an important tool for the simulation and analysis of turbulent flows. It offers the best promise in the foreseeable future for the estimation of noise from flows at Reynolds Numbers of interest in both open and closed systems. In aeroacoustics, LES plays an important role in the study of aerodynamical generated noise of numerous practical cases that range from air jets, high-lift devices or landing gears in an aircraft to the rear-view mirror of a car or the fan of a wind mill.[1,2] Combustion noise is, on the contrary, less understood than aeroacoustics. This is due to the different physical phenomena implied such as the addition of unsteady heat release to the already turbulent flow. Still LES has been successfully applied to partially premixed and non-premixed open flames[3,4] as well as in more complex cases such as gas turbine combustors.

Computational techniques for the estimation of sound can be classified into two broad categories: direct computations and indirect, or hybrid, computations. LES is well presented in these two categories. Direct computations resolve the flow field together with the sound radiation. A compressible LES code is therefore

*Corresponding author. Ph.D. Student, CFD Team, 42, Av. Gaspard Coriolis; silva@cerfacs.fr. Tel: (33).(0)5.61.19.31.10
†Professor, Université Montpellier II, I3M - CNRS UMR 5149 - CC51, franck.nicoud@univ-montp2.fr
‡Professor, GAUS, Mechanical Engineering Department, Université de Sherbrooke, stephane.moreau@usherbrooke.ca.

required in addition to high-resolution numerical schemes in order to minimize both dispersion and dissipation. Moreover, the computational domain must be large enough to include the sources of noise as well as part of the acoustic near field.[6] Very expensive computational costs can arise since hydrodynamic and acoustic scales differ to a large amount in typical applications where the Mach number is moderate. This is even more true when dealing with thermoacoustics since the transport equation of each species must be considered in order to solve the problem of compressible multicomponent reactive flows.

In hybrid approaches, the computation of sound is made at two different levels: 1) model the sources of noise which requires a proper estimation of the flow and the flame dynamic properties and 2) predict the far field acoustic radiation due to the different noise sources. Acoustic propagation is calculated based on equations relevant to acoustic phenomena. The derivation of a wave equation governing sound propagation in an arbitrary mean flow (and therefore accounting for mean flow-acoustic interactions) remains a difficult and controversial task in aeroacoustics.[7]

These theoretical formulations are satisfactory for open systems, i.e. when the acoustic fluctuations produced by the source propagate to the infinite and anechoic far-field. Moreover, in these cases, it is relatively easy to distinguish pure acoustics from hydrodynamic pressure fluctuations in the region of interest (farfield): hydrodynamic pressure fluctuations are negligible in the far field since they typically decay at least as the inverse third power of the distance to the sources.[15] Less is known about aeroacoustics in confined domains where acoustic and hydrodynamic pressure fluctuations are both present. Interesting developments have been done to account for turbulence-body interaction[16,17] . More recently, Schram used a modified Curle's analogy combined with a boundary element method (BEM) for evaluating the acoustic field produced by a non-compact turbulent source in a confined domain.[18]

In the field of combustion noise, it seems that no significative work has been done for evaluating the noise produced by confined flames. In confined reactive flows, interactions exist between the flame, the turbulent flow and the walls of the system. Moreover, hydrodynamic pressure fluctuations might be important and should not be neglected. Consequently, the task of evaluating acoustics from a complete signal of fluctuating pressure becomes difficult. It has been shown in[19] that pressure waves coming from LES are highly disturbed by turbulence and hence a proper comparison between LES and hybrid simulations sometimes is unachievable. The general objective of this study is to investigate some methods to decouple hydrodynamics from acoustics in pressure signals resulting from Large Eddy Simulations of reactive confined flows.

II. Combustion noise through Phillips' analogy

The first attempt to include inhomogeneities of the mean flow into the acoustic wave operator is due to Phillips[20] who derived the following expression:

$$\begin{aligned}\frac{d^2\pi}{dt^2} - \frac{\partial}{\partial x_i}\left(c^2\frac{\partial \pi}{\partial x_i}\right) = &\frac{\partial u_i}{\partial x_j}\frac{\partial u_j}{\partial x_i} + \frac{d}{dt}\left(\frac{\gamma-1}{\rho c^2}\dot{q}\right)\\ &+ \frac{d}{dt}\left[\frac{\gamma-1}{\rho c^2}\left(\nabla\cdot(\lambda\nabla T) - \rho\sum_k Y_k c_{p,k}\mathbf{v}_k\cdot\nabla T + \tau:\nabla\mathbf{u}\right)\right]\\ &- \frac{\partial}{\partial x_i}\left(\frac{1}{\rho}\frac{\partial \tau_{ij}}{\partial x_j}\right) + \frac{d^2}{dt^2}(\ln r)\end{aligned} \tag{1}$$

where π is function of the logarithm of the pressure $\pi = (1/\gamma)\ln(p/p_\infty)$. The first term on the RHS is related to the noise created by turbulence. The second term is the monopole source of noise due to the unsteady heat release induced by the flame. The third one is linked to the noise produced by molecular transport whereas the gradient of the viscous tensor appears in the fourth term. Finally, the last term is known as the non-isomolar combustion source of noise.

In order to simplify this equation, one may consider different realistic assumptions in order to evaluate the acoustics for low Mach number reactive systems.[21] Therefore, it is stated that:

- The pressure level of the oscillations are small compared to the local mean pressure. $p'/p_0 \ll 1$.
- The system is nearly isobaric so that p_0 is nearly constant.
- The mean flow is small so that the convective terms in the equation are negligible.

As a consequence, the acoustic wave equation for low Mach number reacting flows reads

$$\nabla \cdot (c_0^2 \nabla p') - \frac{\partial^2 p'}{\partial t^2} = -(\gamma - 1)\frac{\partial \dot{q}'}{\partial t} - \gamma p_0 \nabla \boldsymbol{v} : \nabla \boldsymbol{v} + \frac{\gamma p_0}{W_0}\frac{\partial^2 W'}{\partial t^2} \tag{2}$$

where c_0, p, γ, $\dot{q}$, $\boldsymbol{v}$, W represent respectivelly the speed of sound, the pressure, heat capacity ratio, the heat release rate, the velocity vector and the mixture molar weight. The symbols $()_0$ and $()'$ define respectivelly mean quantities and fluctuation quantities. As it can be noticed in the left hand side of eq. 2, the speed of sound c is placed inside the divergence operator. This ensures to capture acoustic fluctuations with strong variation of the mean temperature as it occurs close to the flame front.

In the combustion case exposed in this paper, the non-isomolar combustion noise does not play an important role since the reactant mixtures are highly dilluted in nitrogen. Further on, the aerodynamic source of noise is considered small with respect to the noise source associated with the perturbation of the heat release rate.[22] The inhomogeneous wave equation then reduces to

$$\boxed{\nabla \cdot (c_0^2 \nabla p') - \frac{\partial^2 p'}{\partial t^2} = -(\gamma - 1)\frac{\partial \dot{q}'}{\partial t}} \tag{3}$$

Under the harmonic oscillation assumption, in which $p'(x,t) = \hat{p}(x)e^{-i\omega t}$, Eq. 3 becomes

$$\begin{cases} \nabla \cdot c_0^2 \nabla \hat{p} + \omega^2 \hat{p} = -i\omega(\gamma - 1)\hat{\dot{q}} & \text{in } \Omega \\ + \text{ Boundary Conditions} & \text{on } \Gamma \end{cases} \tag{4}$$

where $\omega = 2\pi f$. The quantities $\hat{p}$ and $\hat{\dot{q}}$ are complex amplitudes which depend on space only.

III. Experimental Configuration

This article describes the evaluation procedure of noise due to the combustion within a swirled premixed combustor[26,27] (EC2 Combustor) performing both direct and indirect computations. The experimental study is carried out in the laboratory EM2C (École Centrale Paris). The EC2 combustor consists in two geometrical identical stages for air-fuel injection, a premixer and a combustion chamber. The flame is controlled by the Fuel-Air ratio imposed in each of the two stages and stabilized by a swirled premixed. The test rig accounts for 7 different measurement points of pressure (denoted $M1$ to $M7$ in fig.1) placed at equivalent distances along the combustor.

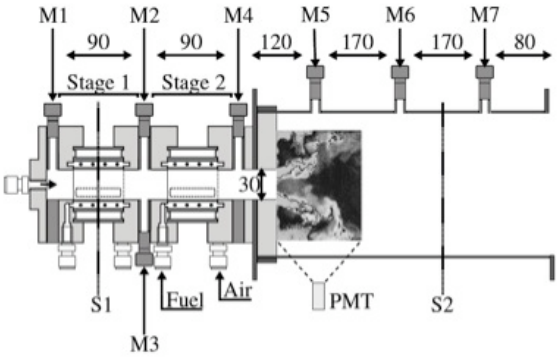

Figure 1. Two staged swirled premixed combustor. (Courtesy of École Centrale Paris)

IV. Combustion noise Analysis

AVBP, developed by CERFACS, is the parallel solver used for the LES computations.[28] In this study, the full compressible Navier Stokes equations are solved on hybrid (structured and unstructured) grids with second order spatial and temporal accuracy. Subgrid stresses are described by the Smagorinksy model. The

flame/turbulence interactions are modeled by the Thickened Flame (TF) model.[29] The spatial discretization is based on the finite volume method with a cell-vertex approach, combined to a numerical scheme derived from the Lax-Wendroff scheme. AVBP has been validated/used for a considerable number of configurations.[30–32]

In[19] the computation of the combustion noise from the EC2 combustor was carried out with two different grid resolutions: A 'coarse' mesh of 3 million cells and a 'refined' mesh of 10 million cells. It was found that both meshes reproduced sufficiently well PIV measurements[33] when considering mean quantities. On the other hand, when RMS values were considered only the refined mesh results agreed well with the experimental results. Figure 3 shows the axial velocity profiles along the cuts displayed in Fig. 2

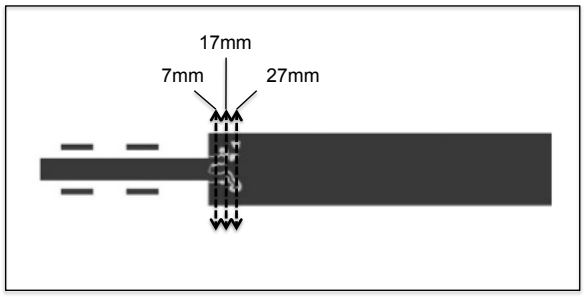

Figure 2. Section cuts for velocity profiles

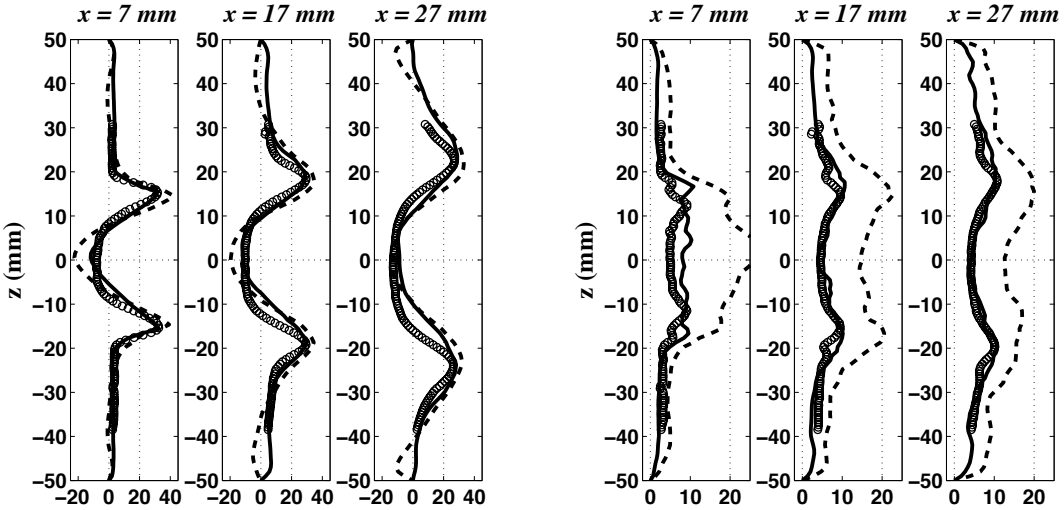

(a) Mean Axial Velocity (b) RMS Axial Velocity

Figure 3. Velocity Profiles: ∘ Experimental PIV measurements

− − − LES 3 million cells, ——— LES 10 million cells

Reproducing flow dynamics in a proper way (see RMS values for the refined mesh in Fig. 3) does not mean necessarily a good estimation of combustion noise. Computation of combustion noise is very challenging, since a good prediction of the rate of change in the flame surface area must be achieved.[34] Figure 4 shows the Sound Pressure Level (SPL) spectrum at microphone 7 (see the location of $M7$ in Fig. 1) for the computations with the refined and coarse meshes as well as the experimental measurements.[33]

It has been observed that in order to correctly evaluate the dynamics of a flame and the acoustics generated by this one, the resolution of the computation (resolution of the mesh and order of the numerical scheme) is of significative importance. The gap seen in fig. 4 between experimental results of the acoustic spectrum and the refined LES is problably due to the lack of resolution of the computation. For this purpose,

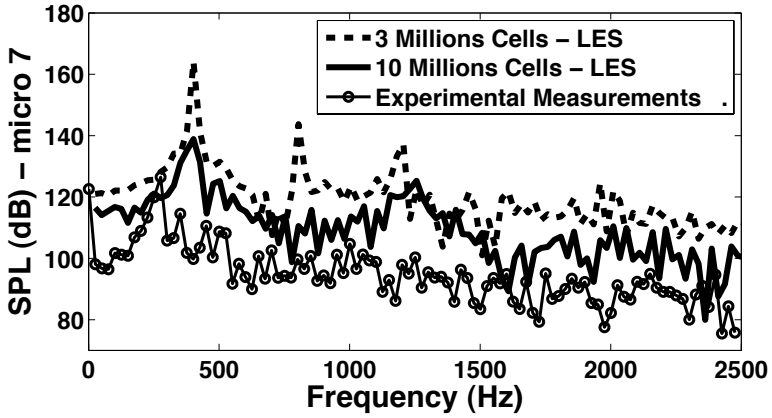

Figure 4. Sound Pressure Level

a computation with 50 million cells is currently being conducted.

Although the estimation of combustion noise through direct computation does not match experimental measurements, it is still a good exercise of analysis to compare direct computation results to those given by hybrid methods. For this comparison to take place, it is assumed that pressure fluctuations from LES contain a negligible amount of hydrodynamics. This comparison is carried out for the 10 million cells mesh and is independent from experimental data.

Overall good agreement is found between both direct and hybrid approaches, as shown if Figs. 5 and 6 which shows the sound pressure levels obtained for microphones 5, 6 and 7 (see the location of $M5$, $M6$ and $M7$ in fig. 1) .

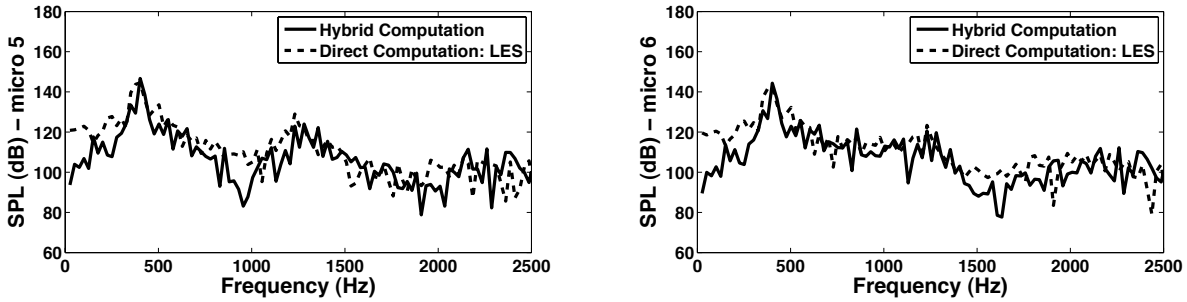

Figure 5. Sound Pressure Levels from the direct and hybrid approaches

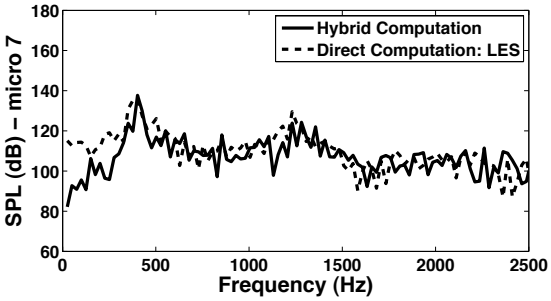

Figure 6. Sound Pressure Levels from the direct and hybrid approaches

Observing with attention fig. **??**, it is noticeable that there are some zones of the spectrum in which an important gap is present between hybrid and direct computations. It is probable, considering the direct computation, that the fluctuations of pressure coming from LES are composed by both acoustic and hydrodynamic contributions. On the other hand, presure fluctuations coming from the hybrid computation are totally due to acoustics. A suitable comparison is then not carried out, and it becomes important to be able to extract acoustics from LES computations in order to evaluate in a proper way the results from the hybrid computation.

V. Filtering a LES pressure field to find the corresponding acoustic field

Velocity fluctuations obtained by LES are composed by both hydrodynamics and acoustics

$$u'_{i,LES} = u'_{i,hyd} + u'_{i,ac} \tag{5}$$

Appling the operator $\partial/\partial t$ to Eq. 5 leads to

$$\frac{\partial u'_{i,LES}}{\partial t} = \frac{\partial u'_{i,hyd}}{\partial t} + \frac{\partial u'_{i,ac}}{\partial t} \tag{6}$$

From linear acoustics, the momentum equation is given by

$$\rho_0 \frac{\partial u'_{i,ac}}{\partial t} = -\frac{\partial p'_{ac}}{\partial x_i} \tag{7}$$

where $[]_0$ and $[]'$ represent respectively the mean and fluctuating flow. Combining this term of eq. 7 into Eq. 6

$$-\frac{1}{\rho_0}\frac{\partial p'_{ac}}{\partial x_i} + \frac{\partial u'_{i,hyd}}{\partial t} = \frac{\partial u'_{i,LES}}{\partial t} \tag{8}$$

Finally the divergence operator to this equation is applied

$$-\frac{\partial}{\partial x_i}\left(\frac{1}{\rho_0}\frac{\partial p'_{ac}}{\partial x_i}\right) + \frac{\partial}{\partial x_i}\left(\frac{\partial u'_{i,hyd}}{\partial t}\right) = \frac{\partial^2 u'_{i,LES}}{\partial x_i \partial t} \tag{9}$$

A. Finding $\frac{\partial \mathbf{u_{i,hyd}}}{\partial \mathbf{x_i}}$

Neglecting viscosity, species diffusion and heat conduction the Navier-Stokes equations for reacting flows read

$$\frac{\partial \rho}{\partial t} + \rho \frac{\partial u_j}{\partial x_j} + u_j \frac{\partial \rho}{\partial x_j} = 0 \tag{10}$$

$$\rho \frac{\partial u_i}{\partial t} + \rho u_j \frac{\partial u_i}{\partial x_j} = -\frac{\partial p}{\partial x_i} \tag{11}$$

$$\rho c_p \frac{\partial T}{\partial t} + \rho c_p u_j \frac{\partial T}{\partial x_j} = \dot{q} \tag{12}$$

In the low-Mach number approximation, the thermodynamic pressure P_0 only depends on temperature. The equation of state is simply

$$K_0 = \rho T \tag{13}$$

Replacing Eq. 13 in the left hand side of the Eq. 12 leads to

$$\rho c_p \frac{\partial K_0/\rho}{\partial t} + \rho c_p u_j \frac{\partial K_0/\rho}{\partial x_j} = \dot{q} \tag{14}$$

The temporal derivative of the density in Eq. 10 is combined with Eq. 14. After some algebra, the divergence of the velocity can therefore be expressed as:

$$\frac{\partial u_j}{\partial x_j} = \frac{1}{c_p K_0}\dot{q} \tag{15}$$

This velocity field is supposed to be composed only by hydrodynamics, due to the fact that in the low Mach number model the acoustic wave length is infinitely long. One can state that the divergence of the fluctuating velocity is

$$\frac{\partial u'_{j,hyd}}{\partial x_j} = \frac{1}{c_p K_0}\dot{q}' \tag{16}$$

B. Finding the Acoustic Pressure

Injecting Eq. 16 into Eq. 9 leads to

$$-\frac{\partial}{\partial x_i}\left(\frac{1}{\rho_0}\frac{\partial p'_{ac}}{\partial x_i}\right) = \frac{\partial}{\partial t}\left(\frac{\partial u'_{i,LES}}{\partial x_i} - \frac{\dot{q}'}{c_p K_0}\right) \tag{17}$$

or in the frequency domain

$$\frac{\partial}{\partial x_i}\left(\frac{1}{\rho_0}\frac{\partial \hat{p}_{ac}}{\partial x_i}\right) = i\omega\frac{\partial \hat{u}_{i,LES}}{\partial x_i} - i\omega\frac{\hat{\dot{q}}}{c_p K_0} \tag{18}$$

Finally, multiplying everywhere by γP_0

$$\frac{\partial}{\partial x_i}\left(c^2\frac{\partial \hat{p}_{ac}}{\partial x_i}\right) = \underbrace{i\omega\gamma P_0\frac{\partial \hat{u}_{i,LES}}{\partial x_i}}_{T1} - \underbrace{i\omega\frac{\gamma P_0\hat{\dot{q}}}{c_p K_0}}_{T2} \tag{19}$$

It has been found by the author that the contribution of $T2$ can be neglected. As a consequence, one can state that for a reactive flow the divergence of the hydrodynamic velocity field ($\frac{\partial u_{hyd}}{\partial x_i}$) can be considered zero as typically done for non-reactive flows. Equation 19 simplifies

$$\mathcal{F}(\hat{p}_{ac}) = \frac{\partial}{\partial x_i}\left(c^2\frac{\partial \hat{p}_{ac}}{\partial x_i}\right) = i\omega\gamma P_0\frac{\partial \hat{u}_{i,LES}}{\partial x_i} \tag{20}$$

VI. LES Vs Hybrid Results

Figures 7 and 8 shows the Sound Pressure Level (SPL) given by the solution of Eq. 20 (LES 'Filtered') and the hybrid computation for microphones 5, 6 and 7.

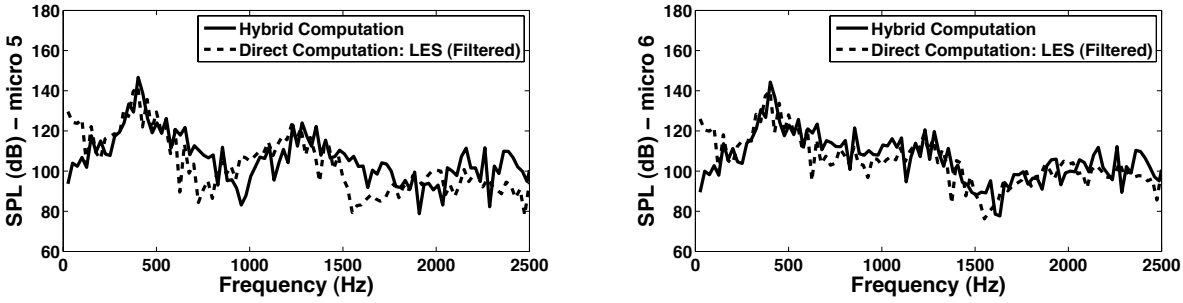

Figure 7. Sound Pressure Levels from the direct and hybrid approaches

After extracting the acoustic field from the complete pressure fluctuation field, it is seen that results match pretty well with the values predicted by the hybrid method, especially for microphones 6 and 7. There is a high contain of hydrodynamic fluctuations at low frequencies (before 400 Hz) that has been removed. Also

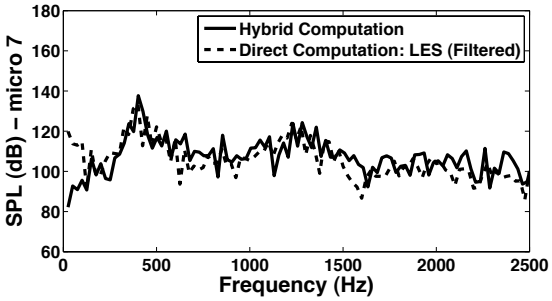

Figure 8. Sound Pressure Levels from the direct and hybrid approaches

the local minimum around 1500 Hz shown in the SPL spectrum for microphone 6 is well recovered after extracting acoustics from LES. The acoustic signal corresponding for microphone 5 present on the contrary, important differences with respect to the one computed by the hybrid approach. The local minima around 1000 Hz corresponding to the hybrid method is recover at a lower frequency (around 750 Hz).

Note that some caution must be taken when computing the Fourier transform of the divergence of the velocity (See T1 Eq. 19). If a rectangular window is applied to the temporal signal, a really good correspondance is seen only for frequencies lower than 400 Hz. On the other hand, if a gaussian window is applied, a good filtering is seen over the entire frequency band, except at a very low frequencies. This is the case for the spectra shown (Figs. 7 and 8) where the signal does not capture the good acoustic level before 200 Hz.

VII. Conclusions

It has been shown that when aiming to compute combustion noise in confined domains by a direct method (LES in this case), the pressure field obtained contains both acoustics and hydrodynamics. Moreover, hydrodynamics was proved to be strong at low frequencies and hence, using a LES pressure field to estimate combustion noise is not enough: extracting acoustics from the complete pressure field is essential. In this paper, a procedure to separate acoustic from hydrodynamics has been proposed. A validation of this procedure is made by comparing the resulting signal to combustion noise predicted by a Hybrid method.

Acknowledgments

This work was supported by the Fondation de Recherche pour l'aéronautique et l'espace (FRAE) through the BRUCO project. The authors also gratefully acknowledge the Centre Informatique National de l'Enseignement Supérior (CINES) for giving access to parallel computers and École Centrale Paris for the interesting discussions and experimental data.

References

[1]A. Oberai, F. Roknaldin and T. Hughes "Computation of Trailing-Edge Noise Due to Turbulent Flow over an Airfoil" AIAA Journal, **40** 2206 - 2216 (2002).

[2]D.J. Bodony and S. K. Lele "On the current status of jet noise predictions using Large-Eddy Simulation" AIAA Journal, **46** 364 - 380 (2008).

[3]H. Pitsch and H. Steiner, "Large-eddy simulation of a turbulent piloted methane/air diffusionn flame (Sandia flame D)" Phys. Fluids , **12**, 2541-2554 (2000).

[4]M. Ihme, H. Pitsch and H. Bodony "Radiation of Noise in Turbulent flames" Proc. Comb. Inst., **32**, 1545-1554 (2009).

[5]F. di Mare, W. Jones and K. Menzies "Large eddy simulation of a model gas turbine combustor" Combust. Flame, **137**, 278-294 (2004).

[6]A. S. Lyrintzis "Integral acoustic methods: From the (cfd) near-field to the (acoustic) far-field" Int. J. Aeroacoustics, **2**, 95-128 (2003).

[7]C. Bailly, C. Bogey and S. Candel "Modelling of sound generation by turbulent reacting flows" Submitted to Int. J. Aeroacoustics (2009).

[8]M. Wang, S. Moreau G. Iaccarisno and M. Roger "LES prediction of wall-pressure fluctuations and noise of a low-speed

airfoil" Int. J. Aeroacoustics, **3** (2009).

[9]S. Bragg "Combustion noise" J. Inst. of Fuel, **36** 12-16 (1963).

[10]M. J. Lighthill "On sound generated aerodynamically: I. General theory" Proc. R. Soc. London Ser. A, **222** 1 - 32 (1954).

[11]W. C. Strahle "On Combustion Generated Noise" J. Fluid. Mech., **49** 399 - 414 (1971).

[12]S. Kotake "On combustion noise related to chemical reactions" J. Sound Vib., **42** 399-410 (1975).

[13]R. Ewert and W. Schröder. "Acoustic perturbation equations based on flow decomposition via source filtering" J. Comput. Physics, **188** 365 - 398 (2003).

[14]C. Bailly and D. Juvand "Numerical solution of acoustic propagation problems using Linearized Euler Equations" AIAA Journal, **38** 22 - 29 (2000).

[15]M. Roger "Aeroacoustics of wall-bounded flows" Von Karman Institute For Fluid Dynamics. Lecture Series. March 9-13 (2009).

[16]N. Curle "The influence of solid boundaries upon aerodynamic sound" Proc. R. Soc. London Ser. A 231, (1955).

[17]H.G. Davies, J.E. Ffowcs Williams "Aerodynamic sound generation in a pipe" J. Sound Vib., **161** 2 (1981).

[18]C. Schram "A boundary element extension of Curle's analogy for non-compact geometries at low-Mach numbers" J. Sound Vib., **322** 264-281 (2009).

[19]C.F. Silva, M. Leyko, F. Nicoud and S. Moreau "Assesment of combustion noise in a premixed swirled combustor via Large-eddy simulation" Submitted to J. Computer and Fluids, (2009).

[20]O. M. Phillips "On the generation of sound by supersonic turbulent shear layers" J. Fluid Mech., **9** 1-28 (1960).

[21]F. Williams "Combustion Theory" The Benjamin/Cummings Publishing Company (1985)

[22]H. Hassan "Scaling of combustion-generated noise" J. Fluid Mech., **49** 445-453 (1974).

[23]A. Pierce "Acoustics. An introduction to its physical principles and applications" Chapter 1 (1991).

[24]F. Nicoud et al. "Acoustic Modes in Combustors with Complex Impedances and Multidimensional Active Flame" AIAA Journal, (2007).

[25]V. Frayssé et al. "A Set of GMRES Routines fo Real and Complex Arithmetics on High Performance Computers." CERFACS Technical Report, (2003).

[26]A. Lamraoui et al. "Acoustic reconstruction of the fuel and air feeding line impedances in a swirled burner during combustion instabilites" In *3rd European Conference for Aerospace Sciences EUCASS* (2009).

[27]A. Lamraoui et al. "Methodology for on the fly acoustic characterization of the feeding lines impedances in a turbulent swirled combustor" In *Proceedings of ASME Turbo Expo 2010: Power for Land, Sea and Air* (2010).

[28]AVBP Code: *http://www.cerfacs.fr/4-26334-The-AVBP-code.php* and *http://www.cerfacs.fr/4-25719-Publications.php*, (2010)

[29]O. Colin et al "A thickened flame model for large eddy simulations of turbulent premixed combustion" Phys. Fluids **12**, 1843-1863 (2000)

[30]L. Selle et al. "Compressible Large-Eddy Simulation of turbulent combustion in complex geometry on unstructured meshes" Combust. Flame. **137**, 4, 489-505 (2004)

[31]S. Roux et al. "Studies of mean and unsteady flow in a swirled combustor using experiments, acoustic analysis and Large Eddy Simulations" Combust. Flame. **141**, 40-54 (2005)

[32]S. Mendez and F. Nicoud "Large eddy simulation of a bi-periodic turbulent flow with effusion" J. Fluid Mech., **46**, 2623-2633 (2008)

[33]N. Tran "Influence de la condition limite acoustique amont sur les instabilités de combustion de grande amplitude: Conception d'un systéme robuste de contrôle d'impédance" Phd Thesis. Ecole centrale Paris. (2009)

[34]P. Clavin, E. D. Siggia "Turbulent premixed flames and sound generation" Combust. Sci. Technol. **78** 147-155 (1991)

[35]T. Schuller, D.Durox and S.Candel "Dynamics of and Noise Radiated by a Perturbed Impinging Premixed Jet Flame" Combust. Flame. **128** 88-110 (2002)

[36]T.D. Butler, P.J. O'Rourke "A numerical method for two-dimensional unsteady reacting flows" 16th Symp. (Int.) on Combustion. The Co